Technische Universität München

Fakultät für Maschinenwesen

Lehrstuhl für Nukleartechnik

Variance Reduction in Calculations of Non-Target Photon and Neutron Doses from High Energy Photon Beam Radiation Therapy via Monte Carlo Simulations

Matthias Immanuel Frankl

Vollständiger Abdruck der von der Fakultät für Maschinenwesen der Technischen Universität München zur Erlangung des akademischen Grades eines

Doktor-Ingenieurs (Dr.-Ing.)

genehmigten Dissertation.

Vorsitzender: Prof. Dr. Tim C. Lüth

Prüfer der Dissertation:

1. Prof. Rafael Macián-Juan, PhD.
2. Prof. Dr. Jan J. Wilkens

Die Dissertation wurde am 11.01.2018 bei der Technischen Universität München eingereicht und durch die Fakultät für Maschinenwesen am 15.10.2018 angenommen.

"Jeder Partikel der Materie kann vorgestellt werden als Garten voller Pflanzen und Teich voller Fische. Doch jeder Zweig der Pflanze, jedes Glied des Tieres, jeder Tropfen der Feuchtigkeit ist wiederum ein solcher Garten - ad infinitum."
Gottfried Wilhelm Leibniz (1646 - 1716)

Abstract

The development of intensity-modulated radiotherapy (IMRT) treatments delivering large amounts of monitor units (MUs), in conjunction with younger ages and longer survival times of cancer patients, recently raised concern about higher risks for secondary malignancies. Precise information about low- and intermediate-level doses outside the treatment field is crucial for a valid risk assessment. However, measurements as well as calculations of out-of-field doses are generally subjected to high uncertainties. In this study, further developed combinations of several variance reduction techniques (VRTs) have been implemented in order to achieve a high precision in Monte-Carlo (MC) radiation transport simulations specifically for the calculation of in- and out-of-field photon and neutron dose equivalent distributions in an anthropomorphic phantom. All simulations have been carried out using the MC-code MCNPX, v.2.7. The computer model included a detailed representation of a Varian Clinac 2100C treatment head and an anatomically realistic whole-body voxel phantom of high resolution. The considered treatment scenario consisted of a prostate 3D-CRT treatment with 4 beam fields at an operation mode of 18 MV. By means of the applied VRTs, very low relative calculation uncertainties for the photon dose equivalent distribution of less than 1 % in-field and below 10 % up to a distance of 35 cm from the field edge could be obtained. Additional neutron dose equivalent, caused by photonuclear reactions in the linear accelerator components at photon energies above about 8 MeV, has been calculated. Relative uncertainties, calculated for each voxel, could be kept below 5 % in most of the voxels of the phantom. Cross sectional photon and neutron dose distributions within the phantom are provided together with the corresponding relative uncertainty per voxel. Furthermore, also organ-averaged photon and neutron equivalent doses were calculated and compared with relevant data available from the literature. The precision in the dose calculations could be pushed to an unprecedented level and now allows a far better estimation of both photon and neutron doses, especially at moderate to large distances from the treatment field where neutrons can become the predominant component of detrimental out-of-field exposure. Applications of this method, among others, are improvements in dose evaluations for sensitive structures, e.g. the fetus of a pregnant patient, and better estimates for late effects such as secondary cancers.

Contents

1 Introduction

This dissertation presents an extended effort in the development of a method to determine detrimental non-target doses to cancer patients in the course of photon radiation therapy treatments. Reliable information about intermediate- and low-level doses outside the treatment field is critical for the risk assessment of developing radiation induced secondary malignancies in the aftermath of radiation therapy. The solution of radiation transport problems involving complex geometries such as the determination of out-of-field doses to a patient, however, poses a highly non-trivial task. In this research project, dose exposures to normal tissues were calculated by means of Monte-Carlo simulations using specific variance reduction techniques. These techniques are essential to overcome the exceptionally high demand for computing power, an intrinsic disadvantage of the Monte-Carlo method when applied to complex radiation transport problems. The work covers development and validation of a Monte-Carlo model representing a medical linear accelerator and is described in detail. Furthermore, the verification of an underlying cross section library, crucial for the Monte-Carlo simulation of neutron contamination during high-energy photon beam treatment, is provided. Finally, the linear accelerator model was applied to simulate a typical treatment scenario involving a detailed, anatomically realistic patient phantom and relevant dose quantities were retrieved.

Section 1.1 of the introduction draws the background of the topic, whereas in section 1.2 the motivation of this thesis is described. Section 1.3 finally outlines the detailed research objectives and gives an overview about the organization of the thesis.

1.1 Background

Besides surgery and systemic therapy, involving chemical, immunological or genetic approaches, radiation therapy is a very commonly used treatment mode in the cure of cancer patients. Radiation treatment, as well as the other treatment techniques, aims at maximal control of the tumor growth under the consideration of sparing normal healthy tissues. Radiation can be delivered to the tumor via placement of radioactive substances in or close to the tumor, called brachytherapy. Another and for most tumor sites preferred approach is the irradiation of the target from the outside, called external beam radiation therapy or teletherapy. Here, several types of radiation can be applied including high-energy X-rays, γ-rays, electrons, protons, neutrons or heavy ions. Although proton and heavy ion radiation therapy is rapidly evolving and become more and more accessible, irradiation with high-energy X-rays still represents by far the most common external beam radiation therapy modality and will continue to play an important role for the treatment of adverse tumors in the near future. High-energy X-rays are produced and delivered to the

patient by means of medical linear accelerators (LINACs). In the early years of external X-ray therapy, tumors were irradiated with coarse, square-fashioned beam field profiles. Often, only single or opposed anterior-posterior and posterior-anterior beam fields were applied. Later, classical conformal X-ray therapy techniques helped reducing high dose exposures to healthy tissues directly adjacent to the tumor. This technique used blocks and compensators specified patient-individually to better conform the beam cross section to the actual shape of the tumor. Multiple gantry angles additionally reduced local dose accumulation in healthy tissue.

The advent of modern diagnostic imaging modalities in the 1970s further enhanced the improvement of dose delivery techniques. Based on closely spaced cross sectional images from the patient anatomy, precise knowledge about the 3-dimensional location of the tumor and adjacent critical structures can be derived. This anatomic information in turn can be used to define target volumes and appropriate margins for 3-dimensional conformal radiation therapy (3D-CRT). Here, the beam field is shaped with so called Multileaf-Collimators (MLCs). MLCs allow a maximal conformation of the beam field to the borders of the target volume by the precise control and adjustment of each of the leafs in the aperture.

An even more advantageous dose distribution can be achieved by delivering beams with non-uniform fluence across the beam fields. This technique is known as intensity-modulated radiation therapy (IMRT). The irregular fluence pattern within a beam field is obtained by the movement of the MLC leafs dividing one beam into several 'beamlets', which, in sum, leads to a non-uniform irradiation in the field plane. The uneven crosssectional total fluence distribution allows IMRT treatment planning with higher dose escalation and tumor control. However, the high number of rather small beamlets required to deliver prescribed doses to the treatment volume generally leads to greater exposures of healthy tissues in the low- and intermediate dose range.

1.2 Motivation of the Thesis

The widespread use of modern radiotherapy techniques such as intensity-modulated radiotherapy (IMRT) applying large amounts of monitor units (MUs) to the patient raised concern about increased non-target organ doses [Fol97, Bre00, Xu08, Tak11]. Those low- and intermediate-level doses, caused by scattered and leakage radiation from LINACs, enhance the risk of radiation induced secondary cancer development and late tissue injuries associated with radiation treatments. The accurate quantification of exposures of healthy tissues and organs at risk (OARs) due to out-of-field radiation has been the issue of many studies in the past. Reviews of articles on this topic are provided by Xu et al. [Xu08] and Takam et al. [Tak11].

In general, there are two approaches to determine dose exposures out-of-field. For this purpose, in vivo measurements or measurements on phantoms simulating the presence of a patient can be used. That includes dose measurements in cubic water or acrylic phantoms as well as in anatomically realistic phantoms consisting of tissue equivalent materials. A disadvantage of this method is that it can be difficult and costly to obtain useful information about the dose distribution within patients. Often, a tradeoff in the accuracy of the results has to be accepted as a consequence of assumptions made in the measurement setups. For example, a reduced complexity of the phantom up to cubic

water phantoms compared with a real patient, a limited number of different phantom materials and simplified material compositions or the averaging of organ doses from a limited number of measurement positions can have significant influence on the quality of the obtained measurement values. Furthermore, measurement uncertainties can be high due to manifold reasons and affect the measurement quality, especially in case of neutron dose equivalent measurements. Kry et al., for instance, measured neutron fluences in the case of a Varian Clinac operating at 18 MV by means of moderated gold foil activation with uncertainties of approximately 10 % [Kry06, Kry07]. In a previous work, a total uncertainty in out-of-field neutron dose equivalent measurements of even 23 % has been assumed [Kry05a]. Various uncorrelated uncertainties contributed to this high value. Among others, there are uncertainties in the count rates of the detectors, the count-rate-to-fluence conversion factor, the fluence-to-dose-equivalent conversion factor and from using only a few neutron energy components for the calculation of dose equivalent as opposed to considering a complete energy distribution. High uncertainties for measurements of detrimental radiation exposures of healthy tissues were also encountered by Wang and Xu, in that case, for the determination of organ equivalent photon-doses by means of MOSFET dosemeters [Wan08].

The second approach in obtaining out-of-field dose information is the calculation of relevant dose-quantities via radiation transport simulations. Accuracy and precision of dose estimates from such simulations greatly depend on the calculation methodology and the level of detail of the computational models used for the LINACs and phantoms. Deterministic calculation methods, however, suffer from inaccuracies affecting the quality of the obtained dose values in particular outside the borders of the treatment field. Howell et al. [How10] and Huang et al. [Hua13], for instance, quantified the accuracy of out-of-field photon doses predicted by commercially available treatment planning systems (TPSs) for clinical treatments carried out with a Varian Clinac 2100. They determined that the TPSs underestimated out-of-field doses by an average of 40 % and 50 %, respectively, over the corresponding ranges of distances from the edge of the field examined. In both investigations, the differences between TPS-calculated doses and doses measured with thermoluminescent detectors (TLDs) increased rapidly with out-of-field distance. Already at distances of about 3.75 cm from the treatment field borders the errors exceeded 25 % and TPS-calculated doses appeared to be rather erratic beyond about 12 cm with errors > 50 %, see figure 1.1.

Monte-Carlo (MC) simulations, on the other hand, are based on random sampling from probabilistic density functions and can offer a higher accuracy, provided that the computational geometry model of the radiation transport problem is sufficiently detailed. MC-simulations with very detailed models, however, demand considerable amounts of time or it is even impossible to get proper results in acceptable timescales at all, making them usually to a 'method of last resort'. Especially out-of-field doses from LINACs are difficult to calculate with the MC-method since contributions from direct and scattered radiation to the dose estimators in these locations are naturally rather low. Hence, only poor precision can be achieved in low- and intermediate-level dose regions without appropriate variance reduction techniques (VRTs). Even with the application of VRTs, it can be challenging to get meaningful results with rather small relative uncertainties in reasonable timescales. Kry et al., for example, investigated out-of-field doses for 6 MV and 18 MV photon beams using the MC-code MCNPX [Kry06, Kry07]. Depending on the dose level, which is

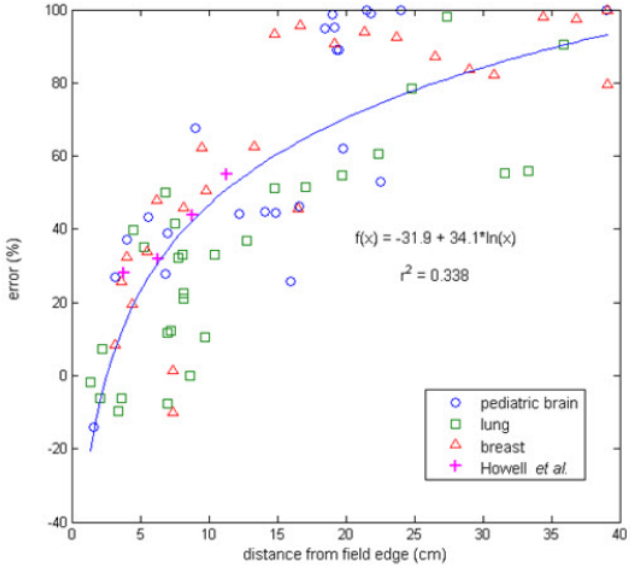

Figure 1.1: Inaccuracy of TPS-calculated photon dose values as a function of distance from the treatment field edge, [Hua13].

decreasing with greater distances to the primary beam field, they calculated out-of-field photon doses with statistical uncertainties of up to 20 % in the case of a 6 MV and 17 % in case of an 18 MV photon beam. In case of secondary neutron dose calculations also other equipment, e.g. the treatment vault, LINAC-gantry and treatment couch, plays a role for the effective dose exposure of the patient, making a solution of the radiation transport problem even more complicated.

In this study, out-of-field equivalent doses in a high-resolution, anthropomorphic phantom of an adult male were calculated following the MC-approach. VRTs were pushed to their limits in order to make the difficult MC-calculations possible and, moreover, computationally affordable. Their successful application relies on a well elaborated combination of parameter sets for every single VRT. In this way, estimated relative uncertainties of calculated absorbed and equivalent doses in each voxel could be kept small over the entire geometry of the phantom, also for distant locations. The obtained results demonstrate a very high degree of precision for non-target organ dose calculations, improving the reliability and usefulness of the information, e.g. for the evaluation of equivalent doses for OARs with a predilection of developing secondary cancer and the subsequent risk assessment of potential late effects and induced secondary malignancies.

1.3 Research Objectives and Thesis Organization

The present PhD. research project aims at the accurate and precise determination of detrimental dose exposures throughout the entire body of the patient during radiation therapy treatment. For this purpose, a fully integrated computer model of a medical LINAC treatment head and an anthropomorphic phantom has been developed. Subsequent MC simulations were performed to achieve the desired results. The following list gives a short overview about the research objectives:

- Development of a Varian Clinac treatment head to greatest possible level of detail including shielding and other surrounding components for the most accurate representation of scatter and leakage radition from the LINAC.
- Validation of the computer model on the basis of available measurement data.
- Integration of a computational, anthropomorphic adult male phantom.
- Benchmark of a newly available photonuclear cross-section data library. This library is used to simulate the production of neutrons via photonuclear reactions within the LINAC treatment head components.
- Application of other, updated radiation transport libraries to guarantee the most accurate handling of the underlying radiation-physical processes.
- MC simulation and precise calculation of photon and neutron organ equivalent doses for specific OARs from a 3D-CRT prostate cancer tretment plan.
- Provision of photon absorbed dose and neutron dose equivalent maps over the entire patient body.
- Uncertainty analysis of selected input parameters.

In chapter 2, all the relevant literature for this project is reviewed. This includes publications about accelerator modeling, especially about detailed LINAC models, and non-target dosimetry regarding external beam therapy. Chapter 3 provides information about the Monte Carlo method in radiation transport problems which will be useful within the scope of this thesis. Section 3.4 about VRTs is of special importance, since VRTs make the precise calculation of useful dosimetric quantities via MC simulations possible in the first place. Some specific perturbation theory for Monte Carlo simulations is explained in section 3.6 as it offers an interesting tool for the sensitivity analysis of calculated dose values under the regimen of uncertain input parameters. Chapter 4 is devoted to the benchmark of the updated photonuclear data library ENDF/B-VII.0. This library serves as a basis for the MC simulation of photonuclear reactions and the production of neutrons in the course of treatment with high-energy photon beams from a LINAC. In chapter 5, the development and validation of the LINAC model is outlined. Furthermore, the integration of an anthropomorphic phantom is described accompanied by details about the treatment setup which will be investigated in terms of non-target dose exposure. The results of photon and neutron dose calculations are presented and discussed in the following chapters. Chapter 8 finally summarizes the conclusions and offers an outlook of future work based on this thesis.

2 Literature Review

This chapter provides an overview about published studies which are relevant for this thesis. In section 2.1 radiation transport studies based on MC-calculations with a detailed modeling of medical LINACs are presented. Section 2.2 covers dosimetry studies for Varian Clinacs on out-of-field doses in air, water phantoms or in simplified tissue-equivalent slab phantoms. These publications include measurement studies as well as studies using MC-calculations and are particularly useful for validation purposes later in this work. Section 2.3 gives a review of publications on measurements or calculations of out-of-field doses and also of organ equivalent doses in anatomically realistic patient phantoms during irradiation with a Varian Clinac. Although several publications will appear in more than one of these sections, this procedure allows a suitable classification of available information and provides a good overview about this topic.

For a more comprehensive review of dosimetry studies on external-beam radiation treatment the reader is referred to Xu et al. [Xu08]. They also list studies with MC-models only consisting of beam-line and beam-shaping components and measurement studies on other LINAC models. Moreover, they also present dosimetry studies on other radiation treatment modalities such as tomotherapy, stereotactic radiation therapy, proton and carbon-ion therapy.

2.1 Detailed Monte-Carlo-Modeling of Medical Linear Accelerators

Simplified accelerator models which omit surrounding support structures, shielding or even tertiary collimators like MLCs are not suitable to accurately predict dose distributions outside the treatment field. The contribution of scattered and leakage radiation from the LINAC to the total dose absorbed by a patient can only be properly estimated if all relevant components are adequately represented in the computer model of the LINAC. Picture 2.1 illustrates the possible paths of radiation particles responsible for undesired exposure of the patient outside the primary treatment field. For secondary neutron radiation, however, also backscattering from other structures like the LINAC gantry, treatment couch or the treatment vault itself has to be taken into account. Effects of modeling different accelerator head and room geometries have been investigated by Pena et al. for a Siemens PRIMUS LINAC [Pen05], see subsection 2.1.2.

In the past, many dosimetric studies have been conducted using simulations with simplified or rather coarse LINAC models. With the ever evolving computer power, however, more and more complex models and radiation transport simulations became feasible. An overview about both, studies with detailed Varian Clinacs as well as studies with Siemens PRIMUS models, is provided in chronological order in table 2.1. Included are specifications such as the investigated secondary radiation, the accelerator model, the Monte-Carlo-code used by the authors, operation energies

and, if applicable, details of the tertiary collimation.

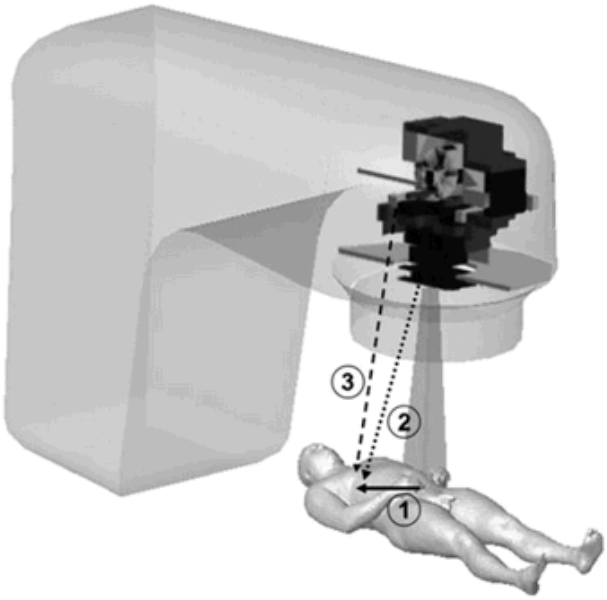

Figure 2.1: Schematic of the contributions to out-of-field doses from medical linear accelerators [DeW13]. (1) Internal patient scatter, (2) scatter from secondary or tertiary collimators and (3) treatment head leakage.

Table 2.1: Detailed Monte-Carlo-models of medical LINACs. Listed are the type of secondary radiation investigated, the LINAC model and details about the implemented model specifications.

Author	Secondary radiation	Accelerator	Model specifications
Mao et al. (1997)	neutron	Varian Clinac 2100/2300C	EGS4/MORSE, 10, 15, 18, 20 MV
Kase et al. (1998)	neutron	Varian Clinac 2100/2300C	EGS4/MORSE, 10, 15, 18, 20 MV
Howell et al. (2005)	neutron	Varian Clinac 2100/2300C	MCNPX, with MLC, 18 MV
Pena et al. (2005)	neutron	Siemens Primus	MCNPX, with MLC
Kry et al. (2006)	photon	Varian Clinac 2100	MCNPX, with 120-leaf MLC, 6 MV
Kry et al. (2007)	neutron and photon	Varian Clinac 2100	MCNPX, with 120-leaf MLC, 18 MV
Becker et al. (2007)	neutron	Siemens Primus	MCNPX, with MLC
Bednarz et al. (2009)	neutron and photon	Varian Clinac 2100C/2300C	MCNPX, with 80-leaf MLC, 6 MV and 18 MV

2.1.1 Varian Clinac Models

In 1997, Mao et al. [Mao97] were the first to develop a rather complex model of a Varian Clinac 2100/2300C. Their geometry description included a total of 85 geometric bodies and was used with the EGS4 Monte-Carlo-code. They presented total neutron yields in different components of the Clinac. Thereafter, Kase et al. [Kas98] used the same model in order to obtain neutron fluence and energy spectra at a number of positions around the LINAC. However, their model didn't consider any tertiary collimation or MLCs. Based on the model from Kase et al., Howell et al. [How05] were the first to calculate neutron production and fluence in and around the treatment head including a MLC. However, the so far most extensive effort in modeling a Varian Clinac 2100 accelerator head and a medical LINAC in general was reported by Kry et al. in 2006 and 2007, with the purpose to calculate out-of-field doses from high-energy photon therapy [Kry06, Kry07]. They considered two operation energies, 6 MV and 18 MV. Geometry and composition of all components were based on a complete set of detailed technical drawings provided by Varian Medical Systems. Beam-line components such as the bremsstrahlung target, primary collimator, flattening filter and jaws were included as well as a detailed 120-leaf Millennium MLC, whose model has been previously developed and validated by Pönisch et al. [Pön06]. Furthermore, also structural elements and shielding components were part of the model.

Some years later, Bednarz et al. described in their paper the development and validation of two Varian Clinac 2100C models of similar complexity, also operating at energies of 6 MV and 18 MV [Bed09c]. With their work, they proved for the first time the feasibility to combine a detailed accelerator model and anatomically realistic computational patient phantoms in order to calculate detrimental doses outside the treatment field by means of MC simulations [Bed08b].

2.1.2 Siemens PRIMUS Models

In 2004, Pena et. al created a Monte Carlo Model of a Siemens PRIMUS consisting of only the beam-line components of the LINAC [Pen04]. In a following work, they modified the model for photoneutron production studies also considering the bending magnet, supporting structures and shielding elements [Pen05]. Using this more complex geometry, they investigated the influence of non-beam-line-components and the walls, floor and ceiling of the treatment vault on the neutron fluence inside the treatment room. As a result, a high dependency of the Monte-Carlo-simulated photoneutron field produced by a Siemens PRIMUS operating at 15 MV on the model complexity of the LINAC and also on the treatment room specifications has been observed. They reported that scattered neutrons account for 8.6 % of the total neutron fluence at the isocenter, 15 % at the position of the treatment couch and 120 % in the room corner.

Becker et al. implemented a detailed Monte Carlo Model to study the photoneutron production of a Siemens Primus and to validate a novel concept of neutron dose measurements [Bec07]. Also part of their study was the assessment of the occupational radiation safety with respect to the neutron source strength of the LINAC operating at 15 MV.

2.2 Varian Clinac Dosimetry Studies without or with Simplified Phantoms

The evolution of radiation treatment technology and the transition from low-energy radiation sources to high-energy LINACs in the 1970s raised concerns about the potential of neutron production by using beam energies in excess of threshold energies for photonuclear reactions. In the following, many dosimetry studies have been performed focusing on the occupational radiation safety (ORS) of operational personnel as listed in [Xu08]. With the growing understanding about potential treatment-induced secondary malignancies numerous dose measurements and calculations were executed to investigate secondary photon and neutron exposures also for the patient covering some of the most widely used radiation therapeutic modalities. In this section only studies on relevant radiation quantities of Varian Clinacs are presented, considering Clinac 2100/2300 C/D or newer models and using no phantoms at all or only simplified homogenous slab or water phantoms. Table 2.2 lists all these publications in cronological order with the name of the author, the method of information retrieval, secondary radiation type under investigation, considered Varian Clinac model and the radiation quantity obtained.

Until the mid 1990s, information on the ORS during the operation of medical LINACs could only be obtained via direct measurements or generic models. The requirements for precise MC radiation transport simulations simply exceeded available computational resources. In 1995, Agosteo et al. were the first to investigate the photoneutron doses in a LINAC radiotherapy room and its entrance maze based on MC-simulations [Ago95]. They particularly paid attention to the effect of neutron absorbers and moderator layers placed upon the maze-walls on the ORS. In 1997 and 1998, respectively, Mao et al. and Kase et al. calculated the neutron fluence around the treatment head of a Varian machine at various beam energies and for the first time using a complex geometry description including more details of the LINAC layout for the radiation transport simulations [Mao97, Kas98]. Kase et al. noted a difference of a factor 2 in the obtained neutron fluences as compared to a simple model geometry description. In fact, their photoneutron yields were in reasonable agreement with measured values considering the large uncertainties of both, calculations and measurements. The investigation aimed at a further use of the results for the calculation of neutron transmission through various shielding configurations and labyrinths so that no phantom was applied, neither for the calculations nor the measurements.

To overcome the lack of available and reliable out-of-field dose information a dedicated task group of the American Association of Physicists in Medicine (AAPM) carried out a measurement study on different LINACs from several manufacturers and water or polystyrene phantoms [Sto95]. As a result, they provided an extended dataset of photon doses outside the primary treatment field. With the upcoming IMRT measurements and calculations of undesired doses outside the treatment field had also to take into account the presence of additional tertiary collimation in the form of MLCs. Mutic and Klein [Mut99] and Stern [Ste99] were among the first to investigate out-of-field doses with and without the installation of a MLC. They studied photon beams at 6 MV and 18 MV operation voltage, yet didn't determine additional neutron doses due to photonuclear reactions at the higher operation energy. In the following, several other research groups published measurement data on out-

of-field photon doses from Varian Clinac models [Van04, Kle06, Ref06, S.06, Sha06, Kry06, Kry07]. The complete dataset of photon doses in a water phantom provided by Kry et al. will be used for the validation of the MC-model in this thesis.

In 2003, an extensive effort was made by Followill et al. to measure the neutron strengths of 36 linear accelerators at high beam energies, including models from Varian, Siemens, Elekta/Philips, and General Electric [Fol03]. Their intention was to provide a comprehensive set of neutron source strength values, Q, for the LINACs in current clinical operation and for use in room shielding calculations. For all machines they reported a strong dependency of the neutron yields on the energy of the applied primary photon beam. On the other side, some other groups investigated neutron doses out-of-field in the patient plane [d'E01, Van04, How05, Ref06]. Vanhavere et al. compared the lateral photon and neutron dose profiles arising from a 18 MV beam by using free-in-air measurements and measurements in a slab-phantom made of Polymethylmethacrylate (PMMA). Outside the treatment beam, the measurements in the PMMA-phantom showed a fast decrease of both, photon absorbed doses and neutron dose equivalent with increasing depth. However, the drop in the neutron dose equivalent with higher distance to the isocenter is less pronounced than for the photon doses. For this reason, neutron dose equivalent exceeds corresponding photon absorbed doses close to the phantom-surface and at distances to the isocenter of 30 cm or more. Yet at higher depths of a few centimeters or more neutron dose equivalent never reaches the photon dose level, no matter at which distance to the isocenter. Furthermore, Vanhavere et al. compared neutron dose rates between conformal and IMRT treatments at 18 MV. For neutrons, they found no significant differences in the dose rates per MU between both treatment modalities. On the other hand, the higher amount of MUs required for IMRT treatments leads to a generally higher neutron dose exposures for patients. This was confirmed by measurements from Howell et al. [How05] and Reft et al. [Ref06]. Reft et al. also investigated photon and neutron doses from 3DCRT- and IMRT-treatments with a voltage of 6 MV and 18 MV, respectively, considering three different LINAC types. They noticed a significant variance in photon and neutron measurements taken from the different LINAC models. In agreement with findings from Followill et al. [Fol03], Reft reported up to 3 times higher neutron doses for the Varian Clinac model than for other LINAC models.

Chibani and Ma published in 2003 calculated dose distributions from photons, neutrons, protons and alpha particles generated by high-energy photon beams in a tissue equivalent phantom [Chi03]. For their MC simulation study, they considered geometry models of the beam-line components of several different accelerator types. Also Zanini et al. applied a rather simple model of a Varian Clinac 2300 C/D for their simulations of the photoneutron field at the patient plane [Zan04]. Another relevant work is the quantitative analysis of the effects of low-dose ionizing radiation in radiation therapy patients by Lehmann et al. [Leh06]. Although they applied a phantom which slightly mimics the real shape of patient, their study is considered as a work dealing with a simplified phantom and therefore still listed here. Their comparison of TLD measurements and calculations of photon out-of-field doses with the MC code PEREGRINE showed that the MC simulations consistently underestimated the doses by approximately 15 % for a realistic treatment configuration. It was concluded that this is most likely due to a lack of detail in the simulations of the linear accelerator outside the main beam line. Howell et al., for instance, had to use a more complex LINAC model to be able to accurately predict neutron fluences [How05]. Also Kry et al.

applied a high level of detail in the modeled LINAC geometry to compare measured out-of-field dose data from conventional fields with calculated data from MC-simulations [Kry06, Kry07]. Their calculated out-of-field photon doses agreed, in average over the various measurement locations, within an accuracy of 17 % when compared to the measurement data. Neutron fluences were within 19 % difference on average. The level of agreement was considered to be acceptable for many out-of-field dose examinations.

For the risk assessment of secondary malignancies as a consequence of radiation therapy treatments information about organ equivalent doses is required. Although it is not unfeasible to obtain such information also on simplified phantoms, in terms of accuracy the use of anatomically realistic phantoms is strongly indicated in those cases. The next section summarizes all relevant work about dose measurements and calculations on recent Varian Clinacs models with the application of more complex, anthropomorphic phantoms.

Table 2.2: Dosimetry studies with Varian Clinacs and no or simplified patient phantoms in cronological order. The acronym ORS stands for occupational radiation safety.

Author(s)	Method	Secondary radiation	Clinac Model	Quantity
Stovall et al. [Sto95]	measurement	photon	2100C	Out-of-field dose
Agosteo et al. [Ago95]	MC simulation	neutron	2100C	ORS
Mao et al. [Mao97]	MC simulation	neutron	2100/2300C	ORS
Kase et al. [Kas98]	MC simulation and measurement	neutron	2100/2300C	ORS
Mutic et al. [Mut99]	measurement	photon	2300C/D	Out-of-field dose
Stern [Ste99]	measurement	photon	2100C	Out-of-field dose
d'Errico et al. [d'E01]	measurement	neutron	2100	Out-of-field dose
Followill et al. [Fol03]	measurement	neutron	2100/2300C, 2500	ORS
Chibani and Ma [Chi03]	MC simulation	neutron, proton and alpha particles	2160C	In- and Out-of-field dose
Vanhavere et al. [Van04]	measurement	photon and neutron	2100C/D	Out-of-field dose
Zanini et al. [Zan04]	MC simulation	neutron	2300C/D	Out-of-field dose
Howell et al. [How05]	MC simulation and measurement	neutron	2100/2300C	Out-of-field dose
Lehmann et al. [Leh06]	MC simulation and measurement	photon	2100C	Out-of-field dose
Klein et al. [Kle06]	measurement	photon	23EX	Out-of-field dose
Reft et al. [Ref06]	measurement	photon and neutron	2100	Out-of-field dose
Sharma et al. [S.06, Sha06]	measurement	photon	2100C/D	Out-of-field dose
Kry et al. [Kry06]	MC simulation and measurement	photon	2100C, 21EX	Out-of-field dose
Kry et al. [Kry07]	MC simulation and measurement	photon and neutron	2100C	Out-of-field dose
Bednarz and Xu [Bed09c]	MC simulation	photon and neutron	2100/2300C	Out-of-field dose

2.3 Varian Clinac Dosimetry Studies with Anthropomorphic Phantoms

Measurements and calculations of out-of-field doses in air or homogenous slab phantoms provide valuable information on the beam characteristics of medical LINACs. The observed behavior of radiation doses outside the primary treatment field can serve as a first approximation of undesired exposures of healthy tissues and, in consequence, also of the corresponding risks of secondary malignancies due to the irradiation. However, treatment- and patient-specific parameters are not accounted for in those cases. A more accurate assessment of dose exposures to organs at risk (OARs) and the risks arising thereof can be achieved via application of anatomically realistic phantoms. Dosimetry data of this kind are far more sparsely available than information involving only simple patient phantoms. In the following, all relevant publications with recent Varian Clinac models on this topic will be summarized. Table 2.3 gives an overview including some specifications of the studies.

Table 2.3: Dosimetry studies with Varian Clinacs and anatomically realistic patient phantoms in cronological order.

Authors	Method	Secondary radiation	Clinac Model	Quantity
Stovall et al. [Sto04]	measurement and generic model	photon	2100C	Organ equivalent dose
Vanhavere et al. [Van04]	measurement	photon and neutron	2300C/D	Organ equivalent dose
Kry et al. [Kry05a, Kry05b]	measurement	photon and neutron	2100C	Out-of-field dose, Organ equivalent dose
Howell et al. [How06]	measurement	photon and neutron	Trilogy, 23EX	Organ equivalent dose
Wang and Xu [Wan08]	measurement	photon	21EX	Organ equivalent dose
Bednarz and Xu [Bed08b]	MC simulation	photon	2100C	Fetal dose
Bednarz et al. [Bed09b]	MC simulation	photon and neutron	2100C	Organ equivalent dose
Howell et al. [How10]	measurement and TPS calculation	photon	2100	Out-of-field dose
Huang et al. [Hua13]	measurement and TPS calculation	photon	2100	Out-of-field dose, Organ equivalent dose

In 2004, Stovall et al. reconstructed gonadal doses for young adult and pediatric cancer patients undergoing radiation therapy [Sto04]. This epidemiological study focused on genetic effects as a consequence of radiation exposure to humans. They used water phantom measurements to estimate doses for a wide range of treatments and a variety of LINAC models. Then they employed differently sized mathematical phantoms to apply the measured results and to determine doses to ovaries, uterus, testes, and pituitary glands for patients ranging in age from newborn to 25

years. Although those mathematical phantoms had a very simple structure consisting of only a few geometrical bodies approximating the shape of the patient, they are still considered as anthropomorphic here.

In some other studies, organ doses from prostate cancer treatments were measured in anatomically realistic phantoms [Van04, Kry05a, Kry05b, How06, Wan08]. Vanhavere et al. investigated doses in an anthropomorphic RANDO phantom from 6 MV IMRT and 18 MV 3D-CRT treatment procedures [Van04]. Photon and neutron organ equivalent doses were estimated by measurements at relevant organ positions which were determined relatively to the position of the prostate. Kry et al. also compared 3D-CRT and IMRT treatments with respect to organ equivalent doses for a selection of OARs [Kry05a]. Like Vanhavere et al., they measured photon and neutron doses in RANDO phantom and at locations specific for each of the organs of interest. Eventually, dose equivalents were determined at 10 anatomic sites in six organs. In a subsequent paper they published calculated risks of fatal secondary malignancies from IMRT treatments based on data from this evaluation [Kry05b]. Another similar study was carried out by Howell et al. applying the male Alderson Radiotherapy Phantom (ART) constructed of tissue equivalent material [How06]. All authors of these studies agree with the observation that the neutron contribution to organ doses, compared to photons, is relatively more important in distant locations for both 3D-CRT and IMRT treatments at beam energies equal or greater than 15 MeV. Furthermore, effective doses were lower for IMRT than for 3D-CRT due to significantly reduced doses close the treatment target. However, IMRT resulted in increased equivalent doses in many organs not directly adjacent to the treatment volume as consequence of an increased number of MUs for treatment delivery.

Currently, Bednarz et al. are the only group which integrated a detailed LINAC model and complex anthropomorphic phantoms for simulation-based dosimetric studies [Bed08b, Bed08a, Bed09b]. In 2008, Bednarz and Xu published a feasibility study to calculate unshielded fetal doses to pregnant patients in 6 MV photon radiotherapy treatments using Monte Carlo methods [Bed08b]. At the Rennselaer Polytechnique Institute (RPI) in Troy, New York, they developed patient models called the RPI-P series computational phantoms for average pregnant females at the end of 3-, 6- and 9-month gestational periods and compatible with ICRP reference values [Bed08b], see figure 2.2.

In subsequent Monte Carlo simulations they calculated absorbed photon doses to the fetus from various treatment plans using the RPI-P3, RPI-P6 and RPI-P9 phantoms. Although the obtained values were accompanied by uncertainties of up to 10 %, they could demonstrate a flexible and accurate fetal dose assessment using Monte Carlo Methods.

In another work, Bednarz et al. applied the so called RPI-Adult Male Computational Phantom, also an in-house development from the RPI, and calculated organ doses from selected prostate treatment plans [Bed09b]. They also considered treatment plans with beam energies of 18 MeV and investigated the contribution of neutrons to organ equivalent doses. In accordance with the available measurement results, Bednarz et al. observed a major role of neutrons for the organ equivalent doses of organs rather distant to the field edge such as lung, esophagus, thyroid and brain. Calculation uncertainties were rather low for photon doses reaching the worst value of 10 % for the thyroid, whereas neutron equivalent doses were more unprecise with uncertainties up to 30 %, in this case for the esophagus. Both articles, [Bed08b] and [Bed09b], are at least in part

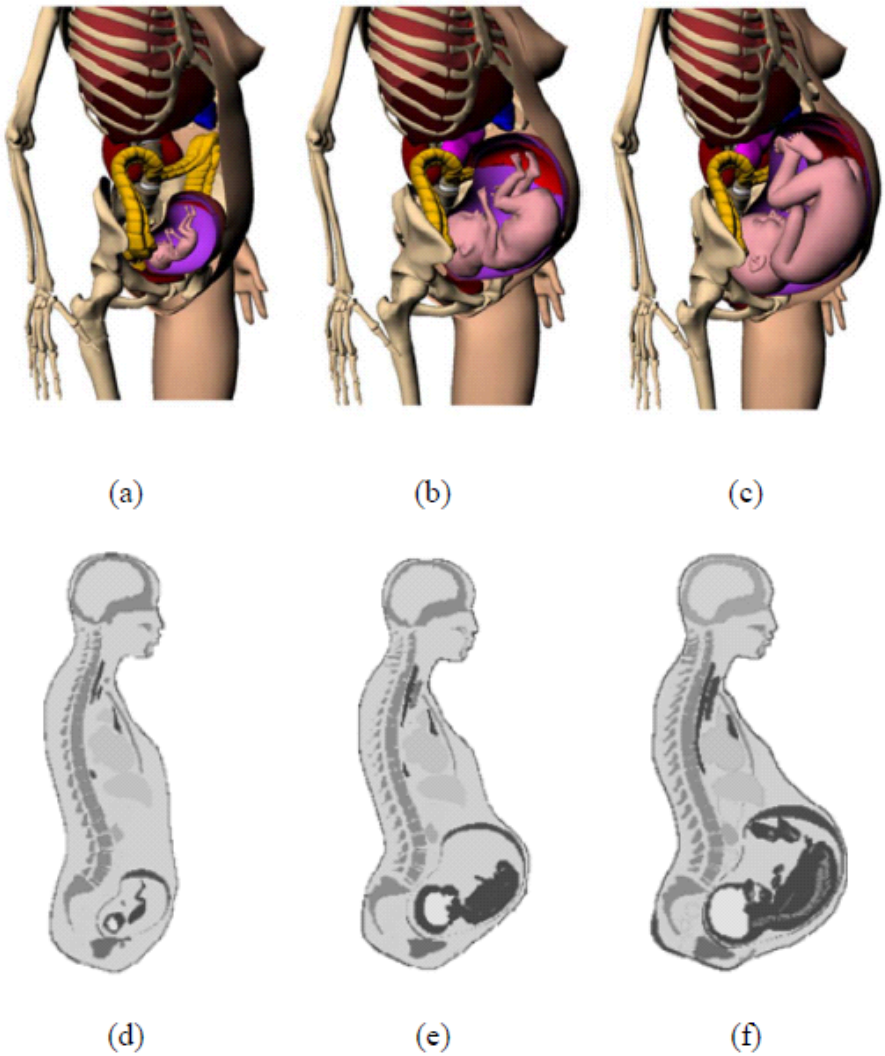

Figure 2.2: Images of the RPI-P series. Subfigures (a),(b) and (c) show 3D representations of pregnant patient models at the end of 3-, 6- and 9-month gestational periods, respectively. (d),(e) and (f) are corresponding sagittal MCNPX plots [Bed08a].

incorporated in Bednarz' thesis [Bed08a].

The works of Howell et al. [How10] and Huang et al. [Hua13], already mentioned in section 1.2, clearly indicate the limitations of commercial TPSs for an accurate determination of doses in the vicinity of the primary treatment field, especially at more distant locations. Both groups compared photon dose measurements and dose values calculated by means of commercial TPSs. Howell et al. used the commercially available TPS Eclipse v8.6 and examined a mantle field irradiation consisting of two opposed anterior-posterior and posterior-anterior 6 MV photon beams. Huang et al., on the other side, made calculations with the Pinnacle v9.0 TPS for three different IMRT treatment plans. The results of both studies showed the TPSs significantly underestimating out-of-field doses. Howell et al. reported an underestimation of 40 % averaged over the range of examined distances to the field edge, whereas Huang et al. observed an underestimation by 50 %

on average at their measurement locations, approaching an error of 100 % at greater distances from the field edge. Both research groups conclude, that, based on their results, the use of TPS-reported peripheral doses could lead to a severe underestimation of secondary cancer induction risks and to a potentially poor clinical decision-making. Thus, they recommend generally not to use TPS-based peripheral dose values for clinical considerations, for instance, in treatment cases of pregnant patients or patients with implantable electronic devices.

3 Monte Carlo Method in Radiation Transport Problems

Monte Carlo methods are a stochastic approach of solving mathematical problems based on the repeated random sampling from known probability density functions, which are specific for the problem considered, in order to obtain numerical results. They can be used in very complex cases where it is difficult or impossible to use other mathematical methods, e.g. deterministic ones. This makes them useful for a wide range of problem classes and applications. The following list of application fields gives just a little glimpse on the broad usage of Monte Carlo Methods:

- Nuclear engineering
- Particle physics
- Radiation protection and shielding
- Medical physics
- Dosimetry and radiation detection
- Astrophysics
- Financial market simulations
- Oil well logging
- Optimization problems

This chapter is devised to give insight into the theory of the Monte Carlo method specifically for radiation transport problems. For this kind of problems, e.g. the dose delivery from a LINAC which has been investigated in the course of this doctoral project, a corresponding Monte Carlo model aiming at the estimation of desired quantities consists in principle of several parts:

- The geometric dimensions of the considered problem scenario. Each Monte Carlo code applicable to radiation transport problems has to provide tools for a proper computational geometric description of the device and/or the part of the environment of interest.
- The different materials assigned to each component of the geometric computer model. For a realistic reproduction of the actual radiation transport of the particles through matter an accurate definition of all the abundant materials in the scenario is mandatory. This definition includes the density of the material as well as its chemical composition, i.e. the atomic or weight fractions of the corresponding elements. In some cases also the isotopic fractions in the elements of the material may play a role.

3.1 Fundamental Terms

This section provides the technical terminology of the Monte Carlo Method for radiation transport problems. It has to be mentioned that the terminology outlined here is MCNP(X)-specific and will be used in the remaining of this thesis. The underlying principles, however, are the same for all common MC codes, e.g. also for FLUKA [Fer05, Böh14] or Geant4 [Ago03]. The following explanations focus on the most fundamental terms and expressions neccessary to develop the subject of this work. A more detailed and comprehensive documentation is given by the Monte Carlo Team at Los Alamos National Laboratory [X-505a, X-505b].

Cell: The entire model universe is specified by geometric units called 'cells'. A Cell contains only one single material or void and its shape is defined by →surfaces also provided in the input of a MC simulation. Cells can have a nearly arbitrary form and complexity.

Cell-Importance ω: Assigning a weight or 'importance' to a cell is a way to draw attention on or off specific parts of the problem geometry. The cell importance plays an important role in the particle population control, see section 3.4.2, ensuring that those geometrical regions with a high influence on the problem solution are sampled properly. If a particle enters a cell with zero importance, the particle is not followed any further and its simulation is hence terminated.

History: The particle history describes its 'destiny' from the source to its end. Due to the application of variance reduction techniques, the history of one primary particle can include several particle paths. Figure 3.1, for instance, shows the history of a neutron passing through a cell with fissionable material.

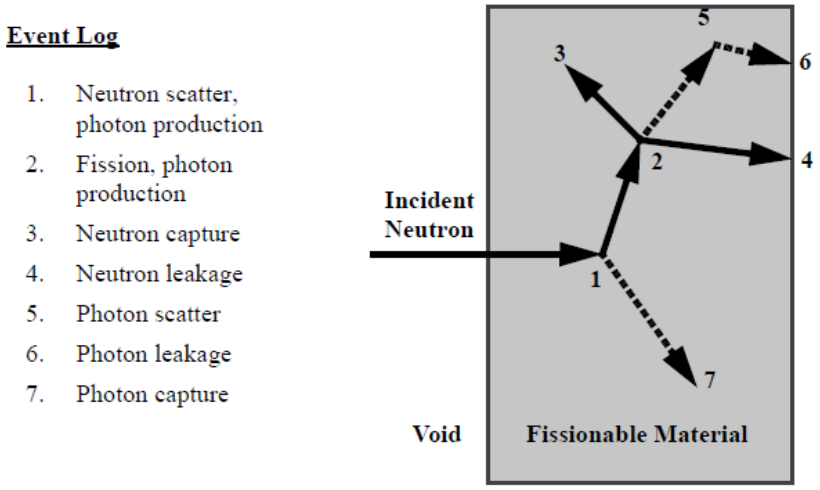

Figure 3.1: Example of a history of a neutron incident on a cell with fissionable material, [X-505a].

Mesh Tally: Mesh tallies are →tallies superimposed on and independent of the problem geometry. A mesh tally stores information separately in each of its meshes. Mesh tallies simplify the determination of a quantity for a high number of equally distributed locations in a problem.

Particle weight W: The particle weight denotes a tally mulitplier assigned to each simulated particle. When a particle with weight W is scored by a tally, its contribution to the tally result is multiplied or 'weighted' by the factor W. In a completely analog Monte Carlo simulation of a physical radiation transport problem, i.e. each simulated particle representing exactly one physical particle, all particles would have unit weight. The particle weights can be changed by variance reduction techniques, see chapter 3.4. They use weighting schemes in order to produce the same mean score of a tally as the natural process, but with far lower calculational than natural variance of the radiation transport process.

Segment: Segments are parts of the path of a simulated particle through the model geometry, see figure 3.6.

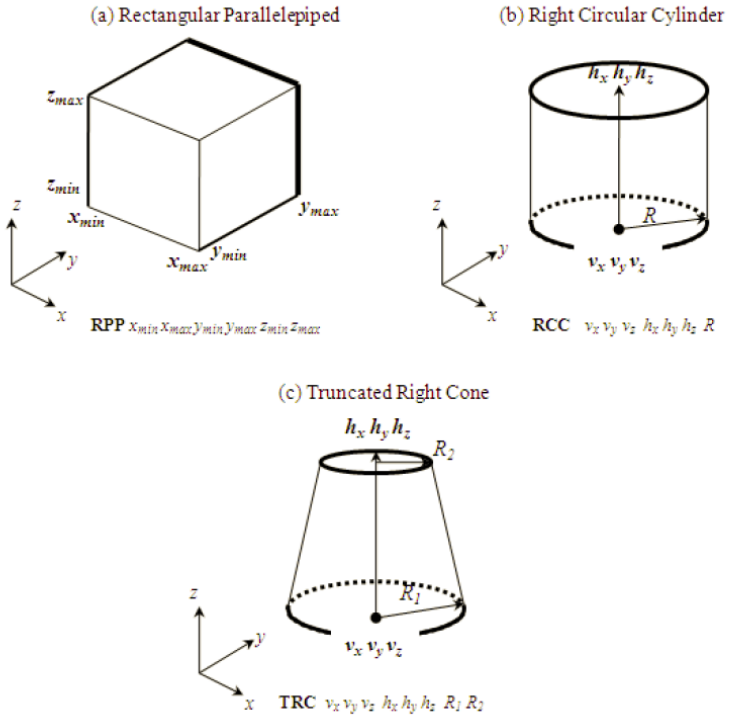

Figure 3.2: Exmples of macrobodies: (a) Rectangular Parallelepiped, (b) Right Circular Cylinder and (c) Truncated Right Cone.

Surface: Surfaces are the delimiters of →cells. They range from simple planes to complex circular or elliptical tori. Combinatorial constructed geometric bodies or 'macrobodies' are an alternative and sometimes more convenient method of defining cells. Figure 3.2 shows some examples of the most commonly used macrobodies. Internally, they are decomposed into standard surfaces with the corresponding surface equations. Each of these surfaces determines one facet of the macrobody and is assigned an individual number according to a predefined sequence which guarantees an unambiguous identification with respect to other standard surfaces. This way, macrobodies can be treated like surfaces and also be mixed with the standard surfaces within one geometry model. All specified surfaces and macrobodies are then used with boolean logic

to define the cells describing the desired geometry. Note, that the abbreviations in figure 3.2, RPP for Rectangular Parallelepiped, RCC for Right Circular Cylinder and TRC for Truncated Right Cone, are MCNP(X)-specific. Also 'surfaces' and 'cells' are MCNP(X)-specific terms. Nevertheless, the concept of surfaces, combined geometric bodies and the process of defining the final geometry by boolean logic can be found also in other MC codes like FLUKA or Geant4.

Tally: A Tally is a virtual detector or estimator of a physical quantity, e.g. the particle flux in a specific region of a geometry or the energy deposition or charge in matter, scoring the contribution of each simulated particle to the solution of the problem. In general, information about the phase space cannot be stored for any point at any time in a MC-calculation (MCC) as this would create an undue demand for memory space. Therefore, desired quantities in one or more regions of interest in the problem geometry have to be specified in advance. In a MC simulation several tallies can be specified storing information, e.g. about the particle current, particle flux, charge through a surface or in a cell or the energy deposition in a cell. Information can also be 'tallied' for a combination of surfaces and surface segments or a combination of cells.

Track: Tracks are parts of the simulated particle path between the crossing of surfaces and/or collision sites. They are created for each particle starting from the source. If a particle is split 2 for 1, e.g. by some variance reduction technique, a second particle track is created with a new particle weight determined by the corresponding VRT and the first track continued with the remaining particle weight. This procedure holds on until all tracks of the initial particle, or, in other words, the whole particle history has ended.

3.2 Material Definition

Each geometric unit or cell in the MC-model of a radiation transport problem has to have exactly one material or void assigned. All materials have to be described as a collection of constituent elements or nuclides and their fractions. The element or nuclide identifiers, in turn, determine which cross-section evaluations will be used in the MC-simulation. The corresponding evaluations have to be made accessible and are referred to via link to the data file location [Pel11].

All materials have to be specified according to a predefined scheme, in MCNPX via so called material data cards. The format of such a material card consists of the material number followed by pairs of ZAID codes and fractions:

Mn ZAID fraction ZAID fraction ...

Here n is the number of the material in the range 1 to 99999 inclusive. The nuclide or element identification number called 'ZAID' uniquely identifies a nuclide or an element. Its form is **ZZZAAA.nnX** where

- **ZZZ** is the atomic number of the element or nuclide.
- **AAA** is equal to 000 for naturally occurring elements, otherwise it is the mass number of the nuclide.

- **nn** is the cross-section evaluation identifier and
- **X** indicates the class of data:
  - for photon interactions X = P
  - for electron interactions X = E
  - for photonuclear interactions X = U

Fractions determine the proportions of nuclides and elements present in the material. If all fractions are positive, then the values are interpreted as atomic fractions. On the other hand, if all fractions are preceded by a minus sign, then MCNPX interprets them as weight fractions. A mixture of positive and negative fractions is not allowed in the same material card. The sum of all fractions doesn't have to be normalized to 1. In case they are not, MCNPX automatically normalizes the fractions to 1, distributing the missing fraction or a surplus proportionally among the specified nuclides and elements of the material.

3.3 Statistical Uncertainties of Monte Carlo Simulations

Due to their stochastic nature the results of MC-calculations are generally subject to uncertainties. It is usually a major task to reduce these uncertainties when MC-simulations are applied to solve a radiation transport problem. This section, essentially based on the descriptions in chapter 2.VI. of [Pel11], shows how calculation uncertainties of MC-simulations are quantified and how the quality of a calculation result can be judged. The following section 3.4 on the other hand provides some strategies and methods to mitigate too high uncertainties.

The quantity of interest in the MC simulation of a radiation transport problem, for example the energy deposition in a specific region, can be expressed analytically as the expected value

$$E(x) = \int x f(x) dx \tag{3.1}$$

of a random variable x whose value depends on the particles' random walk. Here, $f(x)$ is the probability density function of selecting a particle history which scores x to a predefined tally, e.g. the energy deposition tally in a geometry cell scoring the energy deposition from absorbed, scattered or attenuated particles. The function $f(x)$ is often unknown, especially for complex problems. Therefore, MC calculations are used to sample $f(x)$ implicitly, in case of radiation transport problems by simulating the random walk of a large number of particles. The expected value $E(x)$ in equation 3.1 is then approximated by the sample mean

$$\bar{x} = \frac{1}{N} \sum_{i=1}^{N} x_i, \tag{3.2}$$

where x_i is the tally score of the i^{th} history and N is the number of histories calculated in the MC-simulation. In probability theory, x_i would be called the i^{th} particular outcome or *realization* of the random variable x, i.e. the result of a randomly chosen value according to the variable's

probability density function $f(x)$. In the example of an energy deposition tally, x_i would be the energy deposited in the tally region by the i^{th} calculated particle history. Then, the Monte Carlo mean $\bar{x}$ is the average value of the scores x_i from all N histories. Given that the expected value $E(x)$ is finite, the strong law of large numbers states that

$$\bar{x} \to E(x), \text{ for } N \to \infty. \tag{3.3}$$

The variance of the random variable x is then given as

$$Var(x) = \sigma_x^2 = \int (x - E(x))^2 f(x) dx \tag{3.4}$$

$$= E(x^2) - (E(x))^2, \tag{3.5}$$

with the standard deviation σ_x of the possible values for x. Since $f(x)$ is usually unknown, the variance of x cannot be calculated analytically via equation 3.4 or 3.5, respectively. Instead, the true value for the variance can be estimated by calculating

$$s_x^2 = \frac{\sum_{i=1}^{N}(x_i - \bar{x})^2}{N-1} \tag{3.6}$$

$$\approx \overline{x^2} - \bar{x}^2, \text{ for large N.} \tag{3.7}$$

with

$$\overline{x^2} = \frac{1}{N}\sum_{i=1}^{N} x_i^2 \tag{3.8}$$

and s_x as the estimated standard deviation in x. The estimated variance of the mean $\bar{x}$ is now given by

$$s_{\bar{x}}^2 = \frac{s_x^2}{N}. \tag{3.9}$$

The estimated relative statistical error R in the calculation of the approximation $\bar{x}$ can then be expressed by

$$R = \frac{s_{\bar{x}}}{\bar{x}} \tag{3.10}$$

$$= \frac{1}{\bar{x}}\sqrt{\frac{\overline{x^2} - \bar{x}^2}{N}}. \tag{3.11}$$

In a MC simulation, the calculation results for each of the defined tallies are usually accompanied by the corresponding estimated relative statistical errors to be able to interpret the results in an appropriate way. Table 3.1 gives a rough overview about how estimated relative statistical errors[1] have to be related to the reliability of the calculated values.

1 In the following, the estimated relative statistical error is referred to as *relative uncertainty*.

Range of R	Quality of the calculated value
> 0.5	Meaningless
0.2 - 0.5	Factor of a few
0.1 - 0.2	Questionable
< 0.1	Reliable except for point- or ring-detectors
< 0.05	Generally reliable

Table 3.1: Reliability of MC-simulation results

3.4 Variance Reduction Techniques

Monte-Carlo simulations are presently considered to be the most accurate method for the solution of radiation transport problems. On the other hand, its very nature of simulating individual particles and inferring the average behavior of the particles in the system from the average behavior of the individually simulated particles makes the Monte-Carlo method computationally extremely expensive. Indeed, the computer time required by the analog Monte Carlo method is prohibitive and impractical for difficult scenarios as they are common in the application fields mentioned at the beginning of this chapter. In all these cases the probability that the simulation of a particle will contribute to the detector response of interest is too small to achieve a problem solution in reasonable timescales. However, with variance-reducing and biasing techniques the computational efforts required to obtain results of sufficient precision can be reduced dramatically. Here, the expressions variance reduction and biasing refer to fair-game techniques manipulating only the simulation of the radiation particles without distortion of the underlying particle physics.

The kinds of variance reduction techniques suitable to enhance the efficiency of a MC simulation and the selection of appropriate parameters for each technique vary significantly with problem type and objective. Fundamental knowledge of the physics of the problem has to be employed by the user and usually several iterations of adjusting the variance reduction parameter set are necessary to achieve an acceptable level of calculational efficiency. In the following sections different classes of VRTs are introduced and a selection of the techniques most important for this thesis is presented. Among many other types of VRTs all the techniques mentioned in this section are listed in [X-505a]. All details as well as the development process of a useful combination of VRT parameter settings which was finally applied in the dose calculations are provided later in section 5.5.

3.4.1 Truncation Methods

Truncation Methods are the simplest way to reduce computational efforts in MCCs. Parts of the phase space that do not contribute significantly to the solution can be truncated in order to save time.

Geometry Truncation: Unimportant parts of the problem geometry with no or very limited influence on the solution are not included in the model. Implicitly, this is done in every modeling of a

radiation transport problem geometry as the consideration of the entire environment is not only unnecessary but also impossible.

Energy Cutoff: Particles leaving the energy range of interest are terminated so that simulations don't spend computation time anymore in following them. If the energy of a particle falls below a pre-defined threshold its remaining energy is deposited on the spot. This VRT is especially useful for the simulation of charged particles in matter, for example alpha particles or electrons reaching such low energy levels that their remaining potential range in matter becomes negligible.

3.4.2 Population Control Methods

Population Control Methods, on the other hand, are measures to account for the importance of specific regions in the phase space. Important parts of the phase space are those with a significant influence on the estimated output quantity. In regions with high importance the number of particles is increased so that information about possible particle interactions in these areas is well reflected in the tally response. This is done via particle splitting accompanied by a weight adjustment of the produced particles to keep the problem physics unbiased. Vice versa, the number of simulated particles can be decreased by the Russian Roulette method for less important parts of the phase space.

Particle Splitting: Particle splitting is applied at surface crossings. If a particle comes from cell A assigned with importance ω_A and enters cell B with higher importance $\omega_B > \omega_A$, the particle is split into $\frac{\omega_B}{\omega_A}$ particles. The original particle weight W_o is multiplied by the inverse $\frac{\omega_A}{\omega_B}$ and transferred to each of the emerging particles. In case where $\frac{\omega_B}{\omega_A}$ is not an integer, the particle splitting and weighting is done in a probabilistic manner. By adjusting the particle weights, the problem solution remains undistorted in the simulation of a large number of primary particles, since total weight is conserved on average. Particle splitting increases the number of particle tracks with histories leading to a better sampling of important regions. This way, tally variance can be reduced and calculation time saved.

Russian Roulette: Russian Roulette is the counterpart to particle splitting. If the ratio $\frac{\omega_B}{\omega_A}$ of the cell importances is less than one, russian roulette is played, i.e. the particles entering cell B will be killed with probability

$$p = 1 - \frac{\omega_B}{\omega_A}. \tag{3.12}$$

The weight of surviving particles is adjusted again to ensure a fair tally scoring. Surviving particles will receive a weight of

$$W' = W_o \cdot \frac{\omega_A}{\omega_B}. \tag{3.13}$$

Russian roulette is a method to prevent spending too much computational time in sampling regions of small relevance, e.g. regions far away from the tallies with marginal influence on the problem solution.

Weight Windows: With a combination of particle splitting and russian roulette particle weights can be forced to be within a locally specified 'weight window' reflecting the importance of the corresponding region. Weight windows define the limits for the weight of a particle. They can be defined for each cell or as cell-independent mesh-based weight windows superimposed on the problem geometry. Three values, W_U as upper limit, W_L as lower limit and W_S as the survival weight are specified for each window. If a particle enters a cell or mesh with an upper weight-window bound W_U less than its weight, the particle is split (→Particle Splitting). In case it enters the cell or mesh with a weight below the lower limit W_L, it is russian rouletted either setting its weight to W_S or the particle being killed (→Russian Roulette). Figure 3.3 provides an overview of the weight window mechanism.

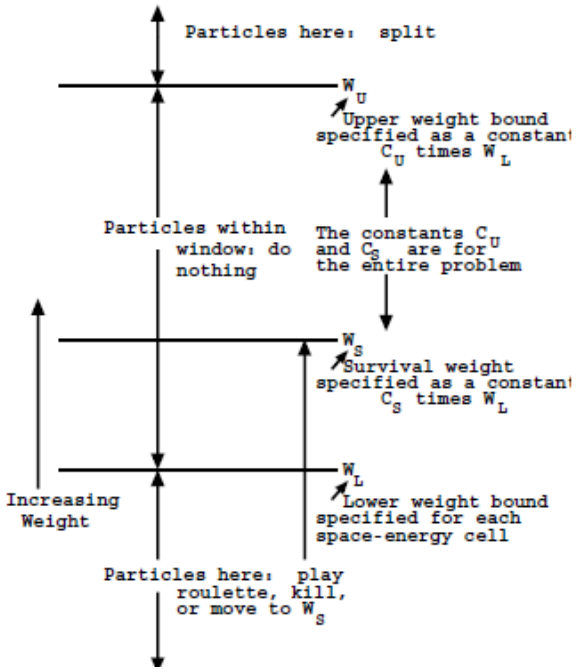

Figure 3.3: Weight Window scheme, [X-505a].

Energy-dependent Weight Windows: Energy-dependent Weight Windows are weight windows limited to predefined energy intervals of the particles under consideration. If the energy range of the particles in a radiation transport problem is wide enough, energy-dependent Weight Windows can further reduce the computational effort taking into account the different physical behavior of particles with different energies.

3.4.3 Modified Sampling Methods

Modified sampling methods introduce a bias in the statistical sampling of specified events of the random walk process in order to increase tally scoring per particle. Particle weights are adjusted in such a way that the sampling of the physically underlying probability density functions finally remains unbiased. Thus, for any Monte Carlo event it is possible to sample from any arbitrary

distribution as long as the particle weight adjustment compensates for the bias. With modified sampling methods probability distributions can be chosen that emphasize particle emission in desired directions or into other desired regions of phase space such as time or energy. Furthermore, even the location or type of particle collisions can be biased using modified sampling.

Implicit Capture: Also known as *Survival Biasing* and *Absorption by weight reduction.* Implicit capture is an efficient VRT applied after each particle collision. The original particle weight W_o is split into a fraction of absorbed weight and a 'surviving' particle weight. With the total microscopic cross section σ_t and microscopic absorption cross section σ_a, the absorption probability is

$$p_a = \frac{\sigma_a}{\sigma_t} \tag{3.14}$$

and the absorbed particle weight is

$$W_a = W_o \cdot p_a. \tag{3.15}$$

The simulation continues with the surviving part of the particle and the remaining weight of

$$W' = W_o - W_a \tag{3.16}$$

$$= W_o \cdot (1 - p_a). \tag{3.17}$$

With this method the time for the simulation of the history of another particle to this point can be saved.

Forced Collisions: Depending on the radiation transport problem, it can be convenient to enforce the simulation of particle collisions in certain cells. Then, entering particles are virtually split into collided and uncollided parts. When Σ is the total macroscopic cross section of the material and d the distance from the particle position to the border of the cell in flight direction, the simulation of the uncollided part of particle continues with an assigned particle weight

$$W_u = W_o \cdot e^{-\Sigma d}. \tag{3.18}$$

The collided part on the other hand will continue with weight

$$W_c = W_o - W_u = W_o \cdot (1 - e^{-\Sigma d}). \tag{3.19}$$

Total weight is again conserved by this VRT:

$$W_o = W_u + W_c. \tag{3.20}$$

Secondary Particle Biasing: Sometimes, secondary particles within a specific energy range of

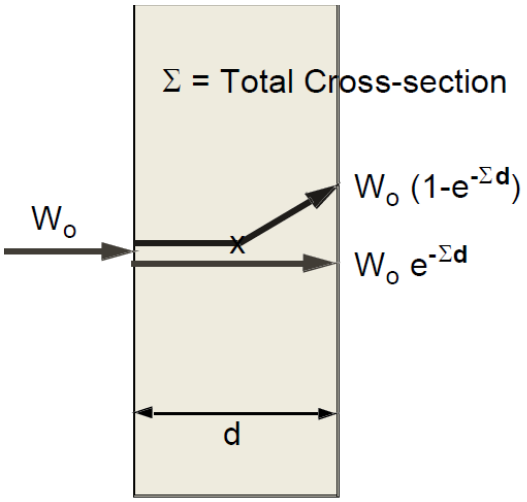

Figure 3.4: Forced Collisions scheme. NB: The flight-vector of the impinging particle does not have to be necessarily perpendicular to the cell border.

the production spectrum can be of more interest than the others. For example, the bremsstrahlung process produces many low-energy photons, but often the high-energy tail of the bremsstrahlung spectrum is more important. In those cases an energy-dependent bias is introduced in the simulation of the secondary particle production making particle tracks within the desired energy range more likely. Appropriate particle weight adjustment is used again to keep the whole method fair and to ensure the simulation of correct physical behavior.

3.4.4 Partially-Deterministic Methods

Partially-Deterministic Methods suspend the regular random walk of simulated particles and apply deterministic-like techniques to transport particles into regions of interest. These techniques include next event estimators and controlling the random number sequence. Only one partially-deterministic VRT has been used within the scope of this thesis.

Point Detector: Point detector tallies provide estimates of the particle flux at a point in the problem geometry. At each source and collision site throughout the Monte Carlo random walk a contribution of the particles to the tally response is calculated deterministically. This way, the variance of a flux estimate can be reduced significantly. The theory behind the deterministic part of this method is outlined in [X-505a, pp. 2-91 - 2-94].

3.5 Energy-Deposition Estimators

Although F6-electron-energy deposition estimators or tallies cause far higher computational efforts in photon dose calculations compared to F6 photon tallies, they take advantage of a much better accuracy. Unlike F6-photon tallies scoring only the energy transfer from photons, F6-electron

tallies calculate energy deposition directly from electrons instead. This difference of kerma and absorbed dose can be important in regions with high dose gradients and electronic disequilibrium such as in the penumbra of the treatment field or near the surface of the phantom at depths less than d_{max}. Kry et al. investigated the relationship between kerma and absorbed dose for a Varian Clinac 2100 operated at 6 MV [Kry06]. Figure 3.5 shows their results for a $10 \times 10\,\mathrm{cm}^2$ field normally incident on a simulated water-tank phantom at 100 cm SSD. Absorbed photon dose is given in the in-plane direction at depths up to 30 cm and 50 cm from the central axis towards the accelerator gantry. Subfigure (b) indicates the deviation between absorbed photon dose and kerma as a local percent difference.

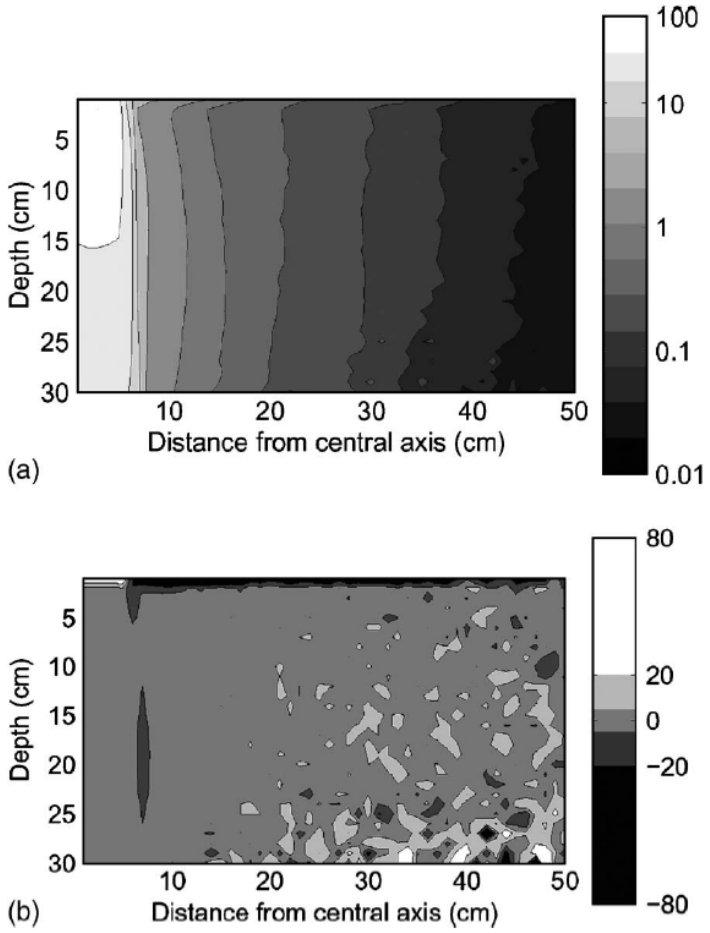

Figure 3.5: (a) Absorbed photon dose in the in-plane from a 6 MV beam with $10 \times 10\,\mathrm{cm}^2$ radiation field. The logarithmic scale is given as a percentage of the maximum dose. (b) %-Difference between photon dose and kerma. Kerma exceeds dose in regions with light gray or white. Dark gray or black denotes a kerma less than dose. Mid-gray indicates agreement within $\pm 5\,\%$, [Kry06]. The alternating differences at higher depth and greater distance to the CAX are artifacts caused by calculation uncertainties and are without physical meaning. Also here an agreement within $\pm 5\,\%$ is expected.

This example clearly demonstrates the systematic error in an approximation of the actual photon

absorbed dose by the kerma and was avoided by using electron-energy deposition tallies in all photon dose calculations in this study.

3.6 Perturbation Theory for Monte Carlo Simulations

In deterministic methods, the sensitivity of a response due to perturbations or small changes in the input data can be determined by performing calculations once with original data and another time including the perturbation. By comparing the corresponding outputs the influence of deviations in the input can be evaluated. This approach remains useful even for very small data perturbations. However, the same strategy is not suitable for Monte Carlo calculations as results are always subject to statistical uncertainties which are superimposed on the tally response. Therefore, small perturbations cannot be detected or quantified precisely enough by comparing the results of two independent calculations. In order to overcome this issue, the differential operator perturbation technique based on the Taylor Series expansion has been developed.

The Differential Operator Technique as it is used in Monte Carlo simulations was introduced in the 1960s by Olhoeft [Olh62], later extended and applied on geometric [Tak70] and cross-section data perturbations [Hal80]. The current implementation of this technique in MCNP covers effects up to the second order but neglects second order cross terms [X-505a]. Nevertheless, it allows the precise determination of the effects of small changes in the problem even if the statistical uncertainty of the calculation is greater than the perturbation. In the following, the basic perturbation theory for Monte Carlo simulations is explained and the Differential Operator Technique is derived.

Let c be a track-length based Monte Carlo response depending on a macroscopic cross-section input data set X. Given the parameter ν, a subset X_ν of X can be defined as

$$X_\nu := \{x_\sigma(E) = C_\sigma(E)e^\nu; \sigma \in \Sigma_P, E \in \boldsymbol{E}\}, \tag{3.21}$$

where σ is an element from a set Σ_P of perturbed macroscopic cross sections, E an energy from a set $\boldsymbol{E}$ of energies and $C_\sigma(E)$ some constant. Note, that the definition of X_ν allows it to be represented by the single parameter ν. Furthermore,

$$\frac{d}{d\nu}x_\sigma(E) = C_\sigma(E)e^\nu = x_\sigma(E) \tag{3.22}$$

and

$$d\nu = \frac{dx_\sigma(E)}{x_\sigma(E)}, \tag{3.23}$$

so that $d\nu$ is just the fractional change in the macroscopic cross-sections of X_ν. This makes the parameter ν useful for sensitivity calculations under perturbed material properties such as density and microscopic cross-sections or even spatial changes. A change Δc in the Monte Carlo response

c due to a deviation $\Delta\nu$ in the input can be expressed by the Taylor Series expansion

$$\Delta c = \sum_n \frac{1}{n!} \frac{d^n c}{d\nu^n} \cdot \Delta\nu^n \tag{3.24}$$

$$= \sum_n u_n \Delta\nu^n, \tag{3.25}$$

where the n^{th}-order coefficient u_n is defined as

$$u_n := \frac{1}{n!} \frac{d^n c}{d\nu^n}. \tag{3.26}$$

The Monte Carlo response c is given by

$$c = \sum_j t_j p_j \tag{3.27}$$

with the tally response estimator t_j and the probability p_j of the particle path segment j. Pathsegment j consists of the tracks in the previous pathsegment $j-1$ plus the current track. Here, t_j is an estimator of c depending only on the last track of pathsegment j. An illustration of the difference between a particle path, pathsegments and tracks is provided in figure 3.6. When r_k is

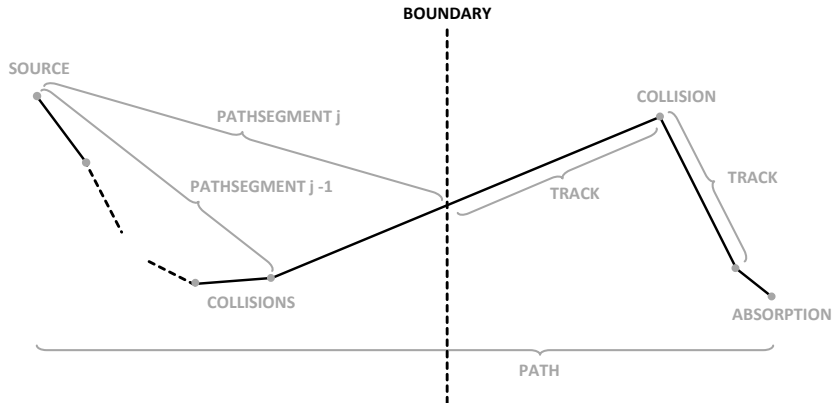

Figure 3.6: Illustration of particle path, path segments and tracks

the probability, that track k occurs, and pathsegment j consists of $m+1$ tracks, then

$$p_j = \prod_{k=0}^{m} r_k. \tag{3.28}$$

The track probabilities r_k can take different forms. If track k starts and ends with a boundary crossing without any collision and track length λ_k,

$$r_k = \exp[-x_{\sigma_T}(E) \cdot \lambda_k], \tag{3.29}$$

where $x_{\sigma_T}(E)$ is the total macroscopic cross section at energy E. Other examples for r_k are detailed in [Hes98] or [X-505a, p. 2-194].

With equations 3.23, 3.27 and the definition of

$$\gamma_{nj} := \sum_{\sigma \in \Sigma_P} \sum_{E \in \boldsymbol{E}} x_\sigma^n(E) \left(\frac{\partial^n}{\partial x_\sigma^n(E)} (t_j p_j) \right) \left(\frac{1}{t_j p_j} \right), \tag{3.30}$$

equation 3.26 can be written as

$$u_n = \frac{1}{n!} \sum_j \gamma_{nj} t_j p_j. \tag{3.31}$$

Some transformations presented in [McK94, Hes98] allow the track-based calculation of the n^{th}-order coefficient to be converted to a history-based one. Then

$$u_n = \frac{1}{n!} \sum_i \left(\sum_{j'} \gamma_{nj'} t_{j'} \right) q_i, \tag{3.32}$$

where the inner sum only involves path segments j' that a part of the particle history i and q_i denotes the probability of history i. Assuming a sample size of N particle histories in the Monte Carlo simulation, the estimate of u_n is

$$\langle u_n \rangle = \frac{1}{Nn!} \sum_i \left(\sum_{j'} \gamma_{nj'} t_{j'} \right). \tag{3.33}$$

Starting with equation 3.33, the first and second order perturbation coefficients can be derived.

First Order Perturbation Coefficient

For the first order, $\langle u_1 \rangle$ is given by

$$\langle u_1 \rangle = \frac{1}{N} \sum_i \left[\sum_{j'} \left(\sum_{k=0}^{m} \beta_{j'k} + R_{1j'} \right) t_{j'} \right] \tag{3.34}$$

with

$$\gamma_{1j'} = \sum_{k=0}^{m} \beta_{j'k} + R_{1j'} \tag{3.35}$$

and $\beta_{j'k}$ and $R_{1j'}$ defined as

$$\beta_{j'k} := \sum_{\sigma\in\Sigma_P}\sum_{E\in\boldsymbol{E}} \frac{x_\sigma(E)}{r_k}\cdot\frac{\partial r_k}{\partial x_\sigma(E)} \tag{3.36}$$

$$R_{1j'} := \sum_{\sigma\in\Sigma_P}\sum_{E\in\boldsymbol{E}} \frac{x_\sigma(E)}{t_{j'}}\cdot\frac{\partial t_{j'}}{\partial x_\sigma(E)}. \tag{3.37}$$

The exact structure of $\beta_{j'k}$ is dokumented in [Hes98]. Together with some modifications and the definition of the tally response estimator [X-505a], $R_{1j'}$ becomes

$$R_{1j'} = \frac{\sum_{\sigma\in\Sigma_P}\sum_{E\in\boldsymbol{E}} x_\sigma(E)}{\sum_{\sigma\in X} x_\sigma(E)}. \tag{3.38}$$

Here, the following cases can be distinguished:

$$R_{1j'} = \begin{cases} 1, & \text{for } \Sigma_P = X, \forall E \\ 0 < \dfrac{\sum_{\sigma\in\Sigma_P}\sum_{E\in\boldsymbol{E}} x_\sigma(E)}{\sum_{\sigma\in X} x_\sigma(E)} < 1, & \text{for } \emptyset \neq \Sigma_P \subset X, \\ 0, & \text{for } \Sigma_P = \emptyset. \end{cases} \tag{3.39}$$

Hence, $R_{1j'}$ is simply the fraction of the perturbed macroscopic cross sections to all macroscopic cross sections involved in the tally. $R_{1j'} = 0$, if no macroscopic cross sections are disturbed. This is the case for the particle fluence or flux tallies F1, F2 and F4 without FM multiplier cards[1].

1 The calculation schemes for a surface current tally F1, a surface flux tally F2 and a cell flux tally F4 are as follows:

$$F1 = \iiiint |\Omega\cdot n|\,\phi(r,\Omega,E,t)\,dA\,d\Omega\,dE\,dt \tag{3.40}$$

$$F2 = \frac{1}{A}\iiiint \phi(r,\Omega,E,t)\,dA\,d\Omega\,dE\,dt \tag{3.41}$$

$$F4 = \frac{1}{V}\iiiint \phi(r,\Omega,E,t)\,dV\,d\Omega\,dE\,dt. \tag{3.42}$$

Obviously, the integrals are independent from macroscopic cross sections so that perturbations thereof are without effect on the tallies.

Second Order Perturbation Coefficient

The differential operator $\gamma_{2j'}$ for the second order perturbation is

$$\gamma_{2j'} = \sum_{\sigma \in \Sigma_P} \sum_{E \in \boldsymbol{E}} x_\sigma^2(E) \left(\frac{\partial^2}{\partial x_\sigma^2(E)} (t_j p_j) \right) \left(\frac{1}{t_j p_j} \right) \tag{3.43}$$

$$= \sum_{k=0}^{m} (\alpha_{j'k} - \beta_{j'k}^2) - R_{1j'}^2 + \left(\sum_{k=0}^{m} \beta_{j'k} + R_{1j'} \right)^2 \tag{3.44}$$

with $\alpha_{j'k}$ defined as

$$\alpha_{j'k} := \sum_{\sigma \in \Sigma_P} \sum_{E \in \boldsymbol{E}} \frac{x_\sigma^2(E)}{r_k} \cdot \frac{\partial^2 r_k}{\partial x_\sigma^2(E)}. \tag{3.45}$$

The explicit calculation of $\alpha_{j'k}$ is outlined in [Hes98]. Then, the estimate of the second order coefficient u_2 is

$$\langle u_2 \rangle = \frac{1}{2N} \sum_i \left[\sum_{j'} \left(\sum_{k=0}^{m} (\alpha_{j'k} - \beta_{j'k}^2) - R_{1j'}^2 + \left(\sum_{k=0}^{m} \beta_{j'k} + R_{1j'} \right)^2 \right) t_{j'} \right]. \tag{3.46}$$

Now, a perturbation of the Monte Carlo response can be approximated using the estimates of the first and second order perturbation coefficients.

Implementation in MCNP

MCNP estimates the perturbation Δc of the tally response with an expansion of equation 3.25 up to the second order:

$$\langle \Delta c \rangle = \langle u_1 \rangle \cdot \Delta\nu + \langle u_2 \rangle \cdot \Delta\nu^2. \tag{3.47}$$

With 3.34 and 3.46, this gives

$$\begin{aligned} \langle \Delta c \rangle = \frac{1}{N} \sum_i \left[\sum_{j'} \left(\sum_{k=0}^{m} \beta_{j'k} + R_{1j'} \right) t_{j'} \right] \cdot \Delta\nu \\ + \frac{1}{2N} \sum_i \left[\sum_{j'} \left(\sum_{k=0}^{m} (\alpha_{j'k} - \beta_{j'k}^2) - R_{1j'}^2 + \left(\sum_{k=0}^{m} \beta_{j'k} + R_{1j'} \right)^2 \right) t_{j'} \right] \cdot \Delta\nu^2. \end{aligned} \tag{3.48}$$

Defining the perturbation factors $P_{1j'}$ and $P_{2j'}$

$$P_{1j'} := \sum_{k=0}^{m} \beta_{j'k} \tag{3.49}$$

$$P_{2j'} := \sum_{k=0}^{m} (\alpha_{j'k} - \beta_{j'k}^2) \tag{3.50}$$

leads to the expression

$$\begin{aligned}
\langle \Delta c \rangle &= \frac{1}{N} \sum_i \left[\sum_{j'} \left(P_{1j'} + R_{1j'} \right) t_{j'} \right] \cdot \Delta\nu \\
&\qquad + \frac{1}{2N} \sum_i \left[\sum_{j'} \left(P_{2j'} - R_{1j'}^2 + \left(P_{1j'} + R_{1j'} \right)^2 \right) t_{j'} \right] \cdot \Delta\nu^2 \qquad (3.51) \\
&= \frac{1}{N} \sum_i \sum_{j'} \left[\left(P_{1j'} + R_{1j'} \right) \cdot \Delta\nu + \frac{1}{2} \left(P_{2j'} - R_{1j'}^2 + \left(P_{1j'} + R_{1j'} \right)^2 \right) \cdot \Delta\nu^2 \right] t_{j'} \qquad (3.52) \\
&= \frac{1}{N} \sum_i \sum_{j'} \left(P_{1j'} \Delta\nu + \frac{1}{2} \left(P_{2j'} + P_{1j'}^2 \right) \Delta\nu^2 \right) t_{j'} \\
&\qquad + \frac{1}{N} \sum_i \sum_{j'} \left(R_{1j'} \Delta\nu + P_{1j'} R_{1j'} \Delta\nu^2 \right) t_{j'}. \qquad (3.53)
\end{aligned}$$

$P_{1j'}$ and $P_{2j'}$ are recorded by MCNP along every track through the perturbed cell. In the case, the response estimator is independent of any perturbed data so that $R_{1j'} = 0$, equation 3.53 is simply reduced to

$$\langle \Delta c \rangle = \frac{1}{N} \sum_i \sum_{j'} \left(P_{1j'} \Delta\nu + \frac{1}{2} \left(P_{2j'} + P_{1j'}^2 \right) \Delta\nu^2 \right) t_{j'}. \tag{3.54}$$

This perturbation value is calculated by default and only corrected by the second term in equation 3.53, if $R_{1j'} \neq 0$.

Accuracy and Limitations of the Perturbation Feature

The first-order perturbation in the tally response estimated by MCNP provides sufficient accuracy for relative perturbations up to 5% of the tally response [X-505a]. For the first and second order, the perturbation estimate is accurate under relative changes less than 20-30% of the tally result. All calculations in this work easily comply with this condition.

Besides, there are other limitations of the MCNP perturbation feature to be mentioned here. In general, it is assumed that perturbations in the relative concentrations or densities of the nuclides involved in the MCC are independent, i.e. second-order differential cross terms in the perturbation output are neglected by MCNP. Possible effects and examples are discussed in [X-505a] and a method for the calculation of second-order cross terms is provided in [Fav01].

Another limitation of the perturbation feature is, that it is not functional for photonuclear

interactions. Therefore, a workaround had to be found in this work to quantify the influence of the uncertainty in the photonuclear cross section data.

4 Photonuclear Cross Section Benchmark for selected Isotopes

Within the scope of this thesis a benchmark of photonuclear cross section data has been performed for a selected set of isotopes. This benchmark was indicated as new evaluated photonuclear cross section data became available and corresponding cross section libraries were released covering a greater number of isotopes. The outcome of the benchmark is presented in this chapter and also has been published previously by the author of this thesis in [Fra16b]. Finally, the benchmarked data and the corresponding cross section library were applied to reproduce photonuclear physics in all simulations of this study with coupled electron-photon-neutron radiation transport, aiming at the most accurate calculation of neutron doses as possible.

Photonuclear physics have long been neglected in the investigation and analysis of radiation transport problems. This was primarily due to a lack of complete evaluated data sets and those available were not amenable to systematic calculation and tabulation [Whi99]. The exclusion of photonuclear interactions was acceptable as systematic errors were rather small in many evaluations. In the past, however, more and more cases were encountered in which photonuclear processes were at least no longer negligible or even represented the most important part of a problem [Bro96, Cha98, Gal96, McC84]. This urged the necessity of developing comprehensive photonuclear data descriptions and a full integration into existing transport codes.

Large international efforts were undertaken to address the first issue. The Nuclear Theory and Application group (T2) at Los Alamos National Laboratory (LANL) produced a set of photonuclear evaluations as a part of the coordinated research project (CRP) under the auspices of the IAEA [Obl98]. In 1999, these evaluations covering photonuclear cross sections and emission spectra of 13 isotopes were released and accepted into the ENDF/B-VI library [Cha99, Cha03]. The results of the entire program, including those from LANL, covered 164 isotopes and were published by the IAEA in 2000 [Cha00]. Essentially based on this data set, a new photonuclear data library was produced as part of ENDF/B-VII.0 and released in 2006 [Cha06]. The corresponding ACE (*A C*ompact *E*NDF) files from LANL for use with MCNPX are called *la150u* and *endf7u* for the whole ENDF/B-VII.0 photonuclear library.

After necessary photonuclear data have been made accessible, existing radiation transport codes had to be updated to be able to handle photonuclear interactions. For MCNPX, this was done by White et al. at LANL [Whi00, Whi03b]. Their work also included the validation of the first photonuclear data set available for MCNPX, *la150u*, with experimental data provided by Barber and George [Bar59]. Other photonuclear benchmark calculations for the transport code COG were performed and published by Heinrichs and Lent [Hei03]. This part of the thesis is devised as a

resumption of White's previous work on the verification and validation of available photonuclear data in connection with MCNPX calculations. Benchmark simulations of all those elements in *endf7u* which are also subject of photonuclear experiments conducted by Barber and George were performed with MCNPX, version 2.7. For the first time, this includes a photonuclear benchmark of natural uranium with MCNPX. Simulation results are compared graphically and in tabular form to experimental values as well as to relevant previous benchmark calculations.

4.1 Experimental Data Basis

In their experiments, Barber and George measured the total neutron yield per incident electron via bremsstrahlung production and subsequent photonuclear reactions for a variety of primary electron energies, target materials and thicknesses. The well documented experimental conditions, parameter and results make their paper a favorable source for comparing integral calculations. The experimental setup is shown schematically in figure 4.1. Their LINAC offered a well characterized electron beam variable over an energy range up to 36 MeV. Absolute beam energies were calibrated to within 2 % error with an energy spread of $\Delta E_0/E_0 = 2\,\%$. Barber and George estimated the absolute accuracy of their results to be $\pm\,15\,\%$.

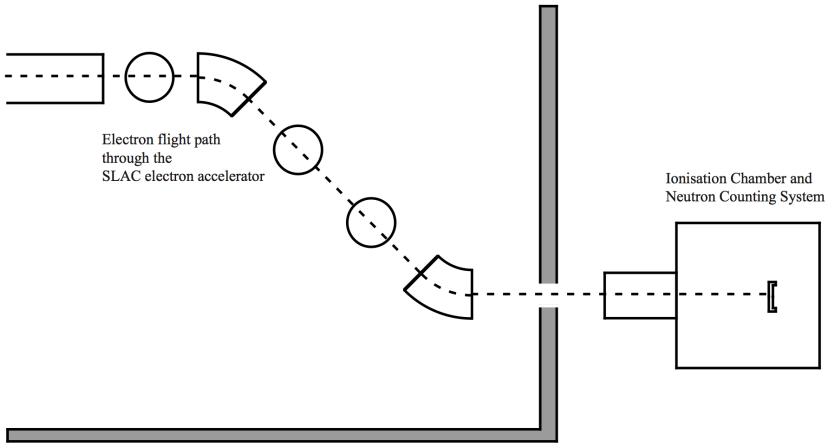

Figure 4.1: Experimental setup for the Barber and George experiments with accelerator, collimators, wedge magnets, ionization chamber and target [Bar59].

4.2 Benchmark Calculations with MCNPX

The computer model setup for benchmark calculations with MCNPX in this study is similar to that used by White in [Whi00, Whi03b] and strictly follows the specifications made by Barber and George. All targets were modeled as 11.43 cm x 11.43 cm square parallelepipeds with varying thicknesses. The electron beam has a diameter of 1.27 cm and is impinging perpendicularly on the target. The effect of variations in the beam energy on the results has been investigated by White and was found to be far lower than the total accuracy of the experiments of $\pm\,15\,\%$ [Whi00].

Therefore and in order to preserve comparability, the electron beams were modeled consisting of mono?energetic electrons like in the works of White et al. [Whi00, Whi03b] and Heinrichs and Lent [Hei03]. The nominal beam energies ranged from 10.3 - 35.5 MeV, see table 3. The neutron yields were calculated as the total neutron current through the 6 facets of the corresponding parallelepiped. The fluence of the photoneutrons escaping the target was determined using a fluence estimator (F1 neutron tally) summing up the neutron fluences through each of the target facets. In total, 10^9 primary electrons were simulated. Furthermore, the following variance reduction techniques were applied in order to achieve the desired statistical precision of the simulation results: Energy cutoffs for electrons and photons just below the photonuclear threshold energies of the corresponding target material and forced collisions for photons within the targets to increase the number of photonuclear reactions.

Photonuclear benchmark calculations from White et al. used the preliminary ACE library *la150u*, whereas in this study the new *endf7u* photonuclear library was applied as well as updated MCNPX standard libraries for neutron, electron and photon interactions, *endf70a - k, el03, mcplib84*. Furthermore, the isotopic material definition for two of the target elements has been improved since the *endf7u* library covers far more nuclides than *la150u*. While *la150u* provides only the isotopes ^{12}C and ^{63}Cu for the elements carbon and copper, *endf7u* also lists the isotopes ^{13}C and ^{65}Cu. Therefore, ^{13}C and ^{65}Cu with their isotopic abundances of 1.1 % for carbon and 30.83 % for copper could be taken into account in the isotopic material descriptions of the targets consisting of naturally occurring carbon or copper, respectively. For carbon, at first sight, this seems to be a rather small change compared to an approximation of natural carbon just with its isotope ^{12}C, but with its lower threshold energy of 4.9 MeV and higher cross sections for photonuclear reactions the presence of ^{13}C might increase photoneutron production yields significantly. On the other side, for Al, Ta and Pb the cross section data are the same for *la150u* and *endf7u* as the photonuclear data

	Density	Thickness	
Target	$[g/cm^3]$	$[g/cm^2]$	$[cm]$
C-I	2.20	38.91	17.6864
Al-I	2.70	24.19	8.9593
Cu-A	8.92	1.372	0.1538
Cu-I	8.92	13.26	1.4866
Cu-II	8.92	26.56	2.9776
Cu-III	8.92	39.86	4.4686
Cu-IV	8.92	53.13	5.9563
Ta-I	16.6	6.21	0.3741
Pb-I	11.34	5.88	0.5185
Pb-II	11.34	11.42	1.0071
Pb-III	11.34	17.30	1.5256
Pb-IV	11.34	22.89	2.0185
Pb-VI	11.34	34.42	3.0353
U-I	18.95	6.17	0.3256
U-II	18.95	12.42	0.6554
U-III	18.95	18.61	0.9821

Table 4.1: Target properties

from LANL simply have been adopted by ENDF/B-VII for these elements. Thus, no significant differences can be expected in the new benchmark simulations compared to White et al. and are included here for the sake of completeness. For uranium, this study provides the first photonuclear benchmark with the transport code MCNPX.

All relevant target parameters and properties are listed in table 4.1. The suffixes I-VI in the target names indicate the target thicknesses rounded to the next multiplicity of one radiation length. Cu-A denotes a "thin" target instead. On the other side, table 4.2 shows the exact isotopic material descriptions for all target elements used in the simulations of this study compared to those used by White [Whi00]. For the COG benchmark calculations, Heinrichs and Lent applied "COGPNUC", a photonuclear data library processed out of the IAEA Photonuclear Data Library [Cha00] for use with the COG transport code. Hence, the material descriptions for the targets of the COG benchmark cover all isotopes also applied in this study, see fourth column of table 4.2.

Table 4.2: Material Description: Isotopic Abundances for Target-Elements

	White, [Whi00]		**This study**	
Target-Element	**Isotope**	**Abundance** [a,b]	**Isotope**	**Abundance** [a,b]
C	^{12}C	98.9	^{12}C	98.9
	-		^{13}C	1.1
Al	^{27}Al	100.00	^{27}Al	100.00
Cu	^{63}Cu	69.17	^{63}Cu	69.17
	-		^{65}Cu	30.83
Ta	^{181}Ta	100.00	^{181}Ta	100.00
Pb	^{206}Pb	24.1	^{206}Pb	24.1
	^{207}Pb	22.1	^{207}Pb	22.1
	^{208}Pb	52.4	^{208}Pb	52.4
U	-		^{235}U	0.72
	-		^{238}U	99.27

[a] in at.%
[b] In case the isotope fractions don't sum up to 100 %, the remaining fraction is distributed proportionally among the abundances of the available isotopes.

4.3 Results

Table 4.3 shows the results of all benchmark calculations. They are compared to experimental values provided by Barber and George [Bar59] and to other benchmark calculations from White et al. [Whi03b] and Heinrichs and Lent [Hei03]. All simulation results of this study had negligible relative uncertainties below 0.1 %. In general, a reasonably good agreement within about 20 % of the experimental values from Barber and George can be observed.

For carbon, White et al. observed an underestimation of the neutron yield, especially at the lowest beam energy with 35 %. They hypothesized that this might be an effect of ignoring the contributions of ^{13}C to the total photoneutron production, which has a far lower neutron production threshold and therefore plays a more important role at lower energy levels. Indeed, significantly higher yields were obtained taking into account the heavier isotope of carbon in the new simulations, see figure 4.2. Although the calculated yields for carbon better agree with those from Barber and George, there is still an underestimation of the neutron yields so that deviations observed by White can only partially be explained by the absence of ^{13}C in the material description of the modeled target.

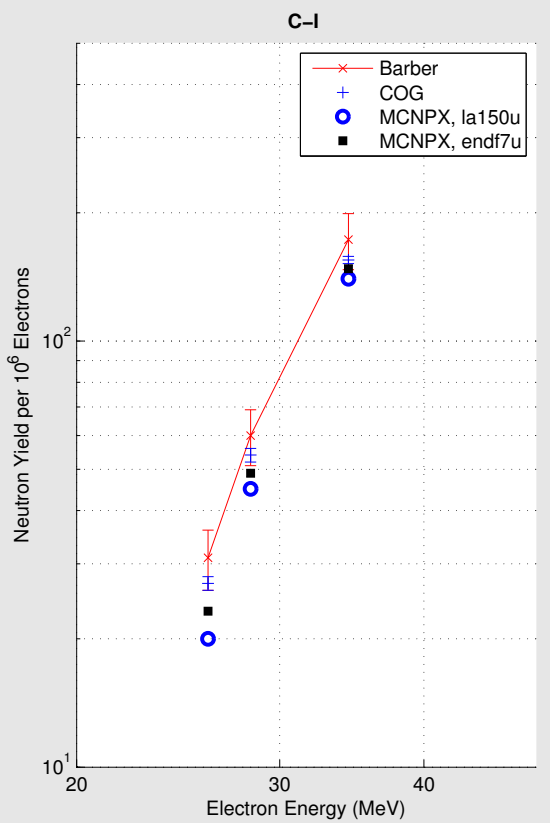

Figure 4.2: Neutron yield per 10^6 electrons incident on the carbon target.

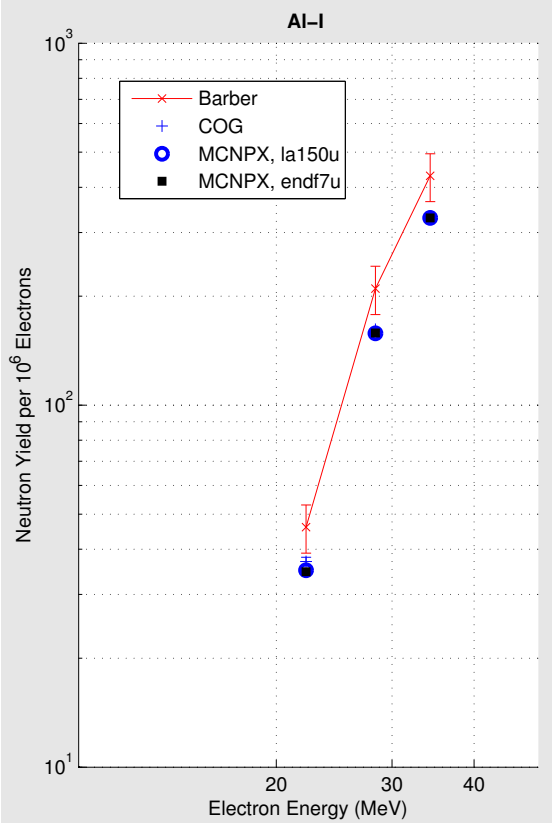

Figure 4.3: Neutron yield per 10^6 electrons incident on the aluminium target.

As expected, the differences between the new calculations and the values from White et al. are

rather insignificant for Al, Ta and Pb, since corresponding cross section data are the same in *la150u* and *endf7u*, see figures 4.3,4.4 and 4.5. Merely for thicker targets slightly lower neutron yields can be observed.

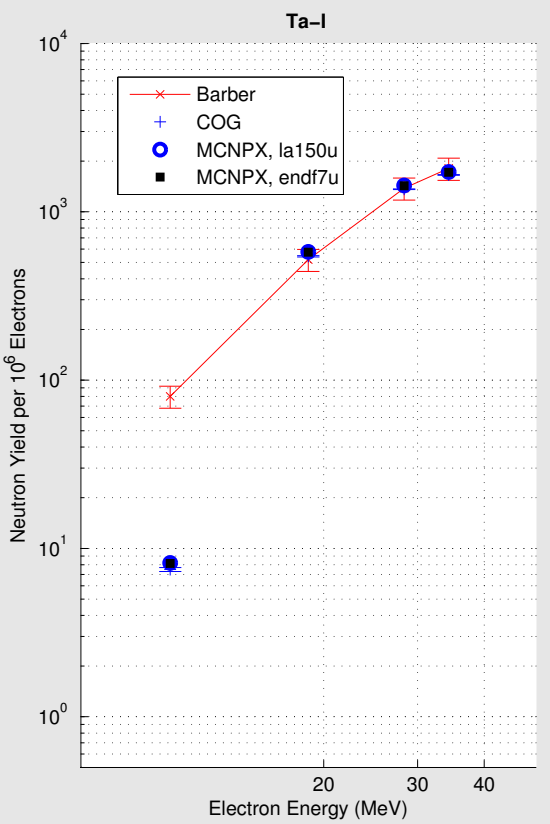

Figure 4.4: Neutron yield per 10^6 electrons incident on the tantalum target.

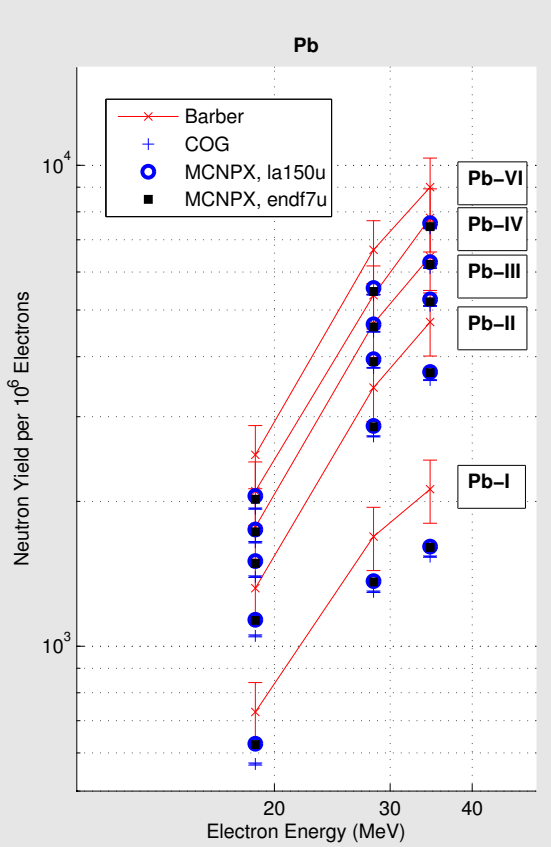

Figure 4.5: Neutron yield per 10^6 electrons incident on the lead targets.

In this study, both stable isotopes ^{63}Cu and ^{65}Cu were considered for calculations with copper targets. Due to this, neutron fluences were consistently higher than those from White et al. [Whi03b]. Although both studies show a similar behavior in the neutron yields for copper, the new calculations offer a better agreement with experimental values except for the low energy beams incident on the thick targets Cu-I -IV. The remarkably large underestimation of the yields for the ”thin” Cu-A target over the entire energy range observed by White et al. could be reduced somewhat, but still remains significant (fig. 4.6). A possible reason for this may be the greater importance of electro-disintegration effects in thin targets which could not be accounted for in the simulations.

In figure 4.7, it can be seen that neutron yields for uranium targets calculated with MCNPX are in good agreement with the values from Barber and George. They show the same behavior as those from COG with an underestimation of the experimental values. This underestimation increases for both COG and MCNPX simulations as energy increases.

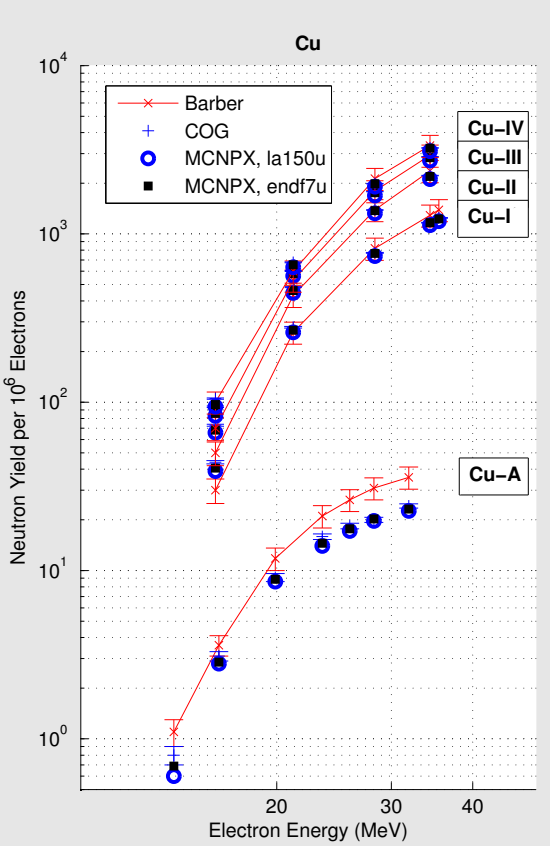

Figure 4.6: Neutron yield per 10^6 electrons incident on the copper targets.

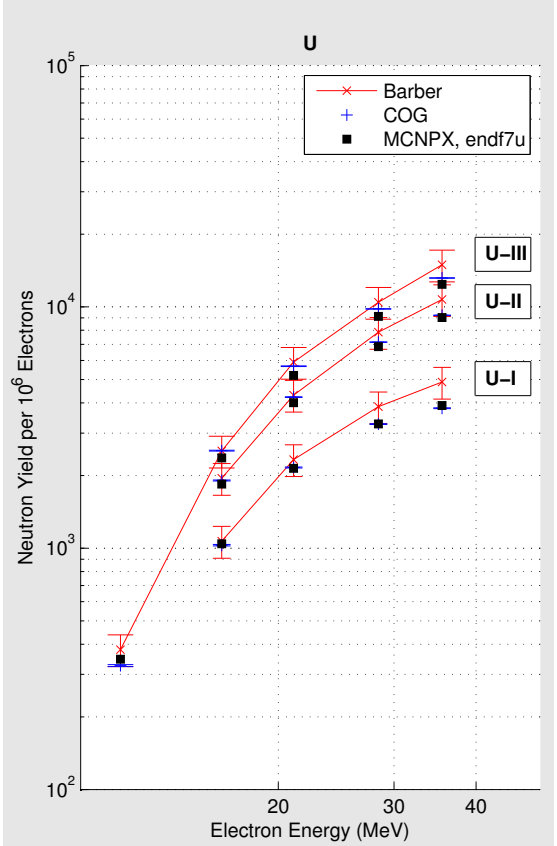

Figure 4.7: Neutron yield per 10^6 electrons incident on the uranium targets.

Generally, the agreement between the experimental data and calculated neutron yields is good. Nevertheless, calculated results appear to be almost consistently low. The integral nature of the experiments as well as of the simulations makes the results sensitive to electron transport, bremsstrahlung production and photon transport processes. Possible systematic errors in the experimental measurements, however, are unknown. Another cause for disagreements between experiments and calculations may be a lack of electro-disintegration effects in the simulations. On the other side, systematic errors introduced by missing isotopes in the material descriptions of the simulations could be avoided almost completely with the *endf7u* library.

Table 4.3: Experimental and calculated neutron yields

Target	Energy	Neutron Yields per 10^6 Electrons				Difference[d]
	(MeV)	Experiment[a]	MCNPX, *endf7u*	MCNPX, *la150u*[b]	COG[c]	(%)
C-I	26.0	31 ± 5	23	20	27 ± 1	−25.1
	28.3	60 ± 9	49	45	54 ± 2	−18.4
	34.4	173 ± 26	148	140	155 ± 3	−14.6
Al-I	22.2	46 ± 7	35	35	37 ± 1	−24.6
	28.3	210 ± 32	158	158	162 ± 1	−24.7
	34.3	430 ± 65	329	329	332 ± 2	−23.5
Cu-A	13.9	1.1 ± 0.2	0.7	0.6	0.8 ± 0.1	−37.4
	16.3	3.6 ± 0.5	2.9	2.8	3.1 ± 0.2	−20.7
	19.9	11.8 ± 1.8	8.9	8.6	9.1 ± 0.5	−24.9
	23.5	21.1 ± 3.2	14.5	14.0	15.9 ± 0.6	−31.2
	25.9	26.3 ± 3.9	17.7	17.2	18.4 ± 0.7	−32.7
	28.2	30.9 ± 4.6	20.2	19.7	20.0 ± 0.7	−34.5
	31.9	35.8 ± 5.4	23.2	22.6	24.2 ± 0.7	−35.2
Cu-I	16.1	30 ± 5	41	39	44 ± 1	35.3
	21.2	260 ± 39	268	260	279 ± 3	3.1
	28.3	820 ± 123	765	739	772 ± 4	−6.7
	34.4	1290 ± 194	1165	1128	1166 ± 5	−9.7
	35.5	1390 ± 209	1228	1189	1245 ± 5	−11.6
Cu-II	16.1	50 ± 8	68	66	73 ± 1	36.4
	21.2	430 ± 65	460	446	483 ± 3	7.0
	28.3	1390 ± 209	1375	1325	1387 ± 6	−1.1
	34.4	2370 ± 356	2194	2117	2221 ± 7	−7.4
Cu-III	16.1	70 ± 11	86	83	94 ± 1	22.5
	21.2	530 ± 80	580	562	602 ± 4	9.5
	28.3	1800 ± 270	1754	1688	1784 ± 6	−2.6
	34.4	2930 ± 440	2834	2729	2873 ± 8	−3.3
Cu-IV	16.1	100 ± 15	97	94	105 ± 1	−3.2
	21.2	600 ± 90	655	634	677 ± 4	9.1
	28.3	2130 ± 320	1987	1910	1989 ± 7	−6.7
	34.4	3350 ± 503	3227	3104	3241 ± 8	−3.7
Ta-I	10.3	80 ± 12	8.1	8.2	7.5 ± 0.2	−89.8
	18.7	520 ± 78	575	578	544 ± 5	10.6
	28.3	1380 ± 207	1427	1433	1362 ± 7	3.4
	34.3	1810 ± 272	1718	1726	1655 ± 8	−5.1
Pb-I	18.7	730 ± 110	625	627	569 ± 3	−14.4
	28.3	1690 ± 254	1360	1366	1298 ± 5	−19.5
	34.5	2120 ± 318	1605	1611	1536 ± 5	−24.3
Pb-II	18.7	1320 ± 198	1131	1135	1051 ± 5	−14.3
	28.3	3450 ± 518	2860	2871	2731 ± 7	−17.1
	34.5	4720 ± 708	3705	3717	3575 ± 8	−21.5
Pb-III	18.7	1770 ± 266	1487	1503	1395 ± 5	−16.0
	28.3	4690 ± 704	3906	3953	3792 ± 8	−16.7
	34.5	6460 ± 969	5203	5264	5099 ± 9	−19.5
Pb-IV	18.7	2100 ± 317	1729	1748	1645 ± 6	−17.7
	28.3	5370 ± 806	4613	4668	4506 ± 9	−14.1
	34.5	7770 ± 1166	6220	6290	6114 ± 10	−19.9
Pb-VI	18.7	2500 ± 375	2021	2053	1933 ± 6	−19.1
	28.3	6670 ± 1000	5465	5556	5381 ± 9	−18.1
	34.5	9000 ± 1350	7453	7575	7387 ± 10	−17.2
U-I	16.4	1070 ± 161	1043	N/A	1029 ± 7	−2.5
	21.1	2330 ± 350	2143	N/A	2161 ± 10	−8.0
	28.4	3860 ± 579	3272	N/A	3268 ± 12	−15.2
	35.5	4880 ± 732	3904	N/A	3802 ± 14	−20.0
U-II	16.4	1950 ± 293	1844	N/A	1907 ± 9	−5.4
	21.1	4310 ± 647	4005	N/A	4229 ± 14	−7.1
	28.4	7850 ± 1178	6838	N/A	7143 ± 18	−12.9
	35.5	10735 ± 1610	9029	N/A	9229 ± 21	−15.9
U-III	11.5	380 ± 57	347	N/A	326 ± 3	−8.8
	16.4	2530 ± 380	2366	N/A	2536 ± 11	−6.5
	21.1	5900 ± 885	5203	N/A	5676 ± 17	−11.8
	28.4	10460 ± 1569	9130	N/A	9814 ± 22	−12.7

Table 4.3 – continued from previous page

35.5	14940 ± 2241	12396	N/A	13175 ± 25	-17.0

[a] see Barber and George [Bar59].
[b] see White et al. [Whi03b].
[c] see Heinrichs and Lent [Hei03].
[d] Percent difference is given as the difference between the fluence calculated in this study (MCNPX, *endf7u*) and the fluence measured by Barber and George [Bar59] divided by the measured fluence times 100.

5 Monte Carlo Model

The ultimate objective of this work is to investigate the out-of-field doses during a RT treatment session. This investigation requires a full MC model of the entire scenario of a RT treatment, which basically consists of the LINAC, the patient and the relative position to each other. A major step of the study is the implementation and validation of an accelerator model in the used Monte Carlo radiation transport code. As a suitable candidate for this research project, the Varian Clinac 2100C from Varian Oncology Systems, Palo Alto, CA, has been chosen. There were several reasons for this choice:

- First, for the Varian Clinac 2100C essential machine specifications regarding geometry and materials are available. They are needed for an accurate and detailed setup of a MC model and allow the development of a useful LINAC model at the first place.
- Secondly, relevant measurement data are accessible which can be used for the validation of the developed Monte Carlo model, see section 2.2 of the literature review.
- Third, the Varian Clinac 2100C has been object of several investigations in the past as one of the worldwide most commonly operated medical linear accelerators, which also becomes apparent from the listed publications in section 2.3 of the literature review. Thus, the results of this work are comparable to to those of other studies and improvements in the modeling, the quality of the calculated dose quantities and the drawn conclusions can be set into a common context.

For all simulations of this work the general purpose Monte Carlo radiation transport code MCNPX, version 2.7, was applied [Pel11]. Among the different available, established and well-benchmarked Monte Carlo codes like Geant4 [Ago03], FLUKA [Fer05, Böh14], EGSnrc [Kaw15] and PENELOPE [Sal11], especially the use of MCNPX has advantages for this research project:

- MCNPX provides not only coupled electron-photon transport, but also coupled electron-photon-neutron transport. The integrated simulation of the neutron transport allows for a detailed analysis of the neutron contamination of a high energy photon beam applied by a medical LINAC and the resulting adverse neutron doses for a RT-patient.
- MCNPX is capable of the simulation of photonuclear reactions. This feature is crucial for the simulation and investigation of the neutron contamination of high energy photon beams since it originates from photonuclear reactions in the beam-intercepting components of a LINAC. Moreover, a new photonuclear cross section dataset, as part of ENDF/B-VII.0 [Cha06], is accessible in the suitable ACE-data file format. Chapter 4 provided a comprehensive benchmark of this new cross section library.
- With MCNPX, also the moderation of fast and epithermal neutrons within the patient body tissues along with the thermal neutron transport can be taken into account. It was shown by Vanhavere et al. that the thermal neutron component of the neutron depth dose is significant, especially at greater phantom depths [Van04]. Hence, neutron moderation as well as the thermal neutron transport itself has been considered in the physics settings of the MC-simulation for neutron dose calculations. The thermal neutron transport is done by means of the S(α,β) library ENDF70SAB, also based on ENDF/B-VII.0. Section 5.3.2 gives a more detailed insight in the applied materials and cross section data of the model.
- For MCNPX, a variety of different computational anthropomorphic phantoms has been developed. Hence, a model of a medical LINAC combined with a computational phantom can be used to reproduce the scenario of a clinical RT-treatment case. With such an integrated

model it is possible to simulate the radiation transport and to describe the exact dose delivery to a patient. Then, the dose distribution and the organ doses received by the patient can be assessed in a next step.

Section 5.1 provides all relevant characteristics of the LINAC model including the geometric specifications of the machine as well as the materials and cross sections which were used in the model. In the subsequent section 5.2 the validity of the developed model is proved by comparison with available measurement data. In the case of neutron emissions from the LINAC, measurements data were scarcely available so that also calculated data from other research groups were set side by side with results from this study to draw a more complete picture of the MC model behavior and to better judge it. Once a proper simulation of the dose delivery from the LINAC has been verified, the model was combined with a patient phantom and integrated into one single model. The concept of anthropomorphic voxel phantoms and the choice of the specific phantom used on this work is outlined in section 5.3. Then, the following section 5.4 discusses the application of the integrated model to a clinical case. The scenario foreseen for the simulations and finally implemented in the integrated model was a prostate treatment plan. The last section 5.5 of this chapter is dedicated to the variance reduction techniques finally applied to cope with the infeasibly massive demand of computational resources emerging from the complexity of the developed MC-model.

5.1 LINAC Model Setup

As a first step towards a full computer model of a RT treatment scenario, the model of the LINAC treatment head was implemented. The next sections give the geometric details and the material definitions of the LINAC computer model.

5.1.1 Geometry Definition

The model of the Varian Clinac used for all simulations was based on several information sources. Raw data about dimensions and materials of beam-line components were provided by the Varian Oncology Systems. The confidential blueprints were limited to only beam-line components and are briefly explained in the following. Due to proprietary restrictions by the manufacturer no further details on these particular components and their model geometries can be given.

Target: The accelerated electrons are directed at the target where they lose their energy in the form of bremsstrahlung. The target consists of a tungsten button of about 0.5 mm thickness and radius 3 mm embedded on top of a copper base. Tungsten as a high-Z target material is used in order to optimize the bremsstrahlung production from the electrons. The target support on the other hand is made of copper with its high thermal conductivity. It stops the remaining electrons and efficiently dissipates the in the target produced heat.

Primary Collimator: The primary collimator is located directly beneath the target. Its aperture is conically shaped defining the maximal field size of the bremsstrahlung beam from the target. The collimator is made out of tungsten which provides an effective shielding of the high energy photons outside the primary beam dimensions.

Vacuum Window: The X-ray beam leaves the vacuum system through a window made of beryllium. The metal has a low density and low atomic mass, and hence low absorption of X-rays. This makes beryllium the preferred material for the vacuum window where a low energy transmission from the photon beam is desired.

Flattening Filter: The LINAC produces a photon dose distribution which is strongly forward peaked. In order to produce a radiation field of uniform intensity a flattening filter is inserted in the beam. This beam flattener is thicker in the center than on the outer edge to create the uniform intensity pattern. For different operation modes, i.e. beam energies, of the LINAC

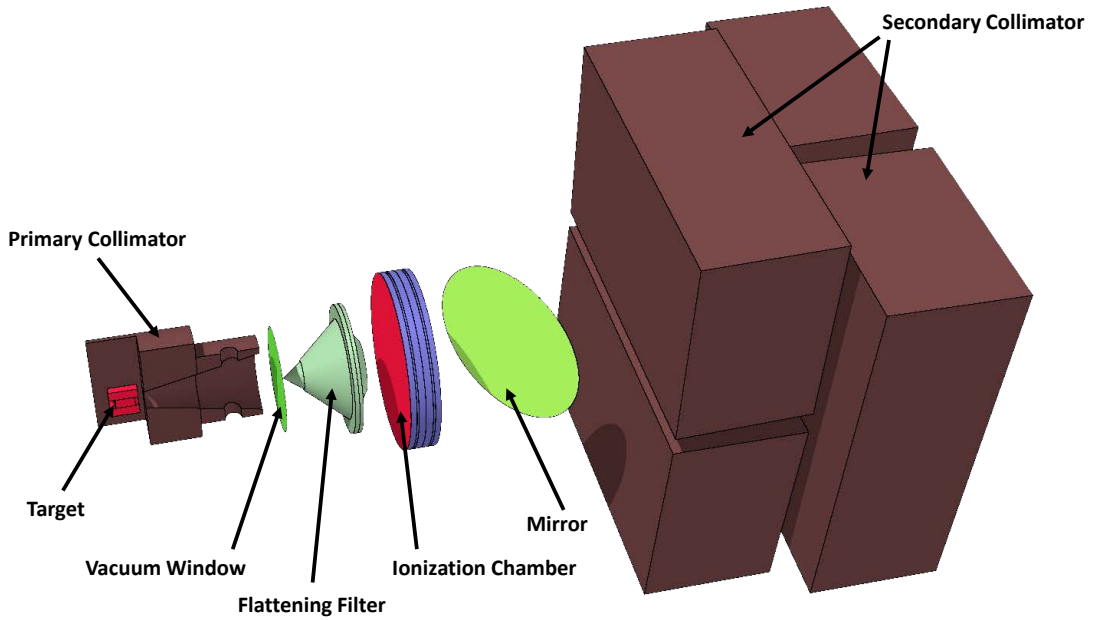

Figure 5.1: 3D-visiualization of the modeled beam-line components. Target, target support and primary collimator are clipped along the beam line for a better illustration. The tertiary multi-leaf collimator is not displayed.

different types of flattening filters have to be applied. The modeled flattening filter, shown in figures 5.1 and 5.4, is made of free-machining steel with a conical insert of tantalum and has a specific design for Clinacs operating at 18 MV.

Ionization Chamber: The flattened beam is incident on an ionization chamber monitoring the applied dose. As transmission type monitoring system it can be modeled as several flat and equidistant plates.

Field Light Mirror: In order to control the patient positioning before treatment, the LINAC provides a simulation option. It is based on a light ray exactly reproducing the outline of the radiation beam field. The light beam of a field lamp outside the beam-line is reflected by a mirror so that the reflected light has the same direction as the x-ray beam. Then the light beam is collimated by the beam-shaping devices imitating the shape of the actual treatment x-ray beam.

Secondary Collimator: The secondary collimator consists of four tungsten blocks conforming the beam to a rectangular or square shape at the isocenter of the LINAC. Two collimator jaws are arranged in the Y-direction and another pair in the X-direction. When the jaws are moved the divergence of the x-ray beam has to be taken into account in order to avoid the development of transmission penumbra caused by the beam only going through a part of the collimator, see the schematic in figure 5.2. This is done by guiding the upper (Y) jaws along an arc centered approximately on the target. The lower (X) jaws, on the other hand, travel in a linear fashion while pivoting keeps the jaws faces focused on the target.

Tertiary Collimator: The tertiary collimator conforms the produced x-ray beam to the shape finally needed for the irradiation of the treatment planning volume. The Clinac uses a multileaf collimator (MLC), the Millennium 80-leaf MLC composed of two sets of opposing 40 leaves. Each of the leaves can be moved separately by computer controlled electric motors. In this way the outline of the emerging radiation field can be precisely defined and adjusted according

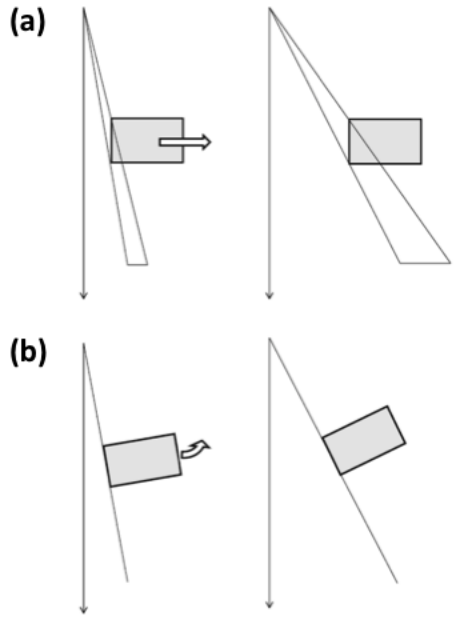

Figure 5.2: Transmission penumbra and jaw pivoting [Che09]. **(a)** Production of a penumbra in case of unadjusted orientation of the collimator jaw. **(b)** Pivoting of the jaw to keep the focus on the target.

to the needs of the treatment plan. Figure 5.3 shows cross-sectional plots of the modeled 80-leaf MLC in the cross- and the in-plane.

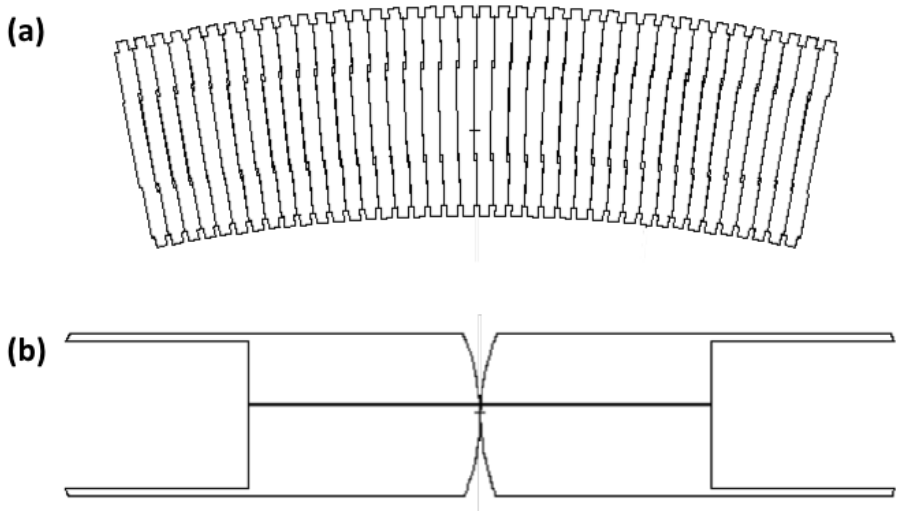

Figure 5.3: 2D-plots of the MLC model. **(a)** One of the two 40-leaf banks in the cross-plane (y-z-plane). The leafs are ordered along an arc to account for the divergence of the beam. **(b)** Two leaves in the in-plane (x-z-plane) opposing at the isocenter. The leaves are moved linearly in and out of the field. Their ends are rounded to keep the penumbra size approximately constant under changes of the leaf position.

The drawings directly provided by the manufacturer omitted the structures located around the beam-line such as support structures, the bending magnets and shielding components of the Clinac accelerator head. However, the surrounding structures have to be taken into account and implemented in the LINAC model in order to accurately simulate the scattered and leakage radiation transport from the treatment head as sketched in figure 2.1. This scattered and leakage radiation significantly contributes to the out-of-field doses so that its consideration is necessary for a proper assessment of the out-of-field exposure of the patient. The other component of adverse out-of-field exposure consists of radiation scattered within the patient and leaving the primary treatment field, also indicated in figure 2.1.

Kase et al. [Kas98] and Bednarz et al. [Bed08a, Bed09c] on the other hand presented sufficient information on the components surrounding the beam-line. Data sets were available in the form of EGS and MCNPX input. These data sets were combined to a complete representation of the treatment head with a high level of detail using geometric primitives like surfaces and cells as explained in section 3.1 about fundamental terms of the Monte Carlo Method. Figure 5.4 shows the created 3-dimensional model of the entire treatment head, clipped along the beam-line to have a better overview about the inner model structure. Besides most of the beam-line components, apart from the MLC, all the surrounding structures and also the bending magnet guiding the accelerated electrons towards the tungsten target are indicated. The exact model specifications in the shape of MCNPX input file format, based on the information from Kase et al. [Kas98], Bednarz et al. [Bed08a, Bed09c] and Varian Oncology Systems, are provided in Appendix B.

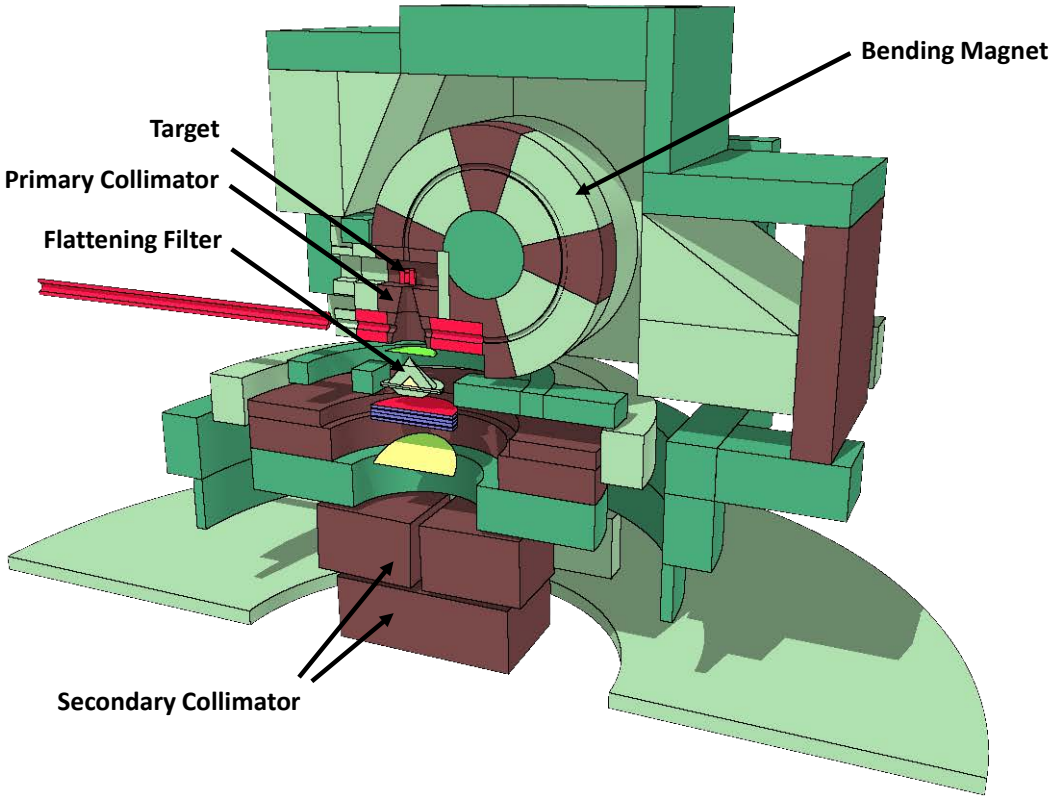

Figure 5.4: 3-dimensional visualization of the Clinac model, clipped along the beam line. Besides the beam-line components, also support structures, the bending magnets and shielding components are represented. The tertiary multi-leaf collimator downstream of the secondary collimator is also part of the model but not displayed in this picture.

5.1.2 Materials and Cross Section Data

Information about materials in the beam-line components of the LINAC was provided by the manufacturer Varian Oncology Systems, Palo Alto, CA. The material description along with the geometry for support structures and surrounding components of the beam-line were given by Bednarz and Kase et al. [Bed08a, Kas98]. Although the material compositions for those components were defined in a rather coarse way, i.e. using only a few elements, they are considered as sufficiently accurate reflecting the true radiation transport such as scattering and radiation leakage through these structures.

For simulations aiming at the calculation of photon doses all the materials in the accelerator head were defined by a combination of naturally occurring elements. This has been done following the format described in section 3.2. The corresponding part of the simulation input file is reported as listing B.16 in appendix B.1. This element-based material description is absolutely sufficient for the the calculation of photon absorbed doses and derived dose quantities, which relies on the simulation of photoatomic reactions such as coherent and incoherent photon scattering, photoelectric reactions as well as pair production, and, furthermore, on the simulated electron transport. The reason for this is that photoatomic and electron interactions with matter only depend on the properties of the constituent *elements* of the material. The corresponding photoatomic cross section library and electron transport data used for all MC-simulations in this work are shown in table 5.1.

Photoneutron dose calculations, on the other side, require a more detailed *isotopic* specification of the relevant materials since the underlying cross-sections for photonuclear interactions are highly isotope-specific. Cross sections from two isotopes of one and the same element can even differ by several orders of magnitude, e.g. for the different carbon-isotopes [Cha06]. Hence, in order to perform simulations also taking into account photonuclear interactions and the associated neutron emissions, all the elemental ZAIDs appearing in the material description of the LINAC head had to be replaced by a corresponding set of isotopic ZAIDs. Although, as described in chapter 4, huge efforts were made to increase the availability of photonuclear cross-section data for numerous nuclides, there are still many isotopes for which cross section data are available for photoatomic reactions but not yet for photonuclear or neutron interactions. To handle these exceptions in a comfortable way, the mix-and-match option offered by MCNPX was used [Pel11]. Like this, a nuclide can be part of a material description without the necessity that its cross-section libraries exist for all kinds of interactions, photoatomic, photonuclear as well as neutron interactions. The mix-and-match option just lets MCNPX ignore particle interactions for nuclides for which cross sections are unknown or not yet available. Table 5.1 lists the cross-section libraries used for photonuclear interactions and the subsequent neutron transport in the MC-simulations. The isotopic material definition for the LINAC head model is provided in listing B.21 of appendix B.2.

Cross section library/		**Applied in Simulations for**	
Data table	**Purpose**	**Photon-Doses**	**Neutron-Doses**
el03	Electron transport	yes	yes
mcplib84	Photon transport	yes	yes
endf7u	Photonuclear interactions	no	yes
endf66	Neutron transport	no	yes

Table 5.1: Cross section libraries and electron data table used for radiation transport simulations in the LINAC, [Cha06, Whi03a, Whi12, X-505a]. The photonuclear and neutron cross section libraries were used only for neutron dose calculations.

5.2 Validation of the Accelerator Model

The validation of the modeled LINAC geometry is mandatory in order to guarantee the usefulness of subsequent simulation results. Partially, it has already been published in an article [Fra16a]. The whole procedure and corresponding results, however, are described and presented in the following. The validation of the Clinac model is twofold since the topic of this doctoral project covers the investigation of both photon and neutron doses.

First, a correct photon dose delivery from the LINAC is verified by following a specific validation method, proposed and discussed in several publications [SB02, Kea03, Cho05]. This is done by comparing calculated and measured percent depth dose (PDD) and lateral dose profiles. Section 5.2.1 is dedicated to the validation of the photon dose delivery and divided into two parts: the validation of doses inside the primary treatment field (in-field) and of those outside the beam field (out-of-field).

Second, calculated neutron emissions from coupled electron-photon-neutron simulations are analyzed using available information about neutron fluences from the LINAC. The necessary verification of the neutron yield caused by the LINAC head is provided in section 5.2.2 in order to ensure the reliability of the computer model for further neutron dose calculations. Following this purpose, neutron fluences were calculated in-air and compared with corresponding values from other sources, either measured or also calculated.

5.2.1 Validation of Photon Dose Delivery

For the validation of the created LINAC head model dose measurement data provided by Stephen F. Kry were used [Kry06, Kry07, Bed09c]. In this study, those data were considered as the 'gold standard', a benchmark of Varian Clinac 2100C dose distributions to prove validity of the present model for dose calculations within the reported measurement uncertainty. The entire geometry of the LINAC model including field size, phantom dimensions, phantom material, surface-to-source distance (SSD) was defined in accordance to the validation measurement set-up from Kry et al.

In-field Validation of the LINAC Model

The model setup for the validation of photon absorbed dose inside the treatment field consists of the LINAC head model and a water tank with dimensions 140 cm x 140 cm x 35 cm at a SSD of 100 cm. Field sizes with an extension of $4 \times 4\,cm^2$, $10 \times 10\,cm^2$ and $20 \times 20\,cm^2$ were considered. The Monte Carlo model geometry was modified accordingly. Using this model setup, the mean energy of the primary electron beam was adjusted in several iterations until the obtained dose profiles best fitted the measurement data. The Gaussian energy distributions always had a FWHM of 3 % of the nominal particle energy. Exact electron beam characteristics were not available from the manufacturer. The applied parameter tuning approach, however, has been described, proved and used in numerous previous works, among others, in [SB02, Kea03, Cho05, Bed09c].

To determine photon absorbed doses in the cubic phantoms track length estimates of the electron energy deposition were calculated using the type 1 electron 'PEDEP' mesh tally provided by MCNPX [Pel11, p. 5-165]. With the exception of a different normalization, type 1 electron 'pedep' mesh tallies are analogous to F6:e electron heating tallies, but allow scoring the absorbed photon dose in voxels along one or more dimensions [Pel11]. This way, dose was calculated along the central axis to get the percent depth dose (PDD) distributions. Additionally, lateral dose profiles were calculated in the cross plane direction for field sizes and at depths for which measurement data were available [Bed08a, Bed09c]. All distributions were normalized to 1 cGy at maximum buildup at distance d_{max} for each particular field size.

The acceptance criterion for the in-field validation was an average of the percent local difference between calculated doses and measurement data of less than 2 % in the fall-off region from d_{max} to a depth of 30 cm. First, simulations with a mean energy of the primary electrons of 18.0 MeV

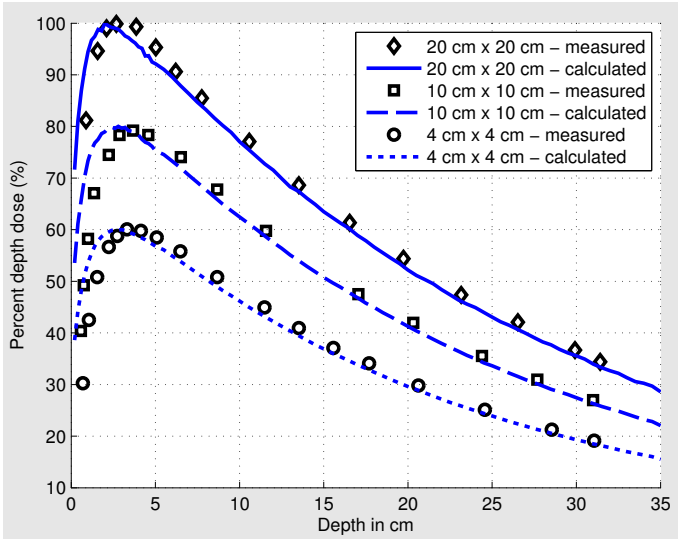

Figure 5.5: PDD curves for 4 x 4, 10 x 10 and 20 x 20 cm^2 fields. Curves are normalized to corresponding dose at d_{max}. For clarity, values for the 10 x 10 and 20 x 20 cm^2 fields are scaled by a factor of 0.8 and 0.6, respectively.

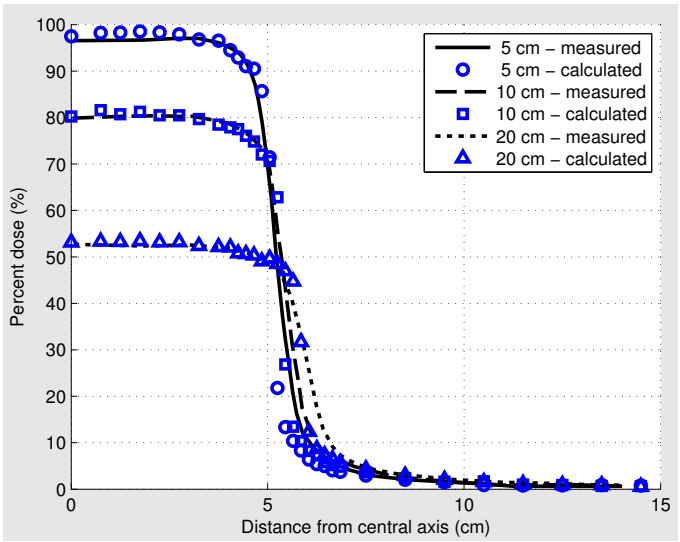

Figure 5.6: Lateral photon dose profiles for a 10 x 10 cm^2 field at depths of 5, 10 and 20 cm in the water phantom. All curves are normalized to dose at d_{max}.

were performed. At this energy, however, the average local difference from the resulting PDD to the measured one exceeded 3 % and was too high to fulfill the acceptance criterion. Then, the mean energy has been successively increased to 18.5 MeV at which the average local difference has dropped to 1.9 % and the calculated dose values were within the acceptance criteria. Plots of the measured and calculated PDD curves for the different field sizes are provided in figure 5.5. The rather high discrepancies on the phantom surface can be explained by the missing wall structure of the water phantom in the MC simulations as wall material and thickness are unknown. Nevertheless, this effect is considered to be negligible for this purpose [Bed09c]. For lateral dose profiles the average of the percent local differences between measurement and calculation had to be

less than 2 % in the plateau region and the average distance less than 0.2 cm in the penumbra region. Both conditions could be kept with a mean electron energy of 18.5 MeV. Figure 5.6 shows the measured and calculated lateral dose profiles at different depths in the phantom. The uncertainties in the calculated photon doses were below 1 % in all in-field validation simulations.

Out-of-field Validation of the LINAC Model

The out-of-field photon doses were also validated using a type 1 electron 'pedep' mesh tally. The phantom material, however, had to be modified according to Kry's out-of-field photon measurement setup and changed to acrylic with a composition of 8 wt.% hydrogen, 60 wt.% carbon and 32 wt.% oxygen. Furthermore, the phantom density was set to 1.17 g/cm^3. Then, absorbed photon dose distributions were calculated in-plane, at a depth of 3.75 cm and for three field sizes:

- 4 x 4 cm^2 defined by the MLC, jaw positions at 4.2 x 4.2 cm^2,
- 10 x 10 cm^2 defined by jaws, MLC fully retracted,
- 20 x 20 cm^2 defined by jaws, MLC fully retracted.

Large voxel sizes to minimize statistical uncertainties could be avoided by applying the same VRTs as in the eventual simulations of the photon doses in the treatment scenarios. The corresponding VRTs are outlined in section 5.5.2. For the out-of-field validation of the photon doses the voxels of the mesh tally had dimensions of 0.5 cm in beam-line direction and 1 cm in each of the other directions. All calculated dose values were normalized to 1 MU and compared to the photon dose measurements provided by Kry et al. [Kry07].

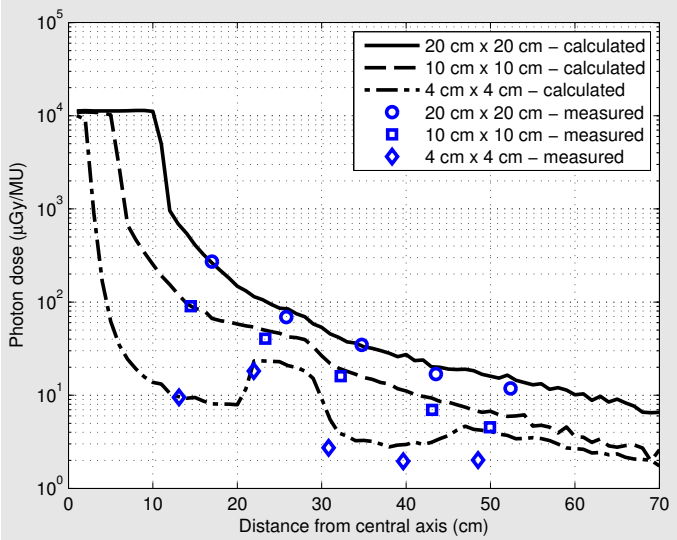

Figure 5.7: Measured and calculated out-of-field absorbed photon doses for field sizes of 4 x 4 cm^2, 10 x 10 cm^2 and 20 x 20 cm^2 at a depth of 3.75 cm in an acrylic phantom.

In figure 5.7 the results of the out-of-field validation are plotted for all of the field sizes considered. The graph for the 4 x 4 cm^2 field clearly indicates a dose peak at about 21 cm to 29 cm distance from the central axis. This can be explained by the missing shielding of the photons in this region due to the abrupt ending of the MLC. Only at larger distances beyond about 30 cm from the CAX, the dose is reduced again to lower values. This effect cannot be observed for the other field sizes since the MLC has been retracted totally in those cases.

The comparison between the measured and calculated out-of-field absorbed photon doses shows a very good agreement for all field sizes up to a distance of about 30 cm from the central axis. At greater distances, calculated values tended to overestimate the measured dose values. Especially

for the small field size of $4\,\mathrm{x}\,4\,\mathrm{cm}^2$ an average local difference of 55.4 % could be observed over the entire range from the CAX. This is due to the - for this small fields - larger influence of support structures of the LINAC head on the out-of-field radiation for which available geometry information is not as detailed as for beam-line components. For the $10\,\mathrm{x}\,10\,\mathrm{cm}^2$ and $20\,\mathrm{x}\,20\,\mathrm{cm}^2$ fields, however, average local differences were only 15.8 % and 23.3 %, respectively. In any case, calculated out-of-field photon doses can be taken as conservative evaluation of the actual photon radiation exposure as the dose values either match or exceed the corresponding measurements.

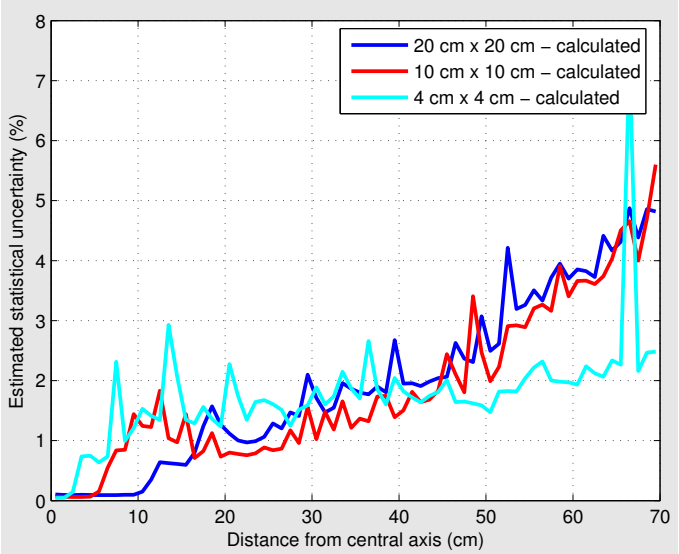

Figure 5.8: Estimated statistical uncertainties in the out-of-field dose calculations for each of the fields from figure 5.7. Uncertainties are given as the estimated standard deviation in percent relative to the calculated doses in the voxels.

The statistical uncertainties in the calculated photon dose values are displayed in figure 5.8. In average, the uncertainties were below 1.9 %, 2.0 % and 2.3 % for photon doses outside the $4\,\mathrm{x}\,4\,\mathrm{cm}^2$, $10\,\mathrm{x}\,10\,\mathrm{cm}^2$ and $20\,\mathrm{x}\,20\,\mathrm{cm}^2$ field, respectively. For all field sizes, uncertainties never exceeded 5 % for distances from the CAX up to 60 cm. These statistical results demonstrate that a proper determination of photon doses can be achieved with a high precision even at greater distances from the CAX. The measurement uncertainty reported by Kry et al. was 3.2 %.

5.2.2 Validation of Neutron Emissions

Since the photonuclear libraries available for MC simulations are not well established yet, verification and validation of those data play an important role. This issue has been extensively addressed by White in his thesis for prominent target, filter and shielding materials used in medical electron accelerators like the Clinac 2100C [Whi00]. Isotopes with low atomic numbers present in the biological materials are included in the model description, but their photoneutron contribution is, compared to isotopes with a high atomic number Z, considered as negligible due to their high threshold energies and very low photoneutron yields [Cha00, Cha06]. In this study, the photoneutron production has been validated against calculated and measured in-air neutron fluences provided by Kry et al. [Kry07] and Bednarz et al. [Bed09c]. The neutron fluence has been calculated using a partially deterministic fluence estimator (F5-tally) for different field sizes at different positions in the patient plane (100 cm SSD). At each source or collision site throughout the MC random walk a contribution of the particles to the mean fluence at the specified locations is calculated deterministically. All settings were consistent with those reported by Kry and Bednarz.

The locations were on the central axis, at 30 cm and 60 cm distance from the isocenter towards the accelerator gantry and 30 cm to 50 cm in the opposite direction from the isocenter, see table 5.2. Three field sizes were considered:

- $0 \times 0\,cm^2$ with both the jaws and the MLC closed,
- $9 \times 9\,cm^2$ defined by the MLC, jaws set to $10 \times 10\,cm^2$,
- $20 \times 20\,cm^2$ defined by jaws, MLC fully retracted.

The estimated uncertainty of the measurements reported by Kry was approximately 10 %.

Table 5.2: In-air neutron fluences at different distances from the central axis for different field sizes of a Varian Clinac 2100C operating at 18 MV. Positive distances correspond to locations from the isocenter towards the accelerator gantry and negative distances to positions extending from the isocenter away from the gantry.

Field size	Distance	Calculated Fluence[a]			Measured Fluence[a]	Difference[b]
(cm^2)	(cm)	This study	Bednarz et al.[c]	Kry et al.[d]	Kry et al.[d]	(%)
0×0	60	55.7	82.3	98	78	−28.6
	30	66.8	98.5	103	75	−10.9
	0	65.0	85.9	103	89	−27.0
	−30	74.2	91.0	93	83	−10.6
9×9	60	56.3	88.8	95	109	−48.3
	30	75.5	111.2	104	80	−5.6
	−30	81.0	99.8	93	74	9.5
20×20	0	152.6	204.5	174	160	−4.6
	−50	72.3	92.7	86	102	−29.1

[a] Fluences in units of 10^3 neutrons/cm^2/MU
[b] Percent difference is given as the difference between the fluence calculated in this study and the fluence measured by Kry et al. [Kry07] divided by the measured fluence from Kry et al. times 100.
[c] [Bed09c]
[d] [Kry07]

The results of the calculated in-air neutron fluences are listed in table 5.2. Differences between the calculated neutron fluences and those reported by Kry et al. [Kry07] are given in the last column of the table. It can be seen that almost all calculated data underestimated the measured fluences. This can be explained by a systematic error introduced in the computer model by omitting structures like the LINAC gantry or the treatment vault as corresponding geometric data were not available. In reality, these structures backscatter the emitted neutrons to some extent. The highest discrepancy of -48.3 %, for example, can be seen at the nearest location towards the - in the computer model missing - accelerator gantry. A computer model complemented by this structure would lead to a higher fluence at this very location. Moreover, Pena et al. investigated the influence of the treatment room on the neutron fluence at several locations [Pen05]. They reported that scattered neutron fluence from the treatment vault accounts for 8.6 % of the total fluence at the isocenter and 15 % at the treatment couch, respectively. These missing contributions to the neutron fluence explain the gaps that can be observed in table 5.2. Although their study is based on a Siemens PRIMUS LINAC operating at 15 MV, the results are essentially transferable to this case. Therefore and in front of reported measurement uncertainties for neutron fluences of approximately 10 %, the calculated fluence values are considered to be acceptable. The reader, however, has to be aware, that due to this model restriction the calculated neutron doses are no conservative estimates but rather mark a lower bound of the actual neutron radiation exposure. For all calculated neutron fluences relative uncertainties were below 1 %.

5.3 Anthropomorphic Voxel Phantom

Voxel phantoms consist of small volume elements (voxels) used to describe three-dimensional objects like a person in analogy to the pixels of an image in two dimensions. With their large number of voxels, they are one of the most detailed representations of human anatomy at the present time. Since the calculation of high resolution dose distributions requires a high level of detail in the computational models representing the patient, an anatomically realistic voxel phantom, the adult male phantom from ICRP Publication 110 [Int09] shown in figure 5.9, is used in this study.

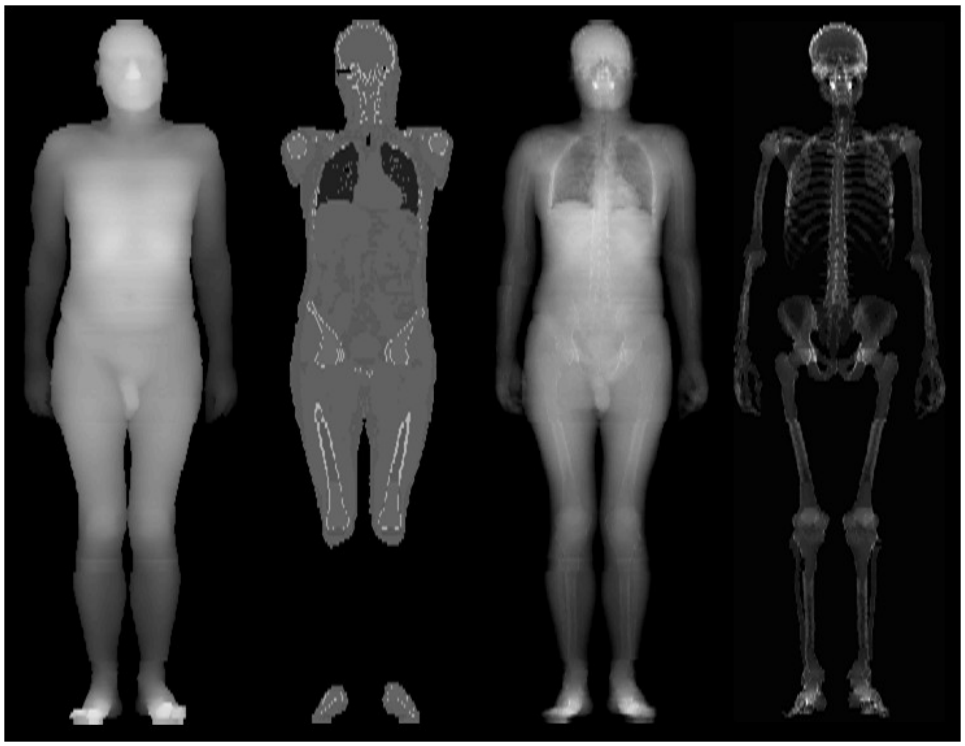

Figure 5.9: Different renderings of the ICRP adult male phantom published in [Int09], From left to the right: Anterior surface, coronal slice with mass density, mass density integrated over coronal slices, calcium content integrated over coronal slices. Courtesy from [War11].

5.3.1 Geometry Description

The ICRP reference male and female voxel phantoms were developed by Zankl et al. [Zan05, Zan07]. They used the whole-body clinical computed tomography image sets of a real male and real female. Their height and mass were 176 cm and slightly below 70 kg for the male and 167 cm and 59 kg for the female. The original male voxel phantom, known as "Golem", had dimensions of $2.08 \times 2.08\,\mathrm{mm}^2$ in-plane and a height of 8 mm, resulting in a voxel volume of $34.6\,\mathrm{mm}^3$ [Zan01]. In order to construct voxel phantoms representing the reference adults as specified in the ICRP Publication 89 [Int02] and following the 2007 Recommendations of the ICRP [Int07] the models had to be modified. First, the skeleton mass of the original models have been adjusted to the reference values by voxel scaling. In case of the reference male only the in-plane voxel dimensions had to be rescaled, since the original body height matched the value of 176 cm required by the ICRP reference. The skeleton volumes have been derived from reference data from ICRP Publications

70 and 89 [Int95, Int02] and mass density data of the ICRU Report 46 [ICR92]. This resulted in a slightly higher voxel volume of $2.137 \times 2.137 \times 8\,\mathrm{mm}^3$ or $36.54\,\mathrm{mm}^3$ for the male phantom. Then, individual organ masses were adjusted to the reference values by adding or subtracting a corresponding number of organ voxels. Finally, lymphatic nodes were included in the models and an appropriate number of adipose tissue voxels have been added or subtracted to adjust the whole-body masses to their reference values. The selection and segmentation of the tomographic data and all modifications to create the reference computational phantoms are outlined in more detail in chapters 2-4 of the ICRP Publication 110 [Int09]. Figure 5.9 provides different graphical representations of the reference male voxel phantom.

Figure 5.10: Graphical representations of the male (left) and female (right) computational phantoms. The following organs are indicated by different surface colors: breast, bones, colon, eyes, lungs, liver, pancreas, small intestine, stomach, teeth, thyroid and urinary bladder. Muscle and adipose tissue are held transparent. The voxelized surfaces have been smoothed for illustration purposes. Courtesy of ICRP Publication 116 [Int10].

5.3.2 Specification of Human Tissues and Cross Section Data

The ICRP reference male voxel phantom finally consists of a three-dimensional array of 7.096.760 voxels, arranged in 220 transversal slices, 127 coronal rows and 254 sagittal columns. For each of these voxels an organ ID is assigned which indicates the kind of organ filling in the voxel. The first lines of this huge 3-dimensional matrix are reproduced in listing B.8, appendix B.1. The definition of an organ consists of the material, i.e. the organic tissue, and its density. This differentiation

between organ and tissue is useful as one and the same tissue can be used for the specification of several similar organs having the same or also a different tissue density. In this way, tissues don't have to be defined multiple times so that the phantom eventually has 140 organs[1] with a total of only 53 tissues defined. In listing B.7 of appendix B.1, the specification of all phantom organs is given referring to their tissue composition.

The material definition of all the tissues is, like the material definition for the LINAC head components, twofold and depends on the objective of the MC-simulation, i.e. the calculation of photon or neutron doses. An elemental material description is sufficient for photon dose calculations as already outlined in subsection 5.1.2. Table A.1 lists all the different tissue types of the ICRP phantom with their elemental composition. This information is transformed into the necessary MCNP format, see file excerpt B.17, appendix B.1. For neutron dose calculations, on the other side, those definitions had to be provided in the isotopic format of listing B.22, appendix B.2.

A new feature in the neutron dose calculations is the treatment of thermal neutrons. There are no thermal neutron cross section data available for organic tissues so that the tissues were approximated, depending on their hydrogen-, carbon- and oxygen-content, by light water or polyethylene for which there exist S(α,β) data in the cross-section library ENDF70SAB. This means that, once a neutron reached a thermal level, the transport trough these tissues is simulated as if they would consist of light water or polyethylene, respectively. This procedure is followed exclusively for the transport of neutrons in the thermal energy range. Furthermore, the approximation with light water or polyethylene was done only for a bit more than half of the tissues in the ICRP phantom with a reasonable agreement in the elemental contents. All S(α,β) approximations for the organic tissues are listed in the last column of table A.1. In the end, the applied cross section libraries and data tables applied in the simulations for photon and neutron dose calculations in the ICRP phantom extend to the list shown in table 5.3.

Cross section library/		**Applied in Simulations for**	
Data table	**Purpose**	**Photon-Doses**	**Neutron-Doses**
el03	Electron Transport	yes	yes
mcplib84	Photon Transport	yes	yes
endf7u	Photonuclear Interactions	no	yes
endf66	Neutron Transport	no	yes
endf70sab	Thermal Neutron Transport	no	yes

Table 5.3: Cross section libraries and electron data table used for radiation transport simulation in the anthropomorphic phantom, [Cha06, Whi03a, Whi12, X-505a]. The photonuclear, neutron and thermal neutron cross section libraries were used only for neutron dose calculations.

After all, the presented implementation of the voxel phantom is based entirely on the supplementary material provided in appendices A and B of the ICRP Publication 110 [Int09]. Figure 5.9, with different renderings of the male and female phantoms, and figure 5.10 displaying specific organs by different surface colors convey an idea of the phantom structure.

1 Here, the term *organ* is not used in the conventional sense. It rather denotes individually segmented structures or body compounds. Besides the actual organs such as liver or kidneys, this also includes, for example, teeth or residual tissues in head, trunk, legs and arms. Even bladder contents, the contents of the gastrointestinal tract and the air inside the patient body are, for the sake of simplicity, considered as 'organs'.

5.4 Application of the Accelerator Model to a Clinical Treatment Case

The fully integrated model of the detailed Varian Clinac and the anthropomorphic phantom was finally applied to simulate a 3D-CRT prostate treatment scenario. The treatment plan consists of 4 fields of an 18 MV beam, applied from 4 different angles to the phantom and delivering in total 1260 MUs to yield a prescribed dose of 10 Gy in the planning target volume (PTV). A schematic of the treatment setup can be seen in figure 5.11. All the information on gantry angles, field sizes and prescribed monitor units is provided in table 5.4.

The jaw and MLC-leaf positions in the geometry model had to be adjusted for each of the field sizes. Also the position of the LINAC with respect to the phantom had to be changed as the treatment beams are applied with different gantry angles. In the computer model, only the relative position of the phantom to the treatment head is important. From the modeling point of view it is far more comfortable to rotate the phantom instead of all the components of the LINAC-model. Hence, corresponding rotation matrices were applied on the phantom geometry leaving the part of the integrated computer model regarding the LINAC at rest.

All modifications of the jaw- and MLC-settings and the phantom position were implemented using translation vectors and rotation matrices. The transformation data regarding the phantom itself are part of the main input files for photon- and photoneutron-dose calculations, respectively, provided in B.1 and B.20 of appendix B. Transformation data for the leaf-positioning of the MLC and the jaw-settings on the other hand are given in B.2 - B.5 and B.12 - B.12.

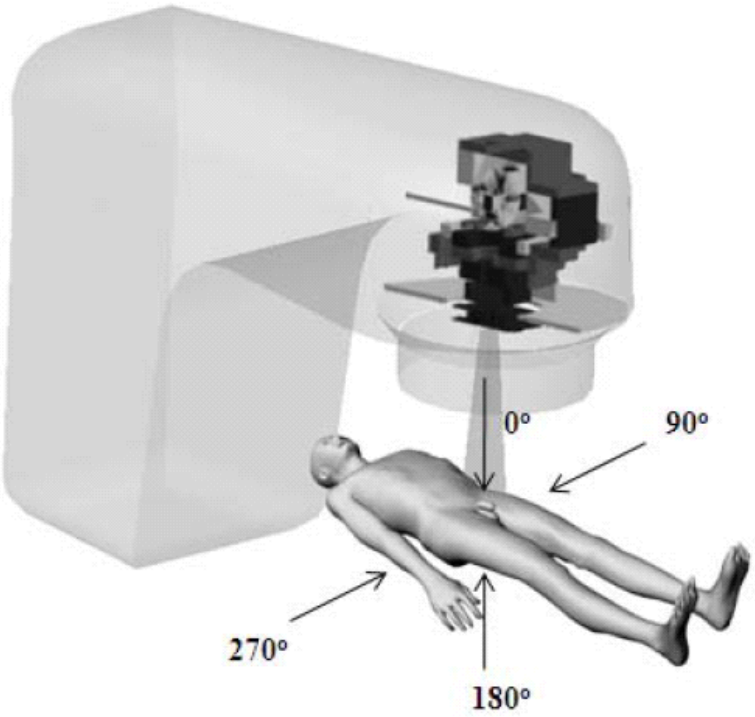

Figure 5.11: Schematic of the treatment setup for the 4-field prostate 3D-CRT, [DeW13].

This treatment setup was chosen in order to compare and discuss the obtained simulation results with those from previous dosimetry studies applying the same setup. Bednarz et al. investigated this treatment plan involving the RPI-Adult Male computational phantom [Bed09b, Zha08b, Zha08a].

Table 5.4: Details of the 3D-CRT treatment plan used in this study.

	Gantry angle (°)	Field size (cm^2)	Prescribed MU
4-field 3D-CRT	0	7 x 9.54	315
	90	7 x 7.96	315
	180	7 x 9.96	315
	270	7 x 7.64	315

They calculated intermediate- and low-level non-target doses by means of MC simulations, their study, however, partially revealed high uncertainties in the dosimetric results. Also Wang and Xu used the same treatment setup and parameters for their measurements. Their results, on the other side, were subject of consistently high uncertainties with nearly erratic values at some locations. A detailed comparison of all relevant dose- and uncertainty-values is presented later in this thesis, in section 6.2, table 6.1. Bednarz et al. used the RPI-Adult Male phantom and Wang and Xu a RANDO phantom for their dosimetry studies. Nevertheless, the results are suitable for a comparison with values obtained on the ICRP reference male phantom.

Figure 5.12: MCNPX cross section plot of the Clinac and ICRP phantom in the y-z-plane (in-plane) for a 0° gantry angle. Different materials are indicated by different grey values. Some structures, e.g. vacuum window and mirror, are not displayed as their thickness is below the resolution of the picture.

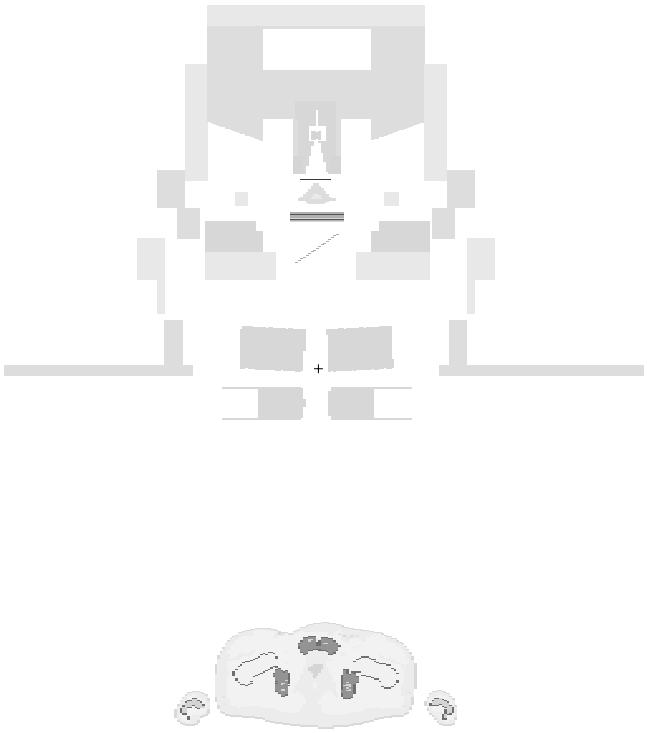

Figure 5.13: MCNPX cross section plot of the Clinac and ICRP phantom in the x-z-plane (cross-plane) for a 0° gantry angle.

5.5 Applied Variance Reduction

The application of variance reduction in the tally response of the MC dose calculations represents an essential part of this project. Without a proper combination of suitable VRTs it would have been impossible to gain any reliable dose values at all. Here, several factors contribute to the enormous complexity of the considered radiation transport problems.

First of all, the composition of a detailed LINAC treatment head and a high resolution anthropomorphic voxel phantom leads to an extremely complicated total problem geometry, as can be seen in figures 5.12 and 5.13. This high level of detail for both, the LINAC and the patient geometry, is intended and benefits the accuracy and reliability of the obtained dose values. On the other hand, the large number of surfaces and cells used to define the LINAC head as well as the sheer amount of phantom voxels heavily increase the required calculation time. But not only the problem geometry, especially the scenario of a 3D-CRT treatment itself creates an immense demand in terms of computational resources. Different irradiation angles have to be simulated and the calculated dose values have to be superimposed to get the total dose of a RT treatment. This procedure effectively multiplies the efforts necessary to calculate only one set of radiation doses to the patient.

Besides the geometry and the described scenario, also the specific radiation transport mechanisms of the considered problem contribute to the high complexity of the simulations. In the case of neutron dose calculations an entire cascade of particle interactions has to be considered and sampled appropriately. This cascade begins with accelerated electrons producing bremsstrahlung photons which in turn produce photoneutrons via photonuclear reactions. The emitted neutrons are then moderated and finally thermalized by the light elements in the body tissues of the patient. Step by step, all these physical processes have to be properly reproduced by the simulations.

In addition, dose calculations with high precision requirements substantially increase the for the solution needed computation time. Especially out-of-field dose calculations for OARs further away from the primary treatment beam, e.g. for the thyroid or the esophagus in case of a prostate treatment, pose a considerable challenge with respect to the desired precision with an uncertainty of not more than a few percent. In these locations, the dose level from leakage and scattered radiation is naturally rather low making it extremely difficult to simulate the trajectories of enough particles for a sufficiently precise estimation of the corresponding dose quantities.

The problem geometry, the considered particle physics and the required precision consequently culminate in tremendously complex radiation transport problems. In unbiased analog MC simulations the probability of an individual particle to contribute to the specified dose tallies would be so small that any calculation became useless. In order to solve such difficult radiation transport problems and to make the corresponding MC simulations not only possible but also computationally practical an elaborated framework of several VRTs had to be developed and applied.

As mentioned in section 3.4, all the VRTs require parameter settings which are highly problem-specific and therefore difficult to determine. Detailed knowledge of the relevant particle physics has to be employed to identify an effective set of VRT-parameters for the simulations and to coerce important particles to contribute to the dose quantities of interest. However, already Booth and Hendricks noted [Boo84]:

> "*The selection* [of useful VRT-parameters] *is more art than science, and typically, the user makes a few short trial runs and uses the information these trials provide to better guess the parameters; that is, the user learns to adjust parameters on the basis of previous experience.*"

This iteration process of adjusting the VRT-parameters can take days or even weeks for very complicated scenarios as it is the case for the problems described in this thesis. In fact, the VRT-parameter settings developed here eventually can not be considered as optimal in the sense that there are no better parameter sets enhancing the performance of the MC simulations even further. Nevertheless, they represent an appropriate and balanced effort of saving computer time required for the execution of the MC simulations with a certain precision and the user-time spent in developing these VRT-parameter sets.

In the following sections the selection of relevant VRTs is made and the development process of corresponding parameters is outlined. The objective of calculating photon as well as neutron doses from a radiation treatment is pursued using two different simulation models, one aiming at the estimation of only photon doses and another one just for neutron doses. This approach of separated simulations allows to optimize the variance reduction specifically for the calculation of the particle dose of interest, photon or neutron dose, respectively. In this way, the time to achieve reasonable results can be reduced significantly when compared to one single simulation determining both photon and neutron doses at the same time. Hence, two separate VRT-schemes were developed exploiting the fundamentally different physical behavior of photons and neutrons in matter.

Before all the applied VRTs and their corresponding parameter values are described, special attention on the control of the particle population in the simulations via weight windows is paid and prefixed in subsection 5.5.1. In this subsection, the application of mesh-based weight windows is justified and a tailored method for the generation of weight windows, designed specifically for the radiation transport problems considered here, will be presented. All details regarding VRTs in photon dose calculations, including also corresponding energy-dependent weight window maps, are then given in the following subsection 5.5.2. Subsection 5.5.3 on the other hand represents the counterpart for neutron dose calculations.

5.5.1 Weight-Window-Generation

Weight windows were chosen as the preferred method to control the particle population and to sample the more important regions in the MC simulations. Compared to the plain use of particle splitting and Russian roulette as they are explained in subsection 3.4.2, weight windows, especially energy-dependent weight windows, have several advantages:

- A weight window discriminates on particle weight before deciding the appropriate action whereas the particle splitting and Russian roulette are done regardless of particle weight. Due to this weight independency the particle splitting and Russian roulette preserve any weight fluctuations introduced by other biasing techniques. Weight windows, however, can control these fluctuations by requiring all particles in a mesh to have a weight $W_L < W < W_U$, see subsection 3.4.2 and figure 3.3.
- Weight windows can, as it is done for this study, be defined energy- and space-dependent. Particle splitting on the other hand is only space dependent.
- The weight windows are applied at surfaces and collision sites increasing the effectivity of the VRT. The application of particle splitting and Russian roulette, however, is limited to surface crossings.
- Since particle splitting is based on the ratio of the importances across the surfaces of a geometry, the number of particles in a simulation can be potentially unstable. In the worst case, unbalanced cell importances, for example with too high ratios between adjacent cells, can lead to an avalanche-like exponential growth of the particle number in a simulation making it too slow and useless for the solution of the problem. Weight windows avoid these instabilities with absolute weight bounds.
- Furthermore, MCNPX provides a method that automatically generates weight window importance functions, the so called weight window generator. He estimates the importances of the phase space regions based on one or more preliminary runs of the MC simulation and works regardless of what other variance reduction techniques are used in the calculation. With this feature, it is possible to achieve a far better sampling according to the importance of a region than the user could do it ever manually.

This weight window generator has been used to generate the weight window maps finally used in the dose calculations. All details about the functionality of the weight window generator can be found in [Boo84, Pel11, X-505a, X-505b]. In the following, however, the focus is set on problem-specific aspects and essential information guiding through the development of an effective set of weight window maps for the photon and neutron dose calculations of this project.

A direct application of the weight window generator on the radiation transport problem as it was described in the previous section is highly inconvenient. The RT treatment plan for the investigated clinical case consists of several irradiations from different angles. For this reason, the rotation angle of the phantom in the computer model has to be changed accordingly leading to a different geometry set-up for each of the corresponding MC simulations. In order not to have to develop a new VRT-parameter set for each each of these set-ups the final parameter setting should ideally be flexible enough and applicable independently from the beam direction. This aspect is especially important for weight windows as the definition of a weight window mesh depends on the problem geometry. Instead of producing another weight window set for every scenario with a different irradiation angle, one single weight window mesh has been defined for a simplified cylindrical water phantom which encloses the outline from the ICRP-phantom at all possible rotation angles. Figures 5.14a and 5.14b show this simplified geometry in different planes. Figures 5.15 and 5.16 illustrate the simplification and indicate the shape of the cylinder superimposed on the actual ICRP-phantom positions, for instance, at irradiation angles of 0° and 90°. It can be seen that the cylinder doesn't contain the entire phantom and truncates the legs and the arms of the phantom. Instead, the simplified phantom rather concentrates on body parts with especially radiosensitive

organs and therefore encompasses only the trunk and the head of the patient. All weight window sets were finally generated based on this simplified water phantom model.

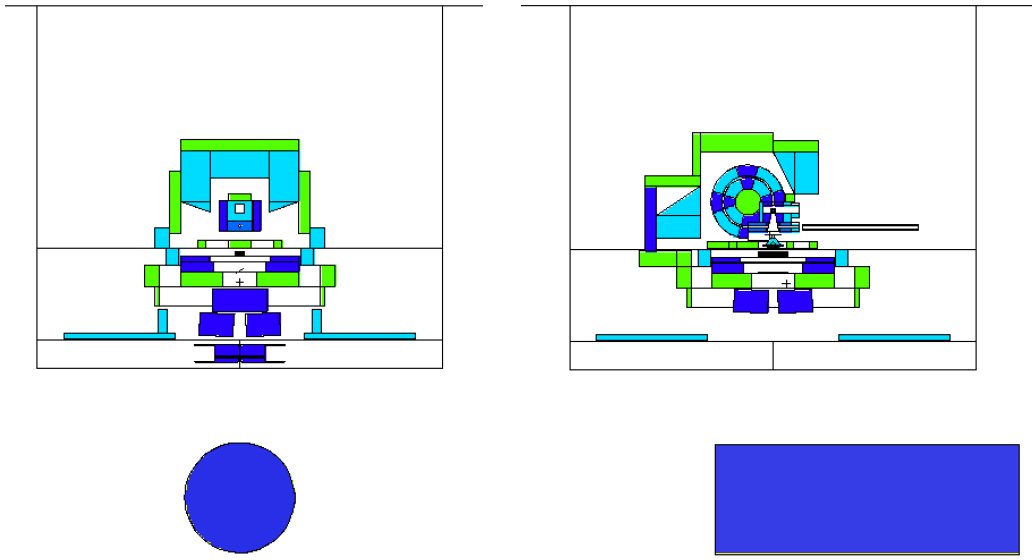

(a) x-z-plane (cross-plane)

(b) y-z-plane (in-plane)

Figure 5.14: Simplified cylindrical water phantom for weight window generation. Different colors indicate different materials. Air is displayed white.

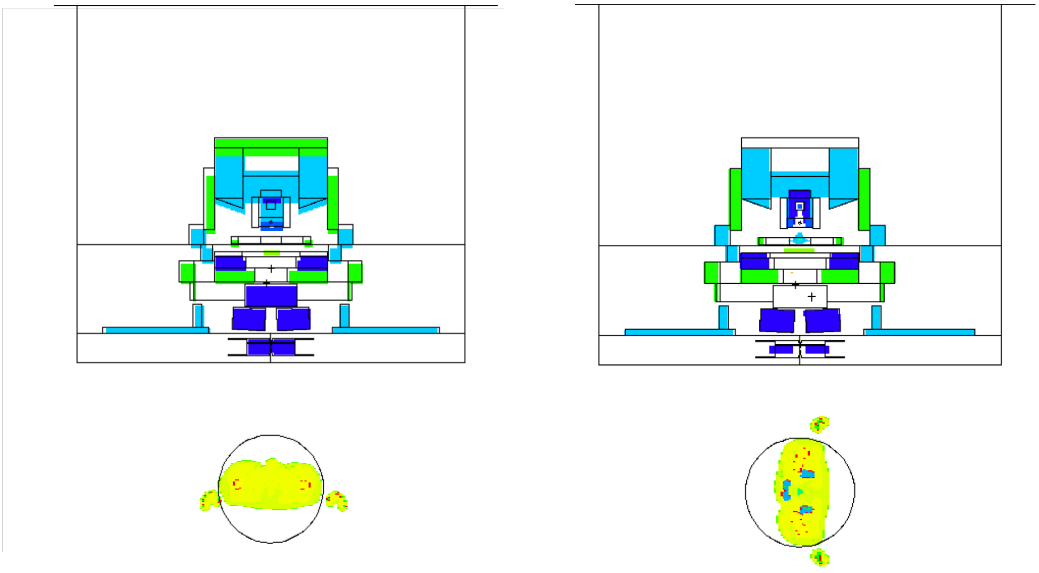

(a) Gantry angle of 0°

(b) Gantry angle of 90°

Figure 5.15: Illustrated approximation of the anthropomorphic phantom by the simplified cylindrical water phantom. The boundaries of the simplified phantom are superimposed on the ICRP phantom. Cross-section plot in the x-z-plane (cross-plane). **NB**: In illustration (b) the phantom is rotated by the angle of 90° for the sake of simplicity. In reality, however, the patient is **not** rotated. Instead, the LINAC treatment head rotates around the patient according to the required irradiation angle.

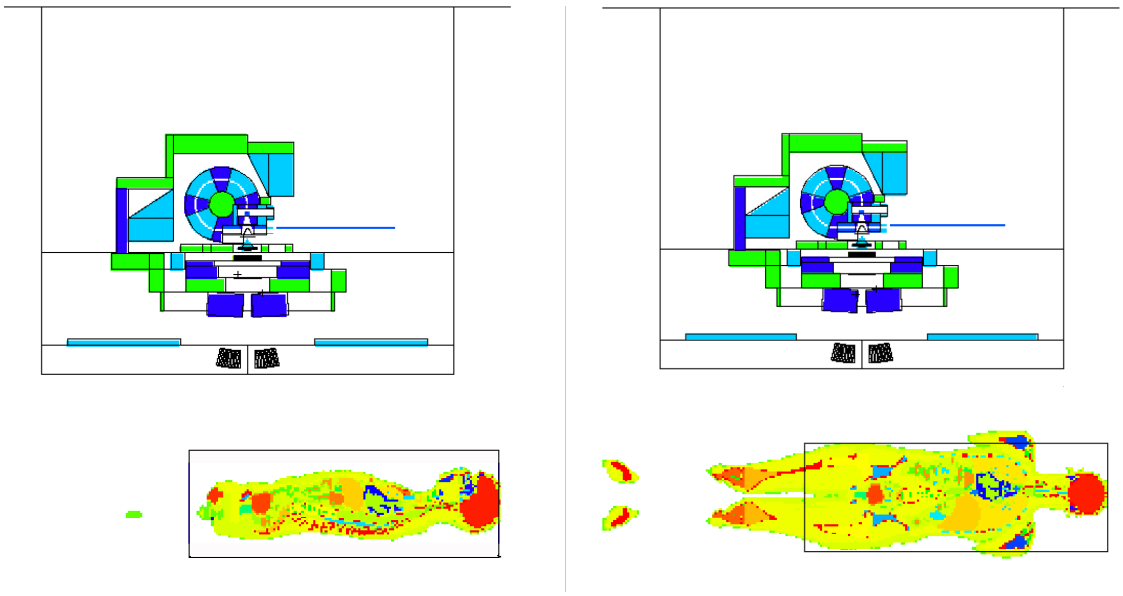

(a) Gantry angle of 0° **(b)** Gantry angle of 90°

Figure 5.16: Boundaries of the simplified computational phantom superimposed on the ICRP phantom truncating legs and arms. Cross-section plot in the y-z-plane (in-plane).

The weight window generator estimates the importance of the regions in the phase space. The importance of a region is the expected tally score of a particle with weight 1 entering this region. Bookkeeping the effects of a number of simulated particles, the region's importance can be estimated as the average

$$\text{region importance} = \frac{\begin{array}{c}\text{total tally score as result of particles (and their}\\ \text{descendants) entering the region}\end{array}}{\text{total weight of the particles entering the region}}. \tag{5.1}$$

After the importance estimation, MCNPX assigns weight windows inversely proportional to the importances for all the regions with an importance greater than 0. This might be counterintuitive, but lower weight window bounds lead in the end to a higher number of particles improving the sampling of the corresponding region and better reflecting its importance for the tally response. According to equation 5.1, the estimated importance for a region is zero if no particle reached to score in the tally after passing through this region. In such a case, the region will not obtain a weight window. When a weight window set is applied in a subsequent simulation providing weight windows only for a part of the regions in the problem geometry, apart from other VRTs no action will be performed for particles entering regions without assigned weight window.

The regions of the phase space are specified a priori by the user. Here, MCNPX provides two possibilities. One possibility is the importance estimation and weight window generation for each geometry cell. Importances, however, are calculated in average, i.e. if the importance within a cell varies widely, for example in the case of a large cell, the estimated average importance might not reflect the real influence of the cell on the tally response. Defining larger cells, on the other side, can be reasonable to provide the most efficient geometry description, although they could be inadequately subdivided for importances. The second option provided by MCNPX avoids this issue. A user-defined mesh, independent from the actual problem geometry, can be superimposed

upon the entire computer model and used only for the importance estimation, the generation of weight windows and their application. The mesh can be defined in a rectangular or in a cylindrical manner. The weight window generator then calculates for each of the mesh facets an estimation of its importance and the corresponding weight window bounds.

Such a cylindrical, (geometry-)cell-independent weight window meshing has been specified for the generalized water phantom, see figure 5.17. Based on this mesh, weight window parameters were determined for an optimal simulation of in- and out-of-field doses from the LINAC. Although the resulting weight windows were not specifically generated for the actual ICRP-phantom and its different rotation angles, they can easily be applied to all simulation scenarios using the original anthropomorphic phantom. This general applicability of the parameter set is extremely useful as the creation of a new weight window set for each single rotation angle of the original phantom becomes unnecessary.

MCNPX supplies the weight window set produced by the weight window generator in the form of an output file suitable for use as an input file in a subsequent calculation. Unfortunately, the first results of the weight window generator are in most cases of poor quality and provide only bad estimates of the importance function. This is because an acceptable importance estimation requires in general a sufficiently large number of tally scores, see equation 5.1. But an insufficient scoring was just the reason for the development of weight windows. The simplified computer model constructed so far includes a tally scoring the energy deposition in the water phantom. In fact, a first calculation with the weight window generator and the cylindrical meshing did not even yield one score for the vast majority of mesh facets.

In order to solve this chicken-and-egg problem a simple trick has been applied: The original tally scoring the energy deposition in the water phantom and used to estimate the region importances has been replaced by a point-detector tally positioned longitudinally and transversally in the middle of the water phantom. The point detector, see also subsection 3.4.4, calculates deterministically a tally response for all particles in the MC simulation undergoing a collision or starting from their point of creation. He is therefore not dependent on the particles eventually reaching the water phantom at one point in their random walk and, hence, avoids the numerator on the right side of equation 5.1 being equal to 0. Although this tally scores the particle flux instead of the actual energy deposition and, moreover, is limited to just one point in the geometry, a first rough estimation of the region importances could be made for many mesh facets. The generated weight window set served then as a 'jump start' for another run of the weight window generator but this time with the original energy-deposition-tally activated. The new weight window set now indicated region importances for the energy deposition in the water. A few additional iterations with the weight window generator refined the obtained parameter set so that it was ready to be used in the final dose calculations.

This procedure was followed two times, once for the creation of a weight window set for in- and out-of-field photon dose calculations and another time for neutron doses. One last aspect to mention here regards the implemented energy dependency of the weight windows. Particles of different energies also interact differently and show a different behavior in matter so that they have not the same probability of reaching a region of interest, in our case the water phantom. As a consequence, the importance of a region varies with the energy of a particle dropping into it. To take this into account the relevant particle energy range of the radiation transport problem has been divided into a few intervals for which separate region importances were calculated. All details about the energy-dependent weight windows generated specifically for photon- and neutron-dose calculations, respectively, are presented in the following subsections.

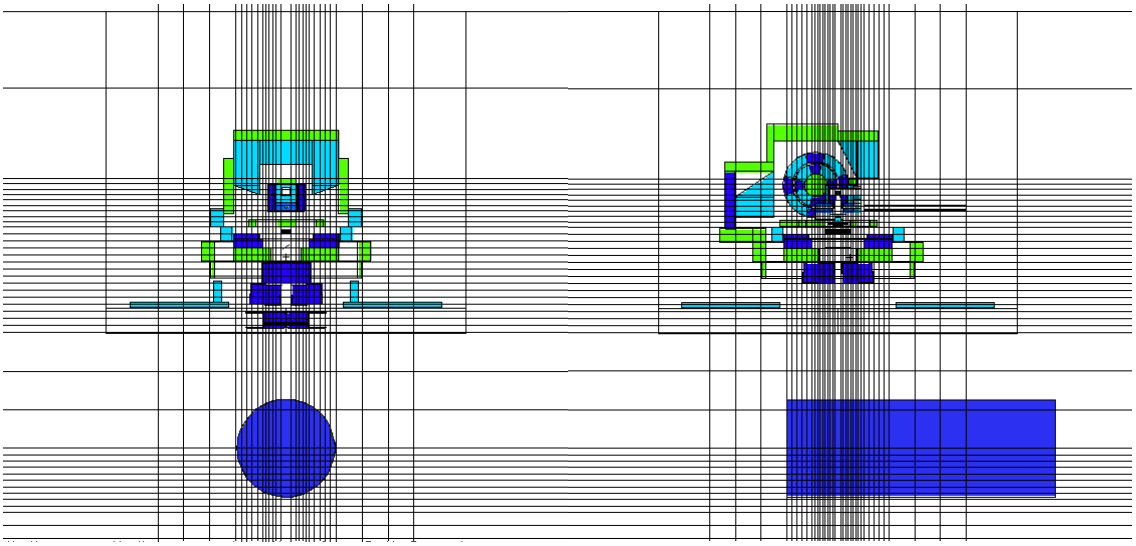

(a) x-z-plane (cross-plane)

(b) y-z-plane (in-plane)

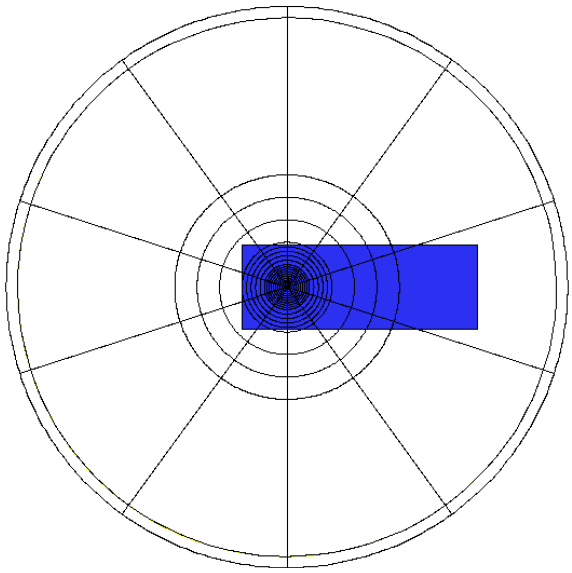

(c) x-y-plane (patient-plane) at SSD of 100 cm

Figure 5.17: Definition of a cylindrical weight window mesh superimposed upon the simplified water phantom model.

5.5.2 Variance Reduction in Photon Dose Calculations

All the VRTs applied in coupled photon-electron MC simulations for the calculation of photon absorbed and equivalent doses are listed in table 5.5. Very efficient VRTs are energy cutoffs for both electrons and photons. With this truncation method, the simulation of particles in the phase space that do not contribute anymore significantly to the solution is terminated and their remaining energy is deposited on the spot. The cut-off energies were set to 100 keV for electrons and 10 keV for photons. This is a reasonable simplification of the MC simulations as the remaining potential range of 100 keV electrons, for example, is only of the order of 100 µm in the body tissues,

hence far below the spatial resolution of the voxel phantom. The termination of photons with an energy of 10 keV or lower on the other hand only introduces an insignificant systematic error in the simulations. In the MCNPX input file, provided in appendix B.1, the energy cutoff of electrons and photons is declared with the lines

cut:e 1e20 0.1
cut:p 1e20 0.01

in the 'data cards'-section.

One more way to enhance the simulation efficiency is to control the sampling of bremsstrahlung photons produced along electron sub-steps. For this, the BNUM parameter in the particle physics declaration for electrons was applied. The corresponding line in the MCNPX input file, provided in appendix B.1, is

phys:e 23.1 j j j j 10

In the biased simulations, the number of created bremsstrahlung photons is increased by a factor of 10 compared to an analog sampling of the bremsstrahlung production. Based on the el03 electron transport library, listed in table 5.1, each of these bremsstrahlung photons is sampled independently for energy and angle with appropriately modified weights. Since the number of photon tracks is 10 times higher than in an analog simulation, an appropriate weight reduction, in our case a multiplication of the individual photon weights with 1/10, is made. MCNPX considers a radiative energy loss of the electron involved equal to the bremsstrahlung energy of the first sampled photon.

Table 5.5: Applied Variance Reduction Techniques in Photon Dose Calculations.

Particle	VRT	Details/Remarks	MCNPX-Card/Option
e	Energy cutoff	Threshold: 100 keV	cut:e
γ	Energy cutoff	Threshold: 10 keV	cut:p
γ	Scaled number of produced bremsstrahlung photons	Factor: 10	phys:e (BNUM)
γ	Energy-dependent Weight-Windows	3 Energy groups: 0-1, 1-10, 10-20 MeV	wwp:p

As a last VRT for photon dose calculations, energy-dependent weight windows have been generated using the weight window meshing presented in figure 5.17. The energy dependency is given by dividing the relevant photon energy range roughly into 3 groups and the generation of 3 corresponding sets of photon weight windows exclusively valid for their respective energy group. The boundary values of the groups were chosen to be 0-1 MeV, 1-10 MeV and 10-20 MeV, taking into account the specific physical behavior of photons with different energies. Depending on their energy, the radiation transport of the photons basically differs by their probability and the way of interacting with matter. Low energy photons have a higher interaction-probability with matter than high energy photons. That makes it more likely for them to scatter through the treatment head and still find their way towards the phantom. The weight window maps shown in figures 5.18 - 5.20 reflect the specific behavior of photons with different energies. In figure 5.18 far more weight window meshes have an assigned value, and therefore a specific importance for the calculation result, than in figure 5.20 for the fraction of photons with a high energy. The values for the weight window bounds are related to the unity weight of the source particles consisting of the initial electrons.

All three weight window maps were stored in a dedicated output file called '*WWINP*'. This external file was then loaded by MCNPX for the final calculation of the photon doses. The invoking line

wwp:p,e 4j -1 3j 100

is located at the very end of the MCNPX input file B.1. The lower weight window bounds are

then retrieved from '*WWINP*'.

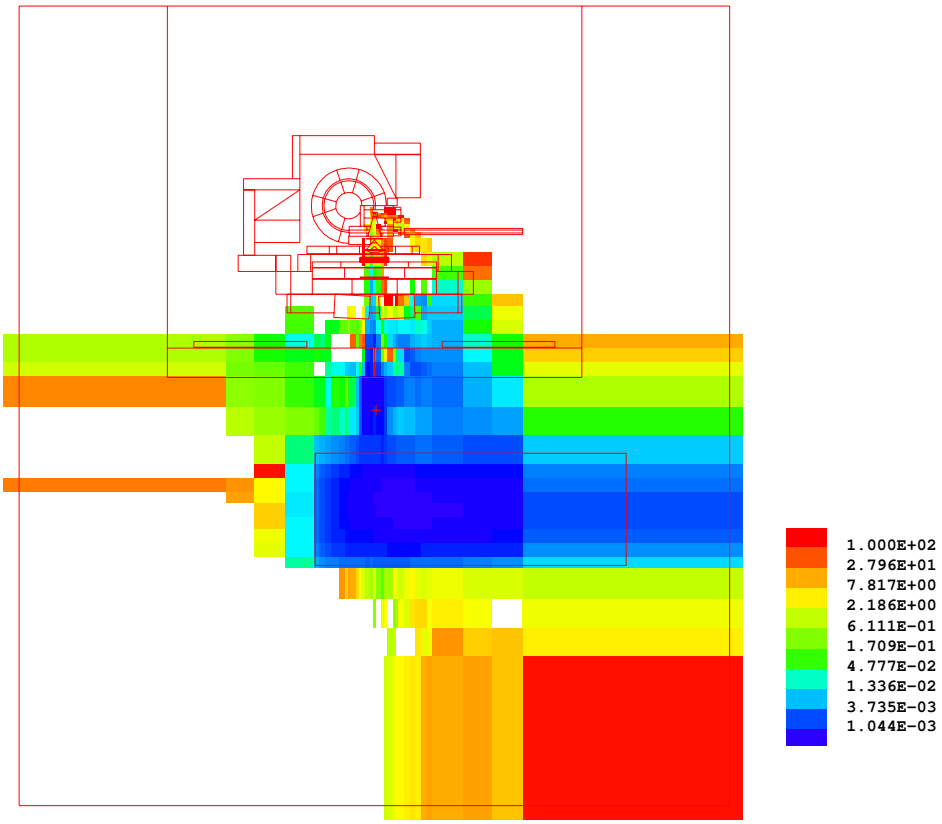

Figure 5.18: Plot of the mesh-based photon weight windows in the y-z-plane (in-plane) covering the energy range between 0 MeV and 1 MeV. The color within each of the meshes indicates the value of the lower bound of the corresponding weight window. No action, apart from other VRTs, is applied to particles entering meshes in white.

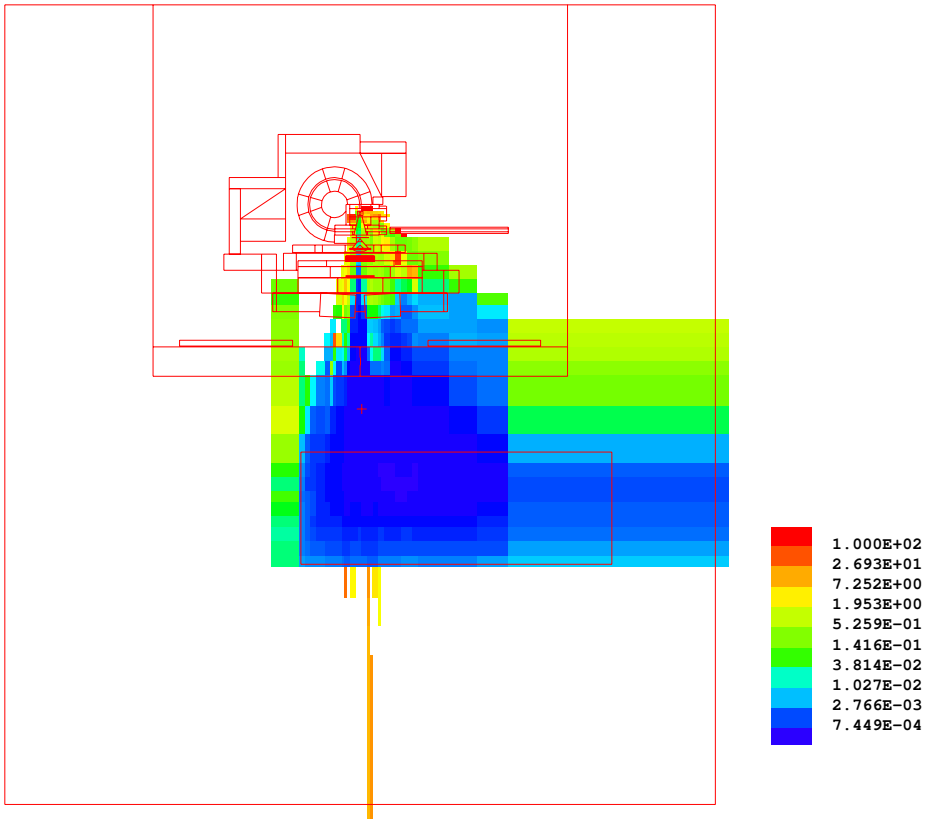

Figure 5.19: Plot of the mesh-based photon weight windows in the y-z-plane (in-plane) covering the energy range between 1 MeV and 10 MeV. The color within each of the meshes indicates the value of the lower bound of the corresponding weight window.

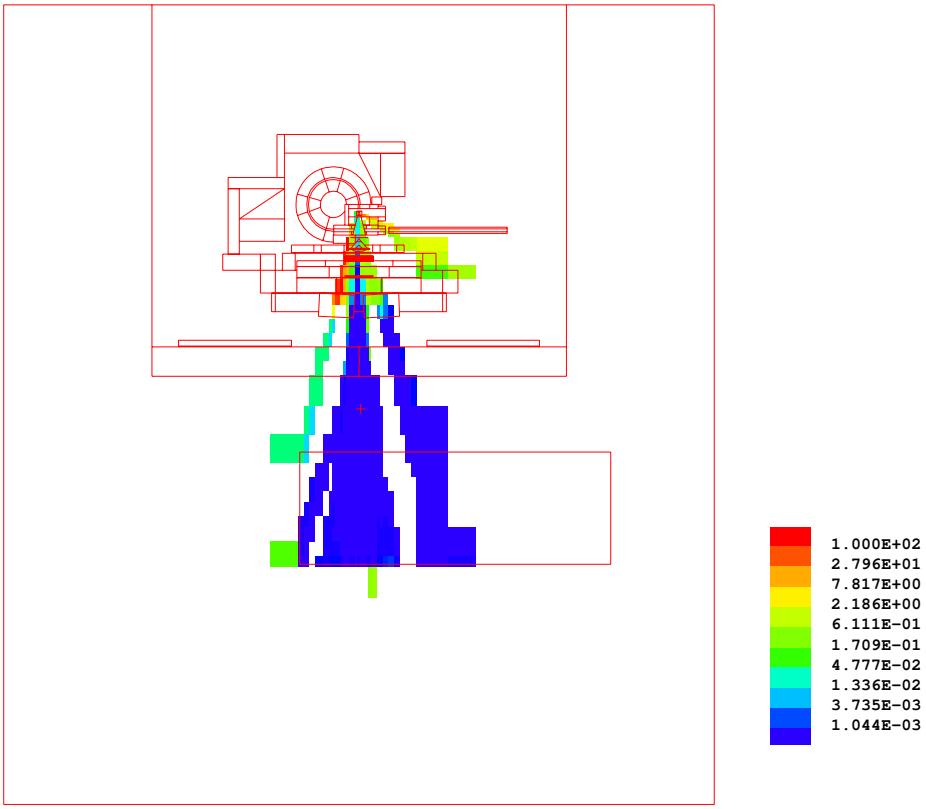

Figure 5.20: Plot of the mesh-based photon weight windows in the y-z-plane (in-plane) covering the energy range between 10 MeV and 20 MeV. The color within each of the meshes indicates the value of the lower bound of the corresponding weight window.

5.5.3 Variance Reduction in Photoneutron Dose Calculations

Calculations of photoneutron dose equivalent distributions in the photon-electron-neutron mode of MCNPX are far more sophisticated than those for photon dose distributions since photonuclear reactions are rare events and statistical uncertainties of subsequent neutron radiation and energy deposition are correspondingly higher. In 2001, White published a memorandum in which he recommended and demonstrated a number of VRTs for the simulation and solution of radiation transport problems involving photonuclear interactions [Whi01]. All these VRTs were applied in the present case to cope with the complications, i.e. the unfeasible solution of the problem in decent timescales, induced by considering photonuclear processes. Also the production of bremsstrahlung with energies mostly below the threshold of photonuclear interactions is problematic in the sense of feasibility and required some more suitable biasing techniques. All VRTs finally used for neutron dose calculations are listed in table 5.6 and explained in the following paragraphs.

Like in the photon dose calculations the energy cut-off VRT has been applied again. This time, however, thresholds were not only set for electrons and photons but also for neutrons. Also the values for the energy cut-off of electrons and photons are different as the objective, the calculation of in- and out-of-field neutron doses instead of photon doses, has changed. Both electron and photon energy cut-offs were fixed at the lowest photonuclear reaction threshold value for all isotopes present in the model. This value is 1.67 MeV, the threshold for photonuclear reactions in beryllium which is used as the material for the vacuum window of the treatment head. For electrons and photons with an energy below 1.67 MeV no photonuclear reactions are possible in the model so

Table 5.6: Applied Variance Reduction Techniques in Neutron Dose Calculations.

Particle	VRT	Details/Remarks	MCNPX-Card/Option
n	Implicit Capture	(Default)	(phys:n)
e	Energy cutoff	Threshold: 1.67 MeV	cut:e
γ	Energy cutoff	Threshold: 1.67 MeV	cut:p
n	Energy cutoff	Threshold: 10^{-2} eV	cut:n
γ	Bremsstrahlung Biasing	Factor: gradually increasing from 1 to 10	bbrem
γ	Scaled number of produced bremsstrahlung photons	Factor: 10	phys:e (BNUM)
γ	Forced Collisions		fcl:p
γ	Photonuclear Biasing		phys:p (ISPN)
γ	Energy-dependent Weight-Windows	3 Energy groups: 0-2 MeV, 1-10 MeV, 10-20 MeV	wwp:p
n	Energy-dependent Weight-Windows	3 Energy groups: 0-2 keV, 2-100 keV, 0.1-5 MeV	wwp:n

that they have no potential to contribute to the neutron doses in the phantom. Therefore, they are consequently terminated in the MC simulation. The energy cut-off for the transport of neutrons through matter, on the other hand, has been set to a thermal level of 10^{-2} eV. The corresponding lines for the energy cut-offs in the MCNPX input file, see page x in appendix y, are

cut:e j 1.67 $ photonuclear threshold for Be
cut:p j 1.67 $ photonuclear threshold for Be
cut:n j 1.0e-8

The values are given in units of MeV.

Again, the absolute number of bremsstrahlung photons produced by the MC simulation has been increased by activation of the BNUM as described in the previous subsection. The scaling factor of 10 was left the same as for the photon dose calculations. The bremsstrahlung process, however, generates many low-energy photons evident from an emphasized low-energy tail of the bremsstrahlung spectrum. Only higher-energy photons above the mentioned energy thresholds for photonuclear reactions, however, are of interest in the MC simulations for the calculation of neutron doses. A way to generate more high-energy photon tracks is the biased sampling of a bremsstrahlung photon towards a larger fraction of the available electron energy by means of the BBREM option in the MCNPX input:

BBREM 1. 1. 46I 10. 91 92 $ 91, 92 materials of target

This method creates a gradually increasing enhancement of the probability that the sampled bremsstrahlung photon receives a particular fraction of the electron energy. Here, the sampling is biased with a factor of 1.0 for the lowest fraction of the electron energy up to 10.0 for the highest available fraction. This biasing scheme applies to each instance of the sampling of a bremsstrahlung photon in the electron target materials, tungsten with the material number 91 and copper with the number 92, and leaves the sampling in other materials unbiased. The bias factors are normalized by the code depending on both the material and the electron energy and the photon weights are adjusted accordingly in each of the different weight groups. A more detailed discussion of the bremsstrahlung energy biasing scheme is provided in chapter 2, page 2-77 of [X-505a].

All produced photons entering a cell of the target or the primary collimator were forced to undergo a collision within these cells. The theory behind this forced collision VRT has been explained at page 28 in subsection 3.4.3 for modified sampling methods. This VRT is particularly useful to exploit the supply of photons produced in the MC simulation so far and to increase the yield of photoneutrons as a result of photonuclear collisions. As a consequence, forced photon collisions enhance the probability for photons to contribute eventually to the estimation of neutron

doses in a later stage of the particle history. Forced collisions are implemented in the MCNP input with the following line:

fcl:p 0 101r 1 4r 0 227r

In this card, the numbers indicate for which cell the forced collisions apply. The technique is activated for only 5 cells, belonging to the target and the primary collimator.

The distance to the next photon collision is determined using the total photon cross section, photoatomic plus photonuclear. Here, the ISPN parameter equal to 1, represented by the fourth entry of the phys:p card in the input, activates the simulation of photonuclear physics:

phys:p 23.1 2j 1

This parameter value also activates a biased treatment of photonuclear collisions. In the unbiased case, the type of collision would be sampled as either photonuclear or photoatomic depending on the ratio of the partial interaction cross sections. The used biasing option on the other hand is similar to the forced collisions technique. The colliding particle is split into two parts. One part is forced to undergo a photoatomic interaction whereas the other will interact photonuclear. Both particle weights are adjusted by the ratio of their actual collision probability. The emission characteristics are then sampled independently for secondary electrons and photons from a photoatomic collision and for secondary particles from photonuclear collisions. Before the sampling of secondary particle emissions from photonuclear interactions a collision isotope is selected based on the ratio of the total photonuclear cross section from each relevant table. Here, it is important to note that unlike photoatomic collisions, which are sampled from a set of elemental tables, photonuclear cross sections are isotope-dependent and photonuclear collisions have therefore to be sampled from a set of isotopic tables.

Once a neutron is produced by the computer simulation it is tracked using implicit capture. Implicit capture or survival biasing, see subsection 3.4.3 about modified sampling methods, effectively increases the chances of a neutron to reach the dose tallies in the region of interest. Before being absorbed and terminated, the code allows the neutron to continue its travel, albeit with a reduced weight. This treatment is the default modus for the transport of neutrons with MCNPX so that no special card is required in the simulation input to invoke the method.

They include again energy cut-offs and energy-dependent weight windows but also forced collisions for photons. The beforehand calculated weight window sets are invoked by the following lines:

wwp:p 4j -1 3j 1
wwp:n 4j -1

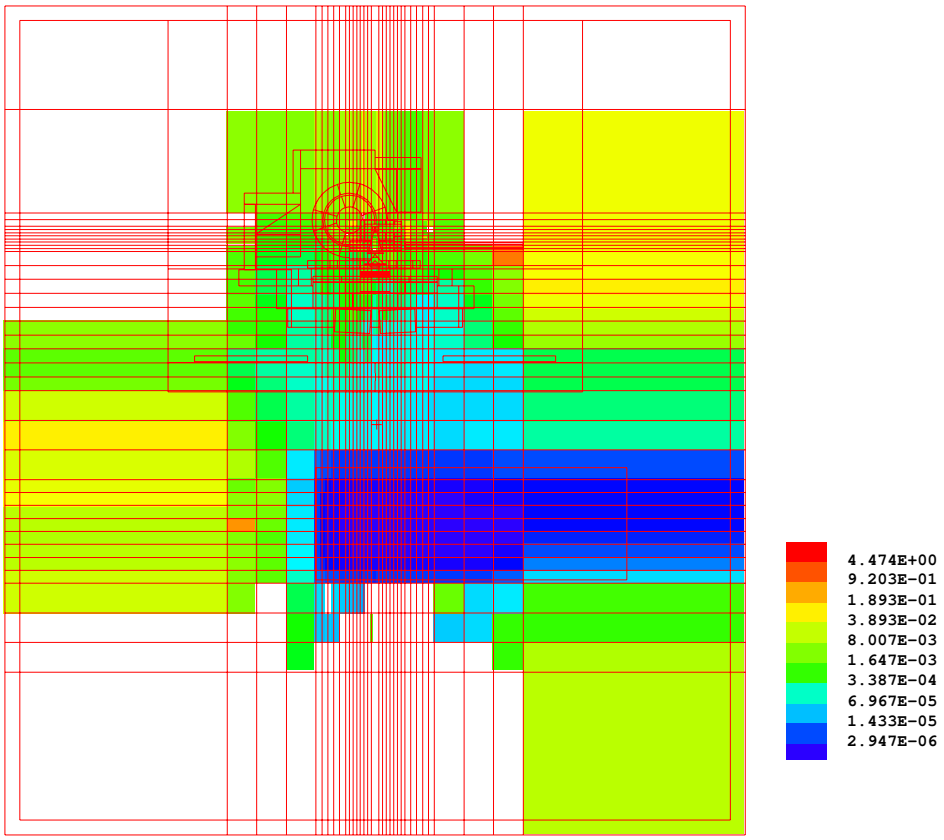

Figure 5.21: Plot of the mesh-based neutron weight windows in the y-z-plane (in-plane) covering the energy range between 0 keV and 2 keV. The color within each of the meshes indicates the value of the lower bound of the corresponding weight window.

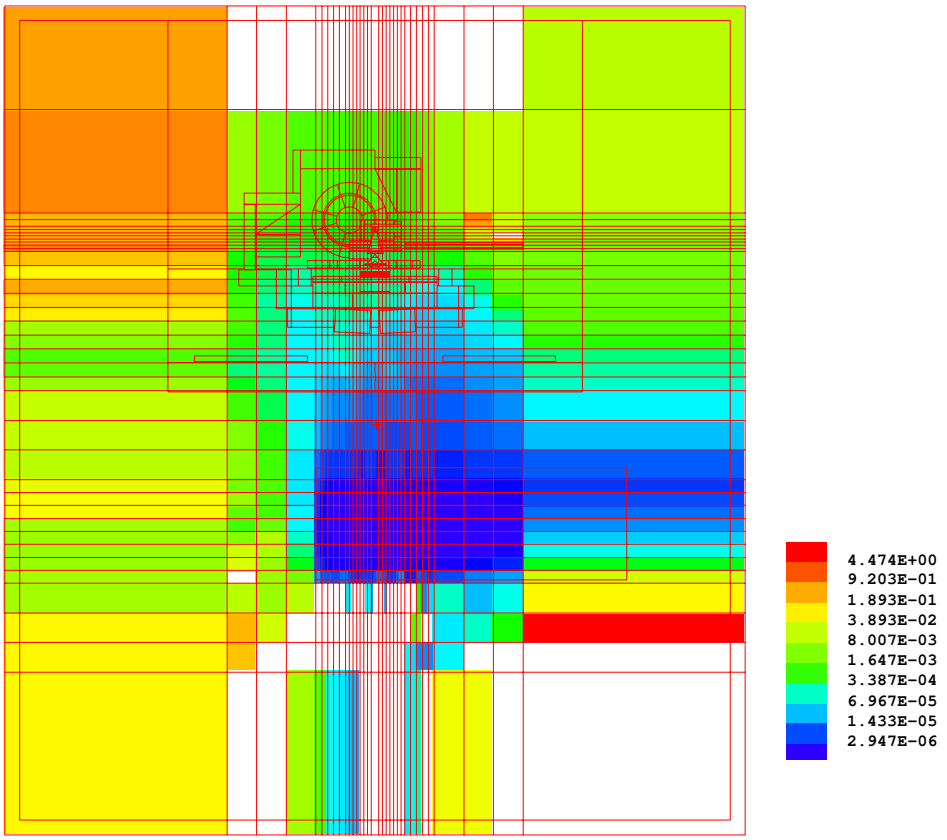

Figure 5.22: Plot of the mesh-based neutron weight windows in the y-z-plane (in-plane) covering the energy range between 2 keV and 100 keV. The color within each of the meshes indicates the value of the lower bound of the corresponding weight window.

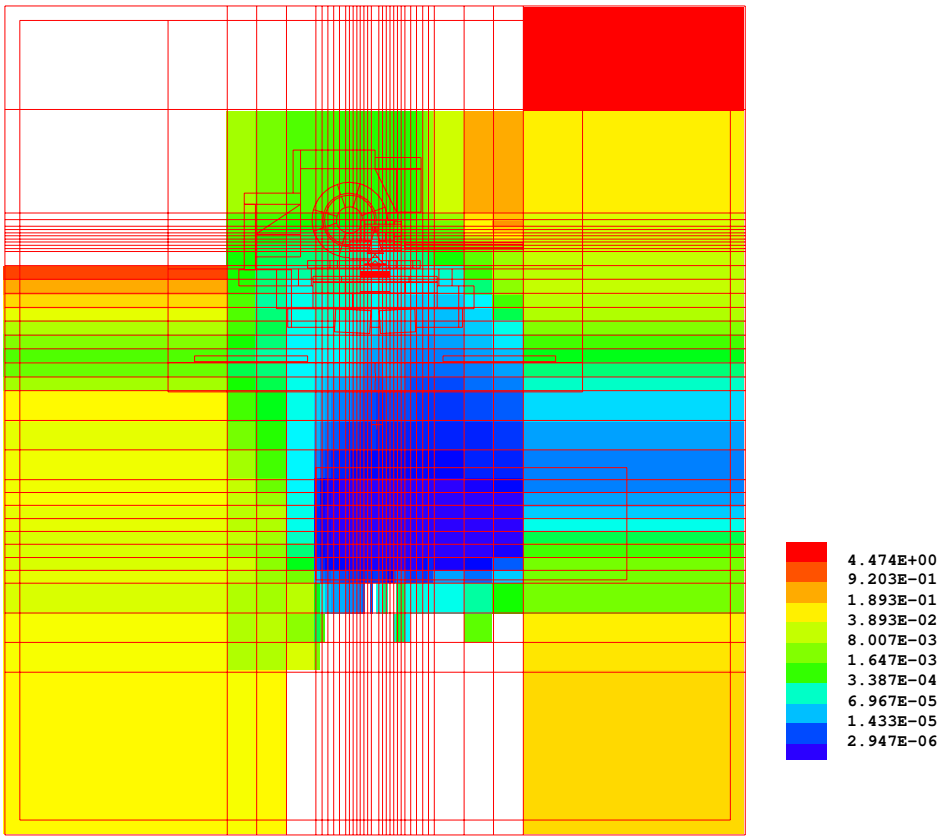

Figure 5.23: Plot of the mesh-based neutron weight windows in the y-z-plane (in-plane) covering the energy range between 100 keV and 5 MeV. The color within each of the meshes indicates the value of the lower bound of the corresponding weight window.

6 Photon Dose Calculations

The implemented MCNPX model, consisting of the input files listed in appendix B.1, has finally been used to calculate photon doses to the ICRP-Adult Male phantom. Two dose quantities were determined at the same time by the simulation: Firstly, absorbed photon doses were scored in each of the voxels throughout the phantom. The results are presented and discussed in section 6.1. The second quantity of interest were photon equivalent doses to selected organs, subject of section 6.2. With MCNPX, also perturbations in cell material density, composition, or reaction cross-section data can be handled. This feature was demonstrated by means of an academic scenario based on the chosen treatment plan and the implemented phantom model. The description of the test case scenario and corresponding simulation results are provided in section 6.3.

Data Processing and Visualization

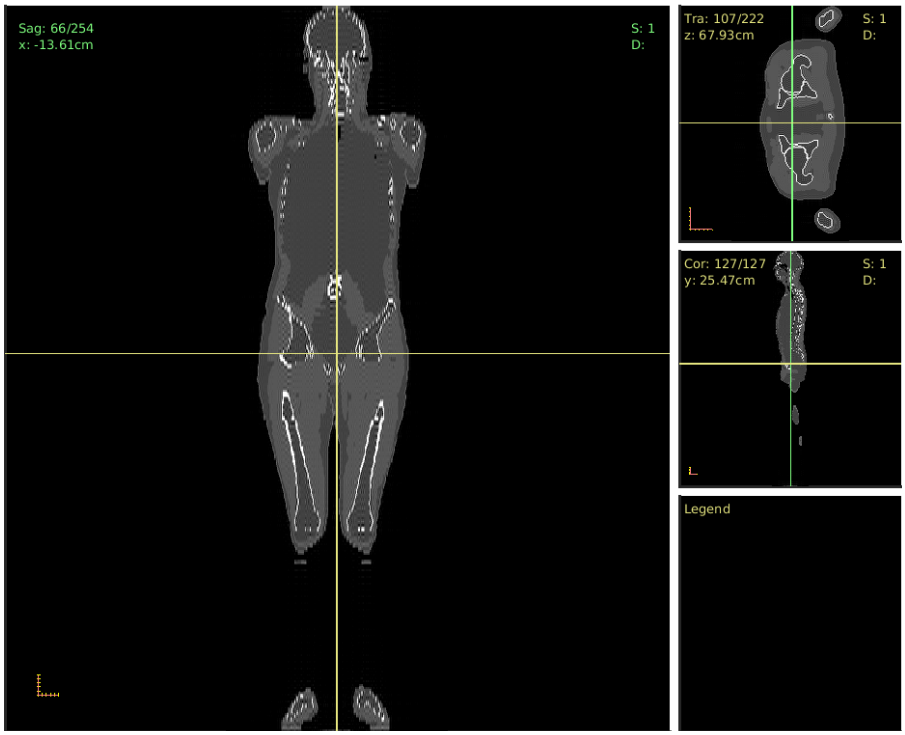

Figure 6.1: Visualization of the ICRP adult male voxel phantom in CERR. Coronal cross-section of the phantom in the main window, transversal and sagittal cross-sectional views in the side-windows on the right.

MCNPX offers the option to store essential calculation results in a dedicated output file. These so called MCTAL-files contain only tally data, in the present case the matrix of estimated photon absorbed doses, and the corresponding relative uncertainty values. The data-structure is well formatted which facilitates further processing, see also appendix B.1 of the MCNPX manual [Pel11]. Furthermore, the files are written directly in readable ASCII-format. In order to analyze and to visualize the data a MATLAB-program was developed capable to read out the simulation output and

to import the data into the MATLAB-based computational environment for radiotherapy research called CERR [Mat15, Dea03]. Also geometry and material data of the ICRP adult male voxel phantom were processed to create a digital representation in CERR. Figure 6.1 shows transversal, sagittal and coronal cross sections of the phantom visualized with the graphical user-interface of CERR.

(a) **(b)**

Figure 6.2: Segmentation of the ICRP adult male voxel phantom based on phantom raw data. The color highlighting of the segmented tissues is not unambiguous. (a) in the coronal plane and (b) in the sagittal plane.

Furthermore, the raw data about the computational have been used to generate a segmentation of the phantom, see figure 6.2. With this segmentation dose volume histograms can be calculated to further analyze doses received by each organ or tissue type, e.g. in case of perturbations in the tissue materials, see section 6.3.

6.1 Photon Absorbed Doses

Photon Absorbed Dose Maps

This preparative data-processing now allows a superposition of the photon dose matrix onto the visualized phantom and thus facilitates an examination of the calculated results. Figures 6.3 and 6.4 show the photon absorbed doses in the coronal and in the transversal phantom plane, respectively, through the PTV of the 3D-CRT-treatment. The unit of the color scale is in Gray. It can be seen that the prescribed treatment dose of 10 Gy, indicated by the red area, is clearly achieved in the PTV around the prostate. This distribution is obtained by summing up the contribution of the energy deposition from all four fields of the 3D-CRT treatment.

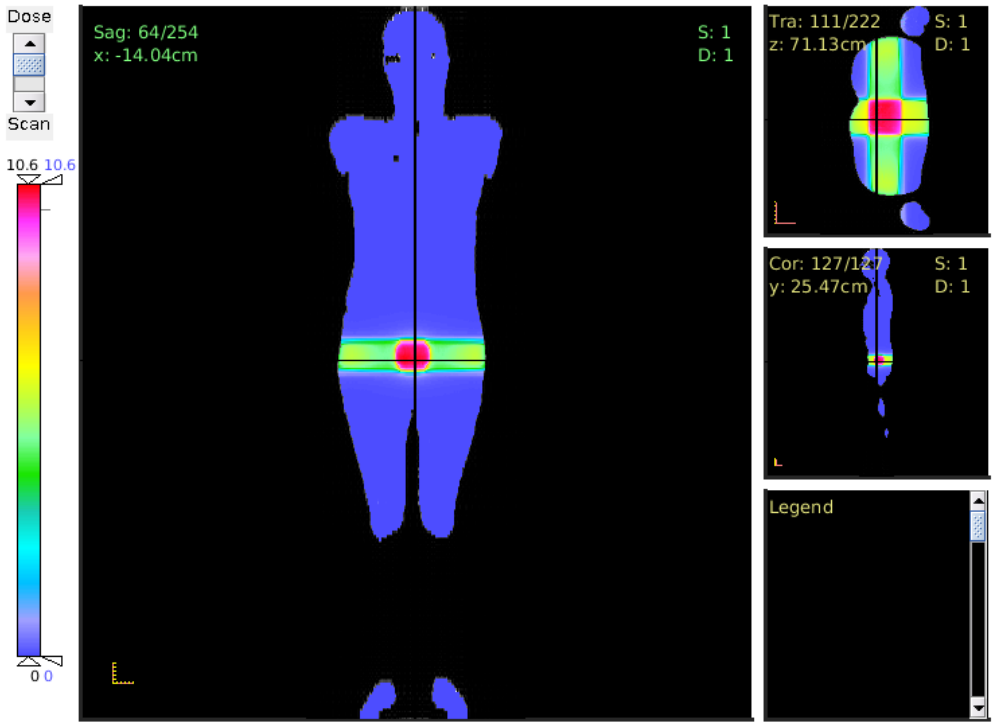

Figure 6.3: Photon absorbed dose distribution of the 3D-CRT treatment in the coronal phantom plane. The unit of the color code is [Gy]. The PTV is covered by the red area indicating a photon dose of 10 Gy or more.

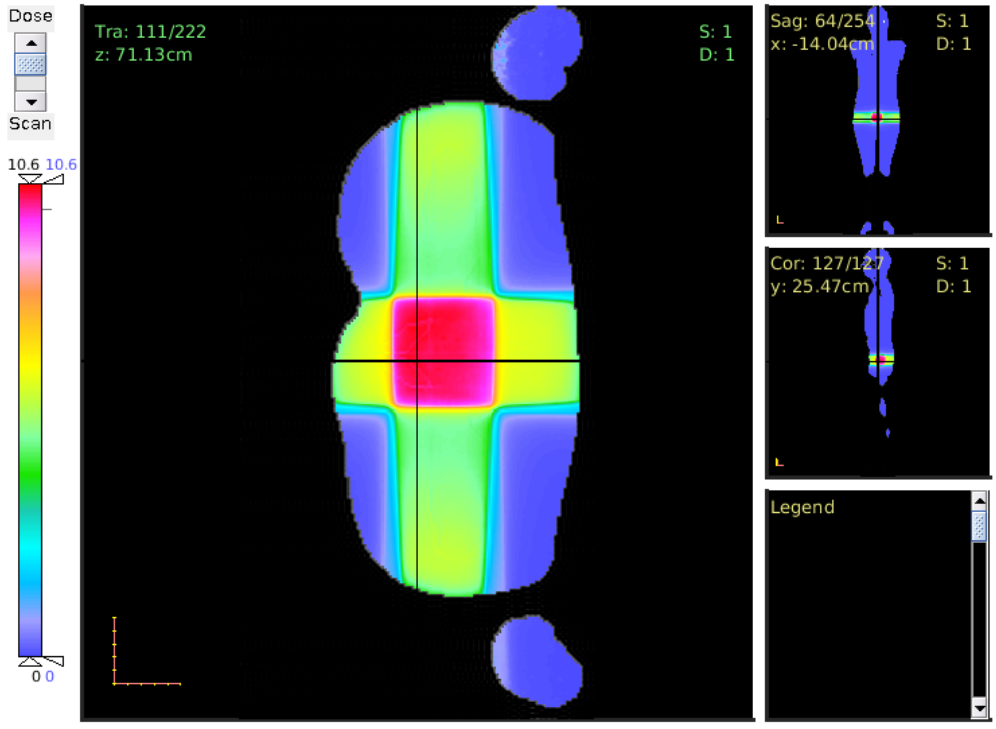

Figure 6.4: Photon absorbed dose distribution of the 3D-CRT treatment in the transversal phantom plane through the PTV. The unit of the color code is [Gy].

Relative Uncertainties of Photon Absorbed Doses

The combination of different VRTs elaborated and described in subsection 5.5.2 was applied in the radiation transport simulations to calculate the photon absorbed doses as well as the photon equivalent doses which are subject of the next subsection. In this way, calculation uncertainties in the dose values could be reduced to a great extent. With the the developed in-house MATLAB-program also relative uncertainty values of the MC-simulation results can be imported into CERR. Figure 6.5 shows the relative uncertainties of the absorbed photon doses visualized in figure 6.3 The relative uncertainty, as it was defined by equation 3.10 in section 3.3, was calculated, like the actual dose values, for each single voxel of the phantom. The values range from close to 0 in and directly around the treatment beam fields, indicating highly reliable dose values, to 1 for useless dose-values.

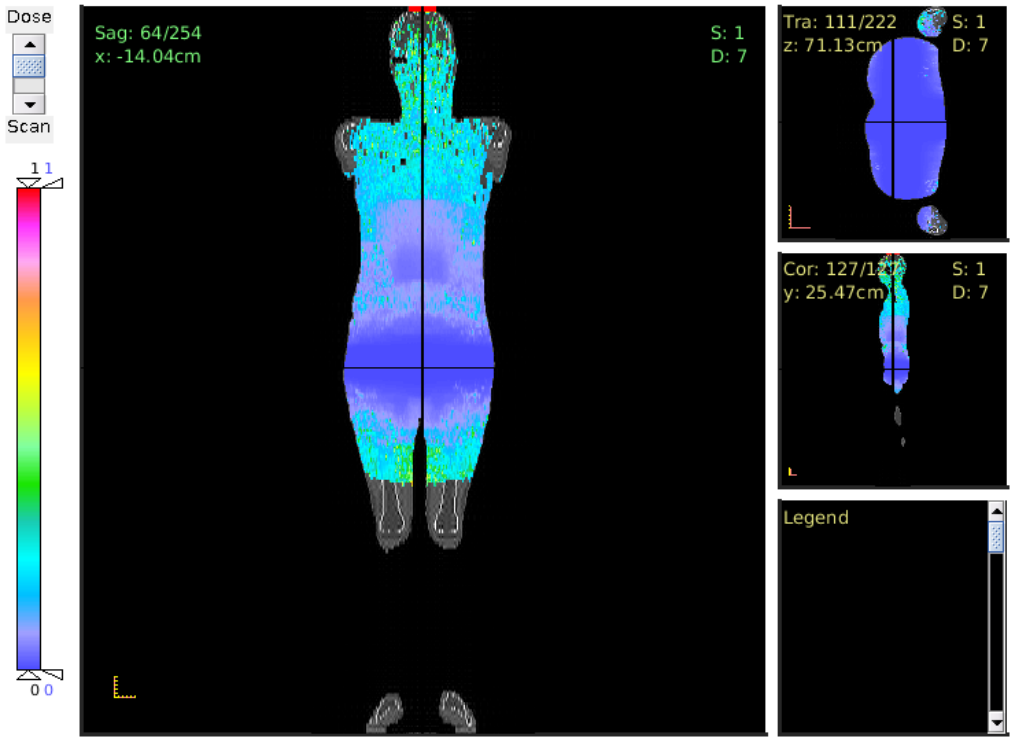

Figure 6.5: Relative uncertainty of the calculated photon dose values in the coronal phantom plane shown in figures 6.3 and 6.7. The relative uncertainties are like the dose values calculated voxelwise. Low relative uncertainty values close to 0 imply reliable dose values and are visualized in bluish colors. The cylindrical fashioned weight window mesh is visible as a pattern in the uncertainties in both the coronal and the sagittal plane. The weight windowing was concentrated on radiosensitive organs and tissues neglecting the arms and legs.

It can be observed that in general very low relative uncertainties were achieved. The uncertainty in the primary treatment field as well as in the closer vicinity is almost 0 as a consequence of the high simulated photon flux. But the precision of dose calculation remains high also at greater distances to the field edge. Figure 6.6 shows a diagram of the relative uncertainties along the axis in the mid-sagittal plane in figure 6.5 (black line). The uncertainty stays below 10 % in a wide range from the field edge in the 118^{th} transversal plane of the phantom until the 162^{nd} slice, corresponding to a distance of more than 35 cm. This high precision in the MC-calculation ensures the reliability of the obtained photon dose values.

The effect of the weight windows on the MC simulation results is clearly visible in picture 6.5. The variance reduction via weight windows is focused on the energy deposition in the radiosensitive organs of the trunk and in the head of the anthropomorphic phantom. The simplified cylindrical water phantom, used for the weight window generation, was therefore dimensioned in such a way that it truncates arms and legs of the patient phantom, see subsection 5.5.1 and figures 5.14 - 5.16. This restriction of the weight windowing is now evident. In most voxels of the arms and legs, outside the borders of the auxiliary water phantom, no energy deposition was scored by the dose-tally. In the calculation of the relative uncertainty via equation 3.10 this leads to a division by 0 so that the uncertainty is not defined in such cases, hence, not displayed in figure 6.5.

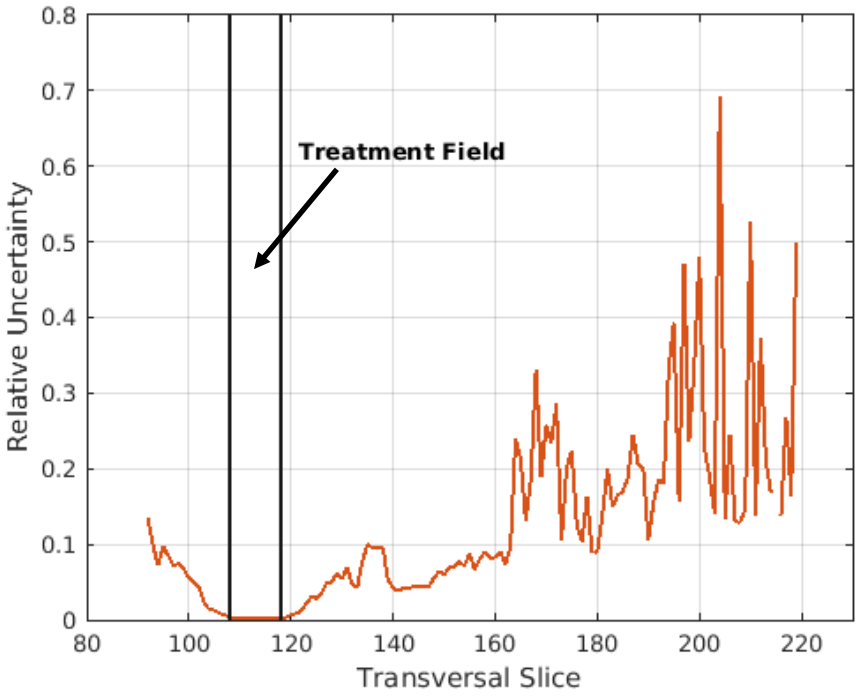

Figure 6.6: Relative uncertainty of the calculated photon dose values along the midsagittal phantom plane of figure 6.3 or 6.5, respectively. The primary treatment field lies between the 108^{th} and 118^{th} transversal phantom plane. The relative uncertainties remain below the level of 10 % until the 162^{nd} transversal slice of the phantom corresponding to a distance of more than 35 cm from the beam field edge.

Another finding of figure 6.5 are slightly lower uncertainty values in the abdomen than in the surrounding tissues. The reason for this are occasionally lower weight window bounds in the part of the weight window mesh covering that region of the phantom. This can be attributed to the statistical nature of the weight window generator causing, to some extent, fluctuations in the produced weight window bounds. The better sampling of this part of the phantom finally results in a little preciser dose values. The effect thereof is more obvious in the lower dose regions of the phantom and is discussed in the next paragraph.

Low- and Intermediate-Level Doses

The following figures allow a closer look on the lower doses received by the tissues in the phantom body further away from the treatment fields. In order to have a more detailed view at the photon dose distribution at lower levels, the display of doses has been limited to a value of 0.1 Gy. For this purpose higher dose values in and directly around the PTV are omitted. In this way the color

code is applied to a far smaller dose range and helps to better depict the actual load to healthy tissues in this dose-regime.

Figure 6.7 shows the low-level photon dose distribution of the 3D-CRT treatment in the coronal phantom plane. It can be seen, that the photon absorbed doses generally decrease with distance to the treatment fields. On the other side, the out-of-field photon dose does not vary greatly with medial-lateral or anterior-posterior position, i.e. with tissue depth. In figure 6.8 photon doses in the transversal phantom plane are provided for various distances from the treatment field edge showing rather uniform distributions.

The decrease of the photon dose with distance from the field edge, however, was found to be not strictly monotone. In the left graphic of figure 6.7 there is a rectangular region visible in the abdomen with slightly higher dose values than in the adjacent tissues, highlighted in figure 6.9. Between this region and the treatment field with its high dose values the calculated photon dose level appears to be lower. These lower values are connected to the higher relative uncertainties and don't reflect the physical reality correctly. The upper plot in figure 6.9 better illustrates this correlation. It directly compares the height of the calculated dose values and their estimated relative uncertainties along the axis in the midsagittal plane in figures 6.7 or 6.5, respectively. The coincidence of high uncertainties and lower dose values points towards an underestimation of the actual photon dose level in this location.

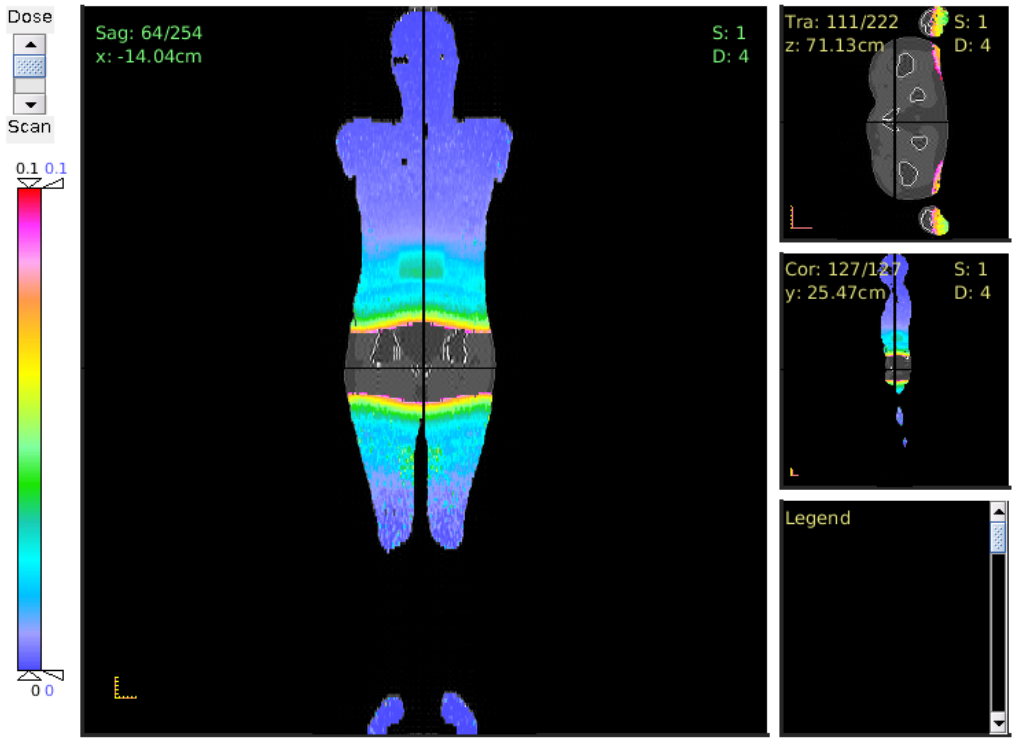

Figure 6.7: Photon absorbed dose distribution of the 3D-CRT treatment in the coronal phantom plane. The dose values are limited to a maximal value of 0.1 Gy in order to provide a better contrast. The unit of the color code is [Gy].

It has to be stated that, although major efforts in terms of variance reduction have been made, in many locations of the phantom more distant to the treatment field the voxelwise calculation of radiation doses is still prone to an underestimation due to an insufficient sampling. There, for the small voxelsize of only $0.0365\,\mathrm{cm}^3$ it is difficult to gain enough information, i.e. enough non-zero

tally scores x_i from the simulated particle histories, to calculate a reliable average value $\bar{x}$ for the energy deposition in the volumes, see equation 3.2. As consequence, the calculated dose values cannot be considered as conservative estimates of the prevailing dose level but rather mark lower dose limits.

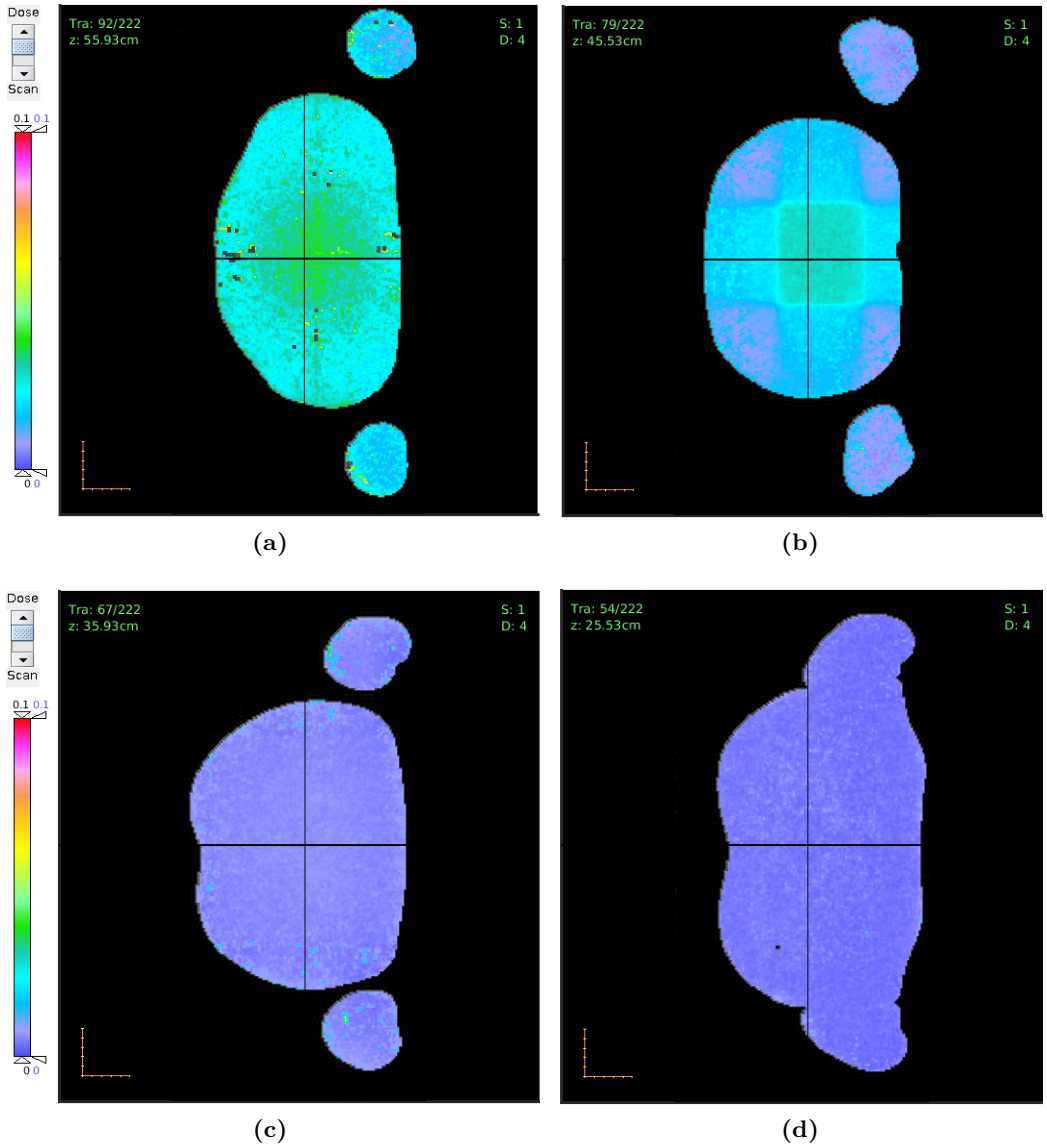

Figure 6.8: Photon absorbed dose distributions of the 3D-CRT treatment in the transversal phantom plane with increasing distance from the beam field edge in superior direction: (a) 10 cm out-of-field; (b) 20 cm; (c) 30 cm; (d) 40 cm. The unit of the color code is [Gy].

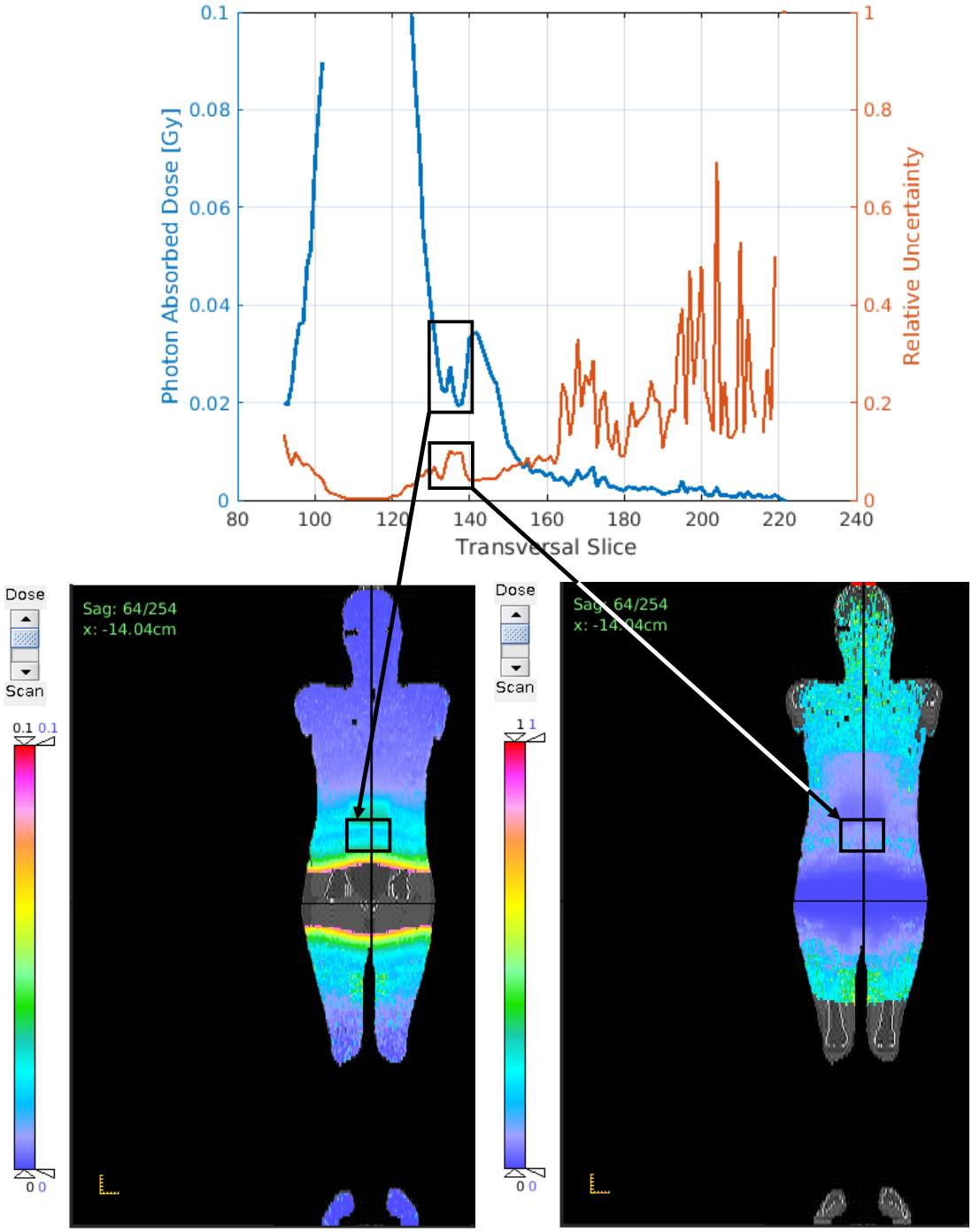

Figure 6.9: Upper diagram: Direct comparison of calculated photon absorbed dose values and corresponding relative uncertainties along the axis in the mid-sagittal plane of figures 6.7 (lower left picture) and 6.5 (lower right picture), respectively. The dose level in the plot is limited to 0.1 Gy. The marked parts of the graphs indicate an underestimation of the actual dose levels associated with a local increase in the relative uncertainties. Lower left picture: Corresponding region in the abdomen with an underestimation of the photon absorbed dose. Lower right picture: Region with increased relative uncertainties.

6.2 Photon Equivalent Doses

During the MC-simulation for the calculation of the photon absorbed dose distribution also estimates of received organ equivalent doses have been determined. Table 6.1 lists the results for selected organs and tissues of the phantom. The corresponding tallies as part of the MCNPX-input file are listed in appendix B.19. Unlike the dose estimates for single voxels organ equivalent dose values suffer from far lower uncertainties. Since they are averaged over much larger volumes the sampling in the MC-simulation is enough to provide a high precision in the dose calculation. For example, even in the brain an uncertainty of under 1 % can be achieved although the voxelwise dose values are already highly unreliable.

Also equivalent dose values from a study carried out by Bednarz et al. [Bed09c] are provided in table 6.1. Although their calculations were done using a different anthropomorphic phantom, the RPI-Adult Male Computational Phantom, the results are generally comparable with the values found in the present study. For example, Bednarz' values for the equivalent doses in liver, spleen, gallbladder and kidneys are almost the same with a difference of less than 10 %. On the other hand, Bednarz et al. report much higher equivalent doses for the colon (+50 %) and the small intestine (+64 %). These large differences can be explained by the location of those parts of the gastrointestinal tract relative close to the primary treatment field. Due to the large gradient of

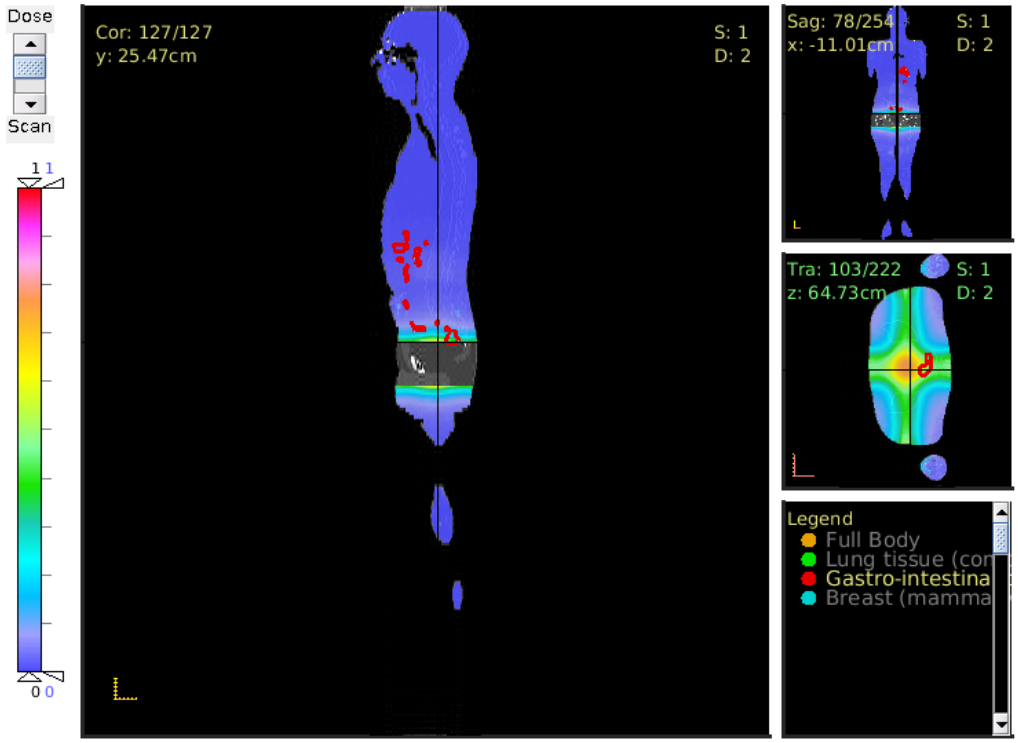

Figure 6.10: Photon absorbed doses in the sagittal phantom plane, limited to a maximal value of 1.0 Gy. The unit of the color code is [Gy]. The gastrointestinal tract, depicted as red structures, is partially located close to the primary treatment field. Small changes of the location can lead to a huge difference in the observed equivalent dose level due to the high photon dose gradient in this region.

the photon dose distribution in this region, even small differences in the model-setups regarding the locations of the gastrointestinal tract and the dose tally can lead to a significant difference in the equivalent dose estimate, see figure 6.10. The same applies to the active bone marrow and

the lymph nodes whose tissues were partially also inside the treatment field. In that case, voxels scoring a very high energy deposition were not included in the calculation of the corresponding organ equivalent dose estimate.

On the contrary, equivalent doses for the esophagus, the thyroid and the brain calculated by Bednarz et al. are much lower, by 44 %, 26 % and 32 %, respectively, than in the present study. These lower dose values are accompanied by relatively high uncertainties with 7.5 % for the esophagus, 9.2 % for the thyroid and 4.4 % for the brain. This correlation points towards a significant underestimation in the dose estimates from Bednarz et al. since, as outlined in the previous section, an underestimation of the true dose level is the consequence of an insufficient sampling associated with a higher calculation uncertainty. In fact, esophagus, thyroid and brain are located far distant from the treatment field making an appropriate sampling of the particle-energy deposition in these regions more difficult. These findings clearly show that a proper sampling with low statistical uncertainties is necessary to prevent an underestimation of the actual radiation exposure and the dose equivalent in non-target tissues and organs.

Table 6.1 also contains measurements of the photon equivalent doses in some organs of interest. The listed measurement data were published by Wang [Wan08], Howell [How06], Kry [Kry05a] and Vanhavere et al. [Van04]. Wang et al. investigated the same CRT-treatment plan as used in this study or the one conducted by Bednarz et al. Their measurements involved a RANDO physical phantom suitable for a comparison of the measured dose quantities with the calculated doses in the ICRP reference male phantom. The measurement uncertainties reported by Wang, however, were very high, partially so high questioning the validity of the corresponding values. Also Kry and Vanhavere used a RANDO phantom while Howell et al. deployed the ART male dosimetry phantom [ICR89] constructed of tissue equivalent material and likewise comparable to the ICRP reference male phantom. Howell and Kry investigated realistic 3D-CRT plans with 18 MV photon beams whereas Vanhavere et al. only considered a $10 \times 10\,\mathrm{cm}^2$ beam field.

Table 6.1: Photon equivalent dose to selected organs in units of μSv per MU from a 4-field 3D-CRT treatment for prostate cancer.

	Photon equivalent dose[a]					
	Calculations		Measurements			
Organ	This study[b]	Bednarz et al.[b,c]	Wang et al.[d]	Howell et al.[e]	Kry et al.[f]	Vanhavere et al.[g]
Stomach	4.89 (0.3)	6.46 (1.9)	18.65 (±1.06)	3.88	14.6	41
Colon	12.66[h] (0.1)	19.02 (1.5)	31.27 (±1.20)	566.8	39.6	2900
Liver	4.73 (0.2)	5.17 (1.6)	18.65 (±1.06)	4.42	15.8	36
Lung	3.22 (0.3)	2.73 (1.5)	0.97 (±0.97)	2.36	5.9	13
Esophagus	2.91 (1.5)	1.64 (7.5)	0.97 (±0.97)	2.12	4.1	10
Pancreas	7.35 (0.3)	4.15 (4.5)				
Brain	1.01 (0.6)	0.69 (4.4)				
Active bone marrow	13.04[h] (0.1)	4.17 (0.9)		3023.2	16.9	
Small intestine	27.85 (0.1)	45.63 (0.6)				
Spleen	4.03 (0.7)	4.37 (3.9)				
Gall bladder	5.68 (0.6)	5.53 (3.8)				
Heart	3.50 (0.4)	2.99 (2.4)				
Lymph nodes	11.49[h] (0.1)	13.39 (2.7)				
Kidneys	8.31 (0.2)	9.10 (2.1)				
Thyroid	2.05 (0.3)	1.52 (9.2)	0.0 (+0.08)	1.54	2.6	13

[a] all values in units of [μSv/MU].
[b] In brackets: corresponding relative uncertainty in percent of the obtained dose value.
[c] [Bed09c].
[d] [Wan08]. In brackets: corresponding uncertainty as absolute deviation from the obtained dose value.
[e] [How06]. Howell et al. reported an uncertainty in the TLD-700 detector readings of less than 3.5 %.
[f] [Kry05a]. Kry et al. reported an uncertainty in the TLD-700 detector readings of 3 %.
[g] [Van04]. No uncertainty range is reported.
[h] Parts of this tissue were within the primary field and not included in the calculation of the corresponding organ equivalent dose.

For the colon, all groups reported far higher photon equivalent doses, in the case of Vanhavere even orders of magnitudes higher, than calculated by Bednarz or in this study. This can be explained again by the large photon absorbed dose gradient within this organ. In general, the measurements were taken by placing the dosemeters in the phantoms at pre-selected cavities representing the typical organ location. However, this approach of point-wise measurements approximating organ-averaged equivalent doses introduces potentially huge systematic errors especially in regions with large dose gradients. Vanhavere et al., for instance, state that the positioning accuracy of the TLDs in their measurements is too low for colon and bladder doses to be considered as representative of the real situation. In fact, for this reason they didn't include these organs in their calculation of an effective photon dose. The method of estimating organ-averaged equivalent doses through pointwise measurements offers therefore only results with a limited accuracy.

The issue of deriving organ equivalent doses from measurements is also obvious for active bone marrow. For bone marrow, being distributed throughout the body, Kry et al. determined an equivalent photon dose of 16.9 μSv/MU. They recorded the photon dose to the bone marrow as the average of the photon doses to 10 other measurement points located at organs of interest. Indeed, the dose of 16.9 μSv/MU matches quite well the calculated value of 13.0 μSv/MU in this study. Howell et al., on the other side, report more than 3.0 mSv/MU for active bone marrow, apparently because at least a part of the selected measurement points fall within the primary field of the prostate therapy.

For the organs besides the colon and active bone marrow, namely the stomach, liver, lung, esophagus and thyroid, the organ equivalent photon doses calculated in this study were consistently higher than those reported by Howell and at the same time lower than those from Kry. These differences can be attributed to systematic differences in the model and measurement setups, for example, in the deployed phantoms and the limited number of measurement points, especially in the case of Kry et al. Nevertheless, considering these minor differences in the dosimetry studies the obtained equivalent dose values are in reasonable agreement. Vanhavere et al., however, reported far higher dose values emerging from a simpler measurement setup taking into account only one $10\,\mathrm{x}\,10\,\mathrm{cm}^2$ treatment field.

6.3 Dose Perturbation Analysis

Besides the MC calculation of the actual photon dose values also the influence of density variations in the organ tissues of the phantom has been investigated. MCNPX provides the option to calculate the difference in the obtained dose values in the presence of small deviations in the material properties of selected regions. Hereby, the differences between unperturbed and perturbed dose values are calculated within the same MC simulation and hence are subject of the exact same calculation uncertainties. This optional calculation feature of MCNPX is remarkable as it allows to evaluate the effects of small perturbations in the simulation input disentangled from the calculation uncertainties of another simulation which would have to be carried out to calculate the perturbed dose values for a comparison with the unperturbed ones. The uncertainties in the dose values of a second simulation would make it impossible to detect differences in the results actually caused by the input perturbations. The perturbation theory behind this simulation feature of MCNPX is based on the Taylor Series expansion and the first and second order differential operator technique which has been explained in section 3.6.

To test the sensitivity of calculated photon dose values under density variations, an anterior-posterior irradiation was simulated. Six cases were considered, three with an increase of 1 %, 5 % and 10 % in the density of the phantom tissues and three cases with a decreased density from the nominal value by the same percentages. The density perturbation was applied to all organs. As a result, the differences between calculated unperturbed and perturbed dose values scaled almost linearly with the relative changes in the organ-densities. This finding can be explained by the linear dependency of the mass energy absorption coefficients from the material densities. Furthermore,

at such high photon energies the photon fluence is not enough disturbed by density changes of a lower order to cause significant nonlinearities between energy absorption in the organs and the corresponding material density, also for tissues located more downstream in the treatment beam.

In order to better demonstrate the perturbation technique a more drastic, however, rather academic scenario has been considered. The 3D-CRT simulation presented in the previous sections has been perturbed by replacing the bone tissues of the femora by titanium. Although the structures of the femora remains unchanged the presence of a titanium femoral prothesis is approximated and mimicked in this way. Figure 6.11 shows the effect of the titanium implants on the photon absorbed dose distribution in and around the PTV. This 'perturbed' dose distribution has been obtained in the course of the same MC simulation carried out for the calculation of the photon absorbed doses depicted in figures 6.3 and 6.4. Hence, also the same relative uncertainties from figure 6.5 apply to this perturbed scenario.

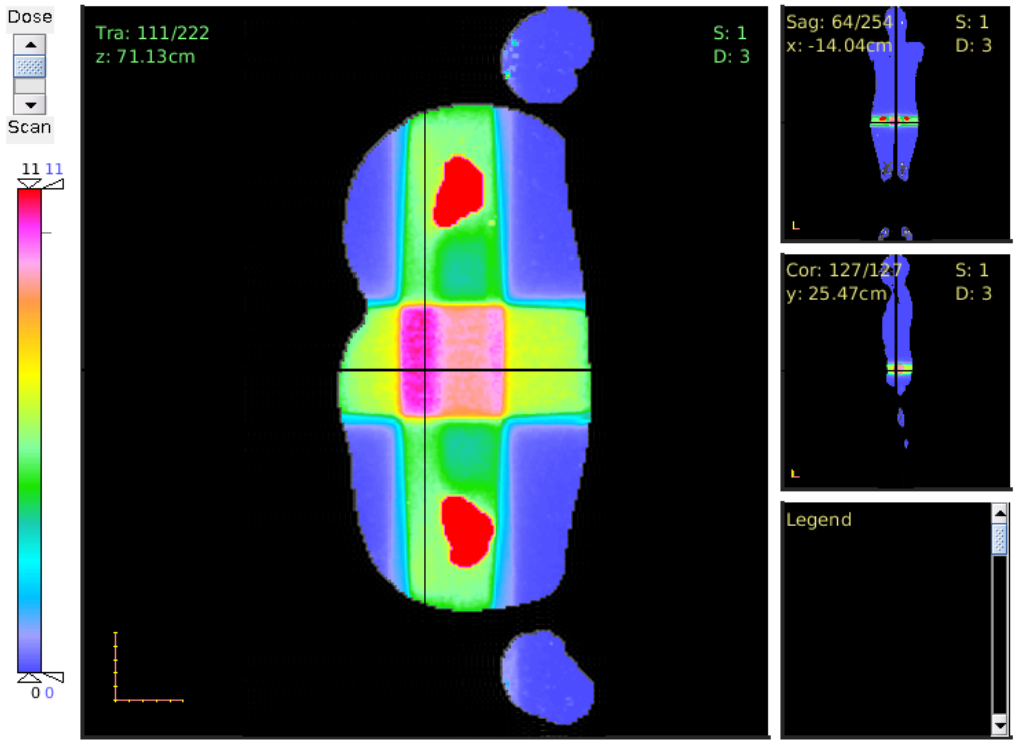

Figure 6.11: Photon absorbed dose distribution of the 3D-CRT treatment in the transversal phantom plane through the PTV. The material of the femora is changed to titanium mimicking a femoral prothesis. The unit of the color code is [Gy]. The displayed dose range is limited to 11 Gy, exceeded only in the titanium.

The presence of the titanium structures clearly reduces the photon absorbed dose in the PTV. The implant partially shields the photon beams from the left-right- and the right-left-lateral irradiations. In order to improve the visibility in the dose distribution map in figure 6.11 the range of displayed dose levels has been limited to 11 Gy. This limit was only exceeded by the energy deposition in the titanium structures and therefore does not affect the dose values in the body tissues. Figure 6.12 shows the dose difference between the perturbed and unperturbed photon dose distribution in the transversal plane. The difference was limited to 2 Gy, again because this value is only exceeded in the titanium implant. Figure 6.13 on the other hand provides a comparison of the perturbed and unperturbed dose volume histograms for prostate, urinary bladder

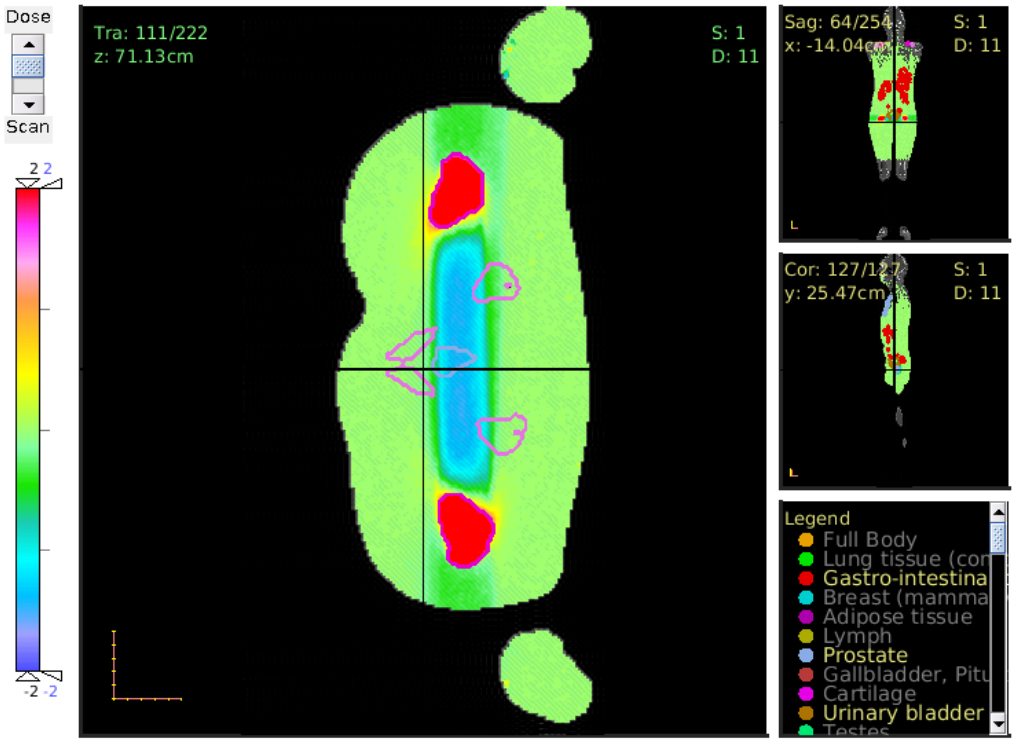

Figure 6.12: Difference in the photon absorbed dose distributions from figures 6.4 and 6.11. The unit of the color code is [Gy]. The displayed dose range is limited to 2 Gy, exceeded only in the titanium. The shielding effect of the titanium femoral implants on the photon absorbed doses in the PTV are clearly visible.

and large intestines. It shows how the entire treatment is affected by the metallic implants. The energy deposition in the prostate and the PTV doesn't reach the prescribed dose of 10 Gy anymore whereas also healthy tissues like urinary bladder and large intestines receive less dose. Although this example is of academic nature as it applies a hypothetical treatment plan for a patient with a metallic femoral implant it demonstrates the potential of the perturbation technique to assess the quality of a treatment plan in the presence of metallic implants or other medical devices and structures.

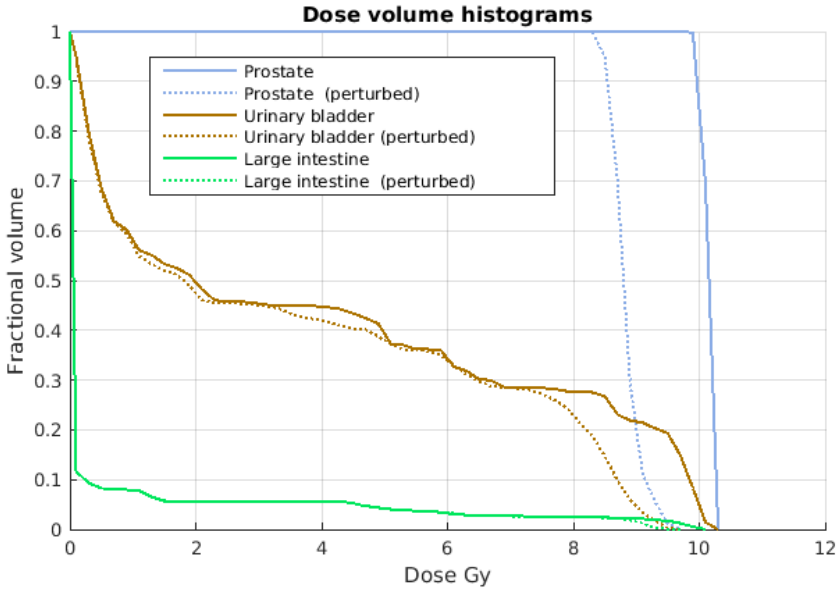

Figure 6.13: Comparison of dose volume histograms with and without metallic implants. Examination of reached dose levels in prostate, urinary bladder and large intestines. For the perturbed simulation imitating an irradiation of the phantom with titanium femoral implants there is a falloff in absorbed photon doses observable in all organs and tissues exposed to the primary treatment beam when compared to a simulation with normal femoral bone tissues.

7 Neutron Dose Calculations

For the calculation of neutron radiation doses, caused by photonuclear reactions in the LINAC and subsequent emission of neutrons, the same geometry model has been used as for photon dose calculations. The corresponding simulation input only differs with respect to the material definitions, the applied VRTs and tallies, see appendix B.2. Two dose quantities were determined: The neutron dose equivalent in all the voxels of the ICRP phantom as well as organ-averaged neutron equivalent doses in the defined organs. The corresponding results are presented and discussed in sections 7.1 and 7.2. Since photonuclear cross-section data themselves are subject to relatively high uncertainties an uncertainty analysis of the neutron dose equivalent yields has been performed. The results are presented in section 7.3.

7.1 Neutron Dose Equivalent Distributions

Neutron dose equivalent was calculated using track length estimates of the neutron energy deposition and corresponding energy-dependent conversion factor tables provided in publication 60 from the International Commission on Radiological Protection [Int91]. The obtained neutron dose equivalent distribution gives insight in the contribution of neutrons to total dose deposition over the whole phantom body. In general, most of the neutron energy deposition occurs close to the phantom surface, see figure 7.1. The energy of fast neutrons is mostly deposited by scattering with hydrogen nuclei and recoiling protons. Hence, the phantom tissues with their high hydrogen contents effectively moderate the impinging neutrons so that the neutron dose rapidly decreases with depth.

Unlike bremsstrahlung photons, the photoneutrons produced in the LINAC are emitted in a rather isotropic fashion. For this reason, the observed neutron dose equivalent distributions at low tissue depths show little dependency on the distance to the primary treatment field, see figure 7.2. The transversal neutron dose equivalent profiles, for example, at distances of 10 cm, 20 cm, 30 cm and 40 cm from the field edge, shown in figures 7.3 (a) - (d), are very similar to the one through the PTV in figure 7.1. Nevertheless, a peak in the neutron dose equivalent of about 20 mSv can be observed at the phantom surface within the 90° and 270° primary treatment fields where photoneutrons escape unhindered through the LINAC aperture. Also for the 0° and 180° angles the dose level appears slightly elevated. Beyond a distance of about 25 cm from the field edge the neutron dose equivalent is higher than the photon dose in tissues close to the surface, cf. figure 6.7.

The peak neutron dose equivalent values found in the primary treatment fields are consistent with measurements published by d'Errico et al. [d'E98]. They measured photoneutron doses in a tissue-equivalent liquid phantom using superheated drop detectors and applying a standard $10 \times 10\,cm^2$ x-ray field from a linear accelerator operated at 18 MV. In 1 cm depth on the central beam axis they obtained 4.5 mSv per Gy photon absorbed dose at maximum build-up. Given 315 monitor units, as for one of the 4 fields of the 3D-CRT treatment listed in table 5.4, this would lead to a neutron dose equivalent of 14.18 mSv in this depth. In fact, figure 7.1 shows similar values 1 cm below the phantom surface on the central beam axes of all 4 primary treatment fields. Although the neutron dose measurements are subject to uncertainties of about 20 % and despite the fact that d'Errico's measurement setup and the simulation model presented in this thesis differ by the deployed phantom as well as the field-size and -shape, the dose values are yet comparable. Hence, those measurements can eventually confirm the reliability of the presented neutron dose simulation results.

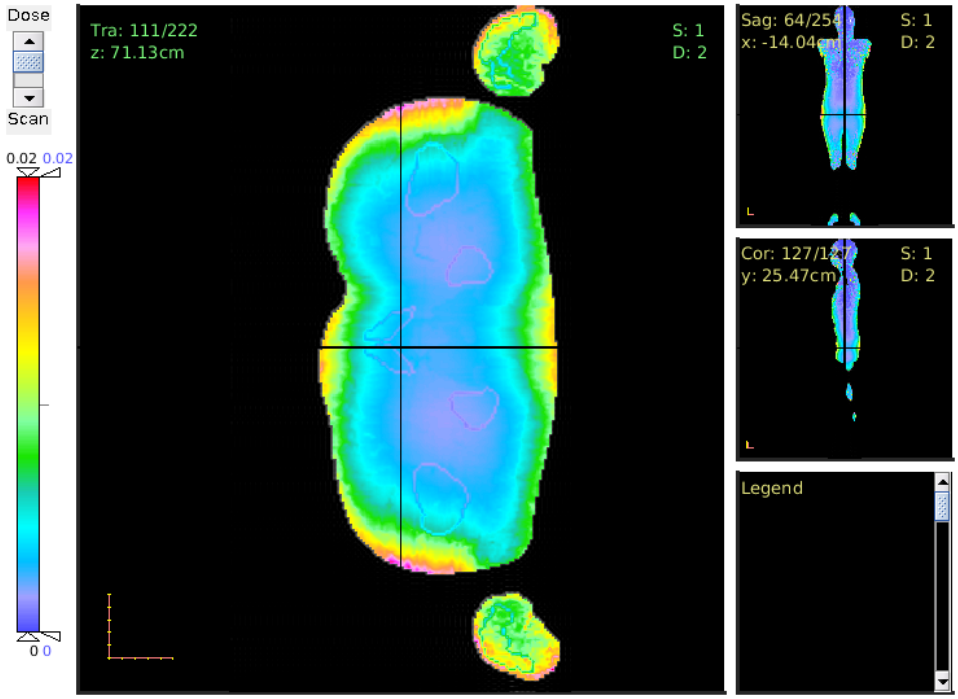

Figure 7.1: Neutron dose equivalent distribution of the 3D-CRT treatment in the transversal phantom plane through the PTV. The unit of the color code is [Sv].

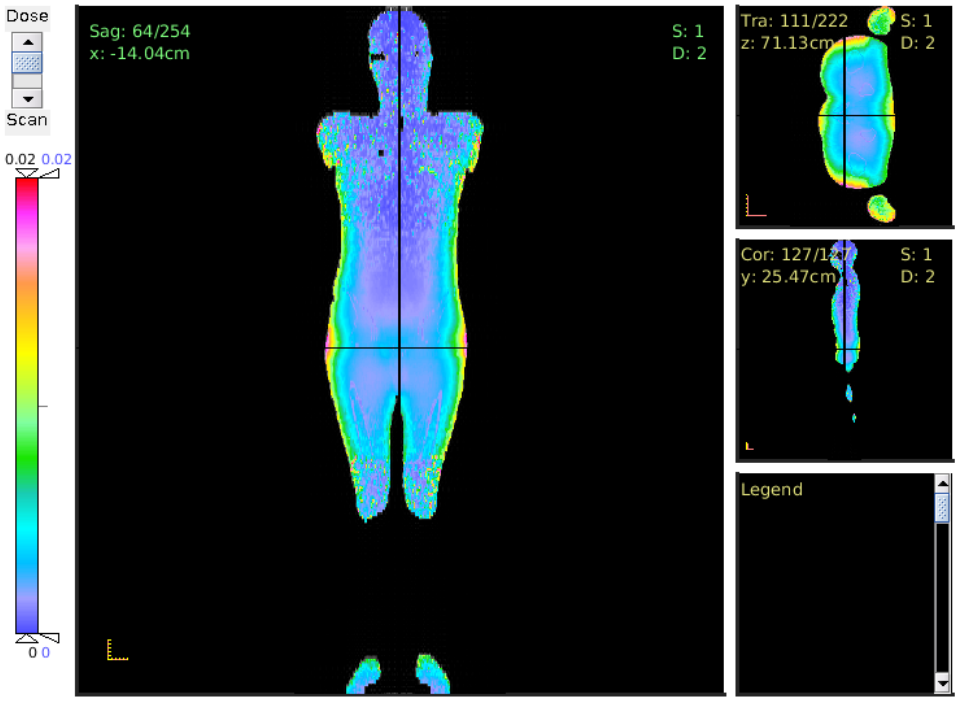

Figure 7.2: Neutron dose equivalent distribution of the 3D-CRT treatment in the coronal phantom plane. The unit of the color code is [Sv].

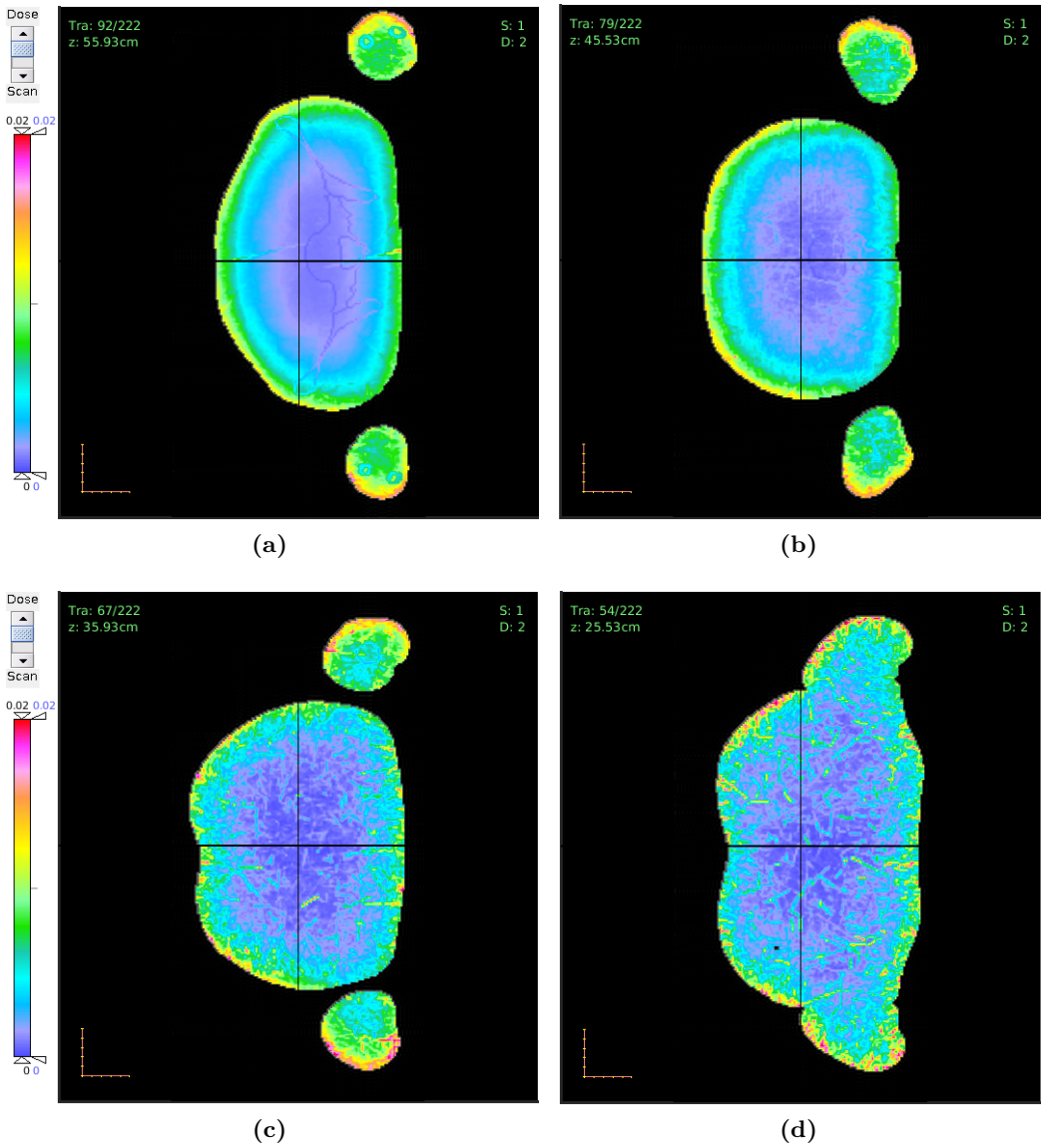

Figure 7.3: Neutron dose equivalent distributions of the 3D-CRT treatment in the transversal phantom plane at different distances from the beam field edge in superior direction: (a) 10 cm out-of-field; (b) 20 cm; (c) 30 cm; (d) 40 cm. The unit of the color code is [Sv]. In all these planes the peak neutron dose equivalent is found on the phantom surface and amounts to nearly 20 mSv.

It is important to note here that the presented neutron dose values cannot be considered as conservative dose level estimates as the MC-model does not include walls, floor and ceiling of the treatment vault. Pena et al. investigated the influence of these structures on the neutron fluence in the treatment room and found a 8.6 % higher total neutron fluence at the isocentre and a 15 % higher fluence at the position of the treatment couch when compared to simulations without consideration of the room walls [Pen05]. Although these percentages for the neutron fluence increase do not directly apply also to the resulting neutron doses, a corresponding increase in the neutron dose level of about the same order of magnitude has to be taken into account.

In addition to this simplification of the geometry model, there is also a restriction in the calculation of the radiation dose resulting from photoneutron emission. Neutron-capture γ-rays

and (n,n')-photons emitted in neutron interactions were not scored during the simulations since those additional photon doses, indirectly caused by the emitted photoneutrons, could not be calculated precisely enough to get meaningful results. D'Errico et al. on the other hand calculated depth-dependent neutron-capture γ-doses and neutron dose equivalent from 18 MV radiotherapy x-ray beams [d'E01]. They carried out MC-simulations with a tissue-equivalent slab phantom so that their results are generally applicable to this case. They found additional neutron-capture γ-doses to be of the order of 0.5 % of the actual neutron dose equivalent[1] at a depth of 1 mm with this value rising to about 3 % at 5 cm depth and about 10 % at 10 cm depth. These findings apply for a primary neutron energy of 0.565 MeV which is approximately also the effective energy of photoneutrons produced by the Varian Clinac at 18 MV. Thus, in order to draw a complete picture of the out-of-field dose exposure additional doses due to secondary photons have to be taken into account, especially at greater phantom depths.

In figure 7.4, relative uncertainties of the neutron dose equivalent distribution are plotted for each voxel in the same coronal plane as in figure 7.2. The values remain generally at a very low level of under 5 %. The effect of the cylindrically shaped weight windows around the PTV can be clearly seen. Only at at the largest distance to the field edge, for example in the brain, relative uncertainties reach high values. Here, also the weight windows have no effect anymore to yield a high precision in the small voxel volumes.

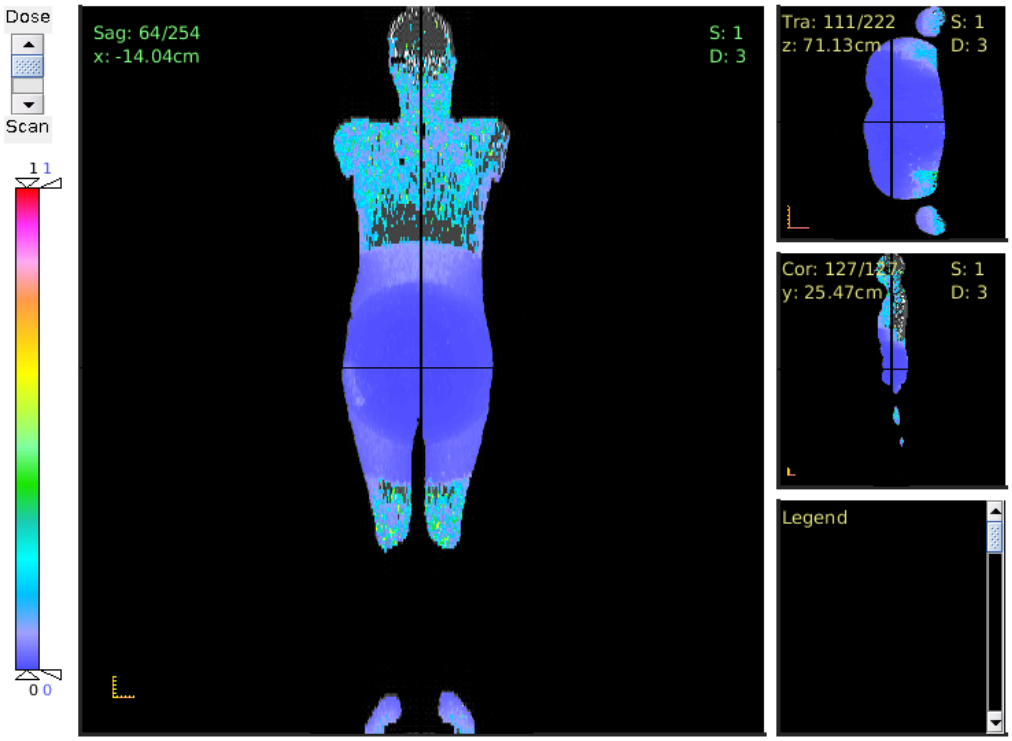

Figure 7.4: Relative uncertainty of the calculated neutron dose equivalent doses shown in figure 7.2.

1 based on quality factors from ICRP publication 60.

7.2 Organ-Averaged Neutron Equivalent Doses

The calculated results for organ-averaged neutron equivalent doses from the investigated 3D-CRT treatment are listed in table 7.1. Neutron equivalent doses range from 0.85 μSv per MU in the pancreas to 2.58 μSv per MU in the colon. To calculate the neutron equivalent dose to organs the neutron dose distributions in the organs were convolved with the energy-dependent radiation weighting factor distribution provided in ICRP publication 60. Like for the calculation of photon equivalent doses, see table 6.1, voxels within the primary treatment field were not taken into account in the average of the organ neutron equivalent doses. This was done for parts of the colon as well as for tissues of active bone marrow and lymphatic nodes. Also the model simplifications explained in the last section concerning the treatment vault missing in the computer model and the disregard of additional neutron-capture γ-doses in the dose calculations have to be considered again. Especially for deep-seated tissues, for example the colon, stomach and liver, neutron-capture γ-doses can account for a significant fraction of the total organ equivalent doses caused by photoneutrons [d'E01].

For all organs very low calculation uncertainties of about 1 % or even below could be achieved. This is the result of scoring the organ doses over far larger volumes than only for single voxels as for the dose equivalent distribution presented in the previous section. Even for organs at great distances to the treatment fields like the thyroid or the esophagus the precision was more than sufficient.

When compared to neutron equivalent doses published by Bednarz et al. it can be seen that the new calculated dose values are consistently lower by a factor of about 2. Although the calculation uncertainties reported by Bednarz are partially very high, e.g. 21.6 % for the neutron equivalent dose in the thyroid or 30.4 % in the esophagus, the encountered differences cannot entirely be explained by them. Also systematic differences in the model geometry of the accelerator and the phantom, as well as in the applied material specifications and cross-section libraries contribute to these discrepancies.

A comparison of the present organ equivalent dose calculations with relevant measurement data from Howell, Kry and Vanhavere et al. is even more complex [How06, Kry05a, Van04]. In the context of determining undesired neutron radiation exposures to patients, neutron dose measurements generally suffer from difficult and coarse measurement methods and high uncertainties. Howell et al., for example, performed only two measurements of the neutron ambient dose equivalent due to the size of the measurement apparatus consisting of a Au^{197}-based Bonner sphere system, one at the isocenter and one 40 cm superior to the isocenter, see figure 7.5. Based on these measurements they approximated the neutron equivalent doses of many organs. The measurement in the isocenter was applied to organs in close proximity to the PTV, the bladder, colon, gonads and bone marrow. The second ambient dose equivalent measurement in 40 cm distance was applied to all other organs. Then, they derived the neutron component of the equivalent dose for each organ by correcting the ambient dose equivalent for the depth of each organ applying neutron depth dose data from d'Errico et al. [d'E01]. This procedure consists of many steps and accumulates many uncertainty factors affecting the quality of the measurement results. Hence, the measured equivalent dose values listed in table 7.1 can provide only a rough orientation about actually prevailing neutron dose levels. Nevertheless, an agreement with the neutron equivalent doses of this study within a factor of less than 2, except for the thyroid, is found.

Kry et al. applied a similar method of calculating neutron equivalent doses from in- and out-of-field measurements with moderated gold foils. Among all research groups in this comparison, they reported the highest neutron equivalent doses for all organs except the colon. Only Vanhavere et al. reported a higher equivalent dose for the colon with 21.5 μSv/MU. In average, Kry's organ equivalent dose values were a factor of 5.4 higher than in this study. Although Kry et al. used a similar method for their work as Howell et al., the differences between the dose values determined by both groups are even higher with a factor of 7.9 in average. However, the method deployed by Kry et al. and outlined in detail in their paper showed exemplarily the extreme difficulties

(a) **(b)**

Figure 7.5: Setups for in- and out-of-field measurements with a 10 in. Bonner sphere carried out by Howell et al. [How06]. (a) at the isocenter and (b) at 40 cm superior to isocenter. Based on those two measurements Howell derived the neutron equivalent doses for all organs. The values are reported in table 7.1.

in deriving useful organ-averaged neutron equivalent dose values from neutron measurements. This method is based on several assumptions, many measurement and calculation steps, each of them subject to significant uncertainties, severely limiting the reliability of the final results. They identified and listed numerous uncorrelated uncertainty sources, in particular, the uncertainty

- in the count rates of the gold foils (6 %),
- in the count-rate-to-fluence conversion factors (2 %),
- in the fluence-to-dose-equivalent at d_{max} conversion factor for the original McCall method (10 %),
- in the fluence due to variations in the average field size (< 1 %),
- in the interpolated fluence at different distances from the central axis (~ 3 %),
- due to the assumption that the four-directional components of the neutron fluence are equal (8 %),
- introduced by considering four-directional components instead of the eight of the actual treatment (18 %) and
- of using two neutron energy components to calculate the dose equivalent at depth in the patient instead of considering a complete energy distribution (2 %).

Based on these contributions of the various uncorrelated uncertainty sources they estimated the total uncertainty in their neutron equivalent dose results to be approximately 23 %. Hence, their dose values are only of low comparability with the values presented in this work.

Vanhavere et al, on the other side, measured neutron doses directly within a plexi-slab phantom. For this, they used a combination of two types of the more compact superheated drop or bubble detectors. One type was only sensitive to fast neutron above 100 keV while the second type primarily measured thermal neutrons. Although the measurement setup just consisted of a plexi-slab phantom irradiated with a $10 \times 10\,\mathrm{cm}^2$ treatment field, their results are in better agreement with the present values than those from Howell and Kry. Nevertheless, the difference still amounts a factor of 3.0 in average.

Table 7.1: Neutron equivalent dose to selected organs in units of μSv per MU from 18 MV x-ray beams. Dose calculations for a 4-field 3D-CRT prostate cancer treatment plan. Measurement data from different measurement setups simulating a prostate cancer RT-treatment. All calculations and measurements were made using Varian linear accelerators.

	Neutron equivalent dose[a]				
	Calculations		Measurements		
Organ	This study[b]	Bednarz et al.[b,c]	Howell et al.[d]	Kry et al.[e]	Vanhavere et al.[f]
Stomach	1.74 (0.3)	1.90 (10.2)	1.05	9.1	6
Colon	2.58[g] (0.2)	4.89 (10.0)	1.90	9.8	21.5
Liver	1.78 (0.3)	4.17 (3.6)	2.43	9.0	4
Lung	1.78 (0.3)	4.51 (3.7)	0.55	7.1	2
Esophagus	1.02 (0.9)	1.95 (30.4)	0.42	5.7	1
Pancreas	0.85 (0.4)	3.44 (1.8)			
Brain	1.18 (0.6)	3.04 (5.1)			
Active bone marrow	1.85[g] (0.3)	3.08 (5.8)	1.57	16.8	
Small intestine	1.73 (0.3)	3.01 (5.4)			
Spleen	1.81 (0.6)	4.77 (11.2)			
Gall bladder	1.32 (0.5)	1.64 (20.1)			
Heart	1.29 (0.3)	3.09 (6.1)			
Lymph nodes	2.51[g] (0.9)	8.06 (15.9)			
Kidneys	1.53 (0.3)	3.31 (12.8)			
Thyroid	2.00 (1.5)	5.49 (21.6)	15.57	10.4	4

[a] all values in units of [μSv/MU].
[b] in brackets: corresponding relative uncertainty in percent of the obtained dose value.
[c] [Bed09c].
[d] [How06]. No measurement uncertainty is reported.
[e] [Kry05a]. Kry et al. assumed a total uncertainty in the out-of-field neutron dose equivalent measurements of 23 %.
[f] [Van04]. No measurement uncertainty is reported.
[g] Parts of this tissue were within the primary field and not included in the calculation of the corresponding organ equivalent dose.

7.3 Uncertainty Analysis of Neutron Dose Equivalent

In addition to the unavoidable systematic errors in the total model geometry, the neutron dose results are also strongly dependent on the photonuclear cross sections used for the Monte Carlo simulations. The vast majority of the photoneutrons is produced in the LINAC components made of tungsten, i.e. the target, the primary collimator, the jaws as well as the MLC. Although for some of the tungsten isotopes there are no experimental data available until now to validate model-based cross-section data, a correct isotopic material description is crucial for the simulation accuracy. Bednarz et al. calculated and compared photoneutron yields using the default LA150U photonuclear cross sections from LANL and those from the Beijing photonuclear library[1] [Bed09a]. After simulating an electron beam with a mean energy of 18.3 MV impacting on thick tungsten plates they determined a difference of approximately 12 to 17 % between the results. The photoneutron yields based on the LA150U data were consistently higher than those using the CNDC data set. These discrepancies were attributed to the oversimplification of using the default LA150U W^{184} cross-sections also for all other naturally occurring isotopes of tungsten as they are not listed by LA150U. This shows that attention has to be paid on a correct isotopic description of the material to obtain unbiased photoneutron yields in MC-simulations.

However, the photonuclear cross sections of the tungsten isotopes themselves are subject of significant uncertainties. In the following subsection the sources of uncertainty in the tungsten cross-section data are briefly outlined. A more detailed view on the evaluation methods can be obtained from the handbook on photonuclear data for applications by Chadwick et al. [Cha00]. Effects of these cross-section uncertainties on the calculated neutron dose equivalent for the investigated 3D-CRT treatment scenario are then analyzed in subsection 7.3.2.

7.3.1 Uncertainty Sources in Photonuclear Cross Section Evaluations

Figure 7.6 shows the photoneutron cross section evaluations[2] from the ENDF/B-VII library for the most abundant tungsten isotopes W^{182}, W^{183}, W^{184}, and W^{186} [3]. For W^{182} the photoneutron evaluation from JENDL[4] has been adopted. Since there were no direct experimental data for (γ,xn) reaction channel available, the evaluation is based on model calculations. First, the photon absorption cross-sections have been calculated using the giant dipole resonance (GDR) model and the quasi-deuteron (QD) model [Cha91]. The input model parameters were adjusted so that the calculated cross-sections better matched experimental data available for the photoabsorption. Based on these parameters, decaying processes such as the emission of photoneutrons were then estimated with a statistical model with pre-equilibrium correction [Cha00].

There was a complete lack of experimental data for photonuclear reactions with W^{183}, so that the evaluation was entirely model-based adopting the same model parameters as of $W^{182,184,186}$. The Beijing photonuclear library from CNDC is the only source providing such cross-sections for W^{183} so that they were adopted by the ENDF/B-VII library.

For W^{184}, the cross-section evaluation from LANL is used. The calculated photoabsorption cross-sections using GDR and QD parameters were modified slightly to better agree with measurement

1 also called China Evaluated Photonuclear Data File developed by the China Nuclear Data Center (CNDC).

2 The cross section values $\sigma(\gamma,xn)$ denote the inclusive photoneutron yield cross-sections and comprise also the multiplicity of neutrons emitted in each reaction event:

$$\sigma(\gamma,xn) = \sigma(\gamma,n) + \sigma(\gamma,np) + \sigma(\gamma,n2p) + ... + 2\sigma(\gamma,2n) + 2\sigma(\gamma,2np) + ... + 3\sigma(\gamma,3n) + ...+ \\ + \bar{\nu}(\gamma,F),$$

where $\bar{\nu}$ is the average multiplicity of photofission neutrons.

3 The isotope W^{180} is neglected in the following considerations due to its low isotopic abundance of only 0.12 % in elemental tungsten.

4 The Japanese Evaluated Nuclear Data Library (JENDL) is compiled by the Japan Atomic Energy Agency (JAEA).

data from Veyssiere et al. [Vey75], see figure 7.6 (c). However, this comparison was made with experimental data obtained from elemental, naturally occurring tungsten. Although W^{184} is the most abundant among all tungsten isotopes with a fraction of 30.70 %, this remarks a systematic error.

The photonuclear cross-sections of W^{186} were evaluated using the described physical models together with experimental data which were available for both, photoabsorption and photoneutron emission. The input parameter were adjusted to improve the quality of the calculated results and to match best the photoabsorption and photoneutron measurement data. The photoneutron cross-section evaluation from JENDL and corresponding measurements from Berman et al. [Ber69] are shown in figure 7.6 (d).

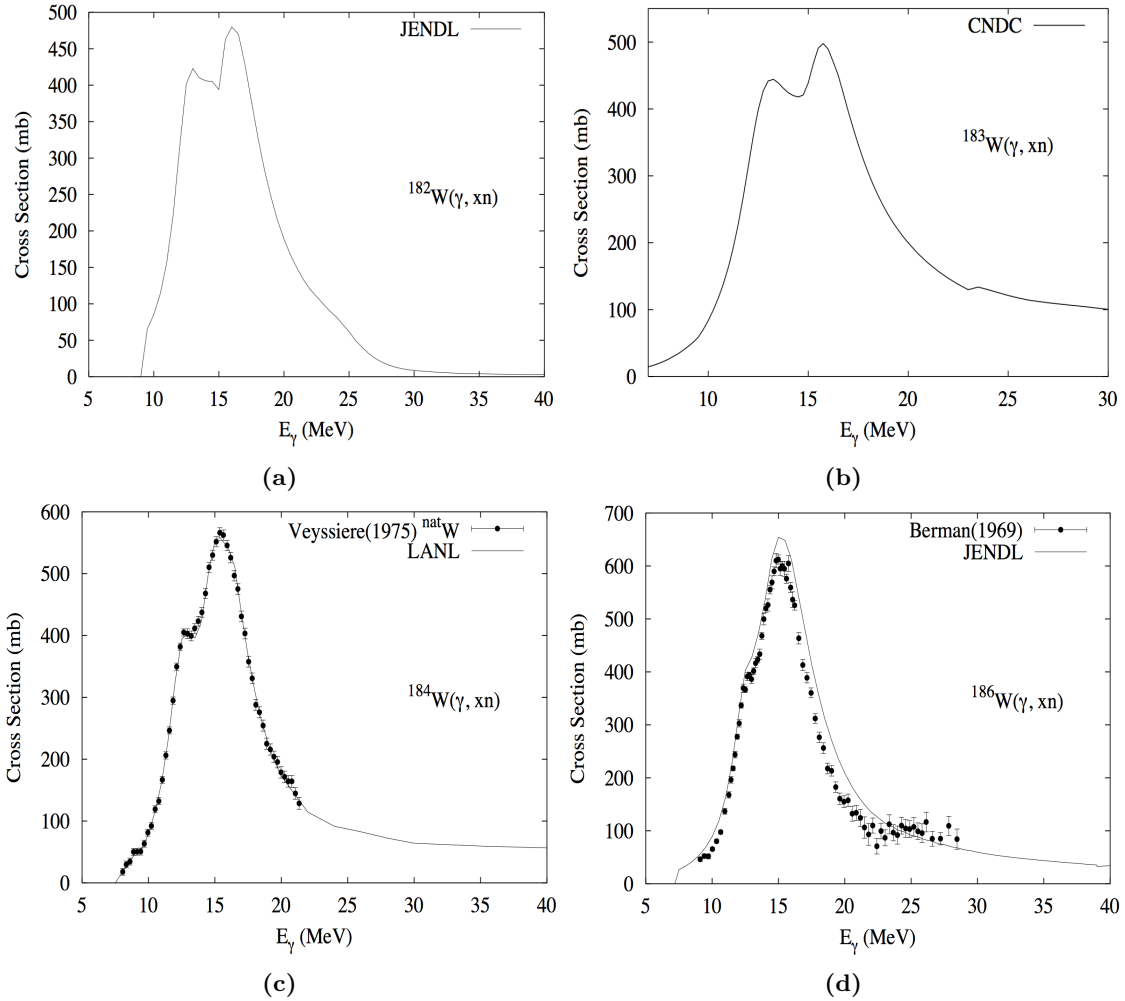

Figure 7.6: Photoneutron cross section data of the most abundant tungsten isotopes: (a) Cross section evaluation for the $W^{182}(\gamma,xn)$ reaction channel from JENDL based on model parameters and calculations best fitting available experimental data for the photoabsorption of W^{182}. (b) Entirely model-based cross section evaluation for W^{183} with model parameters from other tungsten isotopes; (c) Experimental cross section data for W^{184} by Veyssiere et al. [Vey75] and cross section evaluation from LANL; (d) Experimental data for W^{186} by Berman et al. [Ber69] and cross section evaluation from JENDL;

The described methods of evaluating the photoneutron cross-sections for tungsten with incomplete

or even missing experimental data finally lead to cross-section data sets subjected to significant uncertainties. These uncertainties are estimated to range up to about 15 %, based on a comparison of evaluations and experimental data where they were available.

7.3.2 Uncertainty Analysis with Perturbed Cross-Sections

The uncertainties in the cross section data for photonuclear interactions summarized in the previous section indicate a further analysis of the effects of the cross-section uncertainties on the calculated neutron dose equivalent values. The perturbation feature as it was used in section 6.3 considering the photon transport only, however, is not available for photonuclear interactions. Since MC-simulations of photonuclear interactions and the availability of comprehensive photonuclear cross-section data sets are rather recent developments for the solution of radiation transport problems, MCNPX does not provide this feature for photonuclear interactions yet. For this reason an uncertainty analysis was performed running many simulation with manually perturbed cross-section data inputs.

In total 200 simulations with perturbed cross section data sets have been run in order to study the effects on the photoneutron emissions from the LINAC and to determine confidence intervals for the neutron dose equivalent values. The cross section data set for each of the simulations was sampled out of a gaussian distribution around the nominal *endf7u* cross section data for all available tungsten isotopes, independent from the incident photon energy. Since photonuclear cross-section uncertainties for the tungsten isotopes were estimated to range up to 15 %, a standard deviation of $\sigma = 15\,\%$ was chosen for the gaussian distribution around the nominal cross-section values. For the sake of simplicity only the cross-sections for tungsten isotopes were sampled in this way leaving the cross section data for all other isotopes in the model unchanged. As mentioned in the beginning of this section, this simplification does not affect the validity of this analysis since more than 90 % of the photoneutrons are produced in tungsten components of the LINAC treatment head.

Figure 7.7 shows the results of the uncertainty analysis of the neutron dose equivalent values. Isodose lines are plotted in both the transversal and the coronal plane through the PTV. The displayed doses mark the lower limit, the mean and the upper limit, respectively, of the 95 % confidence interval determined from the 200 calculated neutron dose equivalent sets. The peak neutron dose equivalent values in the dose distribution of the lower CI-limit, the mean and the upper CI-limit range from around 40 mSv over 60 mSv to 80 mSv, respectively. Here, it is important to keep in mind that this analysis is subject to calculation uncertainties which originate in independent simulations for each of the sampled cross-section data sets. In figure 7.7 only dose values with a relative calculation uncertainty of less than 15 % are depicted and used for the display of isodose lines. However, although the results of the uncertainty analysis cannot be seen disentangled from the unavoidable simulation uncertainties, the analysis gives a valuable insight in the range of neutron dose equivalent which has to be expected considering the prevalent uncertainties in the tungsten cross-sections. This is especially true as most of the neutron doses have relative calculation uncertainties well below the value of 15 %.

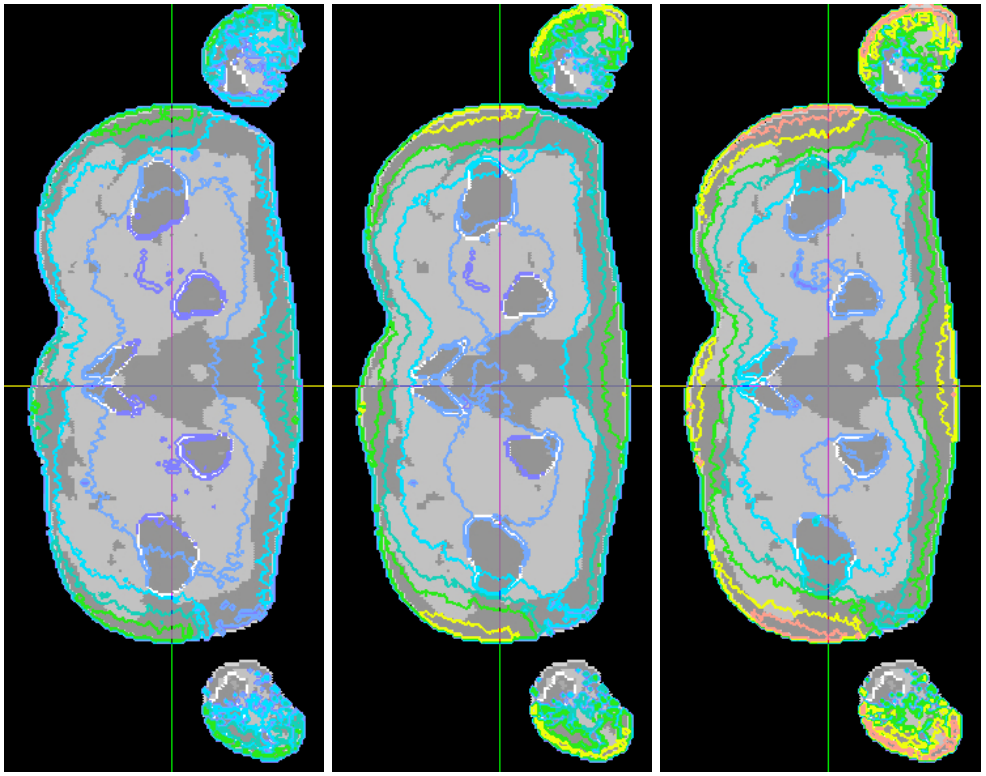

(a) Lower CI bound **(b)** Calculated mean **(c)** Upper CI bound

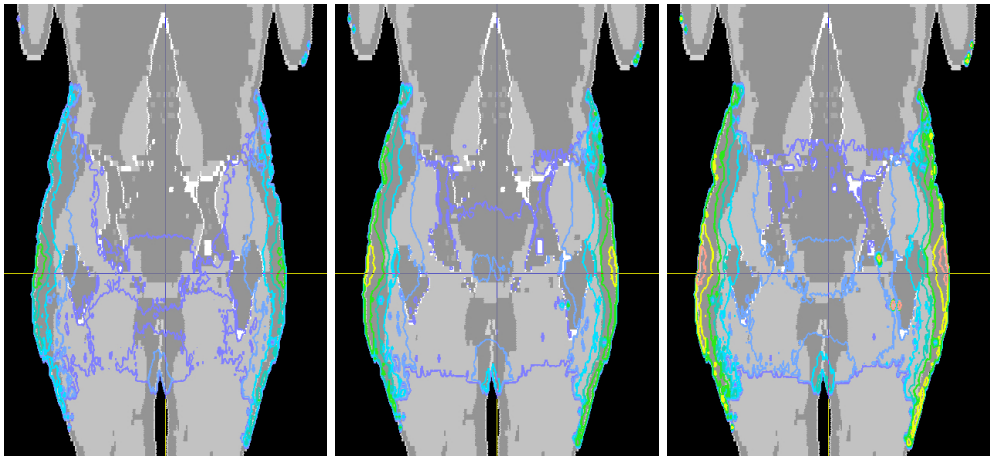

(d) Lower CI bound **(e)** Calculated mean **(f)** Upper CI bound

(g) Isodose legend

Figure 7.7: Uncertainty Analysis with perturbed tungsten cross-sections from the recent *endf7u* library. Isodose lines of the neutron dose equivalent for the mean, the upper and lower limits of the 95 % confidence interval (CI). Plots in the transversal plane (upper figures) and in the coronal plane (bottom figures) through the PTV. Only dose values in voxels with an estimated relative calculation uncertainty smaller than 15 % were considered.

8 Summary and Conclusions

Within the scope of this doctoral project a comprehensive effort has been made to determine non-target doses during high energy photon-radiation therapy. Dose values in- and outside the primary photon beam field were calculated for a selected 3D-CRT treatment plan by means of Monte Carlo simulations using the multiple purpose MC-code MCNPX. The corresponding computer model integrated a detailed representation of the treatment head of a Varian Clinac 2100 and an anthropomorphic voxel phantom complying with the ICRP specifications for reference male adults. With the application of an elaborated set of variance reduction techniques both photon and neutron dose quantities with an unprecedented level of accuracy and precision could be calculated. The accomplishments and findings of this work are summarized in the following.

Accomplishments

1. An accelerator model has been implemented including all beam-line components and many surrounding structures. To the knowledge of the author it is currently the most detailed and complex implementation of a medical LINAC for the purpose of out-of-field dose calculations. The simulation input-file for MCNPX contained hundreds of geometrical cells based on even more geometric primitives combined via boolean logic. The geometry description is based on manufacturer blueprints of the beam-line components and detailed information on the accelerator shielding components provided by Kase et al. [Kas98]. It has been demonstrated that available geometry data of the LINAC design can be adopted for a full Monte Carlo model accurate for the needs of radiation dose calculations.

2. The most recent cross-section and electron-data libraries were deployed in order to achieve the most accurate radiation transport simulation possible. For the simulation of photonuclear interactions the new photonuclear cross-section data set *endf7u* is available as part of the evaluated nuclear data library ENDF/B-VII.0. An outstanding benchmark of photonuclear cross section data has been performed in MCNPX for a selected set of isotopes. This benchmark showed the reliability of the cross section data for which there are also comparable experimental measurements [Fra16b].

3. Besides the moderation of neutrons within the patient body also the transport of thermalized neutrons has been taken into account in the calculation of neutron doses by application of adequate S(α,β) libraries. This step was necessary as most organ tissues consist of light elements moderating neutrons very well. Furthermore, Vanhavere et al. showed with their measurements that the thermal neutron component of the neutron depth dose is not negligible, especially at higher depths inside the phantom [Van04].

4. The in-field validation of the MC-model consisted of a comparison of the photon dose profiles with measurement data that were considered the 'gold standard' for the Varian Clinac operating at the energy of interest. The characteristics used for the comparison were the photon PDDs inside the primary treatment field as well as lateral dose profile curves considering several field sizes and phantom depths. Both, measurements and calculated data were obtained applying a cubic water phantom. The local dose difference between calculation and measurement at all depths considered beyond d_{max} on the PDD curves was less than 2 %. For the lateral dose profiles local differences between calculation and measurement were less than 2 % in the plateau and within 2 mm in the penumbra for all points considered. This validation demonstrated a

successful implementation of the accelerator model including a proper choice of the physics parameters.

5. Also photon dose profiles outside the primary treatment field were calculated and compared to available measurement data sets. It was determined that acceptable agreement was achieved between calculated and measured doses up to 60 cm from the central axis of the primary radiation beam. Using field sizes of $4 \times 4\,cm^2$, $10 \times 10\,cm^2$, and $20 \times 20\,cm^2$, the average local difference between calculation and measurement was 31 % for all field sizes. However, for the most relevant field size of $10 \times 10\,cm^2$ the average difference was only 16 %, an acceptable level of agreement for out-of-field considerations.

6. In addition, the method to calculate neutron contamination produced in the 18 MV accelerator model was validated comparing in-air neutron fluences calculated at a variety of distances from the central axis with previously measured fluences. The comparison showed an underestimation of the newly calculated in-air neutron fluence of in average 17 % with respect to the measurement data. This discrepancy can be well explained by the computer model restrictions summarized later in this chapter. Considering the significant estimated uncertainties in the neutron fluence measurements of approximately 10 % an overall good agreement between calculation and measurement is achieved.

7. Several MATLAB-programs have been written in order to further process the output of the MC-simulations together with the computational framework CERR. This framework included the visualization of the phantom geometry as well as of the obtained photon and neutron dose distributions. Furthermore, it was possible to calculate dose volume histograms for critical tissues using an organ-segmentation relying on the original voxel-data of the phantom.

8. An extensive effort has been made to develop two sets of VRTs for photon and neutron dose calculations, respectively. These combinations of VRTs were necessary to achieve an acceptable level of precision in the calculation results.

Results

1. Photon absorbed doses were calculated for the entire anthropomorphic phantom, in as well as outside of the primary treatment fields. The accuracy in the photon-dose calculations could be enhanced compared to previous calculations found in the literature by scoring actual electron-energy deposition instead of approximating by means of kerma. Avoiding this systematic error in the dose-calculation improved the quality of the dose-information especially at shallow phantom depths and locations close to the treatment field with high dose gradients and electronic disequilibrium. Although some weak spots in the automatically generated weight windows with locally increased calculation uncertainties could be identified, a satisfying calculation precision has been achieved particularly in tissues out-of-field and also in body tissues more distant to the PTV.

2. Neutron dose equivalent calculations resulted in peak doses of 20 mSv for the considered 3D-CRT treatment. These neutron peak equivalent doses were found within the beam fields in the skin and close below. In general, neutron energy deposition occurs rather superficial in the phantom due to the strong moderating effect of light elements present in tissues. It is important to note that concerning these neutron dose results several model restrictions with direct influence on the dose-height have to be considered. These model restrictions are summarized in a separate paragraph later in this chapter.

3. Besides absorbed photon doses also organ-averaged photon equivalent doses were calculated for selected organs and compared with available data from similar studies. The equivalent doses range from 1.0 μSv per MU for the brain to 27.9 μSv/MU for the small intestine. A

good agreement with other calculated organ equivalent dose values was found for a case also examining dose exposures from a 3D-CRT prostate treatment. Differences in the dose values can be attributed to small systematic differences in the computer models of the LINAC and especially of the used patient phantom. A comparison with available measurement data, however, was more difficult since systematic differences in obtaining information about organ-doses were much larger. Measurement setups and procedures described in the literature suffered from unavoidable inaccuracies, e.g. the pointwise approximation of organ-doses with single measurements. Furthermore, relevant dose measurements were available for only a handful of organs. Nevertheless, taking into account these restrictions the measurement data were consistent with the photon equivalent dose values calculated in this study.

4. Calculated neutron equivalent doses range from 0.9 μSv/MU for the pancreas to 2.6 μSv/MU for the colon. However, the same model restrictions as for the calculation of neutron dose equivalent apply here and lead to an underestimation of the true neutron equivalent doses, see the next paragraph. Comparing neutron equivalent doses with measurements was possible only to a limited extent due to the quality of the corresponding measurement data.

5. An uncertainty analysis with respect to the photonuclear cross-sections responsible for the vast majority of the photoneutron emissions in the LINAC has been performed. The result was a peak neutron dose equivalent of 35 mSv in the upper limit of the confidence interval calculated for all phantom voxels. This peak was found as expected again on the phantom surface. For tissues at higher depths the upper limit of the confidence interval was around 30 % higher than the mean in the corresponding voxels.

Restrictions

The computer model for the calculation of all the presented neutron dose values contains some necessary simplifications. The following restrictions deserve special attention and have to be taken into account as they directly affect the calculated dose results:

1. Backscattering of secondary neutron radiation contributes considerably to the total neutron radiation exposure of phantoms and patients, respectively. Neutrons are scattered by the equipment in the treatment room and in particular by the treatment vault itself. Omitting these structures in the implementation of the MC-model introduces therefore a significant systematic error in the following calculation of neutron doses. The effect of the treatment room on the neutron fluence at the position of the patient has been quantified previously in a comparative study. Additional neutron fluences range up to about 15 % if also the treatment room is included in the computer model. Hence, all neutron dose results presented in this work are subject to this reservation and can not be considered as conservative estimates.

2. A further restriction in the neutron dose calculations is the neglect of neutron capture γ-rays. The calculation of their contribution to the total neutron dose would have caused undue complications and enormous extra efforts. Instead, additional dose from neutron capture γ-rays can be accounted for consulting results from the literature. D'Errico et al. reported for the prevalent primary neutron energy of around 0.5 MeV additional neutron induced photon doses in the order of 0.5 % of the neutron recoil dose equivalent close to the phantom surface rising to about 10 % at 10 cm penetration depth [d'E01]. These percentages have to be added to correct the underestimation in the corresponding calculations of both, neutron dose equivalents and organ-averaged equivalent doses.

Conclusions

1. An unprecedented level of accuracy and precision could be achieved in the MC-calculations of out-of-field radiation doses. The simulations performed in this study showed that especially

the generated weigh window sets reveal a high efficacy and contribute significantly to the calculation precision. The presented results provide reliable information about undesired photon and neutron dose exposures to healthy tissues of RT-patients based on a proper implementation of a MC-model of a medical LINAC. The feasibility and potential of such complex simulations along with their advantages compared to measurements have been demonstrated.

2. An extensive review of available measurement data sets of neutron doses and neutron equivalent doses in particular showed clearly the enormous difficulties with which the empirical determination of neutron dose values is confronted. Measurements involving anthropomorphic phantoms are therefore prone to high uncertainties severely limiting their reliability as well as the comparability with simulation results. In fact, they effectively demonstrate the usefulness of accurate and precise dose calculations based on a validated computer model and detailed simulations.

3. With the help of VRTs, the calculation precision for organ-averaged photon and neutron equivalent doses dropped below, partially even far below the level of accuracy in the validation of the MC-model. This makes the validation to a bottleneck for further improvements in the MC-simulations and dose calculations. For photon dose calculations the precision of both measurement data and calculated values are high enough for an excellent validation. However, lacking availability of geometry data, especially of LINAC components close to the beam-line and support and shielding structures, affect the model quality and prevent a better matching in the validation. For the validation of photoneutron emissions and subsequent neutron dose calculations, on the other side, also information about the equipment surrounding the LINAC and the treatment vault itself would be required for a thorough validation. This makes the entire procedure very complex so that approximations of additional neutron fluences due to scattering in those structures have to be applied. The simulation of photonuclear reactions also requires cross-section libraries for all relevant isotopes which are not always available or highly uncertain. Moreover, the validation of calculated neutron emissions, having an extremely high precision itself, faces an intrinsic uncertainty of more than 10 % in the corresponding measurement data. In conclusion, these difficulties in the provision of reliable input data eventually limit the power of MC-simulations for the calculation of photon and neutron doses.

Outlook

The achievements of this project, although valuable by themselves, have to be seen in a greater context and are only a small contribution to an improved assessment of high-energy photon beam RT treatments. The following points give an outlook on possible and worthwhile future steps to further exploit the results of this study and to continue the work done so far:

1. The focus of the present study is the determination of out-of-field doses from a 3D-CRT treatment, yet the new standard in the RT with high-energy X-ray beams is the IMRT. Both 3D-CRT and IMRT treatments, however, use the MLC to shape the treatment field matching optimized dose distributions determined from treatment planning. In 3D-CRT treatments different field patterns are used for each gantry angle while this is further complicated in IMRT. There each field is composed of multiple segments or 'beamlets' eventually producing an effective radiation intensity modulation. Modeling many individual MLC segments requires a large amount of computation power and is therefore rather unpractical. Instead, all MLC configurations for a given angle can be simplified to one single configuration approximating the true beam field by an equivalent circular field, see [Bed08a]. Certainly, this method will not reproduce the correct dose distribution in and close to the PTV, but the systematic error is negligible for out-of-field dose calculations. The weight window maps produced in this project can be easily adopted to this 'equivalent circular field'-method in order to determine out-of-field doses also for IMRTs.

2. The automatically generated weight window maps don't have to be produced again for future dose calculations of other treatment plans with this LINAC. On the contrary, the existing weight window sets can serve as base for their continued development further exploiting their potential. Also a manual manipulation of the weight windows to correct local weaknesses in the importance sampling could improve the efficacy of this VRT.

3. Potential late effects and induced secondary malignancies can be better estimated based on accurate and precise MC-calculations of organ equivalent doses. Moreover, in specific cases MC-simulations can also help to evaluate doses to other sensitive structures outside the primary treatment field, for example, to the fetus of a pregnant patient [Bed08b]. Even DVHs for a better assessment of the dose levels received by the fetus can be offered by the presented computational framework. In this way, suitable countermeasures for the reduction of radiation exposures to the fetus can be investigated. Also for patients with implanted electronic devices like cardiac pacemakers appropriate actions could be taken after an assessment of the doses out-of-field in order to ensure functionality of these devices [Hua13].

4. The simulation-feature of considering also the thermal neutron transport within the body-tissues offers now the possibility to estimate increased (n,γ)-doses from metal implants after capture of thermalized neutrons. Those dosimetric considerations are especially relevant for patients with HIP prostheses undergoing pelvic irradiation [Ref03]. Although it was - within the scope of this thesis - not possible to calculate additional neutron-capture γ-rays for the entirety of the patient phantom, the applied VRTs could be modified and tailored specifically for such scenarios of pelvic irradiation making an assessment of emerging (n,γ)-doses feasible.

5. In conjunction with large-scale epidemiological studies, accurate models and precise MC-simulations could even be used to enhance risk models for late effects and improve understanding of the dose-response-relationship as proposed by Kry et al. [Kry07]. However, the implementation of various RT-scenarios for a detailed evaluation of many treatments still appears to be a major obstacle of this approach. To overcome this problem pursuing the idea outlined in the next point might be necessary.

6. Existing computational environments like CERR could be extended by an automatic import and export from and to MC-codes in order to facilitate the handling of MCCs of dose exposures outside the primary treatment field for clinically relevant RT-treatment cases. In fact, first steps to do so were already taken by other research groups [War15]. However, there are persisting difficulties in providing individualised phantoms for use in MCCs effectively slowing down such efforts.

Bibliography

[Ago95] Agosteo, S.; Foglio, A. P.; Maggioni, B.; Sanguist, V.; Terrani, S. and Borasi, G.: Radiation transport in a radiotherapy room. *Health Physics* (1995), vol. 68(1): pp. 27–34

[Ago03] Agostinelli, S.; Allison, J.; Amako, K.; Apostolakis, J.; Araujo, H.; Arce, P.; Asai, M.; Axen, D.; Banerjee, S.; Barrand, G.; Behner, F.; Bellagamba, L.; Boudreau, J.; Broglia, L. et al.: Geant4 - a simulation toolkit. *Nuclear Instruments and Methods in Physics Research Section A: Accelerators, Spectrometers, Detectors and Associated Equipment* (2003), vol. 506(3): pp. 250–303

[Bar59] Barber, W. C. and George, W. D.: Neutron Yields from Targets Bombarded by Electrons. *Physical Review* (1959), vol. 116: pp. 1551–1559

[Bec07] Becker, J.; Bruncкhorst, E. and Schmidt, R.: Photoneutron production of a Siemens Primus linear accelerator studied by Monte Carlo methods and a paired magnesium and boron coated magnesium ionization chamber system. *Physics in Medicine and Biology* (2007), vol. 52(21): pp. 6375–6387

[Bed08a] Bednarz, B.: *Detailed Varian Clinac Accelerator Modeling for Calculating Intermediate- and Low-level Non-target Organ Doses from Radiation Treatment*, ProQuest, Ann Arbor (2008)

[Bed08b] Bednarz, B. and Xu, X. G.: A feasibility study to calculate unshielded fetal doses to pregnant patients in 6-MV photon treatments using Monte Carlo methods and anatomically realistic phantoms. *Medical Physics* (2008), vol. 35(7): pp. 3054–3061

[Bed09a] Bednarz, B.; Han, B. and Xu, X. G.: Comparison of Photoneutron Yields in Tungsten Calculated by MCNPX Using Different Photonuclear Cross-Section Data for Typical Radiation Therapy Energies. *Nuclear Technology* (2009), vol. 168(2): pp. 270–273

[Bed09b] Bednarz, B.; Hancox, C. and Xu, X. G.: Calculated organ doses from selected prostate treatment plans using Monte Carlo simulations and an anatomically realistic computational phantom. *Physics in Medicine and Biology* (2009), vol. 54(17): pp. 5271–5286

[Bed09c] Bednarz, B. and Xu, X. G.: Monte Carlo modeling of a 6 and 18 MV Varian Clinac medical accelerator for in-field and out-of-field dose calculations: development and validation. *Physics in Medicine and Biology* (2009), vol. 54(4): pp. N43–N57

[Ber69] Berman, B. L.; Kelly, M. A.; Bramblett, R. L.; Caldwell, J. T.; Davis, H. S. and Fultz, S. C.: Giant Resonance in Deformed Nuclei: Photoneutron Cross Sections for Eu^{153}, Gd^{160}, Ho^{165}, and W^{186}. *Physical Review* (1969), vol. 185: pp. 1576–1590

[Boo84] Booth, T. E. and Hendricks, J. S.: Importance estimation in forward Monte Carlo calculations. *Nuclear Technology/Fusion; (United States)* (1984), vol. 5(1): pp. 90–100

[Bre00] Brenner, D. J.; Curtis, R. E.; Hall, E. J. and Ron, E.: Second Malignancies in Prostate Carcinoma Patients After Radiotherapy Compared with Surgery. *Cancer* (2000), vol. 88: pp. 398–406

[Bro96] Brown, T. H.: Shielding Design of the Electron Beam Stop for the Dual-Axis Radiographic Hydrotest Facility (DARHT), in: *Radiation Protection and Shielding Topical Meeting*, American Nuclear Society, No. Falmouth, Massachusetts, April 21-25, pp. 102–109

[Böh14] Böhlen, T. T.; Cerutti, F.; Chin, M. P. W.; Fassò, A.; Ferrari, A.; Ortega, P. G.; Mairani, A.; Sala, P. R.; Smirnov, G. and Vlachoudis, V.: The FLUKA Code: Developments and Challenges for High Energy and Medical Applications. *Nuclear Data Sheets* (2014), vol. 120: pp. 211–214

[Cha91] Chadwick, M. B.; Obložinský, P.; Hodgson, P. E. and Reffo, G.: Pauli-blocking in the quasideuteron model of photoabsorption. *Physical Review C* (1991), vol. 44: pp. 814–823

[Cha98] Chadwick, M. B.; Brown, T. H. and Little, R. C.: Photoneutron Production in Electron Beam Stop for Dual-Axis Radiographic Hydrotest Facility (DARHT), in: *Radiation Protection and Shielding Division Topical Conference*, American Nuclear Society, Nashville, Tennessee, April 19-23, pp. 356–363

[Cha99] Chadwick, M. B.; Young, P. G.; Chiba, S.; Frankle, S. C.; Hale, G. M.; Hughes, H. G.; Koning, A. J.; Little, R. C.; MacFarlane, R. E.; Prael, R. E. and Waters, L. S.: Cross-Section Evaluations to 150 MeV for Accelerator-Driven Systems and Implementation in MCNPX. *Nuclear Science and Engineering* (1999), vol. 131: pp. 293–328

[Cha00] Chadwick, M. B.; Obložinský, P.; Blokhin, A. I.; Fukahori, T.; Han, Y.; Lee, Y. O.; Martins, M. N.; Mughabghab, S. F.; Varlamov, V. V. and Yu, B. ET AL.: Handbook of photonuclear data for applications: Cross sections and spectra., IAEA TECH-DOC 1178, International Atomic Energy Agency, Vienna, Austria (2000)

[Cha03] Chadwick, M. B.; Young, P. G.; MacFarlane, R. E.; White, M. C. and Little, R. C.: Photonuclear Physics in Radiation Transport - I: Cross Sections and Spectra. *Nuclear Science and Engineering* (2003), vol. 144(2): pp. 157–173

[Cha06] Chadwick, M. B.; Obložinský, P.; Herman, M.; Greene, N. M.; McKnight, R. D.; Smith, D. L.; Young, P. G.; MacFarlane, R. E.; Hale, G. M.; Frankle, S. C.; Kahler, A. C.; Kawano, T.; Little, R. C.; Madland, D. G. et al.: ENDF/B-VII.0: Next Generation Evaluated Nuclear Data Library for Nuclear Science and Technology. *Nuclear Data Sheets* (2006), vol. 107(12): pp. 2931–3060

[Che09] Cherry, P. and Duxbury, A.: *Practical Radiotherapy: Physics and Equipment*, Wiley (2009)

[Chi03] Chibani, O. and Ma, C-M. C.: Photonuclear dose calculations for high-energy photon beams from Siemens and Varian linacs. *Medical Physics* (2003), vol. 30(8): pp. 1990–2000

[Cho05] Cho, S. H.; Vassiliev, O. N.; Lee, S.; Liu, H. H.; Ibbott, G. S. and Mohan, R.: Reference photon dosimetry data and reference phase space data for the 6MV photon beam from Varian Clinac 2100 series linear accelerators. *Medical Physics* (2005), vol. 32(1): pp. 137–148

[d'E98] d'Errico, Francesco; Nath, Ravinder; Tana, Luigi; Curzio, Giorgio and Alberts, Wolfgang G.: In-phantom dosimetry and spectrometry of photoneutrons from an 18 MV linear accelerator. *Medical Physics* (1998), vol. 25(9): pp. 1717–1724

[d'E01] d'Errico, F.; Luszik-Bhadra, M.; Nath, R.; Siebert, B. R. and Wolf, U.: Depth Dose-equivalent and Effective Energies of Photoneutrons Generated by 6-18 MV X-ray Beams for Radiotherapy. *Health Physics* (2001), vol. 80(1): pp. 4–11

[Dea03] Deasy, J. O.; Blanco, A. I. and Clark, H. V.: CERR: A computational environment for radiotherapy research. *Medical Physics* (2003), vol. 30(5): pp. 979–985

[DeW13] DeWerd, L. A. and Kissick, M.: *The Phantoms of Medical and Health Physics: Devices for Research and Development*, Biological and Medical Physics, Biomedical Engineering, Springer New York (2013)

[Fav01] Favorite, J. A. and Parsons, D. K.: Second-Order Cross Terms in Monte Carlo Differential Operator Perturbation Estimates, LA-UR-01-1640, Los Alamos National Laboratory, Los Alamos, NM (2001)

[Fer05] Ferrari, A.; Sala, P. R.; Fassò, A. and Ranft, J.: *FLUKA: A multi-particle transport code (program version 2005)*, CERN, Geneva (2005)

[Fol97] Followill, D.; Geis, P. and Boyer, A.: Estimates of whole-body dose equivalent produced by beam intensity modulated conformal therapy. *International Journal of Radiation Oncology*Biology*Physics* (1997), vol. 38(3): pp. 667–672

[Fol03] Followill, D.; Stovall, M.; Kry, S. F. and Ibbott, G. S.: Neutron source strength measurements for Varian, Siemens, Elekta, and General Electric linear accelerators. *Journal of Applied Clinical Medical Physics* (2003), vol. 4(3): pp. 189–194

[Fra16a] Frankl, M. and Macián-Juan, R.: Monte Carlo simulation of secondary radiation exposure from high-energy photon therapy using an anthropomorphic phantom. *Radiation Protection Dosimetry* (2016), vol. 168(4): pp. 537–545

[Fra16b] Frankl, M. and Macián-Juan, R.: Photonuclear Benchmarks of C, Al, Cu, Ta, Pb, and U from the ENDF/B-VII Cross-Section Library ENDF7U using MCNPX. *Nuclear Science and Engineering* (2016), vol. 183(1): pp. 135–142

[Gal96] Gallmeier, F. X.: A photoneutron production option for MCNP4A, in: *Radiation Protection and Shielding Topical Meeting*, American Nuclear Society, No. Falmouth, Massachusetts, April 21-25, pp. 780–786

[Hal80] Hall, C. G.: *Monte Carlo perturbation theory in neutron transport calculations*, University of London (1980)

[Hei03] Heinrichs, D. P. and Lent, E. M.: *Photonuclear Benchmarks with a Comparison of COG and MCNPX Results*, Lawrence Livermore National Laboratory, Livermore, CA, UCRL-CONF-200552 (2003)

[Hes98] Hess, A. K.; Hendricks, S. J.; McKinney, G. W. and Carter, L. L: Verification of the MCNP Perturbation Correction Feature for Cross-Section Dependent Tallies, LA-13520, Los Alamos National Laboratory, Los Alamos, NM (1998)

[How05] Howell, R. M.; Ferenci, M. S.; Hertel, N. E. and Fullerton, G. D.: Investigation of secondary neutron dose for 18 MV dynamic MLC IMRT delivery. *Medical Physics* (2005), vol. 32(3): pp. 786–793

[How06] Howell, R. M.; Hertel, N. E.; Wang, Z.; Hutchinson, J. and Fullerton, G. D.: Calculation of effective dose from measurements of secondary neutron spectra and scattered photon dose from dynamic MLC IMRT for 6 MV, 15 MV, and 18 MV beam energies. *Medical Physics* (2006), vol. 33(2): pp. 360–368

[How10] Howell, R. M.; Scarboro, S. B.; Kry, S. F. and Yaldo, D. Z.: Accuracy of out-of-field dose calculations by a commercial treatment planning system. *Physics in Medicine and Biology* (2010), vol. 55(23): pp. 6999–7008

[Hua13] Huang, J.; Followill, D.; Wang, X. and Kry, S. F.: Accuracy and sources of error of out-of field dose calculations by a commercial treatment planning system for intensity-modulated radiation therapy treatments. *Journal of applied clinical medical physics / American College of Medical Physics* (2013), vol. 14(2): pp. 186–197

[ICR89] ICRU: Tissue substitutes in radiation dosimetry and measurement. ICRU Report 44, Tech. Rep., International Commision on Radiation Units and Measurement, Bethesda, MD (1989)

[ICR92] ICRU: Photon, Electron, Proton and Neutron Interaction Data for Body Tissues. ICRU Report 46, Tech. Rep., International Commision on Radiation Units and Measurement, Bethesda, MD (1992)

[Int91] International Commission on Radiological Protection: ICRP Publication 60, 1990 Recommendations of the International Commission on Radiological Protection. *Annals of the ICRP* (1991), vol. 21(1-3)

[Int95] International Commission on Radiological Protection: ICRP Publication 70, Basic Anatomical & Physiological Data for use in Radiological Protection - The Skeleton. *Annals of the ICRP* (1995), vol. 25(2)

[Int02] International Commission on Radiological Protection: ICRP Publication 89, Basic Anatomical and Physiological Data for Use in Radiological Protection Reference Values. *Annals of the ICRP* (2002), vol. 32(3-4)

[Int07] International Commission on Radiological Protection: ICRP Publication 103, The 2007 Recommendations of the International Commission on Radiological Protection. *Annals of the ICRP* (2007), vol. 37(2-4)

[Int09] International Commission on Radiological Protection: ICRP Publication 110, Adult Reference Computational Phantoms. *Annals of the ICRP* (2009), vol. 39(2)

[Int10] International Commission on Radiological Protection: ICRP Publication 116, Conversion Coefficients for Radiological Protection Quantities for External Radiation Exposures. *Annals of the ICRP* (2010), vol. 40(2-5)

[Kas98] Kase, K. R.; Mao, X. S.; Nelson, W. R.; Liu, J. C.; Kleck, J. H. and Elsalim, M.: Neutron fluence and energy spectra around the Varian Clinac 2100C/2300C medical accelerator. *Health Physics* (1998), vol. 74(1): pp. 38–47

[Kaw15] Kawrakow, I.; Mainegra-Hing, E.; Rogers, D. W. O.; Tessier, F. and Walters, B. R. B.: The EGSnrc code system: Monte Carlo simulation of electron and photon transport, Tech. Rep. PIRS-701, National Research Council Canada (2015)

[Kea03] Keall, P. J.; Siebers, J. V.; Libby, B. and Mohan, R.: Determining the incident electron fluence for Monte Carlo-based photon treatment planning using a standard measured data set. *Medical Physics* (2003), vol. 30(4): pp. 574–582

[Kle06] Klein, E. E.; Maserang, B.; Wood, R. and Mansur, D.: Peripheral doses from pediatric IMRT. *Medical Physics* (2006), vol. 33(7): pp. 2525–2531

[Kry05a] Kry, S. F.; Salehpour, M.; Followill, D. S.; Stovall, M.; Kuban, D. A.; White, R. A. and Rosen, I. I.: Out-of-field photon and neutron dose equivalents from step-and-shoot intensity-modulated radiation therapy. *International Journal of Radiation Oncology*Biology*Physics* (2005), vol. 62(4): pp. 1204–1216

[Kry05b] Kry, S. F.; Salehpour, M.; Followill, D. S.; Stovall, M.; Kuban, D. A.; White, R. A. and Rosen, I. I.: The Calculated risk of Fatal Secondary Malignancies from Intensity-modulated Radiation Therapy. *International Journal of Radiation Oncology*Biology*Physics* (2005), vol. 62(4): pp. 1195–1203

[Kry06] Kry, S. F.; Titt, U.; Pönisch, F.; Followill, D.; Vassiliev, O. N.; White, R. A.; Mohan, R. and Salehpour, M.: A Monte Carlo model for calculating out-of-field dose from a Varian 6 MV beam. *Medical Physics* (2006), vol. 33(11): pp. 4405–4413

[Kry07] Kry, S. F.; Titt, U.; Followill, D. S.; Pönisch, F.; Vassiliev, O. N.; White, R. A.; Stovall, M. and Salehpour, M.: A Monte Carlo model for out-of-field dose calculation from high-energy photon therapy. *Medical Physics* (2007), vol. 34(9): pp. 3489–3499

[Leh06] Lehmann, J.; Stern, R. L.; Daly, T. P.; Rocke, D. M.; Schwietert, C. W.; Jones, G. E.; Arnold, M. L.; Siantar, C. L. and Goldberg, Z.: Dosimetry for Quantitative Analysis of the Effects of Low-Dose Ionizing Radiation in Radiation Therapy Patients. *Radiation Research* (2006), vol. 165(2): pp. 240–247

[Mao97] Mao, X. S.; Kase, K. R.; Liu, J. C.; Nelson, W. R.; Kleck, J. H. and Johnsen, S.: Neutron sources in the Varian Clinac 2100C/2300C medical accelerator calculated by the EGS4 code. *Health Physics* (1997), vol. 72(4): pp. 524–529

[Mat15] The Mathworks, Inc., Natick, Massachusetts: *MATLAB version 8.5.0.197613 (R2015a)* (2015)

[McC84] McCall, R. C. ET AL.: *Neutron Contamination from Medical Electron Accelerators*, NCRP Report No. 79, National Council on Radiation Protection and Measurements, Bethesda, MD (1984)

[McK94] McKinney, G. W.: Theory Related to the Differential Operator Perturbation Technique, X-6:GWM-94-124, Los Alamos National Laboratory, Los Alamos, NM (1994)

[Mut99] Mutic, S. and Klein, E. E.: A reduction in the {AAPM} TG-36 reported peripheral dose distributions with tertiary multileaf collimation. *International Journal of Radiation Oncology*Biology*Physics* (1999), vol. 44(4): pp. 947–953

[Obl98] Obložinský, P.: Summary Report of the 2nd Research Coordination Meeting on Compilation and Evaluation of Photonuclear Data for Applications, Tech. Rep. INDC(NDS)-384, International Atomic Energy Agency, Vienna, Austria (1998)

[Olh62] Olhoeft, J. E.: The Doppler Effect for a non-uniform temperature distribution in reactor fuel elements, WCAP-2048, Westinghouse Electric Corporation, Atomic Power Division, Pittsburgh (1962)

[Pel11] Pelowitz, D.: *MCNPX User's Manual, version 2.7.0, LA-CP-11-00438*, Los Alamos National Laboratory, Los Alamos, NM (2011)

[Pen04] Pena, J; Franco, L; Gómez, F; Iglesias, A; Lobato, R; Mosquera, J; Pazos, A; Pardo, J; Pombar, M; Rodríguez, A and Sendón, J: Commissioning of a medical accelerator photon beam Monte Carlo simulation using wide-field profiles. *Physics in Medicine and Biology* (2004), vol. 49(21): pp. 4929–4942

[Pen05] Pena, J.; Franco, L.; Gómez, F.; Iglesias, A.; Pardo, J. and Pombar, M.: Monte Carlo study of Siemens PRIMUS photoneutron production. *Physics in Medicine and Biology* (2005), vol. 50(24): pp. 5921–5933

[Pön06] Pönisch, F.; Titt, U.; Kry, S. F.; Vassiliev, O. N. and Mohan, R.: MCNPX simulation of a multileaf collimator. *Medical Physics* (2006), vol. 33(2): pp. 402–404

[Ref03] Reft, C. S.; Alecu, R.; Das, I. J.; Gerbi, B. J.; Keall, P.; Lief, E.; Mijnheer, B. J.; Papanikolaou, N.; Sibata, C. and Van Dyk, J.: Dosimetric considerations for patients with HIP prostheses undergoing pelvic irradiation. Report of the AAPM Radiation Therapy Committee Task Group 63. *Medical Physics* (2003), vol. 30(6): pp. 1162–1182

[Ref06] Reft, C. S.; Runkel-Müller, R. and Myrianthopoulos, L.: In vivo and phantom measurements of the secondary photon and neutron doses for prostate patients undergoing 18MV IMRT. *Medical Physics* (2006), vol. 33(10): pp. 3734–3742

[S.06] S., Shamurailatpam D.; Upreti, R. R. and Deshpande, D. D.: Use of peripheral dose data from uniform dynamic multileaf collimation fields to estimate out-of-field organ dose in patients treated employing sliding window intensity-modulated radiotherapy. *Physics in Medicine and Biology* (2006), vol. 51(11): pp. 2987–2995

[Sal11] Salvat, F.; Fernandez-Varea, J. M. and Sempau, J.: *PENELOPE-2011: A Code System for Monte Carlo Simulation of Electron and Photon Transport*, OECD-NEA, Issy-les-Moulineaux, France (2011)

[SB02] Sheikh-Bagheri, D. and Rogers, D. W. O.: Sensitivity of megavoltage photon beam Monte Carlo simulations to electron beam and other parameters. *Medical Physics* (2002), vol. 29(3): pp. 379–390

[Sha06] Sharma, D. S.; Animesh; Deshpande, S. S.; Phurailatpam, R. D.; Deshpande, D. D.; Shrivastava, S. K. and Dinshaw, K. A.: Peripheral dose from uniform dynamic multileaf collimation fields: implications for sliding window intensity-modulated radiotherapy. *The British Journal of Radiology* (2006), vol. 79(940): pp. 331–335

[Ste99] Stern, R. L.: Peripheral dose from a linear accelerator equipped with multileaf collimation. *Medical Physics* (1999), vol. 26(4): pp. 559–563

[Sto95] Stovall, M.; Blackwell, C. R.; Cundiff, J.; Novack, D. H.; Palta, J. R.; Wagner, L. K.; Webster, E. W. and Shalek, R. J.: Fetal dose from radiotherapy with photon beams: Report of AAPM Radiation Therapy Committee Task Group No. 36 (1995), vol. 22(1): pp. 63–82

[Sto04] Stovall, M.; Donaldson, S. S.; Weathers, R. E.; Robison, L. L.; Mertens, A. C.; Winther, J. F.; Olsen, J. H. and Jr., J. D. Boice: Genetic effects of radiotherapy for childhood cancer: Gonadal dose reconstruction. *International Journal of Radiation Oncology*Biology*Physics* (2004), vol. 60(2): pp. 542–552

[Tak70] Takahashi, H.: Monte Carlo Method for Geometrical Perturbation and its Application to the Pulsed Fast Reactor. *Nuclear Science and Engineering* (1970), vol. 41(2): pp. 259–270

[Tak11] Takam, R.; Bezak, E.; Marcu, L.G. and Yeoh, E.: Out-of-field neutron and leakage photon exposures and the associated risk of second cancers in high-energy photon radiotherapy: current status. *Radiation Research* (2011), vol. 176(4): pp. 508–520

[Van04] Vanhavere, F.; Huyskens, D. and Struelens, L.: Peripheral Neutron and Gamma Doses in Radiotherapy with an 18 MV Linear Accelerator. *Radiation Protection Dosimetry* (2004), vol. 110: pp. 607–612

[Vey75] Veyssiere, A.; Beil, H.; Bergere, R.; Carlos, P.; Lepretre, A. and de Miniac, A.: A study of the giant dipole resonance in the A=190 transition region. *Journal de Physique Lettres* (1975), vol. 36(11): pp. L267–L269

[Wan08] Wang, B and Xu, XG: Measurements of non-target organ doses using MOSFET dosemeters for selected IMRT and 3D CRT radiation treatment procedures. *Radiation Protection Dosimetry* (2008), vol. 128(3): pp. 336–342

[War11] Warren, D.: Virtual phantom studies of treatment planning in charged particle radiotherapy, Poster at Particle Therapy Cooperative Group (PTCOG 50) meeting in Philadelphia, PA, May 8-14 (2011)

[War15] Warren, D.: personal communication (2015)

[Whi99] White, M. C.; Little, R. C. and Chadwick, M. B.: PHOTONUCLEAR PHYSICS IN MCNP(X), in: *Proceedings of the ANS on Nuclear Applications of Accelerator Technology*, Long Beach, California

[Whi00] White, M. C: Development and Implementation of Photonuclear Cross-Section Data for Mutually Coupled Neutron-Photon Transport Calculations in the Monte Carlo N-Particle (MCNP) Radiation Transport Code. LA-13744-T. , Los Alamos National Laboratory, Los Alamos, NM (2000)

[Whi01] White, M. C: A Brief Primer for Simulating Photonuclear Interactions with MCNP(X), LA-UR-01-1599, Los Alamos National Laboratory, Los Alamos, NM (2001)

[Whi03a] White, M. C: Photoatomic Data Library MCPLIB04: A New Photoatomic Library Based On Data from ENDF/B-VI Release 8, LA-UR-03-1019, Los Alamos National Laboratory, Los Alamos, NM (2003)

[Whi03b] White, M. C.; Little, R. C.; Chadwick, M. B.; Young, P. G. and MacFarlane, R. E.: Photonuclear Physics in Radiation Transport - II: Implementation. *Nuclear Science and Engineering* (2003), vol. 144(2): pp. 174–189

[Whi12] White, M. C: Further Notes on MCPLIB03/04 and New MCPLIB63/84 - Compton Broadening Data For All Versions of MCNP5, LA-UR-12-00018, Los Alamos National Laboratory, Los Alamos, NM (2012)

[X-505a] X-5 Monte Carlo Team: *MCNP - A General Monte Carlo N-Particle Transport Code, Version 5, Volume I*, LA-UR-03-1987, Los Alamos National Laboratory, Los Alamos, NM (2005)

[X-505b] X-5 Monte Carlo Team: *MCNP - A General Monte Carlo N-Particle Transport Code, Version 5, Volume II*, LA-CP-03-0245, Los Alamos National Laboratory, Los Alamos, NM (2005)

[Xu08] Xu, X. G.; Bednarz, B. and Paganetti, H.: A review of dosimetry studies on external-beam radiation treatment with respect to second cancer induction. *Physics in Medicine and Biology* (2008), vol. 53(13): pp. R193–R241

[Zan01] Zankl, M. and Wittmann, A.: The adult male voxel model "Golem" segmented from whole-body CT patient data. *Radiation and Environmental Biophysics* (2001), vol. 40(2): pp. 153–162

[Zan04] Zanini, A.; Durisi, E.; Fasolo, F.; Ongaro, C.; Visca, L.; Nastasi, U.; Burn, K. W.; Scielzo, G.; Adler, J. O.; Annand, J. R. M. and Rosner, G.: Monte Carlo simulation of the photoneutron field in linac radiotherapy treatments with different collimation systems. *Physics in Medicine and Biology* (2004), vol. 49(4): pp. 571–582

[Zan05] Zankl, M.; Becker, J.; Fill, U.; Petoussi-Henss, N. and Eckerman, K. F.: GSF male and female adult voxel models representing ICRP Reference Man-the present status, in: *The Monte Carlo Method: Versatility Unbounded in a Dynamic Computing World*, American Nuclear Society, La Grange Park, IL

[Zan07] Zankl, M.; Eckerman, K. F. and Bolch, W. E.: Voxel-based models representing the male and female ICRP reference adult-the skeleton. *Radiation Protection Dosimetry* (2007), vol. 127(1-4): pp. 174–186

[Zha08a] Zhang, J.; Na, Y. and Xu, X. G.: Development of Whole-Body Phantoms Representing An Average Adult Male and Female Using Surface-Geometry Methods (2008), AAPM Annual Meeting

[Zha08b] Zhang, J.; Xu, X. G.; Shi, C. and Fuss, M.: Development of a geometry-based respiratory motion-simulating patient model for radiation treatment dosimetry. *Journal of Applied Clinical Medical Physics* (2008), vol. 9(1): pp. 16–28

List of Figures

List of Tables

A Supplementary data

The following table A.1 lists all the materials used for the specification of the organs of the ICRP adult male phantom. Provided are also the chemical composition of each material taken from [Int09]. This information was used for the phantom material-description in the MCNPX-input, see listing B.17, regarding the photon dose calculations.

These data have been processed for use in neutron dose calculations. The material definition in the corresponding part of the MCNPX-input, listing B.22, is based on the isotopic abundances of the materials rather than the elemental. Furthermore, the material specification is accompanied by a S(α,β) approximation where there is a similar material available in the S(α,β) library ENDF70SAB. Those approximations are indicated in the last column of table A.1. For the simulation of thermal neutrons the actually present material is then replaced and treated like the S(α,β) approximation. For example, most of the soft tissues like the skin, liver, brain and heart are approximated by light water (lwtr.10t). On the other hand, tissues with higher carbon-contents like adipose tissue, arm and leg bones are approximated as polyethylene (poly.10t).

Table A.1: List of media and corresponding elemental compositions in percent by mass, for the adult male reference computational phantom.

No.	Medium/Tissue	H_1	C_6	N_7	O_8	Na_{11}	Mg_{12}	P_{15}	S_{16}	Cl_{17}	K_{19}	Ca_{20}	Fe_{26}	I_{53}	S(α,β) approximation
1	**Teeth**	2.2	9.5	2.9	42.1		0.7	13.7				28.9			-
2	**Mineral bone**	3.6	15.9	4.2	44.8	0.3	0.2	9.4	0.3			21.3			-
3	**Humeri, upper half, spongiosa**	8.5	28.8	2.6	49.8	0.2	0.1	3.3	0.4	0.2		6.1			-
4	**Humeri, lower half, spongiosa**	9.7	43.9	1.7	38.1	0.2		2.1	0.3	0.1		3.9			-
5	**Lower arm bones, spongiosa**	9.7	43.9	1.7	38.1	0.2		2.1	0.3	0.1		3.9			-
6	**Hand bones, spongiosa**	9.7	43.9	1.7	38.1	0.2		2.1	0.3	0.1		3.9			-
7	**Clavicles, spongiosa**	9.1	34.8	2.4	45.7	0.2		2.6	0.3	0.1		4.8			-
8	**Cranium, spongiosa**	9.0	33.5	2.5	46.7	0.2		2.6	0.3	0.2	0.1	4.9			-
9	**Femora, upper half, spongiosa**	9.4	38.5	2.2	43.0	0.2		2.2	0.3	0.1		4.1			-
10	**Femora, lower half, spongiosa**	9.7	43.9	1.7	38.1	0.2		2.1	0.3	0.1		3.9			-
11	**Lower leg bones, spongiosa**	9.7	43.9	1.7	38.1	0.2		2.1	0.3	0.1		3.9			-
12	**Foot bones, spongiosa**	9.7	43.9	1.7	38.1	0.2		2.1	0.3	0.1		3.9			-
13	**Mandible, spongiosa**	8.3	26.6	2.7	51.1	0.3	0.1	3.6	0.4	0.2		6.7			-
14	**Pelvis, spongiosa**	9.4	36.0	2.5	45.4	0.2		2.1	0.3	0.2	0.1	3.8			-
15	**Ribs, spongiosa**	8.9	29.2	2.9	50.7	0.2		2.6	0.4	0.2	0.1	4.8			-
16	**Scapulae, spongiosa**	8.7	30.9	2.6	48.3	0.2	0.1	3.0	0.4	0.2		5.6			-
17	**Cervical spine, spongiosa**	10.3	40.0	2.7	44.4	0.1		0.7	0.2	0.2	0.1	1.2	0.1		-
18	**Thoracic spine, spongiosa**	9.9	37.6	2.7	45.9	0.1		1.2	0.2	0.2	0.1	2.0	0.1		-
19	**Lumbar spine, spongiosa**	9.5	34.0	2.8	48.0	0.1		1.8	0.3	0.2	0.1	3.2			-
20	**Sacrum, spongiosa**	10.5	41.9	2.7	43.2	0.1		0.4	0.2	0.2	0.1	0.6	0.1		-
21	**Sternum, spongiosa**	10.4	40.9	2.7	43.8	0.1		0.6	0.2	0.2	0.1	0.9	0.1		-
22	**Humeri and femora, upper halves, medullary cavity**	11.5	63.6	0.7	23.9	0.1			0.1	0.1					poly.10t
23	**Humeri and femora, lower halves, medullary cavity**	11.5	63.6	0.7	23.9	0.1			0.1	0.1					poly.10t
24	**Lower arm bones, medullary cavity**	11.5	63.6	0.7	23.9	0.1			0.1	0.1					poly.10t
25	**Lower leg bones, medullary cavity**	11.5	63.6	0.7	23.9	0.1			0.1	0.1					poly.10t
26	**Cartilage**	9.6	9.9	2.2	74.4	0.5		2.2	0.9	0.3					lwtr.10t
27	**Skin**	10.0	19.9	4.2	65.0	0.2		0.1	0.2	0.3	0.1				lwtr.10t
28	**Blood**	10.2	11.0	3.3	74.5	0.1		0.1	0.2	0.3	0.2		0.1		lwtr.10t
29	**Muscle tissue**	10.2	14.2	3.4	71.1	0.1		0.2	0.3	0.1	0.4				lwtr.10t
30	**Liver**	10.2	13.0	3.1	72.5	0.2		0.2	0.3	0.2	0.3				lwtr.10t

31	**Pancreas**	10.5	15.5	2.5	70.6	0.2	0.2	0.1	0.2	0.2					lwtr.10t
32	**Brain**	10.7	14.3	2.3	71.3	0.2	0.4	0.2	0.3	0.3					lwtr.10t
33	**Heart**	10.4	13.8	2.9	71.9	0.1	0.2	0.2	0.2	0.3					lwtr.10t
34	**Eyes**	9.7	18.1	5.3	66.3	0.1	0.1	0.3	0.1						lwtr.10t
35	**Kidneys**	10.3	12.4	3.1	73.1	0.2	0.2	0.2	0.2	0.2	0.1				lwtr.10t
36	**Stomach**	10.5	11.4	2.5	75.0	0.1	0.1	0.1	0.2	0.1					lwtr.10t
37	**Small intestine**	10.5	11.3	2.6	75.0	0.1	0.1	0.1	0.2	0.1					lwtr.10t
38	**Large intestine**	10.5	11.3	2.6	75.0	0.1	0.1	0.1	0.2	0.1					lwtr.10t
39	**Spleen**	10.2	11.1	3.3	74.3	0.1	0.2	0.2	0.3	0.2		0.1			lwtr.10t
40	**Thyroid**	10.4	11.7	2.6	74.5	0.2	0.1	0.1	0.2	0.1			0.1		lwtr.10t
41	**Urinary bladder**	10.5	9.6	2.6	76.1	0.2	0.2	0.2	0.3	0.3					lwtr.10t
42	**Testes**	10.6	10.0	2.1	76.4	0.2	0.1	0.2	0.2	0.2					lwtr.10t
43	**Adrenals**	10.4	22.1	2.8	63.7	0.1	0.2	0.3	0.2	0.2					lwtr.10t
44	**Oesophagus**	10.4	21.3	2.9	64.4	0.1	0.2	0.3	0.2	0.2					lwtr.10t
45	**Gall bladder, Pituitary gland, Trachea, Thymus, Tonsils, Ureters, ...**	10.4	23.1	2.8	62.7	0.1	0.2	0.3	0.2	0.2					lwtr.10t
46	**Prostate**	10.4	23.1	2.8	62.7	0.1	0.2	0.3	0.2	0.2					lwtr.10t
47	**Lymph**	10.8	4.2	1.1	83.1	0.3		0.1	0.4						lwtr.10t
48	**Breast(mammary gland)**	11.2	51.6	1.1	35.8	0.1		0.1	0.1						poly.10t
49	**Adipose tissue**	11.4	58.8	0.8	28.7	0.1		0.1	0.1						poly.10t
50	**Lung tissue(compressed lungs)**	10.3	10.7	3.2	74.6	0.2	0.2	0.3	0.3	0.2					lwtr.10t
51	**Gastro-intestinal tract-contents**	10.0	22.2	2.2	64.4	0.1	0.2	0.3	0.1	0.4	0.1				lwtr.10t
52	**Urine**	10.7	0.3	1.0	87.3	0.4	0.1			0.2					lwtr.10t
53	**Air**			80.0	20.0										-

B MCNPX Input

B.1 MCNPX Input Files for Photon Dose Calculations

The following files contain all information needed to run the MCNPX simulation for the calculation of photon doses. The main input file called **linac__icrp__am__p__main.inp** is shown in listing B.1. It includes links to auxiliary files containing data to complete the input file. These links are indicated by the string 'read file=' at the beginning of a line and followed by the name of the auxiliary file to be inserted in the main input deck. This method of referring to external files preserves the readability of the input file and also adds some flexibility. In such a way the same input file can be used for simulations with a different gantry angle just by commenting out links to external definitions currently not needed, see lines 11-13 and 44-46. The listings B.2 - B.19 contain all the auxiliary subfiles in the order of their appearance in the main input deck.

Listing B.1: linac__icrp__am__p__main.inp

```
 1  Dose Calculation - Varian Clinac 2100C - 18 MV
 2  c XXXXXXXXXXXXXXXXXXXXXXXXXXXXXXXXXXXXXXXXXXXXXXXXXXXXXXXXXXXXXXXXXXXXXXXXXXXXXXXX
 3  c MAIN INPUT DECK
 4  c Medical Linear Accelerator Model Varian Clinac 2100C - 18 MV
 5  c ICRP adult male phantom
 6  c Photon dose calculations
 7  c *********************************************************************************
 8  c ************************ CELL CARDS *********************************************
 9  c *********************************************************************************
10  read file=varian_mlc_0deg.cel noecho
11  c read file=varian_mlc_90deg.cel noecho
12  c read file=varian_mlc_180deg.cel noecho
13  c read file=varian_mlc_270deg.cel noecho
14  read file=varian_clin_18.cel noecho
15  403 0 -403        imp:p=1 imp:e=1 fill=999 (5)
16  read file=AM_organs noecho
17  read file=AM_matrix noecho
18  999 0 11 imp:p,e=0
19
20  c *********************************************************************************
21  c ************************ SURFACE CARDS ******************************************
22  c *********************************************************************************
23  401   rpp   0 .2137   0 .2137   0 .8
24  402   so  70
25  403 5  rpp 0.0001 54.2797 0.0001 27.1398 0.0001 175.9999
26  read file=varian_mlc.geo noecho
27  read file=varian_clin_18.geo noecho
28
29  c *********************************************************************************
30  c ************************ DATA CARDS *********************************************
31  c *********************************************************************************
32  mode p e
33  c imp:p 1 83r 1 96r 0
34  c imp:e 1 83r 1 96r 0
35  read file=sdef_18pt5_MeV.src noecho
36  DBCN 17j 1
37  cut:e 1e20 0.1
38  cut:p 1e20 0.01
```

```
39 phys:e 23.1 j j j j 10
40 phys:p 23.1
41 c ********************** TRANSFORMATIONS ***************************************
42 c jaws transformation
43 read file=varian_jaws_0deg.tr noecho
44 c read file=varian_jaws_90deg.tr noecho
45 c read file=varian_jaws_180deg.tr noecho
46 c read file=varian_jaws_270deg.tr noecho
47 c ********************************************************************************
48 c phantom transformation
49 c         o1 o2 o3 xx` yx` zx` xy` yy` zy` xz` yz` zz`
50  *TR5 -26.39 90.5  84.43   0 90  90  90 90   0 90 180 90    $ 0deg
51 c *TR5 -15.57 90.5 126.14  90 90 180   0 90  90 90 180 90    $ 90deg
52 c *TR5  26.39 90.5 115.57 180 90  90  90 90 180 90 180 90    $ 180deg
53 c *TR5  15.57 90.5  73.86  90 90   0 180 90  90 90 180 90    $ 270deg
54 c TR5 0 0 0 1 0 0 0 1 0 0 0 1
55 c ********************************************************************************
56 c mirror angle of 35deg
57  *TR6 0 0 21.63 35 90 125 90 0 90 55 90 35
58 c ********************** MATERIALS *********************************************
59 read file=varian_clin_18p_d.mtl noecho
60 read file=AM_materials noecho
61 c ********************** TALLIES ***********************************************
62 read file=photon_dose.tal
63 read file=photon_organ_dose2.tal
64 c ********************************************************************************
65 PRDMP j 1e7 1 1
66 TALNP
67 c print -126 -128 -140 -130
68 nps 1e8
69 wwp:p,e 4j -1 3j 100
```

Listing B.2: varian_mlc_0deg.cel

```
1  c ********************************************************************************
2  c CELL CARDS FOR MLC OF 18 MV ACCELERATOR MODEL
3  c These cells define the MLC-leafs and their positions at a gantry angle of 0 degree.
4  c Using the like and but command with the TRCL command allows us to copy the
5  c initial MLC-leaf to describe the remaining pairs
6  c
7  c By Bryan Bednarz and Bin Han
8  c Modified by Matthias Frankl
9  c ********************************************************************************
10 c MLC Cell Cards
11 3099 0 ((231 -234 237 -238 240 -236):
12       (231 -234 237 -238 235 -209):(232 -234 237 -238 209 -240))
13       #301 #302 #303 #304 #305 #306 #307 #308 #309 #310
14       #311 #312 #313 #314 #315 #316 #317 #318 #319 #320
15 3100 0 ((-231 233 237 -238 235 -209) : (-232 233 237 -238 209 -240) :
16       (-231 233 237 -238 240 -236))
17       #321 #322 #323 #324 #325 #326 #327 #328 #329 #330
18       #331 #332 #333 #334 #335 #336 #337 #338 #339 #340
19 3101 0 ((231 -234 -237 239 235 -209) : (232 -234 -237 239 209 -240) :
20       (231 -234 -237 239 240 -236))
21       #341 #342 #343 #344 #345 #346 #347 #348 #349 #350
22       #351 #352 #353 #354 #355 #356 #357 #358 #359 #360
23 3102 0 ((-231 233 -237 239 235 -209) : (-232 233 -237 239 209 -240) :
24       (-231 233 -237 239 240 -236))
25       #361 #362 #363 #364 #365 #366 #367 #368 #369 #370
26       #371 #372 #373 #374 #375 #376 #377 #378 #379 #380
27 301 91 -18.0 ((-201 202 -218 -219 203 -204) : (205 206 -218 -220 204 -207):
28       (208 206 -218 -220 207 -209) : (208 210 -218 -220 209 -211) :
29       (208 206 -218 -220 211 -212) : (205 206 -218 -220 212 -213) :
30       (-201 202 -218 -219 213 -214))
31       *TRCL=(2.156 0 0 0 90 90 90 0.2854 90.2854 90 89.7146 0.2854)
```

```
302 LIKE 301 BUT *TRCL=(2.112 0 0 0 90 90 90 0.8562 90.8562 90 89.1438 0.8562)
303 LIKE 301 BUT *TRCL=(1.926 0 0 0 90 90 90 1.4270 91.4270 90 88.5730 1.4270)
304 LIKE 301 BUT *TRCL=(1.568 0 0 0 90 90 90 1.9978 91.9978 90 88.0022 1.9978)
305 LIKE 301 BUT *TRCL=(0.842 0 0 0 90 90 90 2.5686 92.5686 90 87.4314 2.5686)
306 LIKE 301 BUT *TRCL=(0 0 0 0 90 90 90 3.1394 93.1394 90 86.8606 3.1394)
307 LIKE 301 BUT *TRCL=(0 0 0 0 90 90 90 3.7102 93.7102 90 86.2898 3.7102)
308 LIKE 301 BUT *TRCL=(0 0 0 0 90 90 90 4.2810 94.2810 90 85.7190 4.2810)
309 LIKE 301 BUT *TRCL=(0 0 0 0 90 90 90 4.8518 94.8518 90 85.1482 4.8518)
310 LIKE 301 BUT *TRCL=(0 0 0 0 90 90 90 5.4226 95.4226 90 84.5774 5.4226)
311 LIKE 301 BUT *TRCL=(0 0 0 0 90 90 90 5.9934 95.9934 90 84.0066 5.9934)
312 LIKE 301 BUT *TRCL=(0 0 0 0 90 90 90 6.5642 96.5642 90 83.4358 6.5642)
313 LIKE 301 BUT *TRCL=(0 0 0 0 90 90 90 7.1350 97.1350 90 82.8650 7.1350)
314 LIKE 301 BUT *TRCL=(0 0 0 0 90 90 90 7.7058 97.7058 90 82.2942 7.7058)
315 LIKE 301 BUT *TRCL=(0 0 0 0 90 90 90 8.2766 98.2766 90 81.7234 8.2766)
316 LIKE 301 BUT *TRCL=(0 0 0 0 90 90 90 8.8474 98.8474 90 81.1526 8.8474)
317 LIKE 301 BUT *TRCL=(0 0 0 0 90 90 90 9.4182 99.4182 90 80.5818 9.4182)
318 LIKE 301 BUT *TRCL=(0 0 0 0 90 90 90 9.9890 99.9890 90 80.0110 9.9890)
319 LIKE 301 BUT *TRCL=(0 0 0 0 90 90 90 10.5598 100.5598 90 79.4402 10.5598)
320 LIKE 301 BUT *TRCL=(0 0 0 0 90 90 90 11.1306 101.1306 90 78.8694 11.1306)
321 LIKE 301 BUT *TRCL=(2.156 0 0 0 90 90 90 0.2854 89.7146 90 90.2854 0.2854)
322 LIKE 301 BUT *TRCL=(2.112 0 0 0 90 90 90 0.8562 89.1438 90 90.8562 0.8562)
323 LIKE 301 BUT *TRCL=(1.926 0 0 0 90 90 90 1.4270 88.5730 90 91.4270 1.4270)
324 LIKE 301 BUT *TRCL=(1.568 0 0 0 90 90 90 1.9978 88.0022 90 91.9978 1.9978)
325 LIKE 301 BUT *TRCL=(0.842 0 0 0 90 90 90 2.5686 87.4314 90 92.5686 2.5686)
326 LIKE 301 BUT *TRCL=(0 0 0 0 90 90 90 3.1394 86.8606 90 93.1394 3.1394)
327 LIKE 301 BUT *TRCL=(0 0 0 0 90 90 90 3.7102 86.2898 90 93.7102 3.7102)
328 LIKE 301 BUT *TRCL=(0 0 0 0 90 90 90 4.2810 85.7190 90 94.2810 4.2810)
329 LIKE 301 BUT *TRCL=(0 0 0 0 90 90 90 4.8518 85.1482 90 94.8518 4.8518)
330 LIKE 301 BUT *TRCL=(0 0 0 0 90 90 90 5.4226 84.5774 90 95.4226 5.4226)
331 LIKE 301 BUT *TRCL=(0 0 0 0 90 90 90 5.9934 84.0066 90 95.9934 5.9934)
332 LIKE 301 BUT *TRCL=(0 0 0 0 90 90 90 6.5642 83.4358 90 96.5642 6.5642)
333 LIKE 301 BUT *TRCL=(0 0 0 0 90 90 90 7.1350 82.8650 90 97.1350 7.1350)
334 LIKE 301 BUT *TRCL=(0 0 0 0 90 90 90 7.7058 82.2942 90 97.7058 7.7058)
335 LIKE 301 BUT *TRCL=(0 0 0 0 90 90 90 8.2766 81.7234 90 98.2766 8.2766)
336 LIKE 301 BUT *TRCL=(0 0 0 0 90 90 90 8.8474 81.1526 90 98.8474 8.8474)
337 LIKE 301 BUT *TRCL=(0 0 0 0 90 90 90 9.4182 80.5818 90 99.4182 9.4182)
338 LIKE 301 BUT *TRCL=(0 0 0 0 90 90 90 9.9890 80.0110 90 99.9890 9.9890)
339 LIKE 301 BUT *TRCL=(0 0 0 0 90 90 90 10.5598 79.4402 90 100.5598 10.5598)
340 LIKE 301 BUT *TRCL=(0 0 0 0 90 90 90 11.1306 78.8694 90 101.1306 11.1306)
341 91 -18.0 (-201 202 -222 223 203 -204) : (205 206 -222 224 204 -207):
      (208 206 -222 224 207 -209) : (208 210 -222 224 209 -211) :
      (208 206 -222 224 211 -212) : (205 206 -222 224 212 -213) :
      (-201 202 -222 223 213 -214)
      *TRCL=(-2.156 0 0 0 90 90 90 0.2854 90.2854 90 89.7146 0.2854)
342 LIKE 341 BUT *TRCL=(-2.112 0 0 0 90 90 90 0.8562 90.8562 90 89.1438 0.8562)
343 LIKE 341 BUT *TRCL=(-1.926 0 0 0 90 90 90 1.4270 91.4270 90 88.5730 1.4270)
344 LIKE 341 BUT *TRCL=(-1.568 0 0 0 90 90 90 1.9978 91.9978 90 88.0022 1.9978)
345 LIKE 341 BUT *TRCL=(-0.842 0 0 0 90 90 90 2.5686 92.5686 90 87.4314 2.5686)
346 LIKE 341 BUT *TRCL=(0 0 0 0 90 90 90 3.1394 93.1394 90 86.8606 3.1394)
347 LIKE 341 BUT *TRCL=(0 0 0 0 90 90 90 3.7102 93.7102 90 86.2898 3.7102)
348 LIKE 341 BUT *TRCL=(0 0 0 0 90 90 90 4.2810 94.2810 90 85.7190 4.2810)
349 LIKE 341 BUT *TRCL=(0 0 0 0 90 90 90 4.8518 94.8518 90 85.1482 4.8518)
350 LIKE 341 BUT *TRCL=(0 0 0 0 90 90 90 5.4226 95.4226 90 84.5774 5.4226)
351 LIKE 341 BUT *TRCL=(0 0 0 0 90 90 90 5.9934 95.9934 90 84.0066 5.9934)
352 LIKE 341 BUT *TRCL=(0 0 0 0 90 90 90 6.5642 96.5642 90 83.4358 6.5642)
353 LIKE 341 BUT *TRCL=(0 0 0 0 90 90 90 7.1350 97.1350 90 82.8650 7.1350)
354 LIKE 341 BUT *TRCL=(0 0 0 0 90 90 90 7.7058 97.7058 90 82.2942 7.7058)
355 LIKE 341 BUT *TRCL=(0 0 0 0 90 90 90 8.2766 98.2766 90 81.7234 8.2766)
356 LIKE 341 BUT *TRCL=(0 0 0 0 90 90 90 8.8474 98.8474 90 81.1526 8.8474)
357 LIKE 341 BUT *TRCL=(0 0 0 0 90 90 90 9.4182 99.4182 90 80.5818 9.4182)
358 LIKE 341 BUT *TRCL=(0 0 0 0 90 90 90 9.9890 99.9890 90 80.0110 9.9890)
359 LIKE 341 BUT *TRCL=(0 0 0 0 90 90 90 10.5598 100.5598 90 79.4402 10.5598)
360 LIKE 341 BUT *TRCL=(0 0 0 0 90 90 90 11.1306 101.1306 90 78.8694 11.1306)
361 LIKE 341 BUT *TRCL=(-2.156 0 0 0 90 90 90 0.2854 89.7146 90 90.2854 0.2854)
362 LIKE 341 BUT *TRCL=(-2.112 0 0 0 90 90 90 0.8562 89.1438 90 90.8562 0.8562)
```

```
363 LIKE 341 BUT *TRCL=(-1.926 0 0 0 90 90 90 1.4270 88.5730 90 91.4270 1.4270)
364 LIKE 341 BUT *TRCL=(-1.568 0 0 0 90 90 90 1.9978 88.0022 90 91.9978 1.9978)
365 LIKE 341 BUT *TRCL=(-0.842 0 0 0 90 90 90 2.5686 87.4314 90 92.5686 2.5686)
366 LIKE 341 BUT *TRCL=(0 0 0 0 90 90 90 3.1394 86.8606 90 93.1394 3.1394)
367 LIKE 341 BUT *TRCL=(0 0 0 0 90 90 90 3.7102 86.2898 90 93.7102 3.7102)
368 LIKE 341 BUT *TRCL=(0 0 0 0 90 90 90 4.2810 85.7190 90 94.2810 4.2810)
369 LIKE 341 BUT *TRCL=(0 0 0 0 90 90 90 4.8518 85.1482 90 94.8518 4.8518)
370 LIKE 341 BUT *TRCL=(0 0 0 0 90 90 90 5.4226 84.5774 90 95.4226 5.4226)
371 LIKE 341 BUT *TRCL=(0 0 0 0 90 90 90 5.9934 84.0066 90 95.9934 5.9934)
372 LIKE 341 BUT *TRCL=(0 0 0 0 90 90 90 6.5642 83.4358 90 96.5642 6.5642)
373 LIKE 341 BUT *TRCL=(0 0 0 0 90 90 90 7.1350 82.8650 90 97.1350 7.1350)
374 LIKE 341 BUT *TRCL=(0 0 0 0 90 90 90 7.7058 82.2942 90 97.7058 7.7058)
375 LIKE 341 BUT *TRCL=(0 0 0 0 90 90 90 8.2766 81.7234 90 98.2766 8.2766)
376 LIKE 341 BUT *TRCL=(0 0 0 0 90 90 90 8.8474 81.1526 90 98.8474 8.8474)
377 LIKE 341 BUT *TRCL=(0 0 0 0 90 90 90 9.4182 80.5818 90 99.4182 9.4182)
378 LIKE 341 BUT *TRCL=(0 0 0 0 90 90 90 9.9890 80.0110 90 99.9890 9.9890)
379 LIKE 341 BUT *TRCL=(0 0 0 0 90 90 90 10.5598 79.4402 90 100.5598 10.5598)
380 LIKE 341 BUT *TRCL=(0 0 0 0 90 90 90 11.1306 78.8694 90 101.1306 11.1306)
```

Listing B.3: varian_mlc_90deg.cel

```
c ********************************************************************************
c CELL CARDS FOR MLC OF 18 MV ACCELERATOR MODEL
c These cells define the MLC-leafs and their positions at a gantry angle of 90 degrees.
c Using the like and but command with the TRCL command allows us to copy the
c initial MLC-leaf to describe the remaining pairs
c
c By Bryan Bednarz and Bin Han
c Modified by Matthias Frankl
c ********************************************************************************
c MLC Cell Cards
3099 0 ((231 -234 237 -238 240 -236):
     (231 -234 237 -238 235 -209):(232 -234 237 -238 209 -240))
     #301 #302 #303 #304 #305 #306 #307 #308 #309 #310
     #311 #312 #313 #314 #315 #316 #317 #318 #319 #320
3100 0 ((-231 233 237 -238 235 -209) : (-232 233 237 -238 209 -240) :
     (-231 233 237 -238 240 -236))
     #321 #322 #323 #324 #325 #326 #327 #328 #329 #330
     #331 #332 #333 #334 #335 #336 #337 #338 #339 #340
3101 0 ((231 -234 -237 239 235 -209) : (232 -234 -237 239 209 -240) :
     (231 -234 -237 239 240 -236))
     #341 #342 #343 #344 #345 #346 #347 #348 #349 #350
     #351 #352 #353 #354 #355 #356 #357 #358 #359 #360
3102 0 ((-231 233 -237 239 235 -209) : (-232 233 -237 239 209 -240) :
     (-231 233 -237 239 240 -236))
     #361 #362 #363 #364 #365 #366 #367 #368 #369 #370
     #371 #372 #373 #374 #375 #376 #377 #378 #379 #380
301 91 -18.0 ((-201 202 -218 -219 203 -204) : (205 206 -218 -220 204 -207):
     (208 206 -218 -220 207 -209) : (208 210 -218 -220 209 -211) :
     (208 206 -218 -220 211 -212) : (205 206 -218 -220 212 -213) :
     (-201 202 -218 -219 213 -214))
     *TRCL=(1.974 0 0 0 90 90 90 0.2854 90.2854 90 89.7146 0.2854)
302 LIKE 301 BUT *TRCL=(1.926 0 0 0 90 90 90 0.8562 90.8562 90 89.1438 0.8562)
303 LIKE 301 BUT *TRCL=(1.720 0 0 0 90 90 90 1.4270 91.4270 90 88.5730 1.4270)
304 LIKE 301 BUT *TRCL=(1.308 0 0 0 90 90 90 1.9978 91.9978 90 88.0022 1.9978)
305 LIKE 301 BUT *TRCL=(0 0 0 0 90 90 90 2.5686 92.5686 90 87.4314 2.5686)
306 LIKE 301 BUT *TRCL=(0 0 0 0 90 90 90 3.1394 93.1394 90 86.8606 3.1394)
307 LIKE 301 BUT *TRCL=(0 0 0 0 90 90 90 3.7102 93.7102 90 86.2898 3.7102)
308 LIKE 301 BUT *TRCL=(0 0 0 0 90 90 90 4.2810 94.2810 90 85.7190 4.2810)
309 LIKE 301 BUT *TRCL=(0 0 0 0 90 90 90 4.8518 94.8518 90 85.1482 4.8518)
310 LIKE 301 BUT *TRCL=(0 0 0 0 90 90 90 5.4226 95.4226 90 84.5774 5.4226)
311 LIKE 301 BUT *TRCL=(0 0 0 0 90 90 90 5.9934 95.9934 90 84.0066 5.9934)
312 LIKE 301 BUT *TRCL=(0 0 0 0 90 90 90 6.5642 96.5642 90 83.4358 6.5642)
313 LIKE 301 BUT *TRCL=(0 0 0 0 90 90 90 7.1350 97.1350 90 82.8650 7.1350)
314 LIKE 301 BUT *TRCL=(0 0 0 0 90 90 90 7.7058 97.7058 90 82.2942 7.7058)
```

```
315 LIKE 301 BUT *TRCL=(0 0 0 0 90 90 90 8.2766 98.2766 90 81.7234 8.2766)
316 LIKE 301 BUT *TRCL=(0 0 0 0 90 90 90 8.8474 98.8474 90 81.1526 8.8474)
317 LIKE 301 BUT *TRCL=(0 0 0 0 90 90 90 9.4182 99.4182 90 80.5818 9.4182)
318 LIKE 301 BUT *TRCL=(0 0 0 0 90 90 90 9.9890 99.9890 90 80.0110 9.9890)
319 LIKE 301 BUT *TRCL=(0 0 0 0 90 90 90 10.5598 100.5598 90 79.4402 10.5598)
320 LIKE 301 BUT *TRCL=(0 0 0 0 90 90 90 11.1306 101.1306 90 78.8694 11.1306)
321 LIKE 301 BUT *TRCL=(1.974 0 0 0 90 90 90 0.2854 89.7146 90 90.2854 0.2854)
322 LIKE 301 BUT *TRCL=(1.926 0 0 0 90 90 90 0.8562 89.1438 90 90.8562 0.8562)
323 LIKE 301 BUT *TRCL=(1.720 0 0 0 90 90 90 1.4270 88.5730 90 91.4270 1.4270)
324 LIKE 301 BUT *TRCL=(1.308 0 0 0 90 90 90 1.9978 88.0022 90 91.9978 1.9978)
325 LIKE 301 BUT *TRCL=(0 0 0 0 90 90 90 2.5686 87.4314 90 92.5686 2.5686)
326 LIKE 301 BUT *TRCL=(0 0 0 0 90 90 90 3.1394 86.8606 90 93.1394 3.1394)
327 LIKE 301 BUT *TRCL=(0 0 0 0 90 90 90 3.7102 86.2898 90 93.7102 3.7102)
328 LIKE 301 BUT *TRCL=(0 0 0 0 90 90 90 4.2810 85.7190 90 94.2810 4.2810)
329 LIKE 301 BUT *TRCL=(0 0 0 0 90 90 90 4.8518 85.1482 90 94.8518 4.8518)
330 LIKE 301 BUT *TRCL=(0 0 0 0 90 90 90 5.4226 84.5774 90 95.4226 5.4226)
331 LIKE 301 BUT *TRCL=(0 0 0 0 90 90 90 5.9934 84.0066 90 95.9934 5.9934)
332 LIKE 301 BUT *TRCL=(0 0 0 0 90 90 90 6.5642 83.4358 90 96.5642 6.5642)
333 LIKE 301 BUT *TRCL=(0 0 0 0 90 90 90 7.1350 82.8650 90 97.1350 7.1350)
334 LIKE 301 BUT *TRCL=(0 0 0 0 90 90 90 7.7058 82.2942 90 97.7058 7.7058)
335 LIKE 301 BUT *TRCL=(0 0 0 0 90 90 90 8.2766 81.7234 90 98.2766 8.2766)
336 LIKE 301 BUT *TRCL=(0 0 0 0 90 90 90 8.8474 81.1526 90 98.8474 8.8474)
337 LIKE 301 BUT *TRCL=(0 0 0 0 90 90 90 9.4182 80.5818 90 99.4182 9.4182)
338 LIKE 301 BUT *TRCL=(0 0 0 0 90 90 90 9.9890 80.0110 90 99.9890 9.9890)
339 LIKE 301 BUT *TRCL=(0 0 0 0 90 90 90 10.5598 79.4402 90 100.5598 10.5598)
340 LIKE 301 BUT *TRCL=(0 0 0 0 90 90 90 11.1306 78.8694 90 101.1306 11.1306)
341 91 -18.0 (-201 202 -222 223 203 -204) : (205 206 -222 224 204 -207):
     (208 206 -222 224 207 -209) : (208 210 -222 224 209 -211) :
     (208 206 -222 224 211 -212) : (205 206 -222 224 212 -213) :
     (-201 202 -222 223 213 -214)
     *TRCL=(-1.974 0 0 0 90 90 90 0.2854 90.2854 90 89.7146 0.2854)
342 LIKE 341 BUT *TRCL=(-1.926 0 0 0 90 90 90 0.8562 90.8562 90 89.1438 0.8562)
343 LIKE 341 BUT *TRCL=(-1.720 0 0 0 90 90 90 1.4270 91.4270 90 88.5730 1.4270)
344 LIKE 341 BUT *TRCL=(-1.308 0 0 0 90 90 90 1.9978 91.9978 90 88.0022 1.9978)
345 LIKE 341 BUT *TRCL=(0 0 0 0 90 90 90 2.5686 92.5686 90 87.4314 2.5686)
346 LIKE 341 BUT *TRCL=(0 0 0 0 90 90 90 3.1394 93.1394 90 86.8606 3.1394)
347 LIKE 341 BUT *TRCL=(0 0 0 0 90 90 90 3.7102 93.7102 90 86.2898 3.7102)
348 LIKE 341 BUT *TRCL=(0 0 0 0 90 90 90 4.2810 94.2810 90 85.7190 4.2810)
349 LIKE 341 BUT *TRCL=(0 0 0 0 90 90 90 4.8518 94.8518 90 85.1482 4.8518)
350 LIKE 341 BUT *TRCL=(0 0 0 0 90 90 90 5.4226 95.4226 90 84.5774 5.4226)
351 LIKE 341 BUT *TRCL=(0 0 0 0 90 90 90 5.9934 95.9934 90 84.0066 5.9934)
352 LIKE 341 BUT *TRCL=(0 0 0 0 90 90 90 6.5642 96.5642 90 83.4358 6.5642)
353 LIKE 341 BUT *TRCL=(0 0 0 0 90 90 90 7.1350 97.1350 90 82.8650 7.1350)
354 LIKE 341 BUT *TRCL=(0 0 0 0 90 90 90 7.7058 97.7058 90 82.2942 7.7058)
355 LIKE 341 BUT *TRCL=(0 0 0 0 90 90 90 8.2766 98.2766 90 81.7234 8.2766)
356 LIKE 341 BUT *TRCL=(0 0 0 0 90 90 90 8.8474 98.8474 90 81.1526 8.8474)
357 LIKE 341 BUT *TRCL=(0 0 0 0 90 90 90 9.4182 99.4182 90 80.5818 9.4182)
358 LIKE 341 BUT *TRCL=(0 0 0 0 90 90 90 9.9890 99.9890 90 80.0110 9.9890)
359 LIKE 341 BUT *TRCL=(0 0 0 0 90 90 90 10.5598 100.5598 90 79.4402 10.5598)
360 LIKE 341 BUT *TRCL=(0 0 0 0 90 90 90 11.1306 101.1306 90 78.8694 11.1306)
361 LIKE 341 BUT *TRCL=(-1.974 0 0 0 90 90 90 0.2854 89.7146 90 90.2854 0.2854)
362 LIKE 341 BUT *TRCL=(-1.926 0 0 0 90 90 90 0.8562 89.1438 90 90.8562 0.8562)
363 LIKE 341 BUT *TRCL=(-1.720 0 0 0 90 90 90 1.4270 88.5730 90 91.4270 1.4270)
364 LIKE 341 BUT *TRCL=(-1.308 0 0 0 90 90 90 1.9978 88.0022 90 91.9978 1.9978)
365 LIKE 341 BUT *TRCL=(0 0 0 0 90 90 90 2.5686 87.4314 90 92.5686 2.5686)
366 LIKE 341 BUT *TRCL=(0 0 0 0 90 90 90 3.1394 86.8606 90 93.1394 3.1394)
367 LIKE 341 BUT *TRCL=(0 0 0 0 90 90 90 3.7102 86.2898 90 93.7102 3.7102)
368 LIKE 341 BUT *TRCL=(0 0 0 0 90 90 90 4.2810 85.7190 90 94.2810 4.2810)
369 LIKE 341 BUT *TRCL=(0 0 0 0 90 90 90 4.8518 85.1482 90 94.8518 4.8518)
370 LIKE 341 BUT *TRCL=(0 0 0 0 90 90 90 5.4226 84.5774 90 95.4226 5.4226)
371 LIKE 341 BUT *TRCL=(0 0 0 0 90 90 90 5.9934 84.0066 90 95.9934 5.9934)
372 LIKE 341 BUT *TRCL=(0 0 0 0 90 90 90 6.5642 83.4358 90 96.5642 6.5642)
373 LIKE 341 BUT *TRCL=(0 0 0 0 90 90 90 7.1350 82.8650 90 97.1350 7.1350)
374 LIKE 341 BUT *TRCL=(0 0 0 0 90 90 90 7.7058 82.2942 90 97.7058 7.7058)
375 LIKE 341 BUT *TRCL=(0 0 0 0 90 90 90 8.2766 81.7234 90 98.2766 8.2766)
```

```
376 LIKE 341 BUT *TRCL=(0 0 0 0 90 90 90 8.8474 81.1526 90 98.8474 8.8474)
377 LIKE 341 BUT *TRCL=(0 0 0 0 90 90 90 9.4182 80.5818 90 99.4182 9.4182)
378 LIKE 341 BUT *TRCL=(0 0 0 0 90 90 90 9.9890 80.0110 90 99.9890 9.9890)
379 LIKE 341 BUT *TRCL=(0 0 0 0 90 90 90 10.5598 79.4402 90 100.5598 10.5598)
380 LIKE 341 BUT *TRCL=(0 0 0 0 90 90 90 11.1306 78.8694 90 101.1306 11.1306)
```

Listing B.4: varian_mlc_180deg.cel

```
c ********************************************************************************
c These cells define the MLC-leafs and their positions at a gantry angle of 180 degrees.
c Using the like and but command with the TRCL command allows us to copy the
c initial MLC-leaf to describe the remaining pairs
c
c By Bryan Bednarz and Bin Han
c Modified by Matthias Frankl
c ********************************************************************************
c MLC Cell Cards
3099 0 ((231 -234 237 -238 240 -236):
     (231 -234 237 -238 235 -209):(232 -234 237 -238 209 -240))
     #301 #302 #303 #304 #305 #306 #307 #308 #309 #310
     #311 #312 #313 #314 #315 #316 #317 #318 #319 #320
3100 0 ((-231 233 237 -238 235 -209) : (-232 233 237 -238 209 -240) :
     (-231 233 237 -238 240 -236))
     #321 #322 #323 #324 #325 #326 #327 #328 #329 #330
     #331 #332 #333 #334 #335 #336 #337 #338 #339 #340
3101 0 ((231 -234 -237 239 235 -209) : (232 -234 -237 239 209 -240) :
     (231 -234 -237 239 240 -236))
     #341 #342 #343 #344 #345 #346 #347 #348 #349 #350
     #351 #352 #353 #354 #355 #356 #357 #358 #359 #360
3102 0 ((-231 233 -237 239 235 -209) : (-232 233 -237 239 209 -240) :
     (-231 233 -237 239 240 -236))
     #361 #362 #363 #364 #365 #366 #367 #368 #369 #370
     #371 #372 #373 #374 #375 #376 #377 #378 #379 #380
301 91 -18.0 ((-201 202 -218 -219 203 -204) : (205 206 -218 -220 204 -207):
     (208 206 -218 -220 207 -209) : (208 210 -218 -220 209 -211) :
     (208 206 -218 -220 211 -212) : (205 206 -218 -220 212 -213) :
     (-201 202 -218 -219 213 -214))
     *TRCL=(2.166 0 0 0 90 90 90 0.2854 90.2854 90 89.7146 0.2854)
302 LIKE 301 BUT *TRCL=(2.122 0 0 0 90 90 90 0.8562 90.8562 90 89.1438 0.8562)
303 LIKE 301 BUT *TRCL=(1.937 0 0 0 90 90 90 1.4270 91.4270 90 88.5730 1.4270)
304 LIKE 301 BUT *TRCL=(1.582 0 0 0 90 90 90 1.9978 91.9978 90 88.0022 1.9978)
305 LIKE 301 BUT *TRCL=(0.867 0 0 0 90 90 90 2.5686 92.5686 90 87.4314 2.5686)
306 LIKE 301 BUT *TRCL=(0 0 0 0 90 90 90 3.1394 93.1394 90 86.8606 3.1394)
307 LIKE 301 BUT *TRCL=(0 0 0 0 90 90 90 3.7102 93.7102 90 86.2898 3.7102)
308 LIKE 301 BUT *TRCL=(0 0 0 0 90 90 90 4.2810 94.2810 90 85.7190 4.2810)
309 LIKE 301 BUT *TRCL=(0 0 0 0 90 90 90 4.8518 94.8518 90 85.1482 4.8518)
310 LIKE 301 BUT *TRCL=(0 0 0 0 90 90 90 5.4226 95.4226 90 84.5774 5.4226)
311 LIKE 301 BUT *TRCL=(0 0 0 0 90 90 90 5.9934 95.9934 90 84.0066 5.9934)
312 LIKE 301 BUT *TRCL=(0 0 0 0 90 90 90 6.5642 96.5642 90 83.4358 6.5642)
313 LIKE 301 BUT *TRCL=(0 0 0 0 90 90 90 7.1350 97.1350 90 82.8650 7.1350)
314 LIKE 301 BUT *TRCL=(0 0 0 0 90 90 90 7.7058 97.7058 90 82.2942 7.7058)
315 LIKE 301 BUT *TRCL=(0 0 0 0 90 90 90 8.2766 98.2766 90 81.7234 8.2766)
316 LIKE 301 BUT *TRCL=(0 0 0 0 90 90 90 8.8474 98.8474 90 81.1526 8.8474)
317 LIKE 301 BUT *TRCL=(0 0 0 0 90 90 90 9.4182 99.4182 90 80.5818 9.4182)
318 LIKE 301 BUT *TRCL=(0 0 0 0 90 90 90 9.9890 99.9890 90 80.0110 9.9890)
319 LIKE 301 BUT *TRCL=(0 0 0 0 90 90 90 10.5598 100.5598 90 79.4402 10.5598)
320 LIKE 301 BUT *TRCL=(0 0 0 0 90 90 90 11.1306 101.1306 90 78.8694 11.1306)
321 LIKE 301 BUT *TRCL=(2.166 0 0 0 90 90 90 0.2854 89.7146 90 90.2854 0.2854)
322 LIKE 301 BUT *TRCL=(2.122 0 0 0 90 90 90 0.8562 89.1438 90 90.8562 0.8562)
323 LIKE 301 BUT *TRCL=(1.937 0 0 0 90 90 90 1.4270 88.5730 90 91.4270 1.4270)
324 LIKE 301 BUT *TRCL=(1.582 0 0 0 90 90 90 1.9978 88.0022 90 91.9978 1.9978)
325 LIKE 301 BUT *TRCL=(0.867 0 0 0 90 90 90 2.5686 87.4314 90 92.5686 2.5686)
326 LIKE 301 BUT *TRCL=(0 0 0 0 90 90 90 3.1394 86.8606 90 93.1394 3.1394)
327 LIKE 301 BUT *TRCL=(0 0 0 0 90 90 90 3.7102 86.2898 90 93.7102 3.7102)
328 LIKE 301 BUT *TRCL=(0 0 0 0 90 90 90 4.2810 85.7190 90 94.2810 4.2810)
```

```
329 LIKE 301 BUT *TRCL=(0 0 0 0 90 90 90 4.8518 85.1482 90 94.8518 4.8518)
330 LIKE 301 BUT *TRCL=(0 0 0 0 90 90 90 5.4226 84.5774 90 95.4226 5.4226)
331 LIKE 301 BUT *TRCL=(0 0 0 0 90 90 90 5.9934 84.0066 90 95.9934 5.9934)
332 LIKE 301 BUT *TRCL=(0 0 0 0 90 90 90 6.5642 83.4358 90 96.5642 6.5642)
333 LIKE 301 BUT *TRCL=(0 0 0 0 90 90 90 7.1350 82.8650 90 97.1350 7.1350)
334 LIKE 301 BUT *TRCL=(0 0 0 0 90 90 90 7.7058 82.2942 90 97.7058 7.7058)
335 LIKE 301 BUT *TRCL=(0 0 0 0 90 90 90 8.2766 81.7234 90 98.2766 8.2766)
336 LIKE 301 BUT *TRCL=(0 0 0 0 90 90 90 8.8474 81.1526 90 98.8474 8.8474)
337 LIKE 301 BUT *TRCL=(0 0 0 0 90 90 90 9.4182 80.5818 90 99.4182 9.4182)
338 LIKE 301 BUT *TRCL=(0 0 0 0 90 90 90 9.9890 80.0110 90 99.9890 9.9890)
339 LIKE 301 BUT *TRCL=(0 0 0 0 90 90 90 10.5598 79.4402 90 100.5598 10.5598)
340 LIKE 301 BUT *TRCL=(0 0 0 0 90 90 90 11.1306 78.8694 90 101.1306 11.1306)
341 91 -18.0 (-201 202 -222 223 203 -204) : (205 206 -222 224 204 -207):
     (208 206 -222 224 207 -209) : (208 210 -222 224 209 -211) :
     (208 206 -222 224 211 -212) : (205 206 -222 224 212 -213) :
     (-201 202 -222 223 213 -214)
     *TRCL=(-2.166 0 0 0 90 90 90 0.2854 90.2854 90 89.7146 0.2854)
342 LIKE 341 BUT *TRCL=(-2.122 0 0 0 90 90 90 0.8562 90.8562 90 89.1438 0.8562)
343 LIKE 341 BUT *TRCL=(-1.937 0 0 0 90 90 90 1.4270 91.4270 90 88.5730 1.4270)
344 LIKE 341 BUT *TRCL=(-1.582 0 0 0 90 90 90 1.9978 91.9978 90 88.0022 1.9978)
345 LIKE 341 BUT *TRCL=(-0.867 0 0 0 90 90 90 2.5686 92.5686 90 87.4314 2.5686)
346 LIKE 341 BUT *TRCL=(0 0 0 0 90 90 90 3.1394 93.1394 90 86.8606 3.1394)
347 LIKE 341 BUT *TRCL=(0 0 0 0 90 90 90 3.7102 93.7102 90 86.2898 3.7102)
348 LIKE 341 BUT *TRCL=(0 0 0 0 90 90 90 4.2810 94.2810 90 85.7190 4.2810)
349 LIKE 341 BUT *TRCL=(0 0 0 0 90 90 90 4.8518 94.8518 90 85.1482 4.8518)
350 LIKE 341 BUT *TRCL=(0 0 0 0 90 90 90 5.4226 95.4226 90 84.5774 5.4226)
351 LIKE 341 BUT *TRCL=(0 0 0 0 90 90 90 5.9934 95.9934 90 84.0066 5.9934)
352 LIKE 341 BUT *TRCL=(0 0 0 0 90 90 90 6.5642 96.5642 90 83.4358 6.5642)
353 LIKE 341 BUT *TRCL=(0 0 0 0 90 90 90 7.1350 97.1350 90 82.8650 7.1350)
354 LIKE 341 BUT *TRCL=(0 0 0 0 90 90 90 7.7058 97.7058 90 82.2942 7.7058)
355 LIKE 341 BUT *TRCL=(0 0 0 0 90 90 90 8.2766 98.2766 90 81.7234 8.2766)
356 LIKE 341 BUT *TRCL=(0 0 0 0 90 90 90 8.8474 98.8474 90 81.1526 8.8474)
357 LIKE 341 BUT *TRCL=(0 0 0 0 90 90 90 9.4182 99.4182 90 80.5818 9.4182)
358 LIKE 341 BUT *TRCL=(0 0 0 0 90 90 90 9.9890 99.9890 90 80.0110 9.9890)
359 LIKE 341 BUT *TRCL=(0 0 0 0 90 90 90 10.5598 100.5598 90 79.4402 10.5598)
360 LIKE 341 BUT *TRCL=(0 0 0 0 90 90 90 11.1306 101.1306 90 78.8694 11.1306)
361 LIKE 341 BUT *TRCL=(-2.166 0 0 0 90 90 90 0.2854 89.7146 90 90.2854 0.2854)
362 LIKE 341 BUT *TRCL=(-2.122 0 0 0 90 90 90 0.8562 89.1438 90 90.8562 0.8562)
363 LIKE 341 BUT *TRCL=(-1.937 0 0 0 90 90 90 1.4270 88.5730 90 91.4270 1.4270)
364 LIKE 341 BUT *TRCL=(-1.582 0 0 0 90 90 90 1.9978 88.0022 90 91.9978 1.9978)
365 LIKE 341 BUT *TRCL=(-0.867 0 0 0 90 90 90 2.5686 87.4314 90 92.5686 2.5686)
366 LIKE 341 BUT *TRCL=(0 0 0 0 90 90 90 3.1394 86.8606 90 93.1394 3.1394)
367 LIKE 341 BUT *TRCL=(0 0 0 0 90 90 90 3.7102 86.2898 90 93.7102 3.7102)
368 LIKE 341 BUT *TRCL=(0 0 0 0 90 90 90 4.2810 85.7190 90 94.2810 4.2810)
369 LIKE 341 BUT *TRCL=(0 0 0 0 90 90 90 4.8518 85.1482 90 94.8518 4.8518)
370 LIKE 341 BUT *TRCL=(0 0 0 0 90 90 90 5.4226 84.5774 90 95.4226 5.4226)
371 LIKE 341 BUT *TRCL=(0 0 0 0 90 90 90 5.9934 84.0066 90 95.9934 5.9934)
372 LIKE 341 BUT *TRCL=(0 0 0 0 90 90 90 6.5642 83.4358 90 96.5642 6.5642)
373 LIKE 341 BUT *TRCL=(0 0 0 0 90 90 90 7.1350 82.8650 90 97.1350 7.1350)
374 LIKE 341 BUT *TRCL=(0 0 0 0 90 90 90 7.7058 82.2942 90 97.7058 7.7058)
375 LIKE 341 BUT *TRCL=(0 0 0 0 90 90 90 8.2766 81.7234 90 98.2766 8.2766)
376 LIKE 341 BUT *TRCL=(0 0 0 0 90 90 90 8.8474 81.1526 90 98.8474 8.8474)
377 LIKE 341 BUT *TRCL=(0 0 0 0 90 90 90 9.4182 80.5818 90 99.4182 9.4182)
378 LIKE 341 BUT *TRCL=(0 0 0 0 90 90 90 9.9890 80.0110 90 99.9890 9.9890)
379 LIKE 341 BUT *TRCL=(0 0 0 0 90 90 90 10.5598 79.4402 90 100.5598 10.5598)
380 LIKE 341 BUT *TRCL=(0 0 0 0 90 90 90 11.1306 78.8694 90 101.1306 11.1306)
```

Listing B.5: varian_mlc_270deg.cel

```
c ******************************************************************************
c CELL CARDS FOR MLC OF 18 MV ACCELERATOR MODEL
c These cells define the MLC-leafs and their positions at a gantry angle of 270 degrees.
c Using the like and but command with the TRCL command allows us to copy the
c initial MLC-leaf to describe the remaining pairs
c
```

```
c By Bryan Bednarz and Bin Han
c Modified by Matthias Frankl
c ******************************************************************************
c MLC Cell Cards
3099 0 ((231 -234 237 -238 240 -236):
     (231 -234 237 -238 235 -209):(232 -234 237 -238 209 -240))
     #301 #302 #303 #304 #305 #306 #307 #308 #309 #310
     #311 #312 #313 #314 #315 #316 #317 #318 #319 #320
3100 0 ((-231 233 237 -238 235 -209) : (-232 233 237 -238 209 -240) :
     (-231 233 237 -238 240 -236))
     #321 #322 #323 #324 #325 #326 #327 #328 #329 #330
     #331 #332 #333 #334 #335 #336 #337 #338 #339 #340
3101 0 ((231 -234 -237 239 235 -209) : (232 -234 -237 239 209 -240) :
     (231 -234 -237 239 240 -236))
     #341 #342 #343 #344 #345 #346 #347 #348 #349 #350
     #351 #352 #353 #354 #355 #356 #357 #358 #359 #360
3102 0 ((-231 233 -237 239 235 -209) : (-232 233 -237 239 209 -240) :
     (-231 233 -237 239 240 -236))
     #361 #362 #363 #364 #365 #366 #367 #368 #369 #370
     #371 #372 #373 #374 #375 #376 #377 #378 #379 #380
301 91 -18.0 ((-201 202 -218 -219 203 -204) : (205 206 -218 -220 204 -207):
     (208 206 -218 -220 207 -209) : (208 210 -218 -220 209 -211) :
     (208 206 -218 -220 211 -212) : (205 206 -218 -220 212 -213) :
     (-201 202 -218 -219 213 -214))
     *TRCL=(2.015 0 0 0 90 90 90 0.2854 90.2854 90 89.7146 0.2854)
302 LIKE 301 BUT *TRCL=(1.967 0 0 0 90 90 90 0.8562 90.8562 90 89.1438 0.8562)
303 LIKE 301 BUT *TRCL=(1.767 0 0 0 90 90 90 1.4270 91.4270 90 88.5730 1.4270)
304 LIKE 301 BUT *TRCL=(1.368 0 0 0 90 90 90 1.9978 91.9978 90 88.0022 1.9978)
305 LIKE 301 BUT *TRCL=(0.348 0 0 0 90 90 90 2.5686 92.5686 90 87.4314 2.5686)
306 LIKE 301 BUT *TRCL=(0 0 0 0 90 90 90 3.1394 93.1394 90 86.8606 3.1394)
307 LIKE 301 BUT *TRCL=(0 0 0 0 90 90 90 3.7102 93.7102 90 86.2898 3.7102)
308 LIKE 301 BUT *TRCL=(0 0 0 0 90 90 90 4.2810 94.2810 90 85.7190 4.2810)
309 LIKE 301 BUT *TRCL=(0 0 0 0 90 90 90 4.8518 94.8518 90 85.1482 4.8518)
310 LIKE 301 BUT *TRCL=(0 0 0 0 90 90 90 5.4226 95.4226 90 84.5774 5.4226)
311 LIKE 301 BUT *TRCL=(0 0 0 0 90 90 90 5.9934 95.9934 90 84.0066 5.9934)
312 LIKE 301 BUT *TRCL=(0 0 0 0 90 90 90 6.5642 96.5642 90 83.4358 6.5642)
313 LIKE 301 BUT *TRCL=(0 0 0 0 90 90 90 7.1350 97.1350 90 82.8650 7.1350)
314 LIKE 301 BUT *TRCL=(0 0 0 0 90 90 90 7.7058 97.7058 90 82.2942 7.7058)
315 LIKE 301 BUT *TRCL=(0 0 0 0 90 90 90 8.2766 98.2766 90 81.7234 8.2766)
316 LIKE 301 BUT *TRCL=(0 0 0 0 90 90 90 8.8474 98.8474 90 81.1526 8.8474)
317 LIKE 301 BUT *TRCL=(0 0 0 0 90 90 90 9.4182 99.4182 90 80.5818 9.4182)
318 LIKE 301 BUT *TRCL=(0 0 0 0 90 90 90 9.9890 99.9890 90 80.0110 9.9890)
319 LIKE 301 BUT *TRCL=(0 0 0 0 90 90 90 10.5598 100.5598 90 79.4402 10.5598)
320 LIKE 301 BUT *TRCL=(0 0 0 0 90 90 90 11.1306 101.1306 90 78.8694 11.1306)
321 LIKE 301 BUT *TRCL=(2.015 0 0 0 90 90 90 0.2854 89.7146 90 90.2854 0.2854)
322 LIKE 301 BUT *TRCL=(1.967 0 0 0 90 90 90 0.8562 89.1438 90 90.8562 0.8562)
323 LIKE 301 BUT *TRCL=(1.767 0 0 0 90 90 90 1.4270 88.5730 90 91.4270 1.4270)
324 LIKE 301 BUT *TRCL=(1.368 0 0 0 90 90 90 1.9978 88.0022 90 91.9978 1.9978)
325 LIKE 301 BUT *TRCL=(0.348 0 0 0 90 90 90 2.5686 87.4314 90 92.5686 2.5686)
326 LIKE 301 BUT *TRCL=(0 0 0 0 90 90 90 3.1394 86.8606 90 93.1394 3.1394)
327 LIKE 301 BUT *TRCL=(0 0 0 0 90 90 90 3.7102 86.2898 90 93.7102 3.7102)
328 LIKE 301 BUT *TRCL=(0 0 0 0 90 90 90 4.2810 85.7190 90 94.2810 4.2810)
329 LIKE 301 BUT *TRCL=(0 0 0 0 90 90 90 4.8518 85.1482 90 94.8518 4.8518)
330 LIKE 301 BUT *TRCL=(0 0 0 0 90 90 90 5.4226 84.5774 90 95.4226 5.4226)
331 LIKE 301 BUT *TRCL=(0 0 0 0 90 90 90 5.9934 84.0066 90 95.9934 5.9934)
332 LIKE 301 BUT *TRCL=(0 0 0 0 90 90 90 6.5642 83.4358 90 96.5642 6.5642)
333 LIKE 301 BUT *TRCL=(0 0 0 0 90 90 90 7.1350 82.8650 90 97.1350 7.1350)
334 LIKE 301 BUT *TRCL=(0 0 0 0 90 90 90 7.7058 82.2942 90 97.7058 7.7058)
335 LIKE 301 BUT *TRCL=(0 0 0 0 90 90 90 8.2766 81.7234 90 98.2766 8.2766)
336 LIKE 301 BUT *TRCL=(0 0 0 0 90 90 90 8.8474 81.1526 90 98.8474 8.8474)
337 LIKE 301 BUT *TRCL=(0 0 0 0 90 90 90 9.4182 80.5818 90 99.4182 9.4182)
338 LIKE 301 BUT *TRCL=(0 0 0 0 90 90 90 9.9890 80.0110 90 99.9890 9.9890)
339 LIKE 301 BUT *TRCL=(0 0 0 0 90 90 90 10.5598 79.4402 90 100.5598 10.5598)
340 LIKE 301 BUT *TRCL=(0 0 0 0 90 90 90 11.1306 78.8694 90 101.1306 11.1306)
341 91 -18.0 (-201 202 -222 223 203 -204) : (205 206 -222 224 204 -207):
```

```
     (208 206 -222 224 207 -209) : (208 210 -222 224 209 -211) :
     (208 206 -222 224 211 -212) : (205 206 -222 224 212 -213) :
     (-201 202 -222 223 213 -214)
     *TRCL=(-2.015 0 0 0 90 90 90 0.2854 90.2854 90 89.7146 0.2854)
342 LIKE 341 BUT *TRCL=(-1.967 0 0 0 90 90 90 0.8562 90.8562 90 89.1438 0.8562)
343 LIKE 341 BUT *TRCL=(-1.767 0 0 0 90 90 90 1.4270 91.4270 90 88.5730 1.4270)
344 LIKE 341 BUT *TRCL=(-1.368 0 0 0 90 90 90 1.9978 91.9978 90 88.0022 1.9978)
345 LIKE 341 BUT *TRCL=(-0.348 0 0 0 90 90 90 2.5686 92.5686 90 87.4314 2.5686)
346 LIKE 341 BUT *TRCL=(0 0 0 0 90 90 90 3.1394 93.1394 90 86.8606 3.1394)
347 LIKE 341 BUT *TRCL=(0 0 0 0 90 90 90 3.7102 93.7102 90 86.2898 3.7102)
348 LIKE 341 BUT *TRCL=(0 0 0 0 90 90 90 4.2810 94.2810 90 85.7190 4.2810)
349 LIKE 341 BUT *TRCL=(0 0 0 0 90 90 90 4.8518 94.8518 90 85.1482 4.8518)
350 LIKE 341 BUT *TRCL=(0 0 0 0 90 90 90 5.4226 95.4226 90 84.5774 5.4226)
351 LIKE 341 BUT *TRCL=(0 0 0 0 90 90 90 5.9934 95.9934 90 84.0066 5.9934)
352 LIKE 341 BUT *TRCL=(0 0 0 0 90 90 90 6.5642 96.5642 90 83.4358 6.5642)
353 LIKE 341 BUT *TRCL=(0 0 0 0 90 90 90 7.1350 97.1350 90 82.8650 7.1350)
354 LIKE 341 BUT *TRCL=(0 0 0 0 90 90 90 7.7058 97.7058 90 82.2942 7.7058)
355 LIKE 341 BUT *TRCL=(0 0 0 0 90 90 90 8.2766 98.2766 90 81.7234 8.2766)
356 LIKE 341 BUT *TRCL=(0 0 0 0 90 90 90 8.8474 98.8474 90 81.1526 8.8474)
357 LIKE 341 BUT *TRCL=(0 0 0 0 90 90 90 9.4182 99.4182 90 80.5818 9.4182)
358 LIKE 341 BUT *TRCL=(0 0 0 0 90 90 90 9.9890 99.9890 90 80.0110 9.9890)
359 LIKE 341 BUT *TRCL=(0 0 0 0 90 90 90 10.5598 100.5598 90 79.4402 10.5598)
360 LIKE 341 BUT *TRCL=(0 0 0 0 90 90 90 11.1306 101.1306 90 78.8694 11.1306)
361 LIKE 341 BUT *TRCL=(-2.015 0 0 0 90 90 90 0.2854 89.7146 90 90.2854 0.2854)
362 LIKE 341 BUT *TRCL=(-1.967 0 0 0 90 90 90 0.8562 89.1438 90 90.8562 0.8562)
363 LIKE 341 BUT *TRCL=(-1.767 0 0 0 90 90 90 1.4270 88.5730 90 91.4270 1.4270)
364 LIKE 341 BUT *TRCL=(-1.368 0 0 0 90 90 90 1.9978 88.0022 90 91.9978 1.9978)
365 LIKE 341 BUT *TRCL=(-0.348 0 0 0 90 90 90 2.5686 87.4314 90 92.5686 2.5686)
366 LIKE 341 BUT *TRCL=(0 0 0 0 90 90 90 3.1394 86.8606 90 93.1394 3.1394)
367 LIKE 341 BUT *TRCL=(0 0 0 0 90 90 90 3.7102 86.2898 90 93.7102 3.7102)
368 LIKE 341 BUT *TRCL=(0 0 0 0 90 90 90 4.2810 85.7190 90 94.2810 4.2810)
369 LIKE 341 BUT *TRCL=(0 0 0 0 90 90 90 4.8518 85.1482 90 94.8518 4.8518)
370 LIKE 341 BUT *TRCL=(0 0 0 0 90 90 90 5.4226 84.5774 90 95.4226 5.4226)
371 LIKE 341 BUT *TRCL=(0 0 0 0 90 90 90 5.9934 84.0066 90 95.9934 5.9934)
372 LIKE 341 BUT *TRCL=(0 0 0 0 90 90 90 6.5642 83.4358 90 96.5642 6.5642)
373 LIKE 341 BUT *TRCL=(0 0 0 0 90 90 90 7.1350 82.8650 90 97.1350 7.1350)
374 LIKE 341 BUT *TRCL=(0 0 0 0 90 90 90 7.7058 82.2942 90 97.7058 7.7058)
375 LIKE 341 BUT *TRCL=(0 0 0 0 90 90 90 8.2766 81.7234 90 98.2766 8.2766)
376 LIKE 341 BUT *TRCL=(0 0 0 0 90 90 90 8.8474 81.1526 90 98.8474 8.8474)
377 LIKE 341 BUT *TRCL=(0 0 0 0 90 90 90 9.4182 80.5818 90 99.4182 9.4182)
378 LIKE 341 BUT *TRCL=(0 0 0 0 90 90 90 9.9890 80.0110 90 99.9890 9.9890)
379 LIKE 341 BUT *TRCL=(0 0 0 0 90 90 90 10.5598 79.4402 90 100.5598 10.5598)
380 LIKE 341 BUT *TRCL=(0 0 0 0 90 90 90 11.1306 78.8694 90 101.1306 11.1306)
```

Listing B.6: varian_clin_18.cel

```
c ******************************************************************************
c CELL CARDS FOR 18 MV ACCELERATOR MODEL
c ******************************************************************************
c Vacuum Definition
1101 0 -12 17 18 21 22 27 701 702 31 32 35 40 41 42 43 44 45 46
      47 48 49 50 51 52 53 54 55 56 58 60 89 67 68 69
      70 72 74 76 77 78 84 90 91 92 93
      #1109 #1110 #1120 #1194 811
1102 0 -59 27 701 702 29 30 57 58
1103 0 -24
1196 0 -26 19
1104 0 -19 15 24
1105 0 -73 67 68
1106 0 -75 62 64 (-812:833:832)
1107 0 -23 24
1108 0 -16 13 14
1109 0 -79 39 #1145
1110 0 -80 #1146 #1120
1111 0 -82 81 21 17
```

```
1112 0 -71 66 64 834
1116 0 -83
1117 0 -61 (832:833)
1118 0 -63 834
1119 0 -65 834
1120 0 -39 702 811
c Target
1122 91 -18.0 -13
1123 92 -8.96 -14 13
1124 92 -8.96 -15 16
c Primary Collimator
1125 91 -18.0 -20 26 19 24
1126 91 -18.0 -25 23 24
c Other
1127 93 -7.87 -17 20 19 24
1128 93 -7.87 -18 19
1129 93 -7.87 -22 23
c Other
1130 92 -8.96 -21 23 25
1131 92 -8.96 -84 83
c Flattening Filter
1132 94 -16.65 -28
801 94 -16.65 -703
1133 93 -7.87 -701 28
802 93 -7.87 -702 703
803 93 -7.87 -27
1134 93 -7.87 -29
1135 93 -7.87 -30
c Other
1136 93 -7.87 -35 34 17 21 39 79 80
1137 93 -7.87 -36 -34 33 -81
1138 93 -7.87 -36 -34 33 82
1139 93 -7.87 -37 -34 33 -81
1140 93 -7.87 -37 -34 33 82
1141 93 -7.87 -38 -34 33 -81
1142 93 -7.87 -38 -34 33 82
c Other
1143 91 -18.0 -34 33 36 37 38 39 17 21 -81
1144 91 -18.0 -34 33 36 37 38 39 17 21 82
1145 91 -18.0 -31
1146 91 -18.0 -32
c Other
1147 95 -11.4 -33 17
1148 95 -11.4 -44
c Other
1149 93 -7.87 -40
1150 93 -7.87 -41
1151 93 -7.87 -42
1152 93 -7.87 -43
1153 93 -7.87 -45
1154 93 -7.87 -46
1155 93 -7.87 -47
1156 93 -7.87 -48
1157 93 -7.87 -49
1158 93 -7.87 -50
c Other
1159 95 -11.4 -51
1160 95 -11.4 -52
1161 95 -11.4 -53 #1160
1162 95 -11.4 -54 #1152
1163 95 -11.4 -77
1164 95 -11.4 -78
c Other
1165 95 -11.4 -56
1166 95 -11.4 -57
```

```
1176 95 -11.4 -58 #1177
1177 95 -11.4 -60 59
c Other
1178 91 -18.0 -62 61
1179 91 -18.0 -64 63
1180 91 -18.0 -55
c Other
1181 93 -7.87 -76 75
1182 93 -7.87 -90
1183 93 -7.87 -91
c Other
1184 95 -11.4 -66 65 #1188 #1189
1185 95 -11.4 -72 71
1186 95 -11.4 -74 73
1187 95 -11.4 -89
c Other
1188 91 -18.0 -67
1189 91 -18.0 -68
1190 91 -18.0 -69
1191 91 -18.0 -70
c Other
1192 93 -7.87 -92
1193 93 -7.87 -93
1194 93 -7.87 -95 94 96 -97
c water phantom 140 x 140 x 35
c 800 96 -1 -800
c vacuum window
811 100 -1.85 -811
c ion chamber
812 92 -8.96   812 -813 -833
813 101 -1.42  813 -814 -833
814 97 -0.0012 814 -815 -833
815 101 -1.42  815 -816 -833
816 92 -8.96   816 -817 -833
817 97 -0.0012 817 -818 -833
818 92 -8.96   818 -819 -833
819 101 -1.42  819 -820 -833
820 97 -0.0012 820 -821 -833
821 101 -1.42  821 -822 -833
822 92 -8.96   822 -823 -833
823 97 -0.0012 823 -824 -833
824 101 -1.42  824 -825 -833
825 92 -8.96   825 -826 -833
826 97 -0.0012 826 -827 -833
827 92 -8.96   827 -828 -833
828 101 -1.42  828 -829 -833
829 97 -0.0012 829 -830 -833
830 101 -1.42  830 -831 -833
831 92 -8.96   831 -832 -833
c mirror
834 102 -1.39 -834
c rest
1195 97 -0.0012 -11 (-233:236:234:238:-239) 403
c 199 6 -1.00 -202 201 -204 203 205 -206
```

The following two files, together with the material specification in B.17, are dedicated to the definition of the voxel phantom model. Listing B.7 specifies all the organs of the phantom. B.8, on the other hand, shows the array of phantom voxels, indicated with their corresponding organ identification number. The entire voxel matrix is extremely huge so that only the first lines of the voxel matrix are reproduced here. The full matrix, however, can be retrieved from [Int09]. The entire implemented phantom including the material definition in B.17 is finally based on supplementary data from ICRP Publication 110 [Int09].

Listing B.7: AM_organs

```
1 43 -1.030 -401 u=1  $ Adrenal,left
2 like 1 but mat=43  rho=-1.030 u=2  $ Adrenal,right
3 like 1 but mat=45  rho=-1.030 u=3  $ Anteriornasalpassage(ET1)
4 like 1 but mat=45  rho=-1.030 u=4  $ Posteriornasalpassagedowntolarynx(ET2)
5 like 1 but mat=29  rho=-1.050 u=5  $ Oralmucosa,tongue
6 like 1 but mat=29  rho=-1.050 u=6  $ Oralmucosa,lipsandcheeks
7 like 1 but mat=45  rho=-1.030 u=7  $ Trachea
8 like 1 but mat=45  rho=-1.030 u=8  $ Bronchi
9 like 1 but mat=28  rho=-1.060 u=9  $ Bloodvessels,head
10 like 1 but mat=28  rho=-1.060 u=10  $ Bloodvessels,trunk
11 like 1 but mat=28  rho=-1.060 u=11  $ Bloodvessels,arms
12 like 1 but mat=28  rho=-1.060 u=12  $ Bloodvessels,legs
13 like 1 but mat=2  rho=-1.920 u=13  $ Humeri,upperhalf,cortical
14 like 1 but mat=3  rho=-1.205 u=14  $ Humeri,upperhalf,spongiosa
15 like 1 but mat=22  rho=-0.980 u=15  $ Humeri,upperhalf,medullarycavity
16 like 1 but mat=2  rho=-1.920 u=16  $ Humeri,lowerhalf,cortical
17 like 1 but mat=4  rho=-1.108 u=17  $ Humeri,lowerhalf,spongiosa
18 like 1 but mat=23  rho=-0.980 u=18  $ Humeri,lowerhalf,medullarycavity
19 like 1 but mat=2  rho=-1.920 u=19  $ Ulnaeandradii,cortical
20 like 1 but mat=5  rho=-1.108 u=20  $ Ulnaeandradii,spongiosa
21 like 1 but mat=24  rho=-0.980 u=21  $ Ulnaeandradii,medullarycavity
22 like 1 but mat=2  rho=-1.920 u=22  $ Wristsandhandbones,cortical
23 like 1 but mat=6  rho=-1.108 u=23  $ Wristsandhandbones,spongiosa
24 like 1 but mat=2  rho=-1.920 u=24  $ Clavicles,cortical
25 like 1 but mat=7  rho=-1.151 u=25  $ Clavicles,spongiosa
26 like 1 but mat=2  rho=-1.920 u=26  $ Cranium,cortical
27 like 1 but mat=8  rho=-1.157 u=27  $ Cranium,spongiosa
28 like 1 but mat=2  rho=-1.920 u=28  $ Femora,upperhalf,cortical
29 like 1 but mat=9  rho=-1.124 u=29  $ Femora,upperhalf,spongiosa
30 like 1 but mat=22  rho=-0.980 u=30  $ Femora,upperhalf,medullarycavity
31 like 1 but mat=2  rho=-1.920 u=31  $ Femora,lowerhalf,cortical
32 like 1 but mat=10  rho=-1.108 u=32  $ Femora,lowerhalf,spongiosa
33 like 1 but mat=23  rho=-0.980 u=33  $ Femora,lowerhalf,medullarycavity
34 like 1 but mat=2  rho=-1.920 u=34  $ Tibiae,fibulaeandpatellae,cortical
35 like 1 but mat=11  rho=-1.108 u=35  $ Tibiae,fibulaeandpatellae,spongiosa
36 like 1 but mat=25  rho=-0.980 u=36  $ Tibiae,fibulaeandpatellae,medullarycavity
37 like 1 but mat=2  rho=-1.920 u=37  $ Anklesandfootbones,cortical
38 like 1 but mat=12  rho=-1.108 u=38  $ Anklesandfootbones,spongiosa
39 like 1 but mat=2  rho=-1.920 u=39  $ Mandible,cortical
40 like 1 but mat=13  rho=-1.228 u=40  $ Mandible,spongiosa
41 like 1 but mat=2  rho=-1.920 u=41  $ Pelvis,cortical
42 like 1 but mat=14  rho=-1.123 u=42  $ Pelvis,spongiosa
43 like 1 but mat=2  rho=-1.920 u=43  $ Ribs,cortical
44 like 1 but mat=15  rho=-1.165 u=44  $ Ribs,spongiosa
45 like 1 but mat=2  rho=-1.920 u=45  $ Scapulae,cortical
46 like 1 but mat=16  rho=-1.183 u=46  $ Scapulae,spongiosa
47 like 1 but mat=2  rho=-1.920 u=47  $ Cervicalspine,cortical
48 like 1 but mat=17  rho=-1.050 u=48  $ Cervicalspine,spongiosa
49 like 1 but mat=2  rho=-1.920 u=49  $ Thoracicspine,cortical
50 like 1 but mat=18  rho=-1.074 u=50  $ Thoracicspine,spongiosa
51 like 1 but mat=2  rho=-1.920 u=51  $ Lumbarspine,cortical
52 like 1 but mat=19  rho=-1.112 u=52  $ Lumbarspine,spongiosa
53 like 1 but mat=2  rho=-1.920 u=53  $ Sacrum,cortical
54 like 1 but mat=20  rho=-1.031 u=54  $ Sacrum,spongiosa
55 like 1 but mat=2  rho=-1.920 u=55  $ Sternum,cortical
56 like 1 but mat=21  rho=-1.041 u=56  $ Sternum,spongiosa
57 like 1 but mat=26  rho=-1.100 u=57  $ Cartilage,head
58 like 1 but mat=26  rho=-1.100 u=58  $ Cartilage,trunk
59 like 1 but mat=26  rho=-1.100 u=59  $ Cartilage,arms
60 like 1 but mat=26  rho=-1.100 u=60  $ Cartilage,legs
61 like 1 but mat=32  rho=-1.050 u=61  $ Brain
62 like 1 but mat=49  rho=-0.950 u=62  $ Breast,left,adiposetissue
63 like 1 but mat=48  rho=-1.020 u=63  $ Breast,left,glandulartissue
```

```
64 like 1 but mat=49  rho=-0.950 u=64  $ Breast,right,adiposetissue
65 like 1 but mat=48  rho=-1.020 u=65  $ Breast,right,glandulartissue
66 like 1 but mat=34  rho=-1.050 u=66  $ Eyelense,left
67 like 1 but mat=34  rho=-1.050 u=67  $ Eyebulb,left
68 like 1 but mat=34  rho=-1.050 u=68  $ Eyelense,right
69 like 1 but mat=34  rho=-1.050 u=69  $ Eyebulb,right
70 like 1 but mat=45  rho=-1.030 u=70  $ Gallbladderwall
71 like 1 but mat=45  rho=-1.030 u=71  $ Gallbladdercontents
72 like 1 but mat=36  rho=-1.040 u=72  $ Stomachwall
73 like 1 but mat=51  rho=-1.040 u=73  $ Stomachcontents
74 like 1 but mat=37  rho=-1.040 u=74  $ Smallintestinewall
75 like 1 but mat=51  rho=-1.040 u=75  $ Smallintestinecontents
76 like 1 but mat=38  rho=-1.040 u=76  $ Ascendingcolonwall
77 like 1 but mat=51  rho=-1.040 u=77  $ Ascendingcoloncontents
78 like 1 but mat=38  rho=-1.040 u=78  $ Transversecolonwall,right
79 like 1 but mat=51  rho=-1.040 u=79  $ Transversecoloncontents,right
80 like 1 but mat=38  rho=-1.040 u=80  $ Transversecolonwall,left
81 like 1 but mat=51  rho=-1.040 u=81  $ Transversecoloncontents,left
82 like 1 but mat=38  rho=-1.040 u=82  $ Descendingcolonwall
83 like 1 but mat=51  rho=-1.040 u=83  $ Descendingcoloncontents
84 like 1 but mat=38  rho=-1.040 u=84  $ Sigmoidcolonwall
85 like 1 but mat=51  rho=-1.040 u=85  $ Sigmoidcoloncontents
86 like 1 but mat=38  rho=-1.040 u=86  $ Rectumwall
87 like 1 but mat=33  rho=-1.050 u=87  $ Heartwall
88 like 1 but mat=28  rho=-1.060 u=88  $ Heartcontents(blood)
89 like 1 but mat=35  rho=-1.050 u=89  $ Kidney,left,cortex
90 like 1 but mat=35  rho=-1.050 u=90  $ Kidney,left,medulla
91 like 1 but mat=35  rho=-1.050 u=91  $ Kidney,left,pelvis
92 like 1 but mat=35  rho=-1.050 u=92  $ Kidney,right,cortex
93 like 1 but mat=35  rho=-1.050 u=93  $ Kidney,right,medulla
94 like 1 but mat=35  rho=-1.050 u=94  $ Kidney,right,pelvis
95 like 1 but mat=30  rho=-1.050 u=95  $ Liver
96 like 1 but mat=28  rho=-1.060 u=96  $ Lung,left,blood
97 like 1 but mat=50  rho=-0.382 u=97  $ Lung,left,tissue
98 like 1 but mat=28  rho=-1.060 u=98  $ Lung,right,blood
99 like 1 but mat=50  rho=-0.382 u=99  $ Lung,right,tissue
100 like 1 but mat=47  rho=-1.030 u=100  $ Lymphaticnodes,extrathoracicairways
101 like 1 but mat=47  rho=-1.030 u=101  $ Lymphaticnodes,thoracicairways
102 like 1 but mat=47  rho=-1.030 u=102  $ Lymphaticnodes,head
103 like 1 but mat=47  rho=-1.030 u=103  $ Lymphaticnodes,trunk
104 like 1 but mat=47  rho=-1.030 u=104  $ Lymphaticnodes,arms
105 like 1 but mat=47  rho=-1.030 u=105  $ Lymphaticnodes,legs
106 like 1 but mat=29  rho=-1.050 u=106  $ Muscle,head
107 like 1 but mat=29  rho=-1.050 u=107  $ Muscle,trunk
108 like 1 but mat=29  rho=-1.050 u=108  $ Muscle,arms
109 like 1 but mat=29  rho=-1.050 u=109  $ Muscle,legs
110 like 1 but mat=44  rho=-1.030 u=110  $ Oesophagus
111 like 1 but mat=42  rho=-1.040 u=111  $ Ovary,left
112 like 1 but mat=42  rho=-1.040 u=112  $ Ovary,right
113 like 1 but mat=31  rho=-1.050 u=113  $ Pancreas
114 like 1 but mat=45  rho=-1.030 u=114  $ Pituitarygland
115 like 1 but mat=46  rho=-1.030 u=115  $ Prostate
116 like 1 but mat=49  rho=-0.950 u=116  $ Residualtissue,head
117 like 1 but mat=49  rho=-0.950 u=117  $ Residualtissue,trunk
118 like 1 but mat=49  rho=-0.950 u=118  $ Residualtissue,arms
119 like 1 but mat=49  rho=-0.950 u=119  $ Residualtissue,legs
120 like 1 but mat=45  rho=-1.030 u=120  $ Salivaryglands,left
121 like 1 but mat=45  rho=-1.030 u=121  $ Salivaryglands,right
122 like 1 but mat=27  rho=-1.090 u=122  $ Skin,head
123 like 1 but mat=27  rho=-1.090 u=123  $ Skin,trunk
124 like 1 but mat=27  rho=-1.090 u=124  $ Skin,arms
125 like 1 but mat=27  rho=-1.090 u=125  $ Skin,legs
126 like 1 but mat=45  rho=-1.030 u=126  $ Spinalcord
127 like 1 but mat=39  rho=-1.040 u=127  $ Spleen
128 like 1 but mat=1  rho=-2.750 u=128  $ Teeth
```

```
   129 like 1 but mat=42  rho=-1.040 u=129  $ Testis,left
   130 like 1 but mat=42  rho=-1.040 u=130  $ Testis,right
   131 like 1 but mat=45  rho=-1.030 u=131  $ Thymus
   132 like 1 but mat=40  rho=-1.040 u=132  $ Thyroid
   133 like 1 but mat=29  rho=-1.050 u=133  $ Tongue(innerpart)
   134 like 1 but mat=45  rho=-1.030 u=134  $ Tonsils
   135 like 1 but mat=45  rho=-1.030 u=135  $ Ureter,left
   136 like 1 but mat=45  rho=-1.030 u=136  $ Ureter,right
   137 like 1 but mat=41  rho=-1.040 u=137  $ Urinarybladderwall
   138 like 1 but mat=52  rho=-1.040 u=138  $ Urinarybladdercontents
   139 like 1 but mat=46  rho=-1.030 u=139  $ Uterus
   140 like 1 but mat=53  rho=-0.001 u=140  $ Airinsidebody
```

Listing B.8: AM_matrix

```
1016 0 -401 u=999 lat=1 fill=0:253 0:126 0:221
     140 140 140 140 140 140 140 140 140 140 140 140 140 140 140 140 140
     140 140 140 140 140 140 140 140 140 140 140 140 140 140 140 140 140
     140 140 140 140 140 140 140 140 140 140 140 140 140 140 140 140 140
     .
     .
     .
```

Listing B.9: varian_mlc.geo

```
c ******************************************************************************
c GEOMETRY CARDS FOR MLC IN 18 MV ACCELERATOR MODEL
c ******************************************************************************
c These surfaces define one MLC leaf the remaining MLCs will be defined
c by the cel transformation card.
c
c By Bryan Bednarz and Bin Han
c
c MLC 1 surfaces
c Segment # 1
201 py 0.1558
202 py -0.1558
203 pz 47.3
204 pz 47.6
c Segment # 2
205 p 0 0 0 0 0.2371 47.6 5 0.2371 47.6
206 p 0 0 0 0 -0.2371 47.6 5 -0.2371 47.6
207 pz 48.9
c 204 pz 47.6
c Segment # 3
208 p 0 0 0 0 0.1788 48.9 5 0.1788 48.9
c 206
209 pz 49.1
c 207 pz 48.9
c Segment # 4
210 p 0 0 0 0 -0.304 49.1 5 -0.304 49.1
c 208
211 pz 51.6
c 209 pz 49.1
c Segment # 5
c 208
c 206
212 pz 51.8
c 211
c Segment # 6
c 205
c 206
213 pz 53.1
c 212
```

```
c Segment # 7
c 201
c 202
214 pz 53.4
c 213
218 c/y 8.0 50.3 7.99
219 px 16.7
220 px 8.67
c MLC 2 surface
222 c/y -8.0 50.3 7.99
223 px -16.7
224 px -8.67
c Carrier
c 221 RPP 0 70 -70 70 45.5 55.5
c 225 RPP -70 0 -70 70 45.5 55.5
231 py 0
232 p 0 0 0 0 -0.06 49.1 5 -0.06 49.1
233 py -70
234 py 70
235 pz 45.5
236 pz 55.5
237 px 0
238 px 70
239 px -70
240 pz 51.61
```

Listing B.10: varian_clin_18b.geo

```
c ******************************************************************************
c GEOMETRY CARDS FOR 18 MV ACCELERATOR MODEL
c ******************************************************************************
c GEOMETRY CARDS
c 11 so 1000.0
11 RCC 0.0 0.0 -70 0.0 0.0 270 200
c 11 RPP -75.0 75.0 -75.0 75.0 -50.0 75.0
12 RPP -70.0 70.0 -70.0 70.0 -70.0 45.5
13 RCC 0.0 0.0 0.0 0.0 0.0 0.0635 0.301
14 RCC 0.0 0.0 0.0635 0.0 0.0 1.016 0.301
15 RCC 0.0 0.0 -0.254 0.0 0.0 1.524 0.889
16 RCC 0.0 0.0 -0.254 0.0 0.0 1.524 0.301
17 RPP -4.445 4.445 -6.349 4.826 -2.54 4.445
18 RCC 0.0 -8.89 0.508 0.0 2.541 0.0 2.54
c 19 RCC 0.0 -8.89 0.508 0.0 12.448 0.0 1.27
19 RPP -1.6 1.6 -8.89 3.558 -1.2 1.6
20 RCC 0.0 0.0 -2.54 0.0 0.0 6.984 3.557
21 RPP -4.445 4.445 -6.349 8.509 4.445 7.8
22 RCC 0.0 -8.89 6.19 0.0 2.541 0.0 1.5
23 RCC 0.0 -8.89 6.19 0.0 17.399 0.0 0.4445
c 24 TRC 0.0 0.0 7.8 0.0 0.0 -6.2 1.945 0.400
24 TRC 0.0 0.0 7.8 0.0 0.0 -6.2 2.1319 0.6010
25 RCC 0.0 0.0 4.445 0.0 0.0 3.355 2.54
26 RCC 0.0 0.0 -2.54 0.0 0.0 1.77 0.302
701 RCC 0.0 0.0 12.444 0.0 0.0 -0.2383 3.5535
702 TRC 0.0 0.0 12.2057 0.0 0.0 -2.1945 2.750 0.850
703 TRC 0.0 0.0 12.2057 0.0 0.0 -1.0952 1.0952 0.002
27 TRC 0.0 0.0 10.0112 0.0 0.0 -1.036 0.762 0.002
28 TRC 0.0 0.0 12.444 0.0 0.0 -0.2383 1.3335 1.0952
29 RCC 0.0 0.0 12.444 0.0 0.0 0.2036 3.554
30 TRC 0.0 0.0 12.6476 0.0 0.0 0.6716 2.39 1.427
31 RPP -7.04 -4.445 -6.349 -0.635 -2.54 7.9385
32 RPP 4.5 7.04 -6.349 -0.635 -2.54 7.9385
33 RCC -3.81 8.65 -2.54 7.62 0.0 0.0 4.445
34 RCC -3.81 8.65 -2.54 7.62 0.0 0.0 12.70
35 RCC -10.15 8.65 -2.54 20.3 0.0 0.0 12.70
36 WED -3.81 -3.3 -6.86 0.0 5.967 -16.762 0.0 11.95 4.32 7.62 0.0 0.0
```

```
37 WED -3.81 12.8 -14.55 0.0 17.02 5.881 0.0 -4.15 12.01 7.62 0.0 0.0
38 WED -3.81 20.82 1.27 0.0 -6.096 17.02 0.0 -12.17 -4.36 7.62 0.0 0.0
39 RPP -10.15 10.15 1.26 8.65 7.8 10.638
40 RPP -10.159 10.159 -15.494 -7.240 -19.812 -5.207
41 WED -10.159 -7.240 -19.812 0.0 7.239 0.0
       0.0 0.0 14.605 20.318 0.0 0.0
42 RPP -20.32 20.32 25.147 40.386 2.287 9.906
43 WED -20.32 25.146 2.287 0.0 0.0 -10.16
       0.0 15.24 0.0 40.64 0.0 0.0
44 RPP -3.81 3.81 -7.62 -4.32 -5.08 -2.55
45 RPP -20.32 -10.16 -15.494 7.366 -19.812 -2.032
46 RPP 10.16 20.32 -15.494 7.366 -19.812 -2.032
47 RPP -20.32 -10.16 7.366 25.146 -19.182 9.906
48 RPP 10.16 20.32 7.366 25.146 -19.812 9.906
49 WED 10.16 -15.494 -2.023 0.0 0.0 3.547
      10.16 0.0 0.0 0.0 22.86 0.0
50 WED -10.16 -15.494 -2.023 -10.16 0.0 0.0
       0.0 0.0 3.547 0.0 22.86 0.0
51 RPP -20.32 20.32 -15.494 0.0 -23.622 -19.820
52 RPP -20.32 20.32 0.0 25.147 -26.162 -19.820
53 RPP -20.32 20.32 25.146 27.686 -26.162 -11.67
54 RPP -20.32 20.32 25.146 44.196 -11.67 -7.873
55 RPP -20.32 20.32 40.386 44.196 -7.87 14.224
56 RPP -7.62 7.62 33.34 46.040 14.225 19.68
57 RPP -3.81 3.81 -7.112 -4.572 11.174 13.714
58 RPP -3.81 3.81 5.08 22.86 11.174 13.714
59 RCC 0.0 0.0 11.174 0.0 0.0 2.54 12.7
60 RCC 0.0 0.0 11.174 0.0 0.0 2.54 15.24
61 RCC 0.0 0.0 16.510 0.0 0.0 1.90 11.43
62 RCC 0.0 0.0 16.510 0.0 0.0 1.90 20.955
63 RCC 0.0 0.0 18.414 0.0 0.0 3.81 10.16
64 RCC 0.0 0.0 18.414 0.0 0.0 3.81 20.955
65 RCC 0.0 0.0 22.230 0.0 0.0 5.075 7.62
66 RCC 0.0 0.0 22.230 0.0 0.0 5.075 20.955
67 1 RPP -9.398 9.398 -11.938 0 28.067 35.867
68 2 RPP -9.398 9.398 0 11.938 28.067 35.867
69 3 RPP -11.938 0 -10.795 10.795 36.703 44.503
70 4 RPP 0 11.938 -10.795 10.795 36.703 44.503
71 RCC 0.0 0.0 19.68 0.0 0.0 7.625 28.26
72 RCC 0.0 0.0 19.68 0.0 0.0 7.625 33.34
73 RCC 0.0 0.0 27.31 0.0 0.0 6.35 28.26
74 RCC 0.0 0.0 27.31 0.0 0.0 6.35 29.53
75 RCC 0.0 0.0 14.0 0.0 0.0 5.68 21.5
76 RCC 0.0 0.0 14.0 0.0 0.0 5.68 25.945
77 RPP -24.394 -20.33 -25.654 32.38 -12.7 8.89
78 RPP 20.33 24.394 -25.654 32.38 -12.7 8.89
79 RPP -10.15 -4.445 -4.06 8.65 -2.54 10.638
80 RPP 4.445 10.15 -4.06 8.65 -2.54 10.638
81 RCC -0.3 8.65 -2.54 0.6 0.0 0.0 8.43
82 RCC -0.3 8.65 -2.54 0.6 0.0 0.0 9.03
83 RCC 0.0 -50.0 6.19 0.0 40.0 0.0 0.5
84 RCC 0.0 -50.0 6.19 0.0 40.0 0.0 1.0
89 RPP -24.40 24.40 28.26 33.33 14.225 19.68
90 RPP -29.49 -24.41 -25.654 44.20 6.985 14.0
91 RPP 24.41 29.49 -25.654 44.20 6.985 14.0
92 RPP -28.175 -25.0 -13.97 13.97 35.0 43.16
93 RPP 25.0 28.175 -13.97 13.97 35.0 43.16
94 CZ 22.86
95 CZ 60.96
96 PZ 43.32 $ originally 45.32
97 PZ 45.225 $ originally 47.225
c water phantom
c 800 rpp -70 70 -70 70 100 135
c vacuum window
811 rcc 0 0 8.66 0 0 0.00254 2.87
```

```
c ion chamber
812 pz 14.89
813 pz 14.8905
814 pz 14.8955
815 pz 15.22
816 pz 15.225
817 pz 15.2255
818 pz 15.33
819 pz 15.3305
820 pz 15.3355
821 pz 15.71
822 pz 15.715
823 pz 15.7155
824 pz 16.1
825 pz 16.105
826 pz 16.1055
827 pz 16.22
828 pz 16.2205
829 pz 16.2255
830 pz 16.54
831 pz 16.545
832 pz 16.5455
833 cz 4.9
c mirror
834 6 rcc 0 0 0 0 0 0.00508 4.9
```

The particle source of the MC simulation consists of electrons impinging on the tungsten-target. Detailed specifications of the source are summarized in the file **sdef_18pt5_MeV.src** of listing B.11. In subsection 5.2.1 about the in-field validation of the LINAC-model a mean electron energy of 18.5 MeV has been derived. The corresponding gaussian electron energy spectrum is part of the source specification.

Listing B.11: sdef_18pt5_MeV.src

```
sdef erg=d4 dir=1 vec=0 0 1 X=d1 Y=d2 Z=-0.25 par=3
sp1 -41 0.10 0
sp2 -41 0.10 0
#     si4   sp4
       l    d
      17.70   0.01
      17.71   0.01
      17.72   0.01
      17.73   0.01
      17.74   0.01
      17.75   0.01
      17.76   0.01
      17.77   0.01
      17.78   0.02
      17.79   0.02
      17.80   0.02
      17.81   0.02
      17.82   0.03
      17.83   0.03
      17.84   0.03
      17.85   0.04
      17.86   0.04
      17.87   0.05
      17.88   0.05
      17.89   0.06
      17.90   0.07
      17.91   0.07
      17.92   0.08
```

```
17.93   0.09
17.94   0.10
17.95   0.11
17.96   0.12
17.97   0.14
17.98   0.15
17.99   0.16
18      0.18
18.01   0.19
18.02   0.21
18.03   0.23
18.04   0.25
18.05   0.27
18.06   0.30
18.07   0.32
18.08   0.35
18.09   0.37
18.10   0.40
18.11   0.43
18.12   0.46
18.13   0.49
18.14   0.53
18.15   0.56
18.16   0.60
18.17   0.64
18.18   0.67
18.19   0.71
18.20   0.75
18.21   0.79
18.22   0.84
18.23   0.88
18.24   0.92
18.25   0.96
18.26   1.01
18.27   1.05
18.28   1.09
18.29   1.14
18.3    1.18
18.31   1.22
18.32   1.26
18.33   1.30
18.34   1.34
18.35   1.38
18.36   1.42
18.37   1.45
18.38   1.49
18.39   1.52
18.40   1.55
18.41   1.57
18.42   1.60
18.43   1.62
18.44   1.64
18.45   1.66
18.46   1.67
18.47   1.68
18.48   1.69
18.49   1.69
18.50   1.69
18.51   1.69
18.52   1.69
18.53   1.68
18.54   1.67
18.55   1.66
18.56   1.64
18.57   1.62
```

```
18.58   1.60
18.59   1.57
18.60   1.55
18.61   1.52
18.62   1.49
18.63   1.45
18.64   1.42
18.65   1.38
18.66   1.34
18.67   1.30
18.68   1.26
18.69   1.22
18.70   1.18
18.71   1.14
18.72   1.09
18.73   1.05
18.74   1.01
18.75   0.96
18.76   0.92
18.77   0.88
18.78   0.84
18.79   0.79
18.80   0.75
18.81   0.71
18.82   0.67
18.83   0.64
18.84   0.60
18.85   0.56
18.86   0.53
18.87   0.49
18.88   0.46
18.89   0.43
18.90   0.40
18.91   0.37
18.92   0.35
18.93   0.32
18.94   0.30
18.95   0.27
18.96   0.25
18.97   0.23
18.98   0.21
18.99   0.19
19      0.18
19.01   0.16
19.02   0.15
19.03   0.14
19.04   0.12
19.05   0.11
19.06   0.10
19.07   0.09
19.08   0.08
19.09   0.07
19.10   0.07
19.11   0.06
19.12   0.05
19.13   0.05
19.14   0.04
19.15   0.04
19.16   0.03
19.17   0.03
19.18   0.03
19.19   0.02
19.20   0.02
19.21   0.02
19.22   0.02
```

```
     19.23   0.01
     19.24   0.01
     19.25   0.01
     19.26   0.01
     19.27   0.01
     19.28   0.01
     19.29   0.01
     19.30   0.01
```

Listing B.12: varian_jaws_0deg.tr

```
c 7 x 9.54
*TR1 0 0 0 0.000 90.000 90.000 90.000 2.270 87.730 90.000 92.270 2.270
*TR2 0 0 0 0.000 90.000 90.000 90.000 2.270 92.270 90.000 87.730 2.270
*TR3 0 0 0 3.092 90.000 86.908 90.000 0.000 90.000 93.092 90.000 3.092
*TR4 0 0 0 3.092 90.000 93.092 90.000 0.000 90.000 86.908 90.000 3.092
```

Listing B.13: varian_jaws_90deg.tr

```
c 7 x 7.96
 *TR1  0 0 0 0.000 90.000 90.000 90.000 2.369 87.631 90.000 92.369 2.369
 *TR2  0 0 0 0.000 90.000 90.000 90.000 2.369 92.369 90.000 87.631 2.369
 *TR3  0 0 0 2.693 90.000 87.307 90.000 0.000 90.000 92.693 90.000 2.693
 *TR4  0 0 0 2.693 90.000 92.693 90.000 0.000 90.000 87.307 90.000 2.693
```

Listing B.14: varian_jaws_180deg.tr

```
c 7 x 9.96
 *TR1 0 0 0 0.000 90.000 90.000 90.000 2.188 87.812 90.000 92.188 2.188
 *TR2 0 0 0 0.000 90.000 90.000 90.000 2.369 92.369 90.000 87.631 2.369
 *TR3 0 0 0 3.111 90.000 86.889 90.000 0.000 90.000 93.111 90.000 3.111
 *TR4 0 0 0 3.111 90.000 93.111 90.000 0.000 90.000 86.889 90.000 3.111
```

Listing B.15: varian_jaws_270deg.tr

```
c 7 x 7.64
 *TR1 0 0 0 0.000 90.000 90.000 90.000 2.404 87.596 90.000 92.404 2.404
 *TR2 0 0 0 0.000 90.000 90.000 90.000 2.404 92.404 90.000 87.596 2.404
 *TR3 0 0 0 2.624 90.000 87.376 90.000 0.000 90.000 92.624 90.000 2.624
 *TR4 0 0 0 2.624 90.000 92.624 90.000 0.000 90.000 87.376 90.000 2.624
```

Listing B.16: varian_clin_18p.mtl

```
c ******************************************************************************
c MATERIAL CARDS FOR 18 MV ACCELERATOR MODEL (PHOTONS)
c ******************************************************************************
m91 74000 -1.0
m92 29000 -1.0
m93 26000 -1.0
m94 73000 -1.0
m95 82000 -1.0
m96 1000 2
     8000 1
c AIR
m97 6000 -0.0001
      7014 -0.7553
      8016 -0.2318
     18000 -0.0128
c Beryllium
m100  4000 -1.0
c KAPTON C22H10N2O5
m101  6000 22
```

```
      1000 10
      7000 2
      8000 5
c MYLAR  C10H8O4
m102  6000 10
      1000 8
      8000 4
c XXXXXXXXXXXXXXXXXXXXXXXXXXXXXXXXXXXXXXXXXXXXXXXXXXXXXXXXXXXXXXXXXXXXXXXXXXXXXXXX
```

Listing B.17: AM_materials

```
m1    1000 -2.2  6000 -9.5  7000 -2.9  8000 -42.1  12000 -0.7
      15000 -13.7    20000 -28.9
m2    1000 -3.6  6000 -15.9  7000 -4.2  8000 -44.8 11000 -0.3 12000 -0.2
      15000 -9.4 16000 -0.3   20000 -21.3
m3    1000 -8.5  6000 -28.8  7000 -2.6  8000 -49.8 11000 -0.2 12000 -0.1
      15000 -3.3 16000 -0.4 17000 -0.2  20000 -6.1
m4    1000 -9.7  6000 -43.9  7000 -1.7  8000 -38.1 11000 -0.2
      15000 -2.1 16000 -0.3 17000 -0.1  20000 -3.9
m5    1000 -9.7  6000 -43.9  7000 -1.7  8000 -38.1 11000 -0.2
      15000 -2.1 16000 -0.3 17000 -0.1  20000 -3.9
m6    1000 -9.7  6000 -43.9  7000 -1.7  8000 -38.1 11000 -0.2
      15000 -2.1 16000 -0.3 17000 -0.1  20000 -3.9
m7    1000 -9.1  6000 -34.8  7000 -2.4  8000 -45.7 11000 -0.2
      15000 -2.6 16000 -0.3 17000 -0.1  20000 -4.8
m8    1000 -9.0  6000 -33.5  7000 -2.5  8000 -46.7 11000 -0.2
      15000 -2.6 16000 -0.3 17000 -0.2 19000 -0.1 20000 -4.9
m9    1000 -9.4  6000 -38.5  7000 -2.2  8000 -43.0 11000 -0.2
      15000 -2.2 16000 -0.3 17000 -0.1  20000 -4.1
m10    1000 -9.7  6000 -43.9  7000 -1.7  8000 -38.1 11000 -0.2
      15000 -2.1 16000 -0.3 17000 -0.1  20000 -3.9
m11    1000 -9.7  6000 -43.9  7000 -1.7  8000 -38.1 11000 -0.2
      15000 -2.1 16000 -0.3 17000 -0.1  20000 -3.9
m12    1000 -9.7  6000 -43.9  7000 -1.7  8000 -38.1 11000 -0.2
      15000 -2.1 16000 -0.3 17000 -0.1  20000 -3.9
m13    1000 -8.3  6000 -26.6  7000 -2.7  8000 -51.1 11000 -0.3 12000 -0.1
      15000 -3.6 16000 -0.4 17000 -0.2  20000 -6.7
m14    1000 -9.4  6000 -36.0  7000 -2.5  8000 -45.4 11000 -0.2
      15000 -2.1 16000 -0.3 17000 -0.2 19000 -0.1 20000 -3.8
m15    1000 -8.9  6000 -29.2  7000 -2.9  8000 -50.7 11000 -0.2
      15000 -2.6 16000 -0.4 17000 -0.2 19000 -0.1 20000 -4.8
m16    1000 -8.7  6000 -30.9  7000 -2.6  8000 -48.3 11000 -0.2 12000 -0.1
      15000 -3.0 16000 -0.4 17000 -0.2  20000 -5.6
m17    1000 -10.3  6000 -40.0  7000 -2.7  8000 -44.4 11000 -0.1
      15000 -0.7 16000 -0.2 17000 -0.2 19000 -0.1 20000 -1.2 26000 -0.1
m18    1000 -9.9  6000 -37.6  7000 -2.7  8000 -45.9 11000 -0.1
      15000 -1.2 16000 -0.2 17000 -0.2 19000 -0.1 20000 -2.0 26000 -0.1
m19    1000 -9.5  6000 -34.0  7000 -2.8  8000 -48.0 11000 -0.1
      15000 -1.8 16000 -0.3 17000 -0.2 19000 -0.1 20000 -3.2
m20    1000 -10.5  6000 -41.9  7000 -2.7  8000 -43.2 11000 -0.1
      15000 -0.4 16000 -0.2 17000 -0.2 19000 -0.1 20000 -0.6 26000 -0.1
m21    1000 -10.4  6000 -40.9  7000 -2.7  8000 -43.8 11000 -0.1
      15000 -0.6 16000 -0.2 17000 -0.2 19000 -0.1 20000 -0.9 26000 -0.1
m22    1000 -11.5  6000 -63.6  7000 -0.7  8000 -23.9 11000 -0.1
       16000 -0.1 17000 -0.1
m23    1000 -11.5  6000 -63.6  7000 -0.7  8000 -23.9 11000 -0.1
       16000 -0.1 17000 -0.1
m24    1000 -11.5  6000 -63.6  7000 -0.7  8000 -23.9 11000 -0.1
       16000 -0.1 17000 -0.1
m25    1000 -11.5  6000 -63.6  7000 -0.7  8000 -23.9 11000 -0.1
       16000 -0.1 17000 -0.1
m26    1000 -9.6  6000 -9.9  7000 -2.2  8000 -74.4 11000 -0.5
      15000 -2.2 16000 -0.9 17000 -0.3
m27    1000 -10.0  6000 -19.9  7000 -4.2  8000 -65.0 11000 -0.2
      15000 -0.1 16000 -0.2 17000 -0.3 19000 -0.1
```

```
m28    1000 -10.2  6000 -11.0  7000 -3.3  8000 -74.5 11000 -0.1
      15000 -0.1 16000 -0.2 17000 -0.3 19000 -0.2  26000 -0.1
m29    1000 -10.2  6000 -14.2  7000 -3.4  8000 -71.1 11000 -0.1
      15000 -0.2 16000 -0.3 17000 -0.1 19000 -0.4
m30    1000 -10.2  6000 -13.0  7000 -3.1  8000 -72.5 11000 -0.2
      15000 -0.2 16000 -0.3 17000 -0.2 19000 -0.3
m31    1000 -10.5  6000 -15.5  7000 -2.5  8000 -70.6 11000 -0.2
      15000 -0.2 16000 -0.1 17000 -0.2 19000 -0.2
m32    1000 -10.7  6000 -14.3  7000 -2.3  8000 -71.3 11000 -0.2
      15000 -0.4 16000 -0.2 17000 -0.3 19000 -0.3
m33    1000 -10.4  6000 -13.8  7000 -2.9  8000 -71.9 11000 -0.1
      15000 -0.2 16000 -0.2 17000 -0.2 19000 -0.3
m34    1000 -9.7  6000 -18.1  7000 -5.3  8000 -66.3 11000 -0.1
      15000 -0.1 16000 -0.3 17000 -0.1
m35    1000 -10.3  6000 -12.4  7000 -3.1  8000 -73.1 11000 -0.2
      15000 -0.2 16000 -0.2 17000 -0.2 19000 -0.2 20000 -0.1
m36    1000 -10.5  6000 -11.4  7000 -2.5  8000 -75.0 11000 -0.1
      15000 -0.1 16000 -0.1 17000 -0.2 19000 -0.1
m37    1000 -10.5  6000 -11.3  7000 -2.6  8000 -75.0 11000 -0.1
      15000 -0.1 16000 -0.1 17000 -0.2 19000 -0.1
m38    1000 -10.5  6000 -11.3  7000 -2.6  8000 -75.0 11000 -0.1
      15000 -0.1 16000 -0.1 17000 -0.2 19000 -0.1
m39    1000 -10.2  6000 -11.1  7000 -3.3  8000 -74.3 11000 -0.1
      15000 -0.2 16000 -0.2 17000 -0.3 19000 -0.2  26000 -0.1
m40    1000 -10.4  6000 -11.7  7000 -2.6  8000 -74.5 11000 -0.2
      15000 -0.1 16000 -0.1 17000 -0.2 19000 -0.1
      53000 -0.1
m41    1000 -10.5  6000 -9.6  7000 -2.6  8000 -76.1 11000 -0.2
      15000 -0.2 16000 -0.2 17000 -0.3 19000 -0.3
m42    1000 -10.6  6000 -10.0  7000 -2.1  8000 -76.4 11000 -0.2
      15000 -0.1 16000 -0.2 17000 -0.2 19000 -0.2
m43    1000 -10.4  6000 -22.1  7000 -2.8  8000 -63.7 11000 -0.1
      15000 -0.2 16000 -0.3 17000 -0.2 19000 -0.2
m44    1000 -10.4  6000 -21.3  7000 -2.9  8000 -64.4 11000 -0.1
      15000 -0.2 16000 -0.3 17000 -0.2 19000 -0.2
m45    1000 -10.4  6000 -23.1  7000 -2.8  8000 -62.7 11000 -0.1
      15000 -0.2 16000 -0.3 17000 -0.2 19000 -0.2
m46    1000 -10.4  6000 -23.1  7000 -2.8  8000 -62.7 11000 -0.1
      15000 -0.2 16000 -0.3 17000 -0.2 19000 -0.2
m47    1000 -10.8  6000 -4.2  7000 -1.1  8000 -83.1 11000 -0.3
       16000 -0.1 17000 -0.4
m48    1000 -11.2  6000 -51.6  7000 -1.1  8000 -35.8 11000 -0.1
       16000 -0.1 17000 -0.1
m49    1000 -11.4  6000 -58.8  7000 -0.8  8000 -28.7 11000 -0.1
       16000 -0.1 17000 -0.1
m50    1000 -10.3  6000 -10.7  7000 -3.2  8000 -74.6 11000 -0.2
      15000 -0.2 16000 -0.3 17000 -0.3 19000 -0.2
m51    1000 -10.0  6000 -22.2  7000 -2.2  8000 -64.4 11000 -0.1
      15000 -0.2 16000 -0.3 17000 -0.1 19000 -0.4 20000 -0.1
m52    1000 -10.7  6000 -0.3  7000 -1.0  8000 -87.3 11000 -0.4
      15000 -0.1   19000 -0.2
m53       7000 -80.0  8000 -20.0
```

The file **photon_dose.tal** in B.18 contains the electron energy deposition tally scoring the dose throughout the entire phantom body. For the calculation of the doses information about the mass of each of the voxels is required. However, in repeated structures like the present tissue matrix of the phantom MCNPX does not calculate the masses automatically. In the present case, the voxel masses could be calculated from the volume of the voxels given by the voxel-dimensions in line 23 of the main input file B.1 and the densities in the organ material specifications of listing B.17. Instead, the mass data have to be provided manually via a SD-card indicating the corresponding value for each single voxel. In order to avoid this complication for the tally specification an uniform density of $1.0\,\mathrm{g/cm^3}$ for all voxels has been assumed. This leads to a mass

of $0.2137\,\mathrm{cm} \cdot 0.2137\,\mathrm{cm} \cdot 0.8\,\mathrm{cm} \cdot 1.0\,\mathrm{g/cm^3} = 0.036534152\,\mathrm{g}$ per voxel indicated in the SD-card of the tally. The calculated dose values where then scaled in a post-processing step using the tissue densities of the organs.

Listing B.18: photon_dose.tal

```
F6:e (1016 < 1016[0:253 0:126 0:221] < 403)
c 0.2137 x 0.2137 x 0.8 =  0.03653415 cc
SD6 0.036534152 7161275r
```

Listing B.19: photon_organ_dose.tal

```
c CAUTION:
c all tally results have to be divided by corresponding tissue densities to get dose!
c
c Organs and tissues of the adult male reference computational phantom
c Organ Organ                                          Tissue Density
c ID                                                   number
f16:e 100 101 102 103 104 105 T  $ Lymphatic nodes        47    1.030
f26:e 110  $ Oesophagus                                       44    1.030
f36:e 113  $ Pancreas                                         31    1.050
f46:e 115  $ Prostate                                         46    1.030
f56:e 122 123 124 125 T $ Skin                             27    1.090
f66:e 126  $ Spinal cord                                      45    1.030
f76:e 127  $ Spleen                                           39    1.040
f86:e 129 130 T $ Testis, left                                     42    1.040
f96:e 132  $ Thyroid                                          40    1.040
f106:e 137  $ Urinary bladder wall                             41    1.040
c REMAINDER (according to ICRP 60): adrenals, left/right, brain, small intestine, kidney
    , muscle, pancreas, spleen, thymus, extrathoracic airways (ET1,ET2)
c missing: uterus
c caution: weighting according to different density of the tissues is missing here!
f116:e 1 2 61 74 89 90 91 92 93 94 106 107 108 109 113 127 131 3 4 T
c caution: weighting according to RBM fractions of the tissues is missing here!
f146:e 14 25 27 29 40 42 44 46 48 50 52 54 56 T $ (active) RBM, tissue numbers
    3,7-9,13-21 see AM_spongiosa.dat
f156:e 14 25 27    40 42 44 46 48 50 52 54 56 T $ (active) RBM, tissue numbers
    3,7-9,13-21 see AM_spongiosa.dat, w/o Femora, upper half, spongiosa
f616:e  61   $ Brain                                          32    1.050
f626:e  62 63 T  $ Breast,  adipose tissue                    49    0.950
f706:e  70   $ Gall bladder wall                             45    1.030
f726:e  72   $ Stomach wall                                  36    1.040
f746:e  74   $ Small intestine wall                          37    1.040
f766:e  76 78 80 82 84 T  $  colon wall                            38    1.040
f866:e  86   $ Rectum wall                                   38    1.040
f876:e  87   $ Heart wall                                    33    1.050
f896:e  89 90 91 92 93 94 T  $ Kidney                        35    1.050
f956:e  95   $ Liver                                         30    1.050
f976:e  97 99 T $ Lung, left, tissue                            50    0.382
```

B.2 MCNPX Input Files for Photoneutron Dose Calculations

The geometry in the MC-model for photoneutron dose calculations is the same as the one for photon dose calculations. Therefore, all cell and surface cards in **linac_icrp_am_p_main.inp** including the corresponding auxiliary files for both, the LINAC and the voxel phantom, are also used in the MCNPX input **linac_icrp_am_pn_main.inp** for the calculation of photoneutron doses. Also the electron spectrum, defined in B.11, and the transformations for the LINAC-jaws and the phantoms remain unchanged. Differences in the simulation input arise from the special material definitions, **varian_clin_18pn.mtl** (listing B.21) and **AM_materials_pn** (listing B.22), needed for the treatment of photonuclear interactions and the radiation transport of neutrons. Also the tallies were adjusted for the scoring of neutron dose equivalent or organ-averaged equivalent doses, respectively. The VRTs specially tailored for photoneutron dose calculations and discussed in section 5.5.3 are defined in lines 38-44 and 71-72 of **linac_icrp_am_pn_main.inp**.

Listing B.20: linac_icrp_am_pn_main.inp

```
1  Dose Calculation - Varian Clinac 2100C - 18 MV
2  c XXXXXXXXXXXXXXXXXXXXXXXXXXXXXXXXXXXXXXXXXXXXXXXXXXXXXXXXXXXXXXXXXXXXXXXXXXXXXXXXXXXXXXXXXXXXXXXXXXXXXXX
3  c MAIN INPUT DECK
4  c Medical Linear Accelerator Model Varian Clinac 2100C - 18 MV
5  c ICRP adult male phantom
6  c Photoneutron dose calculations
7  c ********************************************************************************
8  c ************************ CELL CARDS ********************************************
9  c ********************************************************************************
10 read file=varian_mlc_0deg.cel noecho
11 c read file=varian_mlc_90deg.cel noecho
12 c read file=varian_mlc_180deg.cel noecho
13 c read file=varian_mlc_270deg.cel noecho
14 read file=varian_clin_18b.cel noecho
15 403 0 -403 fill=999 (5)
16 read file=AM_organs noecho
17 read file=AM_matrix noecho
18 999 0 11
19
20 c ********************************************************************************
21 c ************************ SURFACE CARDS *****************************************
22 c ********************************************************************************
23 401   rpp   0 .2137   0 .2137   0 .8
24 402   so  70
25 403 5  rpp 0.0001 54.2797 0.0001 27.1398 0.0001 175.9999
26 read file=varian_mlc.geo noecho
27 read file=varian_clin_18.geo noecho
28
29 c ********************************************************************************
30 c ************************ DATA CARDS ********************************************
31 c ********************************************************************************
32 mode p e n
33 imp:p 1 333r 0
34 imp:e 1 333r 0
35 imp:n 1 333r 0
36 read file=sdef_18pt5_MeV.src noecho
37 DBCN 17j 1
38 BBREM 1. 1. 46I 10. 91 92   $ 91, 92 materials of target
39 cut:e j 1.67   $ photonuclear threshold for Be
40 cut:p j 1.67   $ photonuclear threshold for Be
41 cut:n j 1.0e-6
42 phys:e 23.1 j j j j 10
43 phys:p 23.1 2j 1
44 fcl:p 0 101r 1 4r 0 227r
45 c ********************** TRANSFORMATIONS ***************************************
```

```
c jaws transformation
read file=varian_jaws_0deg.tr noecho
c read file=varian_jaws_90deg.tr noecho
c read file=varian_jaws_180deg.tr noecho
c read file=varian_jaws_270deg.tr noecho
c ******************************************************************************
c phantom transformation
c         o1 o2 o3 xx` yx` zx` xy` yy` zy` xz` yz` zz`
 *TR5 -26.39 90.5  84.43   0 90  90  90 90   0 90 180 90    $ 0deg
c *TR5 -15.57 90.5 126.14  90 90 180   0 90  90 90 180 90    $ 90deg
c *TR5  26.39 90.5 115.57 180 90  90  90 90 180 90 180 90    $ 180deg
c *TR5  15.57 90.5  73.86  90 90   0 180 90  90 90 180 90    $ 270deg
c TR5 0 0 0 1 0 0 0 1 0 0 0 1
c ******************************************************************************
c mirror angle of 35deg
 *TR6 0 0 21.63 35 90 125 90 0 90 55 90 35
c ********************** MATERIALS ********************************************
read file=varian_clin_18n_c.mtl noecho
read file=AM_materials_pn noecho
c ********************** TALLIES **********************************************
read file=neutron_dose_equivalent4b.tal
c ******************************************************************************
PRDMP j 1e6 1 2
TALNP
c print -126 -128 -85 -140 -130
wwp:p 4j -1 3j 1
wwp:n 4j -1
nps 2e7
```

Listing B.21: varian_clin_18pn.mtl

```
c ******************************************************************************
c MATERIAL CARDS FOR 18 MV ACCELERATOR MODEL (PHOTONEUTRON DOSE CALCULATIONS)
c ******************************************************************************
m91      74180 -0.120
     74182 -26.500
     74183 -14.310
     74184 -30.640
     74186 -28.430 pnlib=.70u
mx91:n model 4j
m92      29063 -69.170
     29065 -30.830 pnlib=.70u
m93      26054 -5.850
     26056 -91.750
     26057 -2.120
     26058 -0.280 pnlib=.70u
m94      73181 -100.000 pnlib=.70u
m95      82204 -1.400
     82206 -24.100
     82207 -22.100
     82208 -52.400 pnlib=.70u
mx95:n model 3j
mx95:p 0 j j j     $  no data available for 82204 (janis)
m96      1001 2
      8016 0.99762
      8017 0.00038
      8018 0.002 pnlib=.70u
mx96:n  j j j 8017
mx96:p  0 j j j
c Luft
c der massenanteil an kohlenstoffdioxid in der luft beträgt ca. 0.058 %
c 0.058% x 6 : 22(=6+8+8) =0.015818181 %
c die massenanteile sind absichtlich nicht auf 100% normiert
```

```
m97      6012 -0.015644181
     6013 -0.000174
     7014 -75.252
     7015 -0.278
     8016 -23.124
     8017 -0.009
     8018 -0.048
     18036 -0.004
     18038 -0.001
     18040 -1.275 pnlib=.70u
mx97:n j j j j j j 8017 17000 17000 17000
c Beryllium
m100  4009 1
c KAPTON C22H10N2O5
m101  6012 21.758
      6013 0.242
      1001 10
      7014 1.99268
      7015 0.00732
      8016 4.9881
      8017 0.0019
      8018 0.01
mx101:n j j j j j j j 8017
mx101:p j j 0 j j j j j
c MYLAR  C10H8O4
m102  6012 9.89
      6013 0.11
      1001 8
      8016 3.99048
      8017 0.00152
      8018 0.008
mx102:n j j j j j 8017
mx102:p j j 0 j j j
```

Listing B.22: AM_materials_pn

```
M1 1001 -2.1997470000000003 1002 -0.0002530000000000 6012 -9.3983499999999989
     6013 -0.1016500000000000 7014 -2.8894440000000001 7015
     -0.0105560000000000 8016 -41.9976970000000023 8017 -0.0159980000000000
     8018 -0.0863050000000000 12024 -0.5529300000000000 12025
     -0.0700000000000000 12026 -0.0770700000000000
MX1:N     2j 6000 6000 4j MODEL 12000 12000 12000
MX1:P     0 11j
M2 1001 -3.5995860000000000 1002 -0.0004140000000000 6012 -15.7298700000000000
     6013 -0.1701300000000000 7014 -4.1847120000000002 7015
     -0.0152880000000000 8016 -44.6911359999999931 8017 -0.0170240000000000
     8018 -0.0918400000000000 11023 -0.3000000000000000 12024
     -0.1579800000000000 12025 -0.0200000000000000 12026 -0.0220200000000000
MX2:N     2j 6000 6000 4j MODEL j 12000 12000 12000
MX2:P     0 12j
M3 1001 -8.4990225000000006 1002 -0.0009775000000000 6012 -28.4918399999999998
     6013 -0.3081600000000000 7014 -2.5905360000000002 7015
     -0.0094640000000000 8016 -49.6789859999999948 8017 -0.0189240000000000
     8018 -0.1020900000000000 11023 -0.2000000000000000 12024
     -0.0789900000000000 12025 -0.0100000000000000 12026 -0.0110100000000000
MX3:N     2j 6000 6000 4j MODEL j 12000 12000 12000
MX3:P     0 12j
M4 1001 -9.6988845000000001 1002 -0.0011155000000000 6012 -43.4302700000000002
     6013 -0.4697300000000000 7014 -1.6938120000000001 7015
     -0.0061880000000000 8016 -38.0074169999999967 8017 -0.0144780000000000
     8018 -0.0781050000000000 11023 -0.2000000000000000
MX4:N     2j 6000 6000 4j MODEL j
MX4:P     0 9j
M5 1001 -9.6988845000000001 1002 -0.0011155000000000 6012 -43.4302700000000002
     6013 -0.4697300000000000 7014 -1.6938120000000001 7015
```

```
     -0.0061880000000000 8016 -38.0074169999999967 8017 -0.0144780000000000
     8018 -0.0781050000000000 11023 -0.2000000000000000
MX5:N     2j 6000 6000 4j MODEL j
MX5:P     0 9j
M6 1001 -9.6988845000000001 1002 -0.0011155000000000 6012 -43.4302700000000002
     6013 -0.4697300000000000 7014 -1.6938120000000001 7015
     -0.0061880000000000 8016 -38.0074169999999967 8017 -0.0144780000000000
     8018 -0.0781050000000000 11023 -0.2000000000000000
MX6:N     2j 6000 6000 4j MODEL j
MX6:P     0 9j
M7 1001 -9.0989535000000004 1002 -0.0010465000000000 6012 -34.4276399999999967
     6013 -0.3723600000000000 7014 -2.3912640000000001 7015
     -0.0087360000000000 8016 -45.5889489999999995 8017 -0.0173660000000000
     8018 -0.0936850000000000 11023 -0.2000000000000000
MX7:N     2j 6000 6000 4j MODEL j
MX7:P     0 9j
M8 1001 -8.9989650000000001 1002 -0.0010350000000000 6012 -33.1415499999999952
     6013 -0.3584500000000000 7014 -2.4908999999999999 7015
     -0.0091000000000000 8016 -46.5865190000000027 8017 -0.0177460000000000
     8018 -0.0957350000000000 11023 -0.2000000000000000
MX8:N     2j 6000 6000 4j MODEL j
MX8:P     0 9j
M9 1001 -9.3989190000000011 1002 -0.0010810000000000 6012 -38.0880499999999955
     6013 -0.4119500000000000 7014 -2.1919920000000004 7015
     -0.0080080000000000 8016 -42.8955100000000016 8017 -0.0163400000000000
     8018 -0.0881500000000000 11023 -0.2000000000000000
MX9:N     2j 6000 6000 4j MODEL j
MX9:P     0 9j
M10 1001 -9.6988845000000001 1002 -0.0011155000000000 6012
     -43.4302700000000002 6013 -0.4697300000000000 7014 -1.6938120000000001
     7015 -0.0061880000000000 8016 -38.0074169999999967 8017
     -0.0144780000000000 8018 -0.0781050000000000 11023 -0.2000000000000000
MX10:N     2j 6000 6000 4j MODEL j
MX10:P     0 9j
M11 1001 -9.6988845000000001 1002 -0.0011155000000000 6012
     -43.4302700000000002 6013 -0.4697300000000000 7014 -1.6938120000000001
     7015 -0.0061880000000000 8016 -38.0074169999999967 8017
     -0.0144780000000000 8018 -0.0781050000000000 11023 -0.2000000000000000
MX11:N     2j 6000 6000 4j MODEL j
MX11:P     0 9j
M12 1001 -9.6988845000000001 1002 -0.0011155000000000 6012
     -43.4302700000000002 6013 -0.4697300000000000 7014 -1.6938120000000001
     7015 -0.0061880000000000 8016 -38.0074169999999967 8017
     -0.0144780000000000 8018 -0.0781050000000000 11023 -0.2000000000000000
MX12:N     2j 6000 6000 4j MODEL j
MX12:P     0 9j
M13 1001 -8.2990455000000001 1002 -0.0009545000000000 6012
     -26.3153800000000011 6013 -0.2846200000000000 7014 -2.6901720000000005
     7015 -0.0098280000000000 8016 -50.9758270000000024 8017
     -0.0194180000000000 8018 -0.1047550000000000 11023 -0.3000000000000000
     12024 -0.0789900000000000 12025 -0.0100000000000000 12026
     -0.0110100000000000
MX13:N     2j 6000 6000 4j MODEL j 12000 12000 12000
MX13:P     0 12j
M14 1001 -9.3989190000000011 1002 -0.0010810000000000 6012
     -35.6147999999999954 6013 -0.3852000000000000 7014 -2.4908999999999999
     7015 -0.0091000000000000 8016 -45.2896779999999950 8017
     -0.0172520000000000 8018 -0.0930700000000000 11023 -0.2000000000000000
MX14:N     2j 6000 6000 4j MODEL j
MX14:P     0 9j
M15 1001 -8.8989764999999998 1002 -0.0010235000000000 6012
     -28.8875599999999970 6013 -0.3124400000000000 7014 -2.8894440000000001
     7015 -0.0105560000000000 8016 -50.5767990000000012 8017
     -0.0192660000000000 8018 -0.1039350000000000 11023 -0.2000000000000000
MX15:N     2j 6000 6000 4j MODEL j
```

```
MX15:P     0 9j
M16 1001 -8.6989994999999993 1002 -0.0010005000000000 6012
     -30.5693699999999957 6013 -0.3306300000000000 7014 -2.5905360000000002
     7015 -0.0094640000000000 8016 -48.1826309999999935 8017
     -0.0183540000000000 8018 -0.0990150000000000 11023 -0.2000000000000000
     12024 -0.0789900000000000 12025 -0.0100000000000000 12026
     -0.0110100000000000
MX16:N     2j 6000 6000 4j MODEL j 12000 12000 12000
MX16:P     0 12j
M17 1001 -10.2988155000000017 1002 -0.0011845000000000 6012
     -39.5719999999999956 6013 -0.4280000000000000 7014 -2.6901720000000005
     7015 -0.0098280000000000 8016 -44.2921079999999989 8017
     -0.0168720000000000 8018 -0.0910200000000000 11023 -0.1000000000000000
MX17:N     2j 6000 6000 4j MODEL j
MX17:P     0 9j
M18 1001 -9.8988615000000006 1002 -0.0011385000000000 6012
     -37.1976799999999983 6013 -0.4023200000000000 7014 -2.6901720000000005
     7015 -0.0098280000000000 8016 -45.7884630000000001 8017
     -0.0174420000000000 8018 -0.0940950000000000 11023 -0.1000000000000000
MX18:N     2j 6000 6000 4j MODEL j
MX18:P     0 9j
M19 1001 -9.4989074999999996 1002 -0.0010925000000000 6012
     -33.6361999999999952 6013 -0.3638000000000000 7014 -2.7898079999999998
     7015 -0.0101920000000000 8016 -47.8833599999999961 8017
     -0.0182400000000000 8018 -0.0984000000000000 11023 -0.1000000000000000
MX19:N     2j 6000 6000 4j MODEL j
MX19:P     0 9j
M20 1001 -10.4987925000000004 1002 -0.0012075000000000 6012
     -41.4516700000000000 6013 -0.4483300000000000 7014 -2.6901720000000005
     7015 -0.0098280000000000 8016 -43.0950240000000022 8017
     -0.0164160000000000 8018 -0.0885600000000000 11023 -0.1000000000000000
MX20:N     2j 6000 6000 4j MODEL j
MX20:P     0 9j
M21 1001 -10.3988040000000002 1002 -0.0011960000000000 6012
     -40.4623699999999999 6013 -0.4376300000000000 7014 -2.6901720000000005
     7015 -0.0098280000000000 8016 -43.6935659999999970 8017
     -0.0166440000000000 8018 -0.0897900000000000 11023 -0.1000000000000000
MX21:N     2j 6000 6000 4j MODEL j
MX21:P     0 9j
M22 1001 -11.4986774999999994 1002 -0.0013225000000000 6012
     -62.9194800000000001 6013 -0.6805200000000000 7014 -0.6974520000000000
     7015 -0.0025480000000000 8016 -23.8419229999999978 8017
     -0.0090820000000000 8018 -0.0489950000000000 11023 -0.1000000000000000
MX22:N     2j 6000 6000 4j MODEL j
MX22:P     0 9j
MT22 poly.10t
M23 1001 -11.4986774999999994 1002 -0.0013225000000000 6012
     -62.9194800000000001 6013 -0.6805200000000000 7014 -0.6974520000000000
     7015 -0.0025480000000000 8016 -23.8419229999999978 8017
     -0.0090820000000000 8018 -0.0489950000000000 11023 -0.1000000000000000
MX23:N     2j 6000 6000 4j MODEL j
MX23:P     0 9j
MT23 poly.10t
M24 1001 -11.4986774999999994 1002 -0.0013225000000000 6012
     -62.9194800000000001 6013 -0.6805200000000000 7014 -0.6974520000000000
     7015 -0.0025480000000000 8016 -23.8419229999999978 8017
     -0.0090820000000000 8018 -0.0489950000000000 11023 -0.1000000000000000
MX24:N     2j 6000 6000 4j MODEL j
MX24:P     0 9j
MT24 poly.10t
M25 1001 -11.4986774999999994 1002 -0.0013225000000000 6012
     -62.9194800000000001 6013 -0.6805200000000000 7014 -0.6974520000000000
     7015 -0.0025480000000000 8016 -23.8419229999999978 8017
     -0.0090820000000000 8018 -0.0489950000000000 11023 -0.1000000000000000
MX25:N     2j 6000 6000 4j MODEL j
```

```
MX25:P     0 9j
MT25 poly.10t
M26 1001 -9.5988959999999999 1002 -0.0011040000000000 6012 -9.7940699999999996
     6013 -0.1059300000000000 7014 -2.1919920000000004 7015
     -0.0080080000000000 8016 -74.2192080000000090 8017 -0.0282720000000000
     8018 -0.1525200000000000 11023 -0.5000000000000000
MX26:N     2j 6000 6000 4j MODEL j
MX26:P     0 9j
MT26 lwtr.10t
M27 1001 -9.9988500000000009 1002 -0.0011500000000000 6012
     -19.6870699999999985 6013 -0.2129300000000000 7014 -4.1847120000000002
     7015 -0.0152880000000000 8016 -64.8420500000000004 8017
     -0.0247000000000000 8018 -0.1332500000000000 11023 -0.2000000000000000
MX27:N     2j 6000 6000 4j MODEL j
MX27:P     0 9j
MT27 lwtr.10t
M28 1001 -10.1988269999999996 1002 -0.0011730000000000 6012
     -10.8822999999999990 6013 -0.1177000000000000 7014 -3.2879879999999999
     7015 -0.0120120000000000 8016 -74.3189649999999915 8017
     -0.0283100000000000 8018 -0.1527250000000000 11023 -0.1000000000000000
MX28:N     2j 6000 6000 4j MODEL j
MX28:P     0 9j
MT28 lwtr.10t
M29 1001 -10.1988269999999996 1002 -0.0011730000000000 6012
     -14.0480599999999995 6013 -0.1519400000000000 7014 -3.3876240000000002
     7015 -0.0123760000000000 8016 -70.9272269999999878 8017
     -0.0270180000000000 8018 -0.1457550000000000 11023 -0.1000000000000000
MX29:N     2j 6000 6000 4j MODEL j
MX29:P     0 9j
MT29 lwtr.10t
M30 1001 -10.1988269999999996 1002 -0.0011730000000000 6012
     -12.8608999999999991 6013 -0.1391000000000000 7014 -3.0887160000000002
     7015 -0.0112840000000000 8016 -72.3238249999999994 8017
     -0.0275500000000000 8018 -0.1486250000000000 11023 -0.2000000000000000
MX30:N     2j 6000 6000 4j MODEL j
MX30:P     0 9j
MT30 lwtr.10t
M31 1001 -10.4987925000000004 1002 -0.0012075000000000 6012
     -15.3341499999999993 6013 -0.1658500000000000 7014 -2.4908999999999999
     7015 -0.0091000000000000 8016 -70.4284419999999898 8017
     -0.0268280000000000 8018 -0.1447300000000000 11023 -0.2000000000000000
MX31:N     2j 6000 6000 4j MODEL j
MX31:P     0 9j
MT31 lwtr.10t
M32 1001 -10.6987694999999992 1002 -0.0012305000000000 6012
     -14.1469900000000006 6013 -0.1530100000000000 7014 -2.2916279999999998
     7015 -0.0083720000000000 8016 -71.1267409999999956 8017
     -0.0270940000000000 8018 -0.1461650000000000 11023 -0.2000000000000000
MX32:N     2j 6000 6000 4j MODEL j
MX32:P     0 9j
MT32 lwtr.10t
M33 1001 -10.3988040000000002 1002 -0.0011960000000000 6012
     -13.6523400000000006 6013 -0.1476600000000000 7014 -2.8894440000000001
     7015 -0.0105560000000000 8016 -71.7252830000000046 8017
     -0.0273220000000000 8018 -0.1473950000000000 11023 -0.1000000000000000
MX33:N     2j 6000 6000 4j MODEL j
MX33:P     0 9j
MT33 lwtr.10t
M34 1001 -9.6988845000000001 1002 -0.0011155000000000 6012
     -17.9063300000000005 6013 -0.1936700000000000 7014 -5.2807079999999997
     7015 -0.0192920000000000 8016 -66.1388910000000010 8017
     -0.0251940000000000 8018 -0.1359150000000000 11023 -0.1000000000000000
MX34:N     2j 6000 6000 4j MODEL j
MX34:P     0 9j
MT34 lwtr.10t
```

```
M35 1001 -10.2988155000000017 1002 -0.0011845000000000 6012
     -12.2673199999999998 6013 -0.1326800000000000 7014 -3.0887160000000002
     7015 -0.0112840000000000 8016 -72.9223669999999942 8017
     -0.0277780000000000 8018 -0.1498550000000000 11023 -0.2000000000000000
MX35:N     2j 6000 6000 4j MODEL j
MX35:P     0 9j
MT35 lwtr.10t
M36 1001 -10.4987925000000004 1002 -0.0012075000000000 6012
     -11.2780199999999997 6013 -0.1219800000000000 7014 -2.4908999999999999
     7015 -0.0091000000000000 8016 -74.8177500000000038 8017
     -0.0285000000000000 8018 -0.1537500000000000 11023 -0.1000000000000000
MX36:N     2j 6000 6000 4j MODEL j
MX36:P     0 9j
MT36 lwtr.10t
M37 1001 -10.4987925000000004 1002 -0.0012075000000000 6012
     -11.1790900000000004 6013 -0.1209100000000000 7014 -2.5905360000000002
     7015 -0.0094640000000000 8016 -74.8177500000000038 8017
     -0.0285000000000000 8018 -0.1537500000000000 11023 -0.1000000000000000
MX37:N     2j 6000 6000 4j MODEL j
MX37:P     0 9j
MT37 lwtr.10t
M38 1001 -10.4987925000000004 1002 -0.0012075000000000 6012
     -11.1790900000000004 6013 -0.1209100000000000 7014 -2.5905360000000002
     7015 -0.0094640000000000 8016 -74.8177500000000038 8017
     -0.0285000000000000 8018 -0.1537500000000000 11023 -0.1000000000000000
MX38:N     2j 6000 6000 4j MODEL j
MX38:P     0 9j
MT38 lwtr.10t
M39 1001 -10.1988269999999996 1002 -0.0011730000000000 6012
     -10.9812300000000000 6013 -0.1187700000000000 7014 -3.2879879999999999
     7015 -0.0120120000000000 8016 -74.1194509999999980 8017
     -0.0282340000000000 8018 -0.1523150000000000 11023 -0.1000000000000000
MX39:N     2j 6000 6000 4j MODEL j
MX39:P     0 9j
MT39 lwtr.10t
M40 1001 -10.3988040000000002 1002 -0.0011960000000000 6012
     -11.5748099999999994 6013 -0.1251900000000000 7014 -2.5905360000000002
     7015 -0.0094640000000000 8016 -74.3189649999999915 8017
     -0.0283100000000000 8018 -0.1527250000000000 11023 -0.2000000000000000
MX40:N     2j 6000 6000 4j MODEL j
MX40:P     0 9j
MT40 lwtr.10t
M41 1001 -10.4987925000000004 1002 -0.0012075000000000 6012
     -9.4972799999999999 6013 -0.1027200000000000 7014 -2.5905360000000002
     7015 -0.0094640000000000 8016 -75.9150769999999966 8017
     -0.0289180000000000 8018 -0.1560050000000000 11023 -0.2000000000000000
MX41:N     2j 6000 6000 4j MODEL j
MX41:P     0 9j
MT41 lwtr.10t
M42 1001 -10.5987810000000007 1002 -0.0012190000000000 6012
     -9.8929999999999989 6013 -0.1070000000000000 7014 -2.0923560000000001
     7015 -0.0076440000000000 8016 -76.2143480000000011 8017
     -0.0290320000000000 8018 -0.1566200000000000 11023 -0.2000000000000000
MX42:N     2j 6000 6000 4j MODEL j
MX42:P     0 9j
MT42 lwtr.10t
M43 1001 -10.3988040000000002 1002 -0.0011960000000000 6012
     -21.8635300000000008 6013 -0.2364700000000000 7014 -2.7898079999999998
     7015 -0.0101920000000000 8016 -63.5452089999999998 8017
     -0.0242060000000000 8018 -0.1305850000000000 11023 -0.1000000000000000
MX43:N     2j 6000 6000 4j MODEL j
MX43:P     0 9j
MT43 lwtr.10t
M44 1001 -10.3988040000000002 1002 -0.0011960000000000 6012
     -21.0720899999999993 6013 -0.2279100000000000 7014 -2.8894440000000001
```

```
     7015 -0.0105560000000000 8016 -64.2435080000000056 8017
     -0.0244720000000000 8018 -0.1320200000000000 11023 -0.1000000000000000
MX44:N     2j 6000 6000 4j MODEL j
MX44:P     0 9j
MT44 lwtr.10t
M45 1001 -10.3988040000000002 1002 -0.0011960000000000 6012
     -22.8528300000000009 6013 -0.2471700000000000 7014 -2.7898079999999998
     7015 -0.0101920000000000 8016 -62.5476389999999967 8017
     -0.0238260000000000 8018 -0.1285350000000000 11023 -0.1000000000000000
MX45:N     2j 6000 6000 4j MODEL j
MX45:P     0 9j
MT45 lwtr.10t
M46 1001 -10.3988040000000002 1002 -0.0011960000000000 6012
     -22.8528300000000009 6013 -0.2471700000000000 7014 -2.7898079999999998
     7015 -0.0101920000000000 8016 -62.5476389999999967 8017
     -0.0238260000000000 8018 -0.1285350000000000 11023 -0.1000000000000000
MX46:N     2j 6000 6000 4j MODEL j
MX46:P     0 9j
MT46 lwtr.10t
M47 1001 -10.7987580000000012 1002 -0.0012420000000000 6012
     -4.1550599999999998 6013 -0.0449400000000000 7014 -1.0959960000000002
     7015 -0.0040040000000000 8016 -82.8980669999999975 8017
     -0.0315780000000000 8018 -0.1703550000000000 11023 -0.3000000000000000
MX47:N     2j 6000 6000 4j MODEL j
MX47:P     0 9j
MT47 lwtr.10t
M48 1001 -11.1987120000000004 1002 -0.0012880000000000 6012
     -51.0478799999999993 6013 -0.5521199999999999 7014 -1.0959960000000002
     7015 -0.0040040000000000 8016 -35.7130059999999929 8017
     -0.0136040000000000 8018 -0.0733900000000000 11023 -0.1000000000000000
MX48:N     2j 6000 6000 4j MODEL j
MX48:P     0 9j
MT48 poly.10t
M49 1001 -11.3986890000000010 1002 -0.0013110000000000 6012
     -58.1708399999999912 6013 -0.6291599999999999 7014 -0.7970880000000000
     7015 -0.0029120000000000 8016 -28.6302589999999988 8017
     -0.0109060000000000 8018 -0.0588350000000000 11023 -0.1000000000000000
MX49:N     2j 6000 6000 4j MODEL j
MX49:P     0 9j
MT49 poly.10t
M50 1001 -10.2988155000000017 1002 -0.0011845000000000 6012
     -10.5855099999999993 6013 -0.1144900000000000 7014 -3.1883520000000001
     7015 -0.0116480000000000 8016 -74.4187219999999883 8017
     -0.0283480000000000 8018 -0.1529300000000000 11023 -0.2000000000000000
MX50:N     2j 6000 6000 4j MODEL j
MX50:P     0 9j
MT50 lwtr.10t
M51 1001 -9.9988500000000009 1002 -0.0011500000000000 6012
     -21.9624600000000001 6013 -0.2375400000000000 7014 -2.1919920000000004
     7015 -0.0080080000000000 8016 -64.2435080000000056 8017
     -0.0244720000000000 8018 -0.1320200000000000 11023 -0.1000000000000000
MX51:N     2j 6000 6000 4j MODEL j
MX51:P     0 9j
MT51 lwtr.10t
M52 1001 -10.6987694999999992 1002 -0.0012305000000000 6012
     -0.2967900000000000 6013 -0.0032100000000000 7014 -0.9963600000000000
     7015 -0.0036400000000000 8016 -87.0878609999999895 8017
     -0.0331740000000000 8018 -0.1789650000000000 11023 -0.4000000000000000
MX52:N     2j 6000 6000 4j MODEL j
MX52:P     0 9j
MT52 lwtr.10t
M53 7014 -79.7087999999999965 7015 -0.2912000000000000 8016
     -19.9513999999999996 8017 -0.0076000000000000 8018 -0.0410000000000000
MX53:N     4j MODEL
MX53:P     5j
```

Listing B.23: neutron_dose_equivalent4b.tal

```
F16:n (1016 < 1016[0:253 0:126 0:221] < 403)
c 0.2137 x 0.2137 x 0.8 = 0.036534152 cc
SD16 0.036534152 7161275r
df16 iu=2 fac=-3 ic=99
```

Acknowledgement

Ich möchte an dieser Stelle zuerst meinem Vater danken. Du hast in mir immer mehr gesehen und mir Mut gemacht weiter meinen Weg zu gehen. Ohne dich wäre ich nicht da wo ich jetzt bin und mir würden sicher nicht all die Möglichkeiten offenstehen die es jetzt tun. Das werde ich dir nie vergessen.

I also want to express my deep gratitude towards Prof. Macian. His promotion made it not only possible for me to produce this doctoral thesis, but also to enter the scientific field of medical physics and nuclear engineering. With his help I even found my way to CERN and eventually got the opportunity to work for the LHC project. I am more than grateful for this. I will always stay connected with the NTECH-department and will keep the time with my colleagues, most of all Filippo Pellacani, Dan-Ovidiu Melinte and Andreas Wanninger, in best memory. For sure I will not forget our secretary Petra Popp-Münich. Thank you for all the little helps day to day which made life at NTECH easier when it was hard.

A very special person to me is Maria Kastriotou. Without you I probably wouldn't have managed to finish writing this manuscript. Not being alone while suffering through so many nights and writing in the CERN-library was the greatest support and I am glad that I could return this favor. I thank you so much and I wish you and your young family cordially a warm and bright future.

Then there are Francesca Addesa, Jose Briz Monago and Angelo Infantino which stood by my side in the more difficult times during the past years. I can't tell you, how much this means to me.